

CHARACTERISTICS OF HYDROGEN COMBUSTION IN A DIRECT
INJECTED CONSTANT VOLUME COMBUSTION CHAMBER
USING RAINBOW SCHLIEREN DEFLECTOMETRY

by

TANISHA LATRINA BOOKER

AJAY K. AGRAWAL, COMMITTEE CHAIR

MARCUS D. ASHFORD, CO-CHAIR

JOHN BAKER

K. CLARK MIDKIFF

SEMIH OLCMEN

PAULIUS PUZINAUSKAS

A DISSERTATION

Submitted in partial fulfillment of the requirements
for the degree of Doctor of Philosophy
in the Department of Engineering
in the Graduate School of
The University of Alabama

TUSCALOOSA, ALABAMA

2011

Copyright Tanisha Latrina Booker 2011
ALL RIGHTS RESERVED

ABSTRACT

The nation's need for alternative fuels for Internal Combustion Engines (ICEs) has been a major concern for automotive researchers. The need for a sustainable energy system has lead researchers to consider alternative fuels such as hydrogen and thus, several studies have been conducted on this fuel since the 1930s. In particular, understanding the combustion performance of hydrogen at varying equivalence ratios, ignition timings, and volumetric percentages with other fuels is necessary to optimize engine operations. This study investigates the combustion performance of hydrogen injected into a constant volume combustion chamber (CVCC). The properties studied include flame structure, combustion duration, flame front speed, chamber pressure, and net heat transfer rate. The fuel was injected directly into the chamber containing quiescent air at atmospheric pressure. An ignition system consisting of a coil and a spark plug was used to ignite fuel/air mixtures. This study implemented an optical technique, Rainbow Schlieren Deflectometry, to visualize fuel jet penetration, turbulent fuel-air mixing, flame structure, and flame propagation. Schlieren images were analyzed by a cross-correlation technique to compute flame front speed. A dynamic pressure sensor was used to acquire instantaneous chamber pressures which were used to estimate transient chamber net heat transfer rates.

First, experiments were conducted by varying the fuel supply pressure to the chamber and the overall equivalence ratio. An investigation of the fuel jet penetration showed that it takes the fuel jet 2.25 ms to reach the igniter. This result was helpful in establishing ignition times for

later experiments. Results showed that fuel supply pressure does not affect fuel jet penetration. The fuel jet, however, creates turbulence in the chamber that affects combustion processes. The equivalence ratios tested were $\phi = 1.0, 0.804,$ and 0.318 . Results showed that equivalence ratio has a significant impact on flame front speed which decreased as the equivalence ratio decreased.

Next, experiments were conducted to study the effects of ignition time on combustion processes. A programmable logic controller was added to the experimental setup to control ignition time and aid in sequencing events. The ignition times tested were $t = 3, 5,$ and 10 ms in the early ignition group, $t = 20, 30,$ and 40 ms in the mid-ignition group, and $t = 60, 80, 240,$ and 540 ms in the late ignition group, where $t = 0$ refers to the start of fuel injection. Ignition time affects the flame structure and flame propagation. Results showed that at ignition times prior to the close of the fuel injector, the initial flame front speed is high because of fuel-jet generated turbulence. After the fuel injector closes, increasing the ignition time increases the combustion duration because of dissipating fuel-jet generated turbulence. Ignition time also has significant effects on chamber pressure variations and net heat transfer rates.

Next, the effect of ignition time for varying equivalence ratios was studied. Experiments were conducted at three equivalence ratios, $\phi = 0.6, 0.8,$ and 1.0 and four ignition times, $t = 3$ ms, 10 ms, t_{end} , and $t_{\text{end}} + 50$ ms. An ultra-high speed camera was incorporated into the experimental setup to acquire schlieren images at a frame rate of $50,000$ Hz and exposure time of $19.8\mu\text{s}$. Results show that equivalence ratio has minor effects on chamber pressure variations and net heat transfer rate at early ignition times and on flame structure and flame propagation at any ignition times. Ignition time has a significant effect on all combustion processes.

Finally, experiments were conducted to determine the effect of hydrogen percentages by volume on methane combustion at varying ignition times. A second high pressure injector was

incorporated into the experimental setup to inject the methane into the combustion chamber. Experiments were conducted at the following methane/hydrogen percentages: 23% CH₄ – 77% H₂, 33% CH₄ – 67% H₂, 43% CH₄ – 57% H₂, 53% CH₄ – 47% H₂, and 63% CH₄ – 37% H₂. The two ignition times were $t = t_{\text{end}}$ and $t = t_{\text{end}} + 50$ ms. Results show that combustion duration decreases as hydrogen percentage increases for identical ignition times, and as ignition time decreases at identical hydrogen percentages. Flame front speed increases as hydrogen percentage increases. Peak chamber pressure and peak net heat transfer rate decreases for the late ignition time at fixed hydrogen percentages.

LIST OF ABBREVIATIONS AND SYMBOLS

a_f	Band Pass Filtered Accelerometer Signals
AI	Accelerometer Intensities
ATDC	After Top Dead Center
BMEP	Brake Mean Effective Pressure
BNC	Bayonet-Neill-Concelman
BSFC	Brake Specific Fuel Consumption
BTDC	Before Top Dead Center
BTE	Brake Thermal Efficiency
CFR	Cooperative Fuel Research
CH ₄	Methane
CI	Compression Ignition
CO	Carbon Monoxide
CO ₂	Carbon Dioxide
COD	Coefficient of Determination
C _p	Specific Heat
CVCC	Constant Volume Combustion Chamber
DAQ	Data Acquisition System
DC	Direct Current
DISI	Direct Injected Spark Ignition
E _{fuel}	Energy of Fuel

FFT	Fast Fourier Transform
fps	Frames per second
H ₂	Hydrogen
ICE	Internal Combustion Engine
I/O	Input/Output
L	Distance from Injector
LED	Light Emitting Diode
LHV	Lower Heating Value
m	Mass
M	Molar Mass
<i>N</i>	Number Of Combustion Cycles
N	Number of Moles
NO _x	Nitrogen Oxides
1D	One Dimensional
P	Pressure
<i>p_f</i>	Band Pass Filtered Pressure Signals
PI	Pressure Intensities
PLC	Programmable Logic Controller
PM	Particulate Matter
PP	Peak Pressure
<i>Q</i>	Net Heat Transfer
rpm	Revolutions Per Minute
RSD	Rainbow Schlieren Deflectometry

s	Flame Front Speed
SEC	Specific Energy Consumption
SI	Spark-Ignition
SSR	Solid State Relay
T	Temperature
t	Time
TDC	Top Dead Center
TMI	Timed Manifold Injection
UHC	Unburned Hydrocarbons
v	Molar Specific Volume
V	Volume
φ, ϕ	Equivalence Ratio
μ	Micro

ACKNOWLEDGMENTS

I first thank God, who allowed me to overcome many obstacles that have presented themselves throughout my life and who allowed me to use my knowledge and critical thinking skills to reach this level in my education.

This dissertation is dedicated to my son, Corliss Okane Booker, my parents, West and Martha Booker, my brother Keith Holder, and my aunt, Thelma Holder who sacrificed family time, worked for me in other capacities, supported, and guided me so that I might accomplish this major achievement in my life.

I want to thank Dr. Ajay K. Agrawal, research advisor and dissertation committee chair. His dedication, time, concern, and professionalism are truly appreciated. I want to specially thank Dr. Robert Taylor for his assistance in many aspects of my life. I want to thank my other committee members, Dr. Marcus D. Ashford, Dr. Paulius Puzinauskas, Dr. Kenneth C. Midkiff, Dr. John Baker, and Dr. Semih Olcmen, for their time and input to my research. I want to thank other University of Alabama Department of Mechanical Engineering professors and staff members for their assistance. I am indebted to group members Troy Dent, Tad Driver, Lulin Jiang, Pankaj Kolhe, Joseph Meadows, Dan Mitchell, Yonas Niguse, Heena Panchasara, Daniel Sequera, Benjamin Simmons, Zack Smith, and Justin Williams for their assistance in my research.

I am grateful for my close friends Aaron Adams, Allison Copus, Mebougna Drabo, Felicia Grace, Amanda Lard, Treasure Lyons, and Courtney McNeil.

TABLE OF CONTENTS

ABSTRACT	ii
LIST OF ABBREVIATIONS AND SYMBOLS	v
ACKNOWLEDGMENTS	viii
LIST OF TABLES	xi
LIST OF FIGURES	xii
1. INTRODUCTION	1
1.1 Hydrogen As An Alternative Fuel	1
1.2 Abnormal Combustion Associated With The Use Of Hydrogen	2
1. Knock.....	2
2. Backfire.....	5
3. Pre-Ignition	7
1.3 Objective of the Present Study.....	11
2. COMBUSTION CHARACTERISTICS OF A HYDROGEN JET INJECTED INTO A CLOSED VESSEL	20
3. THE EFFECT OF IGNITION TIME ON COMBUSTION OF STRATIFIED HYDROGEN- AIR MIXTURES IN A CONSTANT VOLUME CHAMBER	56
4. HYDROGEN COMBUSTION IN A STRATIFIED CONSTANT VOLUME COMBUSTION CHAMBER USING ULTRA HIGH SPEED IMAGING	94
5. THE EFFECT OF METHANE/HYDROGEN FRACTIONS AND IGNITION TIME ON COMBUSTION IN A CONSTANT VOLUME COMBUSTION CHAMBER	144

6. CONCLUSIONS AND RECOMMENDATIONS	184
6.1 Conclusions.....	184
6.2 Recommendations.....	185
REFERENCES	186
APPENDIX A.....	188
APPENDIX B.....	189
APPENDIX C.....	190
APPENDIX D.....	191
APPENDIX E.....	192
APPENDIX F.....	193
APPENDIX G.....	194
APPENDIX H.....	195
APPENDIX J.....	197
APPENDIX K.....	200
APPENDIX L.....	202
APPENDIX M.....	205

LIST OF TABLES

2.1 Elapsed Flame Propagation Time for Varying Supply Pressures	51
5.1 Mass and injector duration for varying methane/hydrogen fractions	153

LIST OF FIGURES

1.1	Correlation between data pairs (PP, PI) (top) and (AI, PI) (bottom) based on individual combustion event basis, 300 engine cycles with fixed ignition timing (0bTDC—hydrogen, 2bTDC—gasoline). (a and c) Hydrogen and (b and d) Gasoline [Szwaja et al., 2007]. (Plot from Int. J. of Hydrogen Energy 32 (2007), Figure 3)	13
1.2	Correlation between mean AI and mean PI for hydrogen combustion at spark timing varying at the range from 4 ° BTDC to 12 ° ATDC [Szwaja et al., 2007]. (Plot from Int. J. of Hydrogen Energy 32 (2007), Figure 4)	14
1.3	FFTs of in-cylinder pressure and accelerometer signals computed from 300 combustion events for hydrogen and gasoline. (a) FFT Pressure (hydrogen); (b) FFT Pressure (gasoline); (c) FFT accelerometer (hydrogen); (d) FFT accelerometer (gasoline) [Szwaja et al., 2007]. (Plot from Int. J. of Hydrogen Energy 32 (2007), Figure 5)	15
1.4	The variations of operational limits for pre-ignition with compression ratio changes [Maher & Al-Baghdadi, 2004]. (Plot from Renewable Energy 29 (2004), Figure 2)	16
1.5	The variations of operational limits for pre-ignition with engine speed changes [Maher & Al-Baghdadi, 2004]. (Plot from Renewable Energy 29 (2004), Figure 3)	17
1.6	Effect of compression ratio and equivalence ratio on the indicated thermal efficiency [Maher & Al-Baghdadi, 2004]. (Plot from Renewable Energy 29 (2004), Figure 8)	18
1.7	Effect of compression ratio and equivalence ratio on the specific fuel consumption [Maher & Al-Baghdadi, 2004]. (Plot from Renewable Energy 29 (2004), Figure 9)	19
2.1	Experimental Setup	34
2.2	Combustion Vessel; a) Front View, b) Side View, c) Isometric View	35
2.3	Combustion Vessel	36
2.4	Drawing of Window Collar	37
2.5	Fuel Flow System	38
2.6	Data Acquisition System	39
2.7	Test Vessel System; a) Test Vessel, b) Pressure Sensor, c) Supply Pressure Regulator ...	40
2.8	Injector Calibration Plot for $P_s = 275.8$ kPa, 413.7 kPa, and 551.6 kPa	41

2.9	Rainbow Schlieren Deflectometer; a) Illuminator, b) Aperture, c) Collimating Lens, d) Test Media (Combustion Chamber), e) Decollimating Lens, f) Rainbow Filter, and g) High Speed Camera	42
2.10	Illuminator and Aperture	43
2.11	Gooseneck Fiber Optic Cable (Drawing from Fiber Optic Systems, Inc.)	43
2.12	Collimating Lens, Combustion Chamber, and Decollimating Lens	44
2.13	Rainbow Filter and High Speed Camera	45
2.14	Jet Penetration Distance (L) After Time (t) For Varying Equivalence Ratios, $P_s=275.8$ kPa	46
2.15	Jet Penetration Distance (L) After Time (t) For Varying Supply Pressures, $\phi = 1$	47
2.16	Schlieren Images (250 μ s Intervals) For $P_s=413.7$ kPa and $\phi = 1$	48
2.17	Space-Time Images For $P_s=413.7$ kPa and $\phi = 1$	49
2.18	Schlieren Images (250 μ s Intervals) For $P_s= 275.8$ kPa and $\phi = 1$	50
2.19	Schlieren Images (250 μ s Intervals) For $P_s=413.7$ kPa and $\phi = 0.804$	52
2.20	Schlieren Images (250 μ s Intervals) For $P_s=413.7$ kPa and $\phi = 0.318$	53
2.21	Centerline Flame Velocity For $P_s=275.8$ kPa and Varying Equivalence Ratio	54
2.22	Centerline Flame Velocity For $P_s=413.7$ kPa and Varying Equivalence Ratio	55
3.1	Combustion Chamber	71
3.2	Fuel Flow System	72
3.3	Rainbow Schlieren Deflectometer; a) Illuminator, b) Aperture, c) Collimating Lens, d) Test Media (Combustion Chamber), e) Decollimating Lens, f) Rainbow Filter, and g) High Speed Camera	73
3.4	Ignition Time Groups	74
3.5	Schlieren Images (200 μ s intervals) for $t = 3$ ms	75
3.6	Schlieren Images (200 μ s intervals) for $t = 5$ ms	76
3.7	Schlieren Images (200 μ s intervals) for $t = 10$ ms	77

3.8	Flame front speed for $t = 3, 5,$ and 10 ms	78
3.9	Schlieren Images ($200 \mu\text{s}$ intervals) for $t = 20$ ms	79
3.10	Schlieren Images ($200 \mu\text{s}$ intervals) for $t = 30$ ms	80
3.11	Schlieren Images ($200 \mu\text{s}$ intervals) for $t = 40$ ms	81
3.12	Flame front speed for $t = 20, 30,$ and 40 ms	82
3.13	Schlieren Images ($200 \mu\text{s}$ intervals) for $t = 60$ ms	83
3.14	Schlieren Images ($200 \mu\text{s}$ intervals) for $t = 80$ ms	84
3.15	Schlieren Images ($200 \mu\text{s}$ intervals) for $t = 240$ ms	85
3.16	Schlieren Images ($200 \mu\text{s}$ intervals) for $t = 540$ ms	86
3.17	Flame front speed for $t = 60, 80, 240,$ and 540 ms	87
3.18	Chamber Pressure for $t = 3, 5,$ and 10 ms	88
3.19	Chamber Pressure for $t = 20, 30,$ and 40 ms	89
3.20	Chamber Pressure for $t = 60, 80, 240,$ and 540 ms	90
3.21	Net heat transfer rates for $t = 3, 5,$ and 10 ms	91
3.22	Net heat transfer rates for $t = 20, 30,$ and 40 ms	92
3.23	Net heat transfer rates for $t = 60, 80, 240$ and 540 ms	93
4.1	Combustion Vessel	112
4.2	Fuel Flow System	113
4.3	Rainbow Schlieren Deflectometer; a) Illuminator, b) Aperture, c) Collimating Lens, d) Test Media (Combustion Chamber), e) Decollimating Lens, f) Rainbow Filter, and g) High Speed Camera	114
4.4	Schlieren Images ($100 \mu\text{s}$ intervals) for $\phi = 0.6$ and $t = 3$ ms	115
4.5	Schlieren Images ($100 \mu\text{s}$ intervals) for $\phi = 0.8$ and $t = 3$ ms	116
4.6	Schlieren Images ($100 \mu\text{s}$ intervals) for $\phi = 1.0$ and $t = 3$ ms	117

4.7	Schlieren Images (100 μ s intervals) for $\varphi = 0.6$ and $t = 10$ ms	118
4.8	Schlieren Images (100 μ s intervals) for $\varphi = 0.8$ and $t = 10$ ms	119
4.9	Schlieren Images (100 μ s intervals) for $\varphi = 1.0$ and $t = 10$ ms	120
4.10	Schlieren Images (100 μ s intervals) for $\varphi = 0.6$ and $t = t_{\text{end}}$	121
4.11	Schlieren Images (100 μ s intervals) for $\varphi = 0.8$ and $t = t_{\text{end}}$	122
4.12	Schlieren Images (100 μ s intervals) for $\varphi = 1.0$ and $t = t_{\text{end}}$	123
4.13	Schlieren Images (100 μ s intervals) for $\varphi = 0.6$ and $t = t_{\text{end}} + 50$ ms	124
4.14	Schlieren Images (100 μ s intervals) for $\varphi = 0.8$ and $t = t_{\text{end}} + 50$ ms	125
4.15	Schlieren Images (100 μ s intervals) for $\varphi = 1.0$ and $t = t_{\text{end}} + 50$ ms	126
4.16	Pathlines of specified structures for $t = 3$ ms and $\varphi = 0.6$	127
4.16a	Flame front speeds for corresponding pathlines for $t = 3$ ms and $\varphi = 0.6$	127
4.17	Pathlines of specified structures for $t = 3$ ms and $\varphi = 0.8$	128
4.17a	Flame front speeds for corresponding pathlines for $t = 3$ ms and $\varphi = 0.8$	128
4.18	Pathlines of specified structures for $t = 3$ ms and $\varphi = 1.0$	129
4.18a	Flame front speeds for corresponding pathlines for $t = 3$ ms and $\varphi = 1.0$	129
4.19	Pathlines of specified structures for $t = t_{\text{end}}$ and $\varphi = 0.6$	130
4.19a	Flame front speeds for corresponding pathlines for $t = t_{\text{end}}$ and $\varphi = 0.6$	130
4.20	Pathlines of specified structures for $t = t_{\text{end}}$ and $\varphi = 0.8$	131
4.20a	Flame front speeds for corresponding pathlines for $t = t_{\text{end}}$ and $\varphi = 0.8$	131
4.21	Pathlines of specified structures for $t = t_{\text{end}}$ and $\varphi = 1.0$	132
4.21a	Flame front speeds for corresponding pathlines for $t = t_{\text{end}}$ and $\varphi = 1.0$	132
4.22	Pathlines of specified structures for $t = t_{\text{end}} + 50$ ms and $\varphi = 0.6$	133
4.22a	Flame front speeds for corresponding pathlines for $t = t_{\text{end}} + 50$ ms and $\varphi = 0.6$	133

4.23	Pathlines of specified structures for $t = t_{\text{end}} + 50$ ms and $\phi = 0.8$	134
4.23a	Flame front speeds for corresponding pathlines for $t = t_{\text{end}} + 50$ ms and $\phi = 0.8$	134
4.24	Pathlines of specified structures for $t = t_{\text{end}} + 50$ ms and $\phi = 1.0$	135
4.24a	Flame front speeds for corresponding pathlines for $t = t_{\text{end}} + 50$ ms and $\phi = 1.0$	135
4.25	Chamber pressure at varying equivalence ratios for $t = 3$ ms	136
4.26	Chamber pressure at varying equivalence ratios for $t = 10$ ms	137
4.27	Chamber pressure at varying equivalence ratios for $t = t_{\text{end}}$	138
4.28	Chamber pressure at varying equivalence ratios for $t = t_{\text{end}} + 50$ ms	139
4.29	Net heat transfer rates at varying equivalence ratios for $t = 3$ ms	140
4.30	Net heat transfer rates at varying equivalence ratios for $t = 10$ ms	141
4.31	Net heat transfer rates at varying equivalence ratios for $t = t_{\text{end}}$	142
4.32	Net heat transfer rates at varying equivalence ratios for $t = t_{\text{end}} + 50$ ms	143
5.1	Combustion Vessel	161
5.2	Fuel Flow System	162
5.3	Rainbow Schlieren Deflectometer; a) Illuminator, b) Aperture, c) Collimating Lens, d) Test Media (Combustion Chamber), e) Decollimating Lens, f) Rainbow Filter, and g) High Speed Camera	163
5.4	Schlieren images (500 μ s intervals) for 23% $\text{CH}_4 - 77\%$ H_2 for $t = t_{\text{end}}$	164
5.5	Schlieren images (500 μ s intervals) for 23% $\text{CH}_4 - 77\%$ H_2 for $t = t_{\text{end}} + 50$ ms	165
5.6	Schlieren images (500 μ s intervals) for 63% $\text{CH}_4 - 37\%$ H_2 for $t = t_{\text{end}}$	166
5.7	Schlieren images (500 μ s intervals) for 63% $\text{CH}_4 - 37\%$ H_2 for $t = t_{\text{end}} + 50$ ms ..	167-168
5.8	Combustion Duration For Varying Ignition Times	169
5.9	Pathlines at 23% $\text{CH}_4 - 77\%$ H_2 for $t = t_{\text{end}}$	170
5.9a-e	Flame front speed for each pathline in Figure 9	170

5.10	Pathlines at 23% CH ₄ – 77% H ₂ for t = t _{end} + 50 ms	171
5.10a	eFlame front speed for each pathline in Figure 10	171
5.11	Pathlines at 63% CH ₄ – 37% H ₂ for t = t _{end}	172
5.11a	eFlame front speed for each pathline in Figure 11	172
5.12	Pathlines at 63% CH ₄ – 37% H ₂ for t = t _{end} + 50 ms	173
5.12a	eFlame front speed for each pathline in Figure 12	173
5.13	Pressure at 23% CH ₄ – 77% H ₂ for varying ignition times	174
5.14	Pressure at 33% CH ₄ – 67% H ₂ for varying ignition times	175
5.15	Pressure at 43% CH ₄ – 57% H ₂ for varying ignition times	176
5.16	Pressure at 53% CH ₄ – 47% H ₂ for varying ignition times	177
5.17	Pressure at 63% CH ₄ – 37% H ₂ for varying ignition times	178
5.18	Net heat transfer rates at 23% CH ₄ – 77% H ₂ for varying ignition times	179
5.19	Net heat transfer rates at 33% CH ₄ – 67% H ₂ for varying ignition times	180
5.20	Net heat transfer rates at 43% CH ₄ – 57% H ₂ for varying ignition times	181
5.21	Net heat transfer rates at 53% CH ₄ – 47% H ₂ for varying ignition times	182
5.22	Net heat transfer rates at 63% CH ₄ – 37% H ₂ for varying ignition times	183

CHAPTER 1

INTRODUCTION

1.1 Hydrogen As An Alternative Fuel

The main focus of this research is to investigate hydrogen as an alternative fuel for use in spark-ignited Internal Combustion Engines (ICEs). The search for alternative fuels for ICEs has been pursued for decades. This search is promoted by several factors including the expected future depletion of fossil fuels and hazardous emissions of pollutants from these fuels. In the automotive industry, most spark-ignited ICEs use gasoline as the fuel source while compression-ignition engines use diesel as the fuel source. Harmful pollutants such as oxides of nitrogen (NO_x), unburned hydrocarbons (UHC), carbon monoxide (CO), and particulate matter (PM) are emitted from the combustion of these fuels, which threaten all forms of life. As the demand for fuel increases in the United States and other countries, the availability of fossil fuels is steadily decreasing.

One promising alternative fuel for use in ICEs is hydrogen. Extensive research on the use of hydrogen as an alternative fuel has been conducted since the 1930's [Das, 1990; Das et al., 2000; Maher & Al-Baghdadi, 2004; Srivastva & Agarwal, 2008; Szwaja et al., 2007; Verhelst & Sierens, 2007; Verhelst et al., 2006; Wallner & Lohse-Busch, 2007; Wimmer & Wallner, 2005]. Advantages associated with hydrogen-fueled ICEs include near zero emissions of CO, NO_x , and UHC and zero emissions of carbon dioxide (CO_2). Hydrogen's combustion properties make it a desired fuel as it improves cold start capabilities. The main product of hydrogen combustion is water.

Comparing with liquid fuels, hydrogen does not experience vapor lock, poor mixing, inadequate vaporization, and cold wall quenching to the degree of hydrocarbon (HC) fuels [Szwaja et al., 2007]. If hydrogen is so advantageous, why is it not being used as the main energy source in engines? There are problems associated with hydrogen-fueled engines that must be evaluated and corrected. Knock, pre-ignition, and backfire are combustion problems that must be carefully monitored as they are true obstacles with the use of hydrogen-fueled engines. These abnormal combustion processes affect the overall operating performance and efficiency of ICEs. They limit operating parameters such as the range of equivalence ratios and compression ratios. Also, heat loss through cylinder walls can be much higher for hydrogen combustion compared to conventional fuels because the flame approaches the wall so closely, which negatively affect the overall thermal efficiency.

1.2 Abnormal Combustion Associated With The Use Of Hydrogen

This research will attempt to provide fundamental understanding of problems associated with the use of hydrogen in ICEs. Some problems associated with the use of hydrogen develop as a result of the combustion process and they include knock, backfire, and pre-ignition. Researchers have studied these issues and provided results pertaining to how these issues limit engine operating performance. This section will summarize previous experimental work in the area of abnormal combustion with the use of hydrogen.

1. Knock

Methods for controlling combustion knock in hydrogen-fueled internal combustion engines have been a challenge for researchers. Knock is a major limiting factor for the operating performance of spark-ignited hydrogen-fuelled engines. At equivalence ratios near stoichiometric conditions, the occurrence of knock is greater and therefore leaner mixtures must

be used. This limits the torque output and overall engine performance according to Szwaja et al. [2007]. The purpose of the research in the article was to determine ways to adequately detect knock in hydrogen-fueled engines. This would allow engine operations closer to limitations of knock and thus increase engine performance and reduce the possibility of damage to the engine from knock.

The study was conducted using a port-injected, single-cylinder, spark-ignited cooperative fuel research (CFR) engine. The experimental operating parameters were:

- Compressed hydrogen and 87 octane rated gasoline
- In-cylinder mixture equivalence ratios of 1.0
- E_{fuel} (energy of fuel of a single dose) = 750 J
- Spark timing ranging from 5 degrees BTDC (before top dead center of the compression stroke) to 12 degrees ATDC (after top dead center)
- Compression ratio of 12:1
- Engine speed of 900 rpm

One result of the experiment was that gasoline knock and hydrogen knock have similar peak amplitudes and similar duration and decay rate of oscillations. Pressure intensities (PI), accelerometer intensities (AI), and peak pressure (PP) knock meters were used to quantify the intensity of the knock in the engine for both fuels. The equations used for PI and AI were as follows:

$$PI(N) = \frac{1}{t_2 - t_1} \int_{t_1 = t_{\theta_1}}^{t_2 = t_{\theta_2}} p_f \, dt = \frac{1}{N} \sum_{i=1}^N p_f \, i$$

$$AI(N) = \frac{1}{t_2 - t_1} \int_{t_1}^{t_2} a_f(t) dt = \frac{1}{N} \sum_{i=1}^N a_f(i)$$

whereas p_f and a_f are respectively band pass filtered (4-15 kHz) pressure signals and band pass filtered (4-15 kHz) accelerometer signals and N represents the number of combustion cycles.

Data pairs (PI, AI) and (PI, PP) were plotted and fitted using a linear equation. A coefficient of determination (COD) was computed using least squares analysis. A COD of “0” represented no correlation and a COD of “1” represented an exact correlation. From the graph using data pairs (PI, PP), Figure 1, hydrogen’s COD value was 0.93 and gasoline’s COD was 0.98.

This result suggests that peak pressure and pressure intensities are highly correlated. Data pairs (PI, AI) were also plotted for gasoline and hydrogen. From these plots, Figure 1 (c and d), hydrogen’s COD value was 0.62 and gasoline’s COD value was 0.64. These values were slightly above the 0.6 criteria and suggest sufficient correlation between pressure intensities and accelerometer intensities. This result supports the prospects of closed loop control of engine knock using accelerometers for both fuels. As knock level changed, correlations between AI –PI and PP-PI became stronger. For the PI range of 1 to 50 kPa for hydrogen combustion, at spark timing varying from 4 degrees before top dead center (BTDC) to 12 degrees after top dead center (ATDC), the PI-AI COD value was 0.959 and the PI-PP COD value was 0.992, as shown in Figure 2. This correlation suggests that AI metric, with the removal of signal noise, can be used as a control signal for engine knock in hydrogen combustion.

Studies were also conducted to analyze the frequency components of pressure waves resulting from knock. The Fast Fourier Transform (FFT) of pressure signals and acceleration signals were computed for each combustion event. The results in Figure 3 show differences in

the frequency peaks for hydrogen and gasoline fuels. These differences mainly result from differences in mean gas temperature and differences in crank position for maximum peak pressures of knock during combustion.

Hydrogen and gasoline combustion properties differ from each other. Hydrogen has a higher flame speed at stoichiometric conditions than gasoline. Hydrogen has wider flammability limits than gasoline. Hydrogen also has lower ignition energy and higher autoignition temperatures compared to those of gasoline. Hydrogen's high diffusivity, added to the fact that it is injected as a gas, attributes to greater homogeneity in a mixture with air than liquid gasoline. Thus, hydrogen combustion at an equivalence ratio of 1.0 has reduced combustion time. Therefore end gases spend less time at higher temperatures where autoignition for knock occurs. Hydrogen-air in-cylinder charge has a higher temperature than the gasoline-air charge because of the cooling effect by vaporization of gasoline. These differences point to the changes required for detection and control of knock in hydrogen ICEs.

2. Backfire

Ignition energy is the minimum amount of spark energy required to ignite a mixture. Hydrogen's low ignition energy contributes to abnormal combustion such as backfire and pre-ignition. According to Verhelst et al. [2006], earlier literature cites causes of backfire as:

- Hot spots in the cylinder, particulates, deposits, overheated spark plugs, heated exhaust valves, etc. These hot spots would easily ignite hydrogen because of its low ignition energy and wide flammability limits.
- Low ion concentration in hydrogen/air flame, as compared to hydrocarbon/air flame, causes residual energy in the ignition circuit.

- Ignition in one cylinder causes induced ignition in another cylinder because ignition cables may be placed too close together.
- Combustion on top of the piston leads back up to the inlet valve opening and ignites fresh mixture.
- Pre-ignition in the hydrogen-fueled engine causes an increase in the temperature of the hot spot that led to pre-ignition. This causes another pre-ignition event which again increases the temperature of the hot spot. This process continues until the hot spot reaches the intake valve and causes backfire.

However, in these authors' opinion, the low ignition energy of hydrogen is too easily attributed as the cause of backfire. Hydrogen has a high autoignition temperature. It is unlikely that thermal masses such as inlet valves, spark plugs, and residual gases will reach autoignition temperatures and induce backfire. Also, hydrogen fueled engines require high compression ratios for self-ignition. Therefore, it is highly unlikely that residual gas temperatures would be high enough to initiate ignition. Deposits and particulates are present in low concentration in well-kept hydrogen engines. Therefore they are unlikely to be the cause of backfires. This article related to experiments conducted by eliminating hot spots and uncontrolled spark-induced ignition, but backfire still occurred. The small quenching distance along with the wide flammability limits of hydrogen are therefore more likely causes of backfire. With careful selection of crevice volume and piston rings, hydrogen engines have been ran without the presence of backfire even at stoichiometric conditions. There are some disagreements on the relationship between compression ratio and the incidence of backfire among researchers. Since all of the reasons mentioned above may be probable causes of backfire, engine design should concentrate on controlling these factors.

According to Das et al. [2000], the method of fuel induction plays an important role in the engine performance and emission characteristics of hydrogen-fueled spark-ignited engines. These authors also suggest that fuel formulation techniques in hydrogen engines influence abnormal combustion problems such as backfire and knock. Due to stringent requirements of an engine operating on hydrogen, they studied several methods of fuel induction such as timed manifold injection, carburetion, low pressure direct cylinder injection, and continued manifold injection. Backfire was uncontrollable and severe with carburetion and continuous manifold injection. Timed manifold injection (TMI) system proved to be very effective for a hydrogen-fueled engine.

3. Pre-Ignition

Pre-ignition is the ignition of a fuel-air mixture preceding timed ignition. Pre-ignition near the inlet valve is referred to as backfire. Pre-ignition away from the inlet valve results in engine knock and decreases or deteriorates engine power output and overall engine efficiency. It can lead to excessive temperatures in the engine cylinder and thus raise the possibility of detonation. After spark ignition has occurred in one part of the cylinder, detonation causes thermal ignition in another part. Combustion waves from these two ignition points give rise to excessive pressure rise rate. The hydrogen-air mixture composition affects the detonation velocity [Das, 1990]. Das [1990] also report that the energy requirement for ignition is an order of magnitude less for hydrogen as compared to gasoline. This lower energy requirement ensures prompt ignition but also increases the possibility of pre-ignition. Hydrogen has a wide flammability range – between 4 and 75% by volume. Hydrogen percentage in stoichiometric fuel-air mixture is 29.6% by volume. Because the lean flammability limit is considerably lower than the stoichiometric value, hydrogen fuelled engines can operate with reduced harmful

emissions. According to Verhelst et al. [2006], pre-ignition limits operating conditions including compression ratio, mixture equivalence ratios, and spark timing of hydrogen-fueled spark-ignited engines. Direct injection was shown to be more favorable in preventing backfire than port fuel injection. The maximum power output can be increased using direct injection since richer mixtures close to stoichiometric ratio can be utilized without the threat of backfire. However, pre-ignition can still occur. Late injection can be used to avoid pre-ignition.

Pre-ignition damage according to Heywood [1988] is mostly thermal. Spark plug fusion and piston holing are evidence of pre-ignition damage. Review by Das [1990] identified causes of pre-ignition as hot spots on spark plugs, exhaust valves, sharp projections from casting imperfections, deposits, or particulate matter from either pyrolysis of lubricating oil vapour or inert dust in the air from the intake system. Pre-ignition is more likely to occur during the intake stroke. It leads to extremely high combustion temperatures, rough running, and a decrease in thermal efficiency. The extremely high combustion temperatures lead to detonation. Water injection is a technique proposed to reduce the likelihood of pre-ignition. Water injection cools hot spots and increases the required ignition energy level. This can be done by either spraying the water into the hydrogen stream before it mixes with air or spraying the water into the hydrogen-air mixture in the intake manifold. Das [1990] also pointed out that pre-ignition can be the cause of manifold explosion. From their investigations a correlation between engine speed and detonation level was developed. They found that as engine speed increased from 1500 rpm to 3000 rpm, detonation level dropped from 55 to 30%.

Maher and Al-Baghdadi [2004] developed an analytical model to study the effects of compression ratio, equivalence ratio, and engine speed on the overall performance and emissions of hydrogen-fueled internal combustion engines. Their model was a quasi 1D model that

simulated the compression, combustion, and expansion processes of a hydrogen-fueled spark-ignited engine. They divided the engine cylinder into burned and unburned zones that were separated by a flame front. The zones were analyzed using equations of state, conservation of mass and volume, and the first law of thermodynamics. They developed a system of first order differential equations for the pressure, volume, temperature, mass, heat transfer and mass flow of the two zones. The mass burning rate was given by

$$\frac{dM_b}{dt} = A_{fl} \cdot \rho \cdot S_T$$

A semi-empirical formula was used for the turbulent flame front speed.

$$S_T = 5000 \cdot 0.1 \text{rpm} \cdot B \cdot S \cdot P / T_b^{1.67} \cdot T_b^{0.41} \cdot T_u^{1.25} \cdot \frac{R_{mol}}{EH} \times \frac{X_f \cdot 1 - \varphi \cdot 1 - \frac{R_{mol} \cdot T_b^2}{EH \cdot T_b - T_u}}{\varphi} \times \exp \frac{-EH}{2 \cdot R_{mol} \cdot T_b} \quad 0.5$$

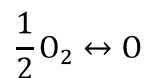
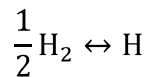
A semi-empirical formula was used for the heat interaction between the fluid and wall.

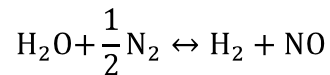
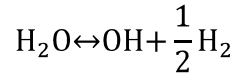
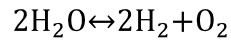
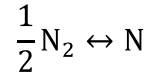
$$-\frac{dQ_{ht}}{dt} = A \cdot 0.26 \frac{k}{B} \frac{U_p \cdot B}{\mu}^{0.7} T - T_w + 0.69 \sigma T^4 - T_w^4$$

A semi-empirical formula was used for the instantaneous energy flow to the crevices.

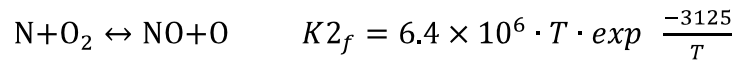
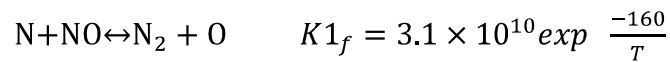
$$\frac{dQ_{cr}}{d\theta} = e + R_{mol} \cdot T \cdot \frac{dN_{cr}}{d\theta}$$

The concentration of the combustion products was determined using ten species and the following reactions:





The chemical equilibrium assumption was used to compute species concentrations and Thermodynamic properties. NO_x formation was determined using the extended Zeldovich mechanism.



The model was applied to an engine with the following specifications:

- Engine Type: Ricardo E6/US single cylinder four stroke
- Bore: 76.2mm
- Connecting Rod Length: 241.3mm
- Stroke: 110mm
- Variable Compression Ratios
- Variable Engine Speed
- Variable Equivalence Ratios

The results of the model were within 3% of the results of the experimental engine.

Figure 4 shows that as compression ratio increases, operational limits for pre-ignition decreases. This is due to the increase in temperature inside the cylinder as the compression ratio increases. This increase in temperature raises the possibility of pre-ignition. Figure 5 show the operational limits for pre-ignition for various engine speeds.

Results show that as engine speed increases, the operational limits for pre-ignition decreases. As engine speed increases, greater turbulence is experienced inside the cylinder. This increased turbulence increases the turbulent flame speed or the rate at which the fuel is burned. The time for complete combustion therefore decreases and this is accompanied by an increase in pressure and temperature, thereby increasing the potential for unstable combustion such as pre-ignition.

As compression ratio increases, indicated thermal efficiency improves. There is a range in the compression ratio in which maximum improvement in thermal efficiency can be achieved. Any increase in compression ratio beyond that range will decrease thermal efficiency because of abnormal combustion. Figure 6 shows how the thermal efficiency is affected by the compression ratio.

The specific fuel consumption is also affected by pre-ignition. An increase in compression ratio beyond a certain operational limit for pre-ignition decreases the specific fuel consumption. Figure 7 shows the effect of compression ratio on specific fuel consumption.

1.3 Objective of the Present Study

The problems of abnormal combustion with hydrogen can be addressed in part by direct injection of fuel into the cylinder, which prevents formation of a premixed charge in the cylinder. Direct injection is also an effective approach to achieve high efficiency and clean combustion for

a wide range of operating conditions. In Direct Injection Spark Ignition (DISI) systems, a high pressure injector delivers the fuel into the cylinder during the compression stroke, and the resulting transient jet is ignited by a spark plug. The flame propagation is determined by the turbulence and stratification created by the fuel jet, and thus, an understanding of these processes and interactions among them is necessary to control the combustion process. Fundamental studies of hydrogen combustion have typically focused on flame propagation in a Constant Volume Combustion Chamber (CVCC) containing a fully premixed charge of fuel and air. These studies however do not consider the turbulence and stratification generated by the fuel jet.

The objective of the present study is to research mixing and combustion processes for hydrogen fueled DISI systems. Hydrogen is injected into a CVCC equipped with viewing windows to observe fuel-air mixing and flame propagation after a spark is created by an igniter. The flow and combustion processes are affected by parameters such as fuel supply pressure, overall equivalence ratio, ignition time, and hydrogen percentages and are therefore the key operating parameters of the experiments. In this study, the air in the CVCC is kept at atmospheric pressure before injecting the fuel, the igniter is located diametrically opposite the fuel injector, and the spark is created at varying ignition times. A high-speed Rainbow Schlieren Deflectometry (RSD) system is used to visualize and quantify the flow and flame characteristics. RSD has been used in the past quantitatively to measure species concentrations and temperature in steady gas flows, study structures of flickering gas-jet diffusion flames, and in many other optical applications [Agrawal et al., 1997; Agrawal et al., 1998; Agrawal et al., 1999; Al-Ammar et al., 1998; Albers & Agrawal, 1999; Shenoy et al., 1998]. However, due to the complexity of this system, RSD was used qualitatively to determine flame structures and propagation and quantitatively to determine combustion time and flame front speeds.

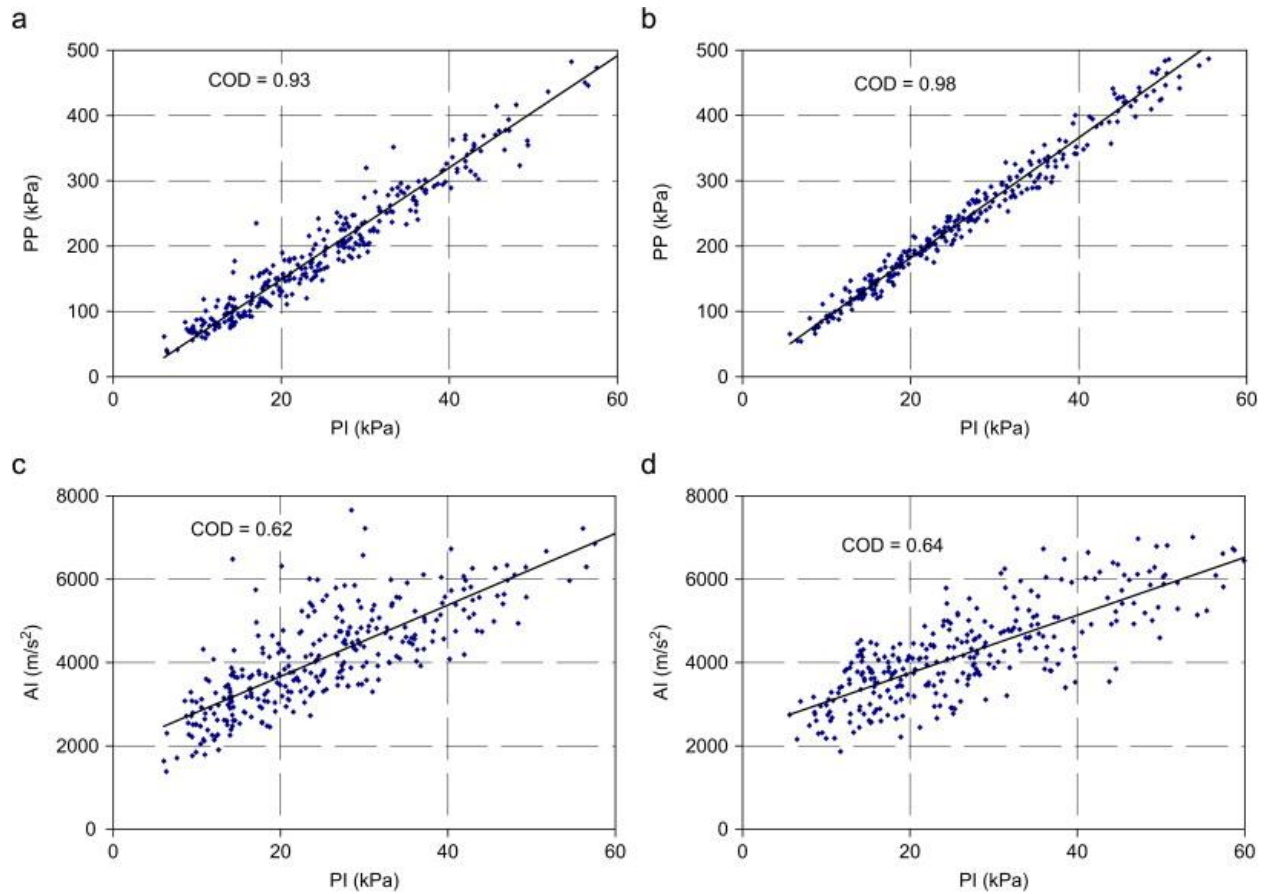


Figure 1. Correlation between data pairs (PP, PI) (top) and (AI, PI) (bottom) based on individual combustion event basis, 300 engine cycles with fixed ignition timing (0bTDC—hydrogen, 2bTDC—gasoline). (a and c) Hydrogen and (b and d) Gasoline [Szwaja et al., 2007].
(Plot from Int. J. of Hydrogen Energy 32 (2007), Figure 3)

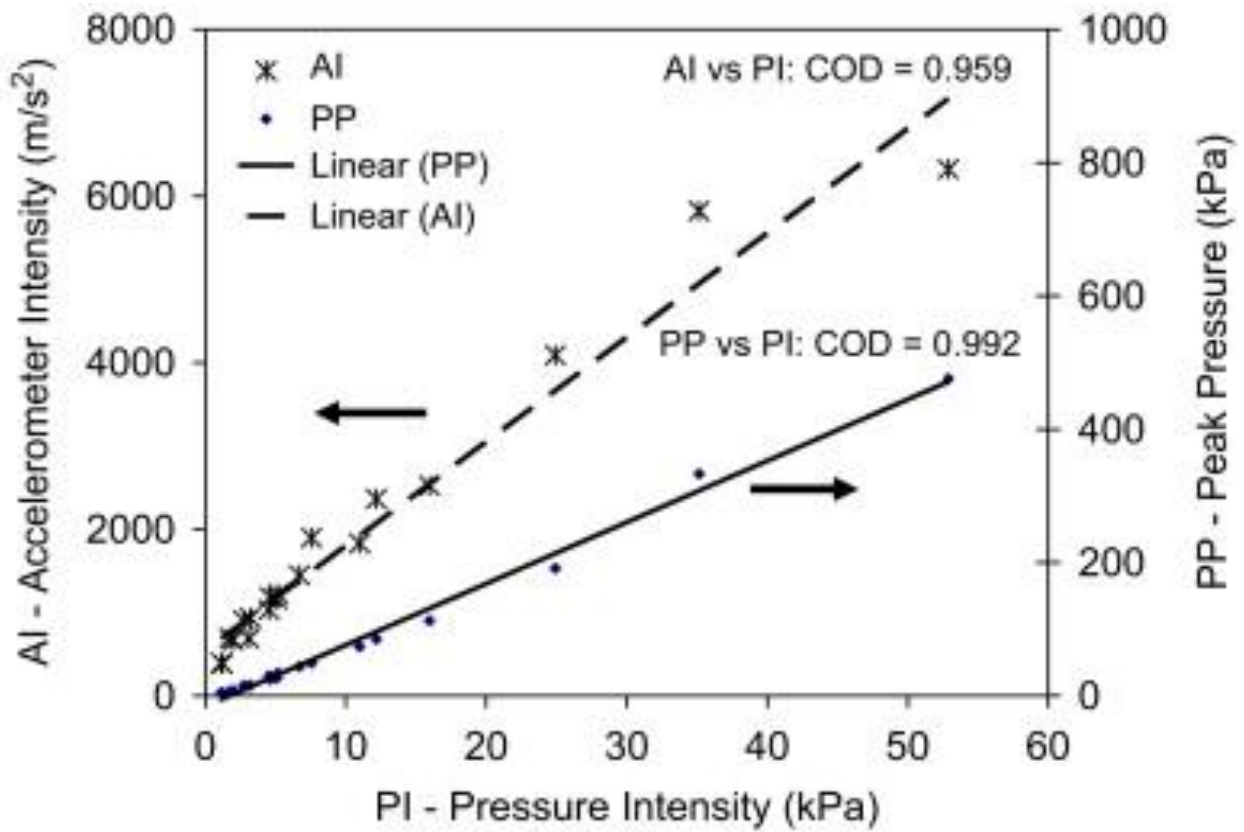


Figure 2. Correlation between mean AI and mean PI for hydrogen combustion at spark timing varying at the range from 4° BTDC to 12° ATDC [Szwaja et al., 2007].
 (Plot from Int. J. of Hydrogen Energy 32 (2007), Figure 4)

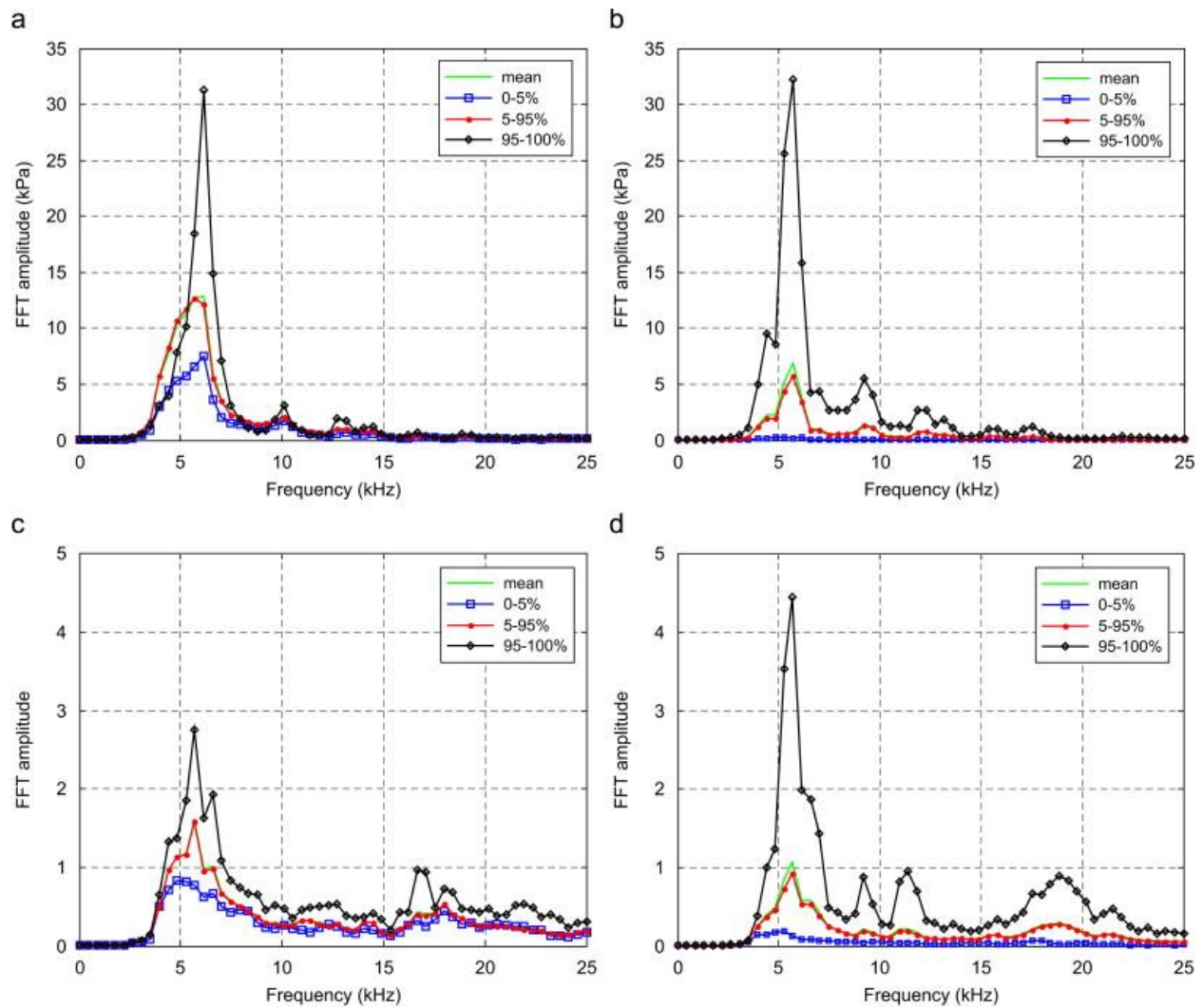


Figure 3. FFTs of in-cylinder pressure and accelerometer signals computed from 300 combustion events for hydrogen and gasoline. (a) FFT Pressure (hydrogen); (b) FFT Pressure (gasoline); (c) FFT accelerometer (hydrogen); (d) FFT accelerometer (gasoline) [Szwaja et al., 2007]. (Plot from Int. J. of Hydrogen Energy 32 (2007), Figure 5)

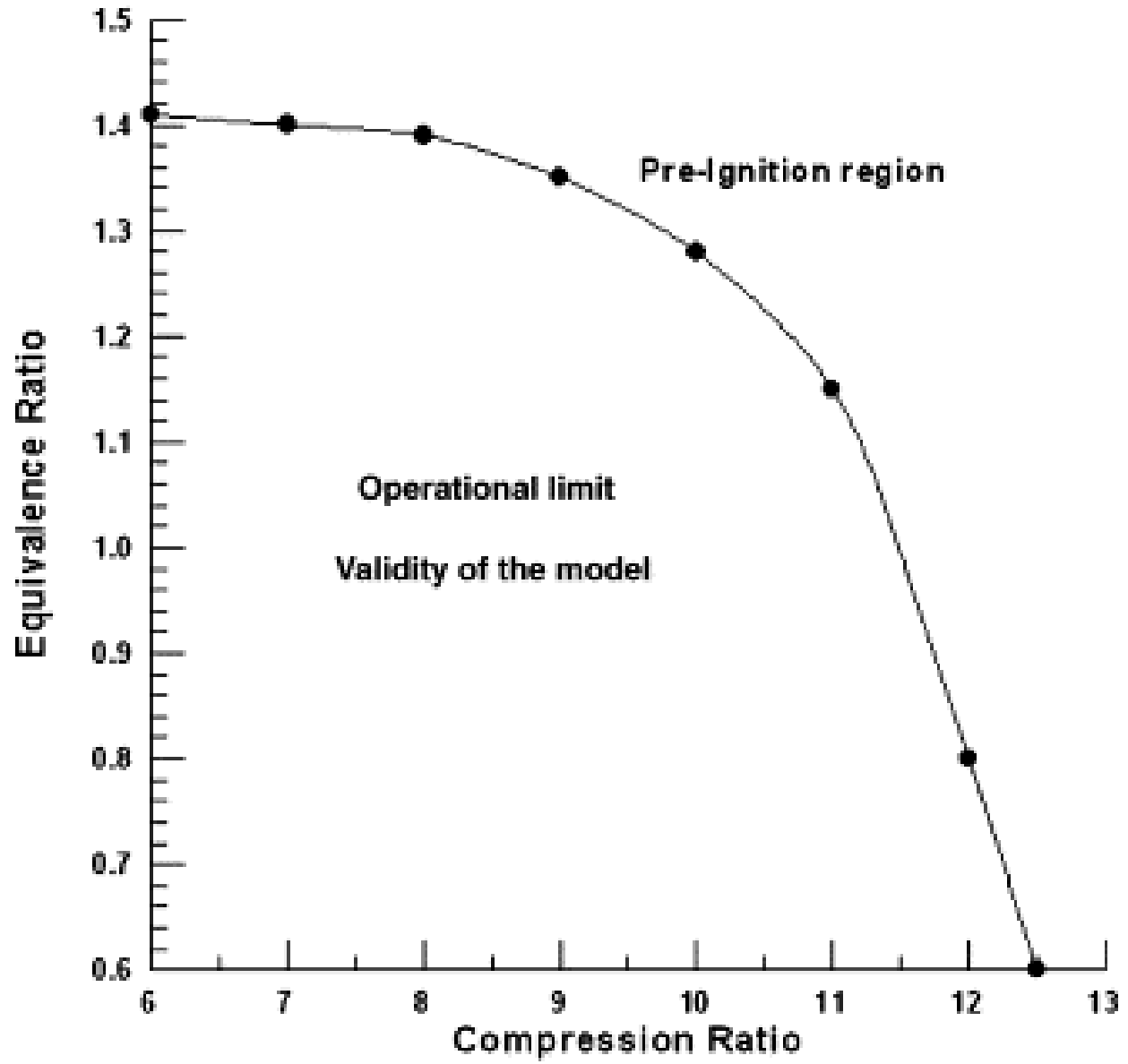


Figure 4. The variations of operational limits for pre-ignition with compression ratio changes [Maher & Al-Baghdadi, 2004]. (Plot from Renewable Energy 29 (2004), Figure 2)

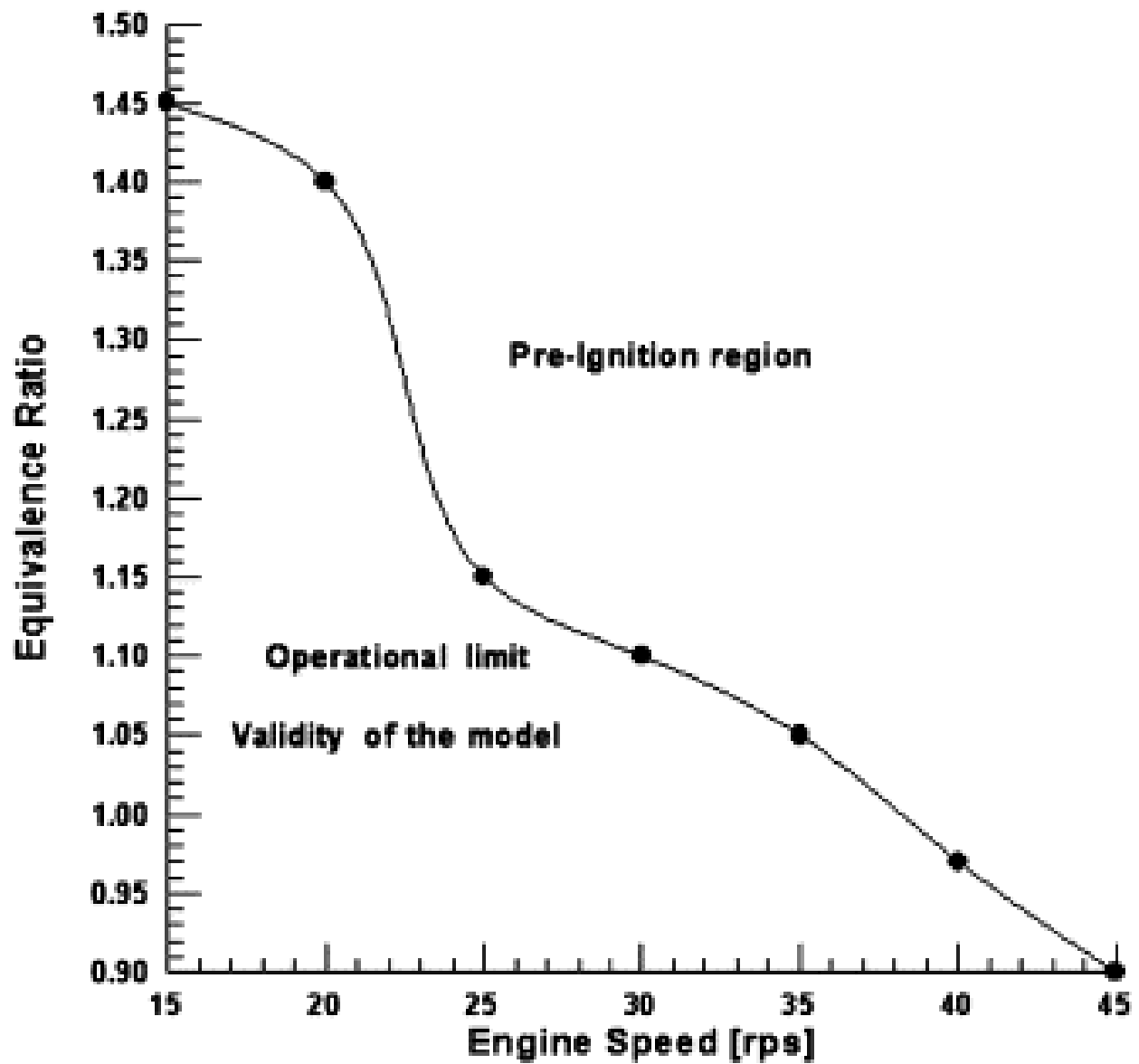


Figure 5. The variations of operational limits for pre-ignition with engine speed changes [Maher & Al-Baghdadi, 2004]. (Plot from Renewable Energy 29 (2004), Figure 3)

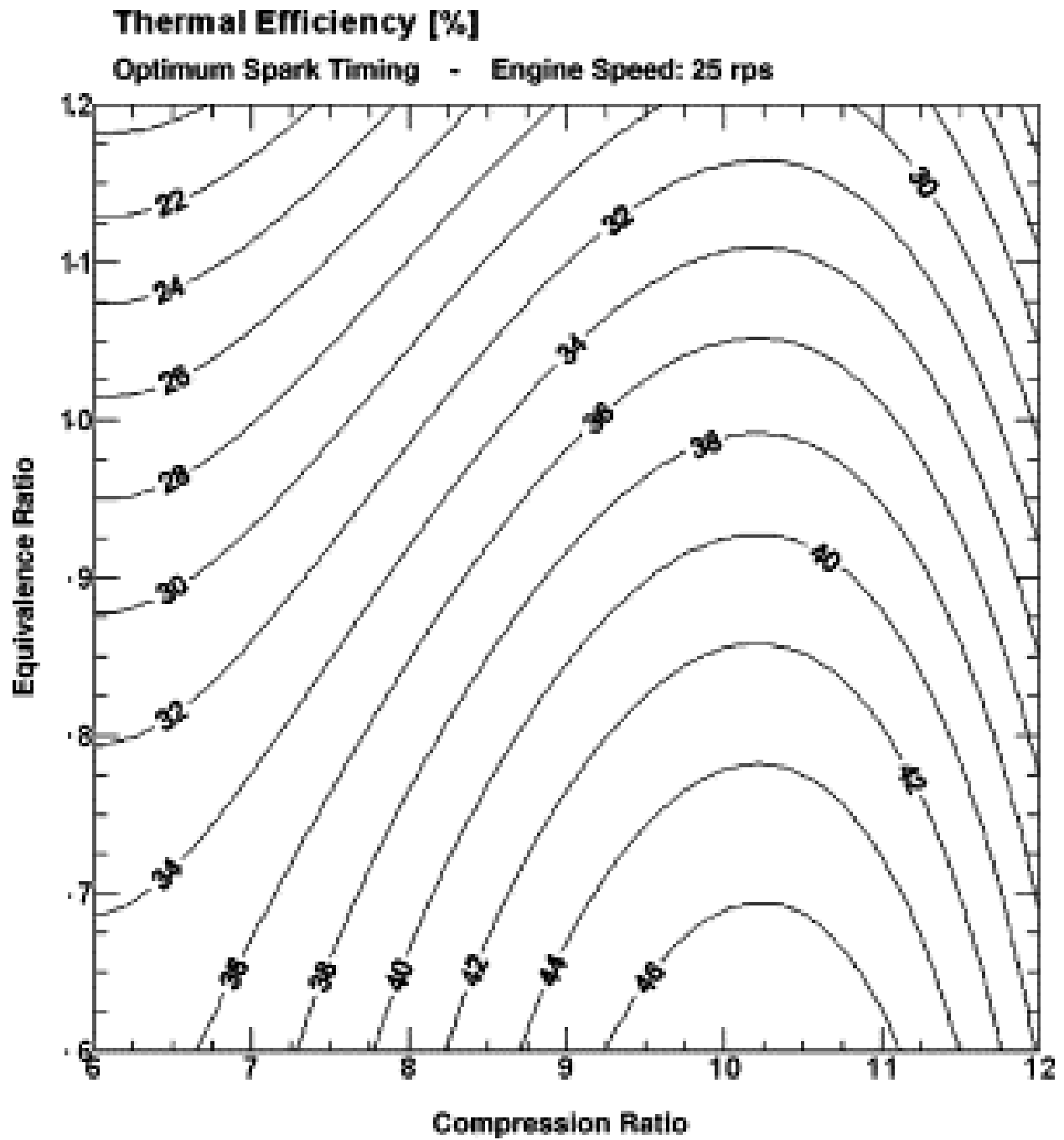


Figure 6. Effect of compression ratio and equivalence ratio on the indicated thermal efficiency [Maher & Al-Baghdadi, 2004]. (Plot from Renewable Energy 29 (2004), Figure 8)

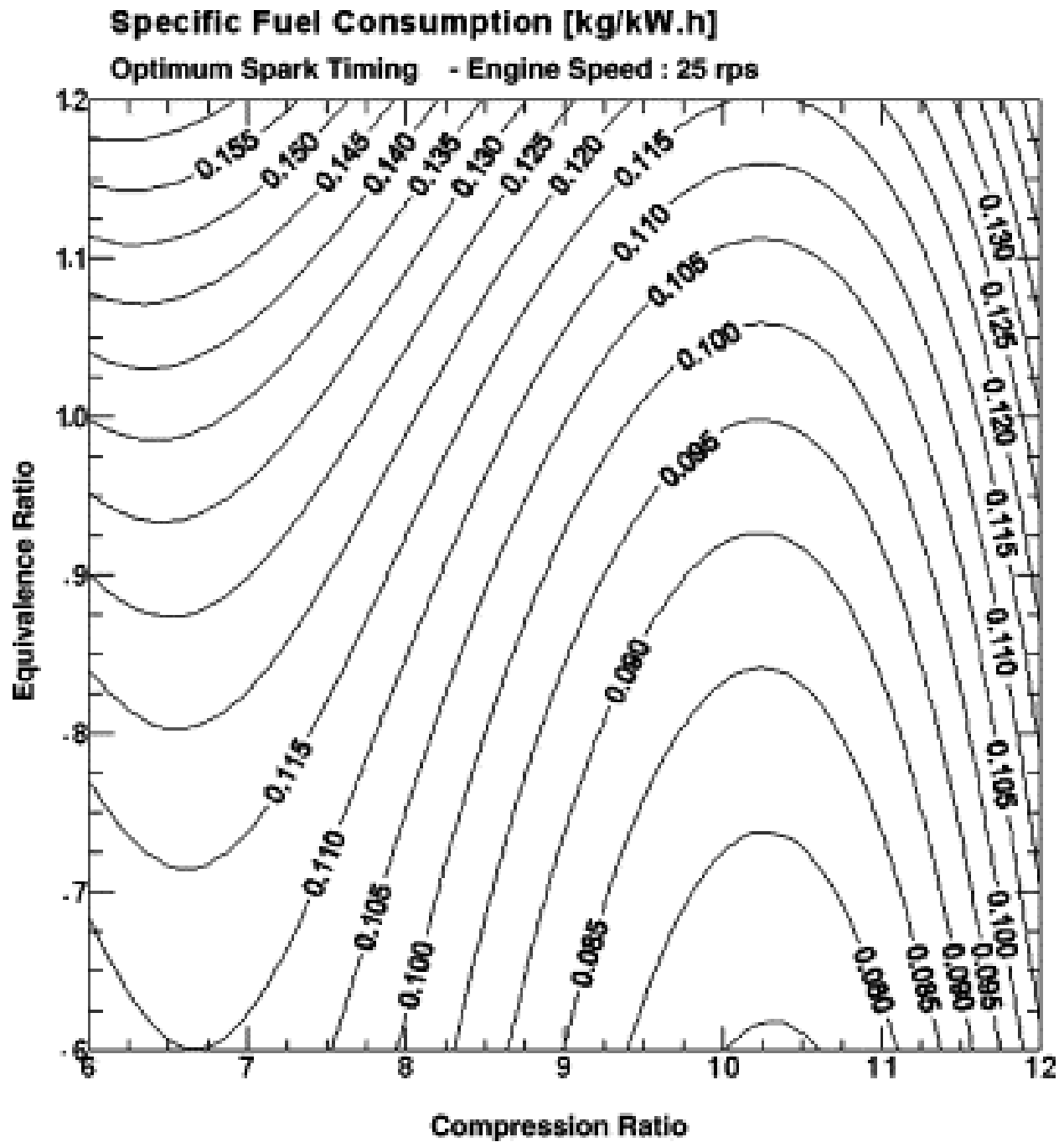


Figure 7. Effect of compression ratio and equivalence ratio on the specific fuel consumption [Maher & Al-Baghdadi, 2004]. (Plot from Renewable Energy 29 (2004), Figure 9)

CHAPTER 2

COMBUSTION CHARACTERISTICS OF A HYDROGEN JET INJECTED INTO A CLOSED VESSEL

Abstract

Rainbow Schlieren Deflectometry (RSD) was used to visualize the turbulent mixing of hydrogen/air and the subsequent combustion of the resulting mixture in a constant volume closed combustion vessel. The pancake-shaped vessel replicated the combustion chamber in an internal combustion engine. Hydrogen was injected from the top side of the vessel into quiescent air at atmosphere pressure, and the mixture was ignited by a spark plug located diametrically opposite the injector. Color schlieren images were acquired at a frame rate of 4000 Hz to analyze the fuel-air mixing and combustion processes. Experiments were conducted by varying the injector supply pressure and overall equivalence ratio. Elapsed time for flame propagation through a given region was determined using space-time images. Results show fine scale structures that vary with the operating conditions to affect parameters such as the flame speed and reaction zone thickness.

Introduction

The main focus of this research is to investigate hydrogen as an alternative fuel for use in spark-ignited Internal Combustion Engines (ICEs). The search for alternative fuels for ICEs has been pursued for decades. This search is promoted by several factors including the expected future depletion of fossil fuels and hazardous emissions of pollutants from these fuels. In the automotive industry, most spark-ignited ICEs use gasoline as the fuel source while compression-ignition engines use diesel as the fuel source. Harmful pollutants such as oxides of nitrogen (NO_x), unburned hydrocarbons (UHC), carbon monoxide (CO), and particulate matter (PM) are emitted from the combustion of these fuels, which threaten all forms of life. As the demand for fuel increases in the United States and other countries, the availability of fossil fuels is steadily decreasing.

One promising alternative fuel for use in ICEs is hydrogen. Extensive research on the use of hydrogen as an alternative fuel has been conducted since the 1930's [Szwaja et al., 2007; Verhelst et al., 2006; Das et al., 2000; Wimmer & Wallner, 2005; Verhelst & Sierens, 2007; Wallner & Lohse-Busch, 2007; Das, 1990; Maher & Al-Baghdadi, 2004; Srivastva & Agarwal, 2008]. Advantages associated with hydrogen-fueled ICEs include near zero emissions of CO, NO_x , and UHC and zero emissions of carbon dioxide (CO_2). Hydrogen's combustion properties make it a desired fuel to improve cold start capabilities. The main product of hydrogen combustion is water. Comparing with liquid fuels, hydrogen does not experience cold wall quenching to the degree of hydrocarbon (HC) fuels, vapor lock, poor mixing, and inadequate vaporization [Szwaja et al., 2007]. However, there are problems associated with hydrogen-fueled engines that must be evaluated and corrected. Knock, pre-ignition, and backfire are combustion problems that must be carefully monitored as they are true obstacles with the use of hydrogen-fueled engines [Szwaja et al., 2007; Verhelst et al., 2006]. These abnormal

combustion processes affect the overall operating performance and efficiency of ICEs and limit operating parameters such as equivalence ratios and compression ratios. Further, the heat loss through cylinder wall can be higher for hydrogen combustion compared to conventional fuels, which negatively affect the overall thermal efficiency.

The problems of abnormal combustion with hydrogen can be addressed in part by direct injection of fuel into the cylinder, which prevents formation of a premixed charge in the cylinder. Direct injection is also an effective approach to achieve high efficiency and clean combustion for a wide range of operating conditions. In Direct Injection Spark Ignition (DISI) systems, a high pressure injector delivers the fuel into the cylinder during the compression stroke, and the resulting transient jet is ignited by a spark plug. The flame propagation is determined by the turbulence and stratification created by the fuel jet, and thus, an understanding of these processes and interactions among them is necessary to control the combustion process. Fundamental studies of hydrogen combustion have typically focused on flame propagation in a Constant Volume Combustion Chamber (CVCC) containing a fully premixed charge of fuel and air. These studies however do not consider the turbulence and stratification generated by the fuel jet.

Specific Objectives

The objective of the present study is to research mixing and combustion processes for hydrogen fueled DISI systems. Hydrogen is injected into a CVCC equipped with viewing windows to observe fuel-air mixing and flame propagation after a spark is created by an igniter. The flow and combustion processes are affected by parameters such as fuel supply pressure, initial chamber pressure, overall equivalence ratio, ignition time, and ignition location. In this study, the CVCC is kept at atmospheric pressure before injecting the fuel, the igniter is located diametrically opposite the fuel injector, and the spark is created at the instant the fuel injection

process terminates. The key operating parameters of the experiment are fuel supply pressure and equivalence ratio. High-speed Rainbow Schlieren Deflectometry (RSD) system is used to visualize and quantify the flow and flame characteristics. Details of the experimental setup, results and discussions, conclusions, and recommendations for future research are provided in the following sections.

Experimental Setup

The experimental setup, Figure 1, consists of a CVCC system and a high-speed RSD system as described below.

Constant Volume Combustion Chamber System

The test apparatus consisted of a CVCC with a fuel injector attached to a fuel supply system. The combustion chamber, shown as a drawing in Figure 2 and photographically in Figure 3, is made from an aluminum block with a cylindrical opening drilled through it. This opening forms the volume of the combustion chamber and it has a diameter of 66.7 mm and a width of 31.8 mm. The combustion space is enclosed by optical windows located in a recessed area on both ends. Each optical window is a fused silica, single surface $1/10^{\text{th}}$ wave optical flat (NT01-915) of diameter 76.2 ± 1 mm and thickness 19.05 ± 1.5 mm. The optical flats are precision polished on one side to ensure accuracy and are pitch polished on the other side. The optical flats are held in place by aluminum collars, Figure 4, that are bolted by eight evenly spaced bolts to the outer surface of the combustion chamber.

Hydrogen was supplied by a compressed gas cylinder as shown in Figure 5. The hydrogen flowed through a test vessel system and a supply pressure regulator before reaching the fuel injector fixed at the top center of the CVCC (see Figure 3). The fuel supply system facilitates calibration of the fuel injector as discussed in the next section. Fuel injector is a

Hoerbiger hydrogen direct injector connected to a Provebo controller powered by a 13.8 V DC regulated power supply. The spark is created by a Champion RV12YC6 spark plug fixed at the bottom center of the CVCC, diametrically opposite from the hydrogen injector. The spark plug is fixed in a coil that is powered by the same power supply as the injector. The hydrogen injector, coil charging, and spark triggering are all connected to the Digital I/O ports of a National Instrument's PCI Data Acquisition System, Figure 6, with a BNC breakout box. The fuel injector and spark times are controlled by a computer code written in National Instrument's LabView software.

Fuel Injector Calibration

The fuel injector was calibrated to control the mass of hydrogen injected into the CVCC for different operating conditions. The calibration process used the test vessel system shown schematically in Figure 5 and photographically in Figure 7. The test vessel consisted of a charging valve on the inlet side, a 300 cm³ double-ended aluminum cylinder (304L-HDF4-300), a T-junction to mount the pressure transducer (Kistler 6041A), an integral bonnet non-rotating stem valve (SS-14DKM4) referred to as the supply valve, and a pressure regulator to control the supply pressure to the injector. The control volume of the test vessel system consisted of all components between the charging valve and pressure regulator. Using water and a graduated cylinder, the volume of the test vessel system was determined to be 314 mL or $3.14 \times 10^{-4} \text{ m}^3$.

Experiments were conducted to calibrate the injector at fuel supply pressures of 275.8 kPa (40 psi), 413.7 kPa (60 psi), and 551.6 kPa (80 psi). The supply pressure regulator to the injector was adjusted to the desired pressure. Then, the injector was opened for a specified period while the vessel pressure measured by the pressure transducer was recorded. This procedure was repeated by gradually increasing the injection period until the mass required for

stoichiometric condition was delivered by the injector. The mass of hydrogen in the vessel before and after the injection was computed using the ideal gas law. The change in mass in the test vessel system is equal to the mass of hydrogen injected into the combustion chamber. This procedure was repeated for each desired supply pressure. The parameters involved in this calibration were supply pressure, injector opening time, and mass of hydrogen. Figure 8 shows the calibration curve in terms of mass of hydrogen injected versus injection duration for different supply pressures. Results show a linear calibration curve with its slope increasing with the supply pressure. For a given supply pressure, the calibration curve can be used to determine the injection duration to deliver a known mass of hydrogen, and hence, to achieve the desired equivalence ratio.

Rainbow Schlieren Deflectometry System

Rainbow Schlieren Deflectometry, an optical technique to visualize density gradients in the flow field was utilized to acquire the necessary data. An inhomogeneous media, for example, hydrogen injected into air, has density gradients that lead to schlieren effects arising from refraction of light rays traveling through the medium. Schlieren effects can result from temperature gradients, mixing of gases of different densities, or high velocity flows. The RSD is an experimental technique to project light ray deflections or displacements in color to a viewing screen. The color schlieren images thus acquired can be quantitatively analyzed to obtain the local distributions of the density field. Rainbow schlieren deflectometry has been used in the past quantitatively to measure species concentrations and temperature in steady gas flows, study structures of flickering gas-jet diffusion flames, and in many other optical applications [Agrawal

Figure 9 illustrates the RSD setup implemented in this study. A beam of light was transmitted from a visible light illuminator with a 250 W halogen projector lamp, Figure 10. The

light was transmitted through a borosilicate gooseneck fiber optic cable, Figure 11, to the source aperture located at the focal point of the collimating lens, Figure 12. The lens is a precision achromatic doublet lens that is 76.2 mm in diameter with a 500 mm focal length. It is coated with a 400-700 nm antireflection coating. The collimated beams or parallel light rays traveled through the test media contained in the CVCC as discussed previously. During experiments, the test media was composed of a non-homogeneous hydrogen-air mixture. After passing through the test media, refracted light rays passed through a de-collimating lens, Figure 12, which refocused light beams onto a rainbow filter. The de-collimating lens has the same properties as the collimating lens, except its focal length is 750 mm. The rainbow filter, Figure 13, is fixed at the focal point of the de-collimating lens. Light rays transmitted through the rainbow filter form an inverted image of the test medium captured by a Red Lake MotionPro HS-4 high speed camera, Figure 13. During experimentation, the camera acquires color schlieren images for 4 seconds at a rate of 4,000 frames per second. The camera was set to single exposure mode, with an exposure time of 247 μ s.

Results and Discussion

The color schlieren images were analyzed to compute the jet penetration depth, average turbulent flame speed, and elapsed time of flame propagation through a given region. The diameter of the combustion chamber is 66.7 mm or 282 pixels, giving a pixel resolution of 236.4 μ m or 4.23 pixels per mm. The tip of the fuel injector is used as the reference point.

Fuel Jet Penetration Depth

Figure 14 shows how the injected fuel penetrates into the chamber over time. The exact moment of fuel injector opening is not captured by the camera since the camera and injector times were not synchronized. Time $t = 0.0$ in Figure 14 refers to the schlieren image prior to the

fuel appearing near the injector tip. Thus, fuel injection starts between $t = 0.0$ and 0.25 ms, as dictated by the temporal resolution of the imaging system. Results show that the jet penetration depth increases exponentially in the beginning and linearly after about 0.50 ms. For a given fuel supply pressure, the jet penetration depth is nearly independent of the overall equivalence ratio, i.e., the mass of hydrogen injected. A higher equivalence ratio requires a longer injection period, which should not affect the initial development of the jet flow. Figure 14 shows that the fuel jet reaches the bottom of the CVCC or location of the spark igniter in about 2.0 ms; the average jet velocity during this period is about 30 m/s. Note that the time for fuel jet to penetrate across the CVCC is much shorter than the fuel injection period of at least 25 ms. Thus, after the fuel jet reaches the spark igniter, the hydrogen flow interacts with the wall of the chamber and then convects towards the injector tip to fill the chamber. The fuel injection process creates significant turbulence before the fuel-air mixture formed in the chamber is ignited.

Figure 15 represents the penetration depth versus time for $\phi = 1.0$ and fuel supply pressures, $P_s = 275.8$ and 413.7 kPa. The penetration depth recorded in the first image at $t = 0.25$ ms is different for the two supply pressures, indicating the need to synchronize the camera and injector times for future experiments. Still, the two curves follow each other and suggest that the fuel supply pressure does not affect the penetration depth in the experiment. This result suggests that the injector flow is most likely choked since the fuel supply to ambient pressure ratio is 3.73 and 5.10 for the two cases (or above the pressure ratio of about 2.0 to achieve the sonic flow).

Flame Characterization

Figure 16 show a series of color schlieren images representing ignition and subsequent flame propagation through the chamber for $P_s = 413.7$ kPa and $\phi = 1.0$. Images were acquired at 4000 Hz, thus the time between images is 0.25 ms. The ignition and end of flame propagation is

captured by nine images, and thus, the total combustion time is slightly greater than 2.0 ms. Note that the exact moments of ignition or end of combustion cannot be detected precisely because of the temporal resolution of 0.25 ms. The average flame speed based on the combustion time and propagation distance of 66.7 mm (or chamber diameter) is about 33.4 m/s. This value is more than 15 times the laminar flame speed of stoichiometric hydrogen-air mixture. Evidently, the fuel injection process has introduced high levels of turbulence in the chamber, which is manifested by the high turbulent flame speed observed in the experiment.

The ignition and subsequent flame propagation processes are 3D and highly asymmetric since the igniter is located at the center of the chamber wall (unlike the center point of the chamber which would create a spherical flame). The color schlieren images in Figure 16 reveal several interesting features of the asymmetric flame propagation process. In the first two images after ignition, the flame is propagating towards the injector and around the chamber wall. It is also spreading laterally (or towards the optical windows) but this movement cannot be captured by the line-of-sight schlieren technique. However, this last point can be illustrated by the fourth image in Figure 16 showing no combustion in the wall region adjacent to the igniter. Thus, it takes the flame at least 0.50 ms to span the half length of the chamber (of about 16 mm), which amount to an average flame speed of about 32 m/s in the lateral direction. The curvature of the flame structure indicates that the fuel is consumed first in the center region and then, in the wall region resulting in distinct side lobes in Figure 16f. Fuel at the injector exit is consumed the last in part because it is farthest away.

Next, the temporal evolution of the flow and flame structure was examined at different axial distances from the injector exit (L) using space-time images created by stacking image data at a specified axial plane from the sequence of instantaneous schlieren images. Figure 17 present

space-time images at several axial locations. Near the injector at $L = 2.13$ mm, the fuel jet is readily identified in the center. A thin bright region towards the end of the fuel jet represents the combustion time followed by black region resulting from the combustion product (water) fogging the windows, and thus, making them opaque. At $L = 13.95$ mm, mixing with air has increased the fuel jet width. A thin bright region signifying combustion and a black region resulting from window fogging are still present. Farther away from the injector at $L = 25.77$ mm, the fuel jet width has increased as well as the transverse width of the visible region since this axial plane is closer to the chamber diameter. In this and subsequent schlieren images, the orange color after the thin combustion region signifies that the water does not condense to completely fog the optical windows. These observations can be related to the heat loss characteristics of the system although a detailed thermal analysis has not been performed so far.

Figure 18 presents a sequence of color schlieren images from start of ignition to end of combustion for the lower fuel supply pressure of 275.8 kPa and $\phi = 1.0$. Results show similar features as discussed already for the higher fuel supply pressure of 413.7 kPa and $\phi = 1.0$. In Figure 18, the combustion duration spans 10 images unlike Figure 16 containing 9 images. However, this difference can be attributed to the spatial resolution of the imaging system (0.25ms), which synchronization of the exact moment when spark was created for the two cases. Next, space-time images were used to determine the elapsed time of the flame at a particular axial location. Table 1 summarize these results and shows that the flames spends slightly more time when closer to the injector than away from it. In general, flame characteristics were not affected by the fuel supply pressure, which is consistent with Figure 15 showing independence of the jet penetration depth on P_s .

Effect of Equivalence Ratio

The next set of experiments was conducted by varying the equivalence ratio for each of the two fuel supply pressures. Results are presented for $P_s = 413.7$ kPa only since the flow and flame properties were nearly independent of the fuel supply pressure. Equivalence ratios are $\phi = 0.804$ and 0.318 , representing overall lean combustion. Note that the fuel injection duration was decreased to reduce the mass of hydrogen injected and thus, to decrease the overall equivalence ratio. Since the mixture was ignited at the end of fuel injection period, leaner mixtures can be expected to have less homogenized fuel-air mixing with localized zones of high turbulence created by the jet flow.

Figure 19 shows the sequence of color schlieren images during the ignition and combustion events for $\phi = 0.804$. The combustion process spans about 13 images or for 3.25 ms. Thus, the average turbulent flame speed has decreased from about 33.4 m/s for $\phi = 1.0$ to about 20.5 at $\phi = 0.804$, which is still an order of magnitude higher than the laminar flame speed of stoichiometric hydrogen-air mixtures. The flame reaches the optical windows in about 0.75 ms, which pertains to lateral turbulent flame speed of about 21 m/s or nearly the same as the flame speed in the vertical direction. Initially, the flame structures are similar to those at the higher equivalence ratio, but the distinct side lobes observed for $\phi = 1.0$ are less prominent for $\phi = 0.804$.

Figure 20 shows the sequence of color schlieren images for $\phi = 0.318$. Flame characteristics are quite different at this lean condition compared to higher equivalence ratio flames. The ignition and combustion processes required nearly 50 images, and thus, the combustion time was approximately 12.5 ms. It pertains to the average turbulent flame speed of about 5.5 m/s or nearly one-fourth of that at $\phi = 0.804$ and one-sixth of that at $\phi = 1.0$. This

reduction in the flame speed is directly related to the slower reaction rates of leaner mixtures. The flame speed is still significantly higher than the laminar flame speed indicating that the turbulence created by the fuel jet is still important. The flame reaches the windows in about 4 ms. Thus, the average lateral flame speed is about 4 m/s, which is lower than the flame speed in the vertical direction. The burning process is homogenized by the fine scale flamelets created within the turbulence flow across the whole field. High levels of turbulence in localized regions of the chamber, incomplete fuel-air mixing introducing local equivalence ratio variations in the chamber, and chemistry of the overall lean combustion are responsible for the observed trends.

Flame velocities in the center of the combustion chamber for $P_s=275.8$ and $P_s=413.7$ kPa are shown in Figures 21 and 22 respectively. Flame velocities peak within the first half of the time required for the centerline flame to either reach the injector tip or is engulfed by wall flames. Afterwards, the velocities decrease until some time close to the injector tip. Peak velocities increase as equivalence ratio increase for both supply pressures.

Conclusions

This experimental study presents flow and flame characteristics of transient hydrogen jets in a constant volume combustion chamber replicating key features of a direct-injection spark-ignition system. Experiments were conducted for air kept in chamber at ambient pressure, while hydrogen was injected at different supply pressures. The resulting mixture was ignited at the end of the fuel injection period. Results show that the fuel supply pressure does not affect the fuel jet penetration, and thus, fuel-air mixing, flame structure, and flame propagation process in the combustion chamber. For a given fuel supply pressure, although the equivalence ratio did not impact initial penetration of the fuel jet, the combustion parameters were affected significantly. In particular, the average turbulent flame speed decreased from 33.4 m/s at $\phi = 1.0$ to 20.5 and

5.5 m/s respectively at $\phi = 0.804$ and 0.318. The overall lean flame exhibited fine-scale flame structures that were not observed in higher equivalence ratio flames. Results show that the fuel jet creates significant turbulence in the fuel-air mixture, with major effects on the flame characteristics. Future work will seek to quantify these effects through analysis of turbulent flow and flames structures for a range of ignition times and ignition locations.

Acknowledgements

Tanisha Booker was supported by the Graduate Assistance in Areas of National Need (GAANN) program of the U.S. Department of Education.

References

- Das L.M. Fuel Induction Techniques For A Hydrogen Operated Engine. *Int. J. Hydrogen Energy* 15 (1990) 833-842.
- Das L.M. Hydrogen Engines: A View Of The Past And A Look Into The Future. *Int. J. Hydrogen Energy* 15 (1990) 425-443.
- Das L.M., Gulati R., Gupta P.K. A comparative evaluation of the performance characteristics of a spark ignition engine using hydrogen and compressed natural gas as alternative fuels. *Int. J. Hydrogen Energy* 25 (2000) 783-793.
- Maher A.R., Al-Baghdadi S. Effect of compression ratio, equivalence ratio and engine speed on the performance and emission characteristics of a spark ignition engine using hydrogen as a fuel. *Renewable Energy* 29 (2004) 2245-2260.
- Srivastva D.K., Agarwal A.K. Laser Ignition of Hydrogen-Air Mixture in a Combustion Bomb. *SAE Int.* 2008-28-0033.
- Szwaja S., Bhandary K., Naber J. Comparisons of hydrogen and gasoline combustion knock in a spark ignition engine. *Int. J. Hydrogen Energy* 32 (2007) 5076-5087.
- Verhelst S., Sierens R. A quasi-dimensional model for the power cycle of a hydrogen-fuelled ICE. *Int. J. Hydrogen Energy* 32 (2007) 3545-3554.
- Verhelst S., Sierens R., Verstraeten S. A Critical Review of Experimental Research on Hydrogen Fueled SI Engines. *SAE Int.* 2006-01-0430.
- Wallner T., Lohse-Busch H. Performance, Efficiency, and Emissions Evaluation of a Supercharged, Hydrogen-Powered, 4-Cylinder Engine. *SAE Int.* 2007-01-0016.

Wimmer A, Wallner T. H2-Direct Injection-A Highly Promising Combustion Concept. SAE
Int. 2005-04-0108.

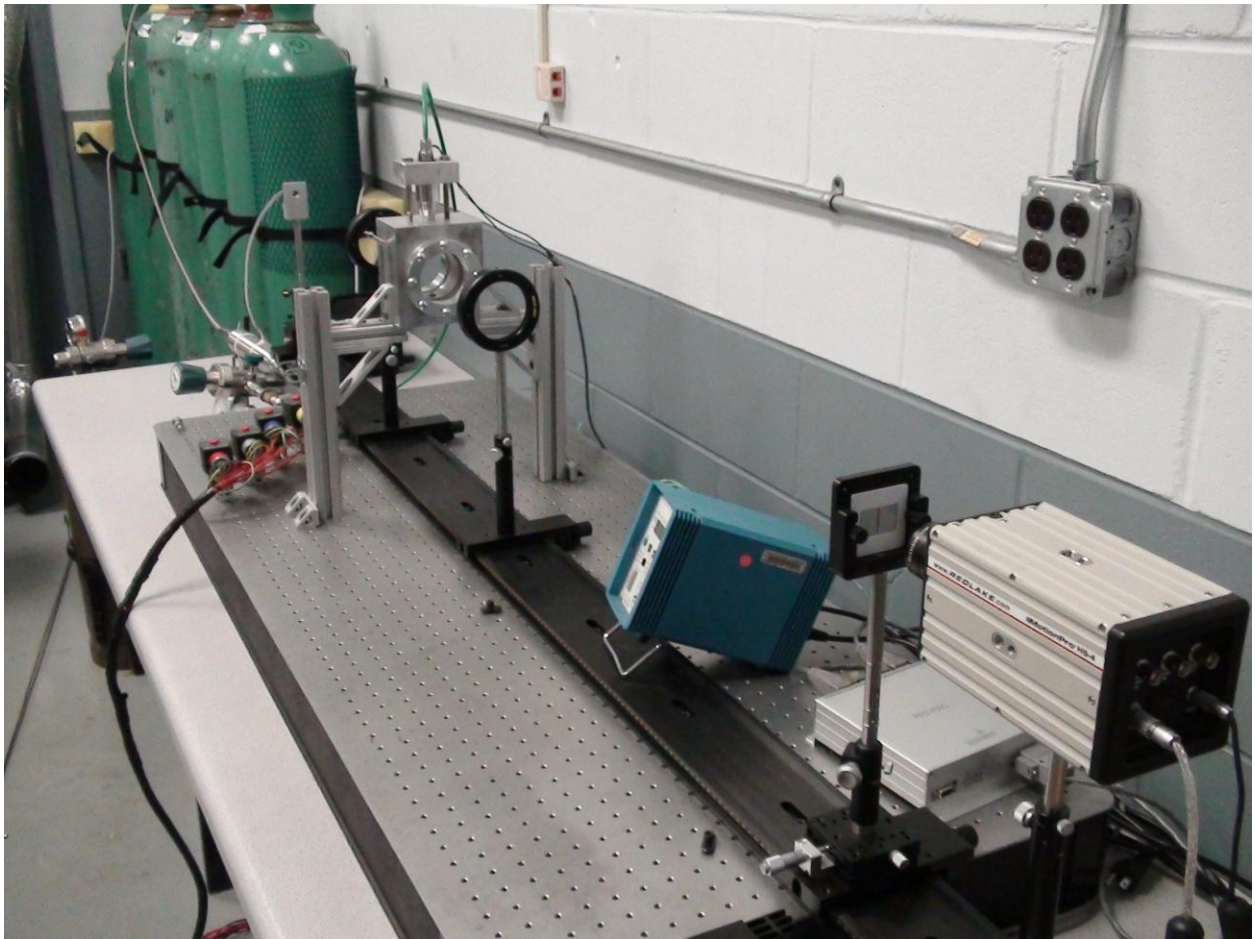


Figure 1. Experimental Setup.

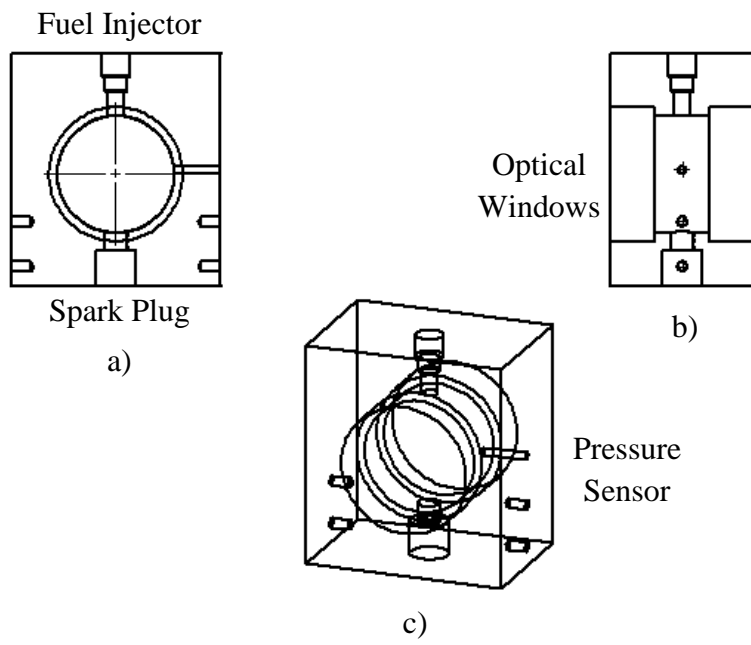


Figure 2. Combustion Vessel; a) Front View, b) Side View, c) Isometric View.

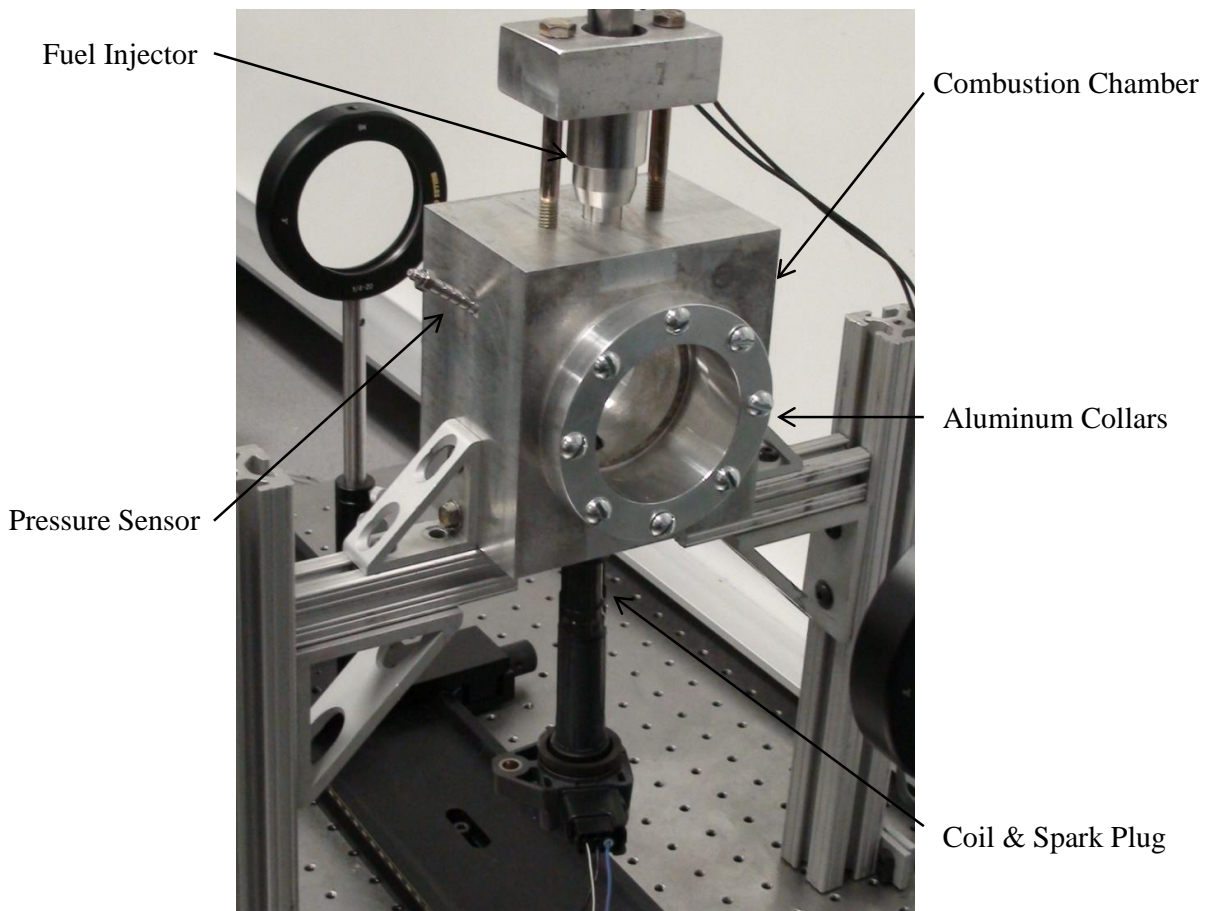


Figure 3. Combustion Vessel.

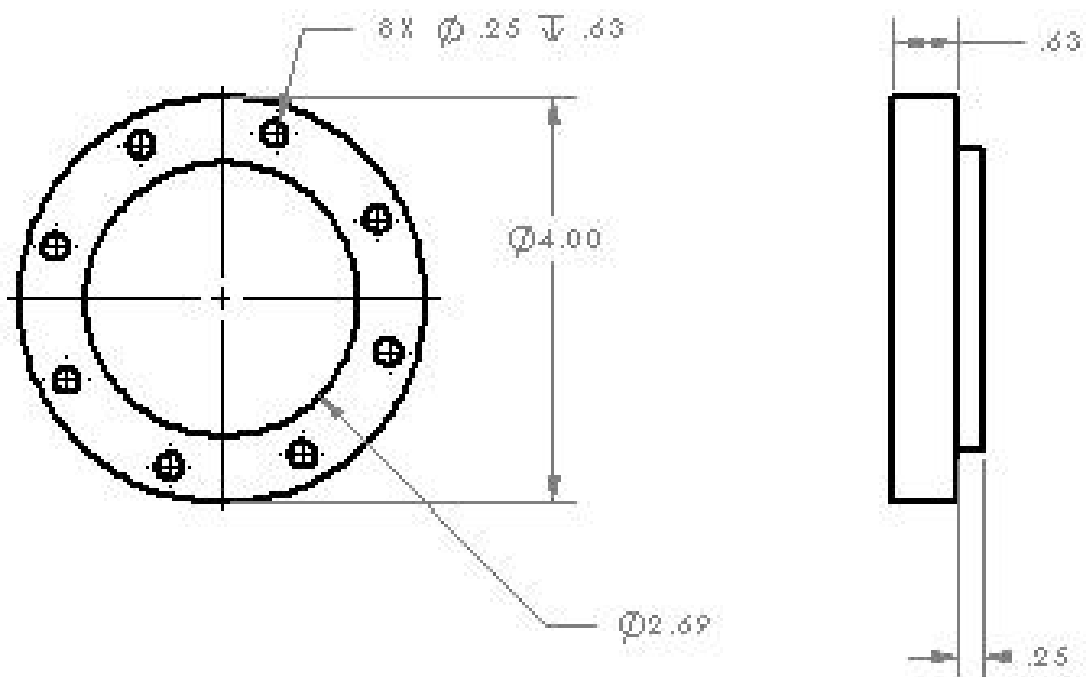


Figure 4. Drawing of Window Collar.

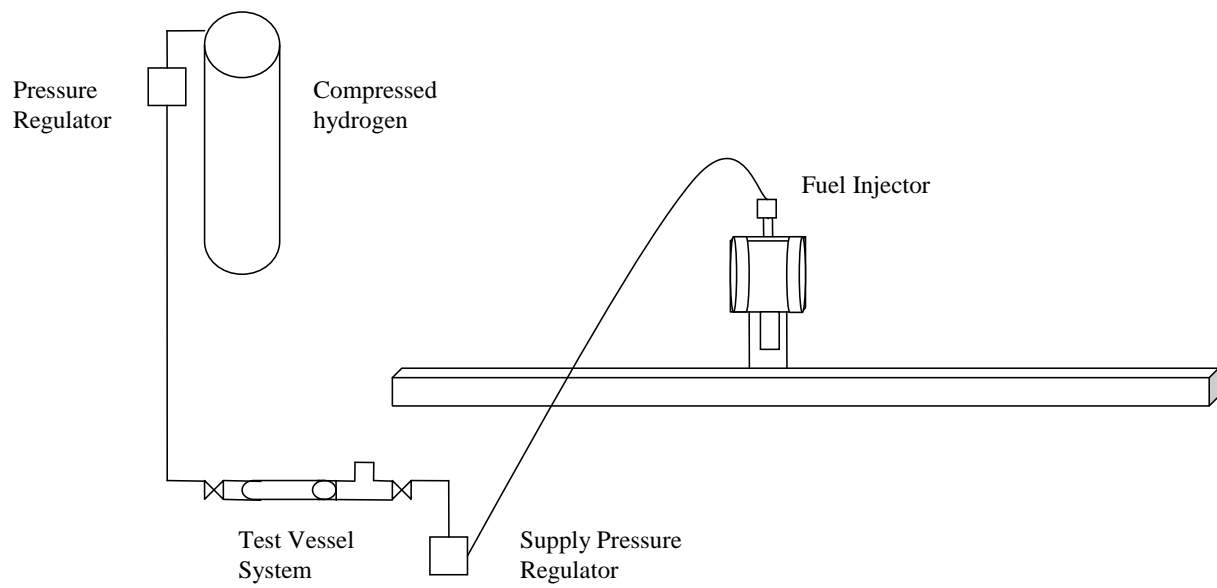


Figure 5. Fuel Flow System.



Spark Triggering

Coil Charging

Injector Triggering

Figure 6. Data Acquisition System.

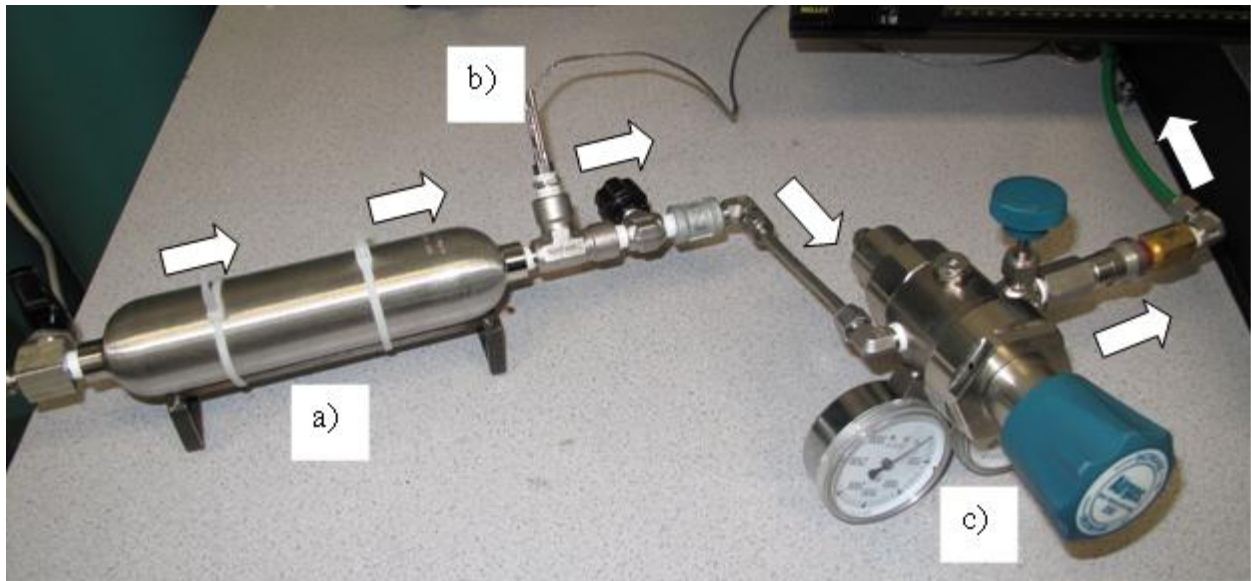


Figure 7. Test Vessel System; a) Test Vessel, b) Pressure Sensor, c) Supply Pressure Regulator.

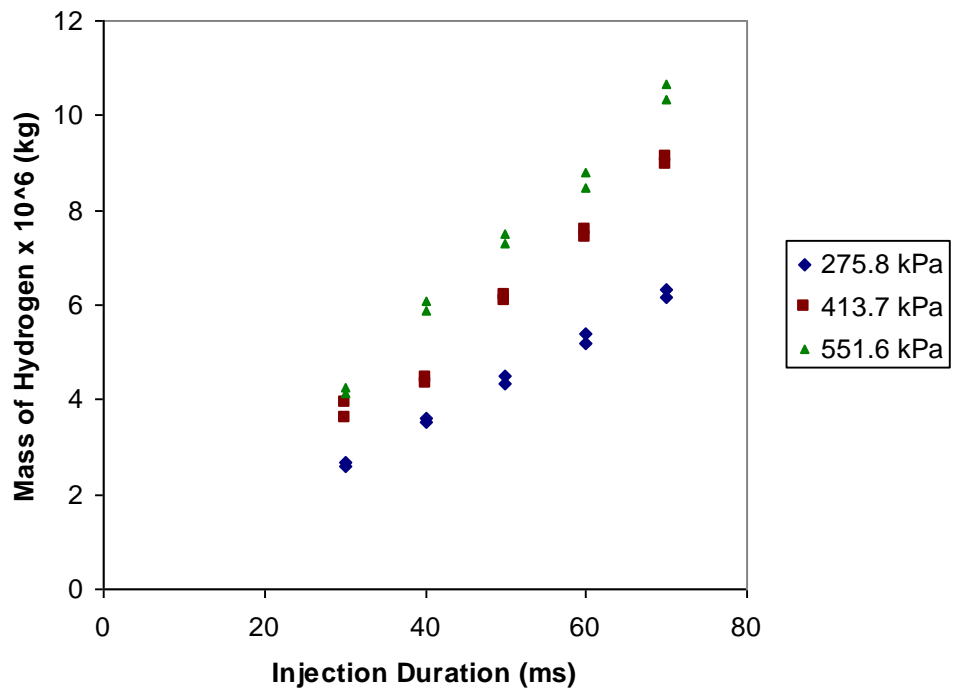


Figure 8. Injector Calibration Plot for $P_s = 275.8$ kPa, 413.7 kPa, and 551.6 kPa.

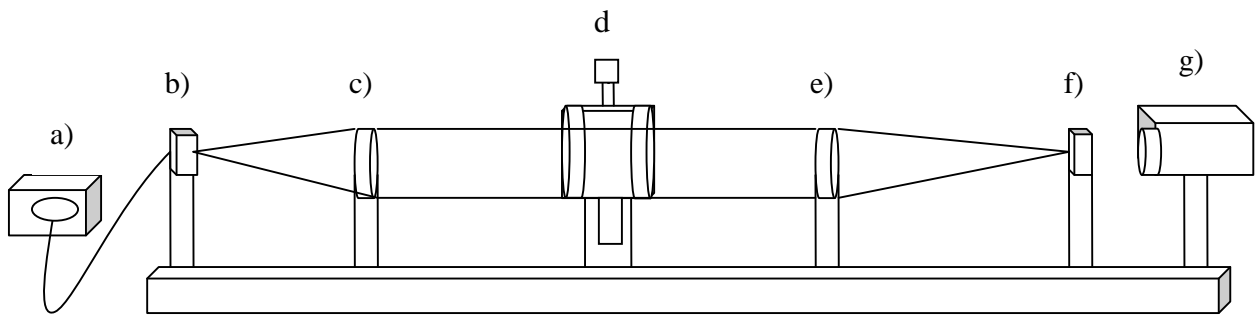


Figure 9. Rainbow Schlieren Deflectometer; a) Illuminator, b) Aperture, c) Collimating Lens, d) Test Media (Combustion Chamber), e) Decollimating Lens, f) Rainbow Filter, and g) High Speed Camera.

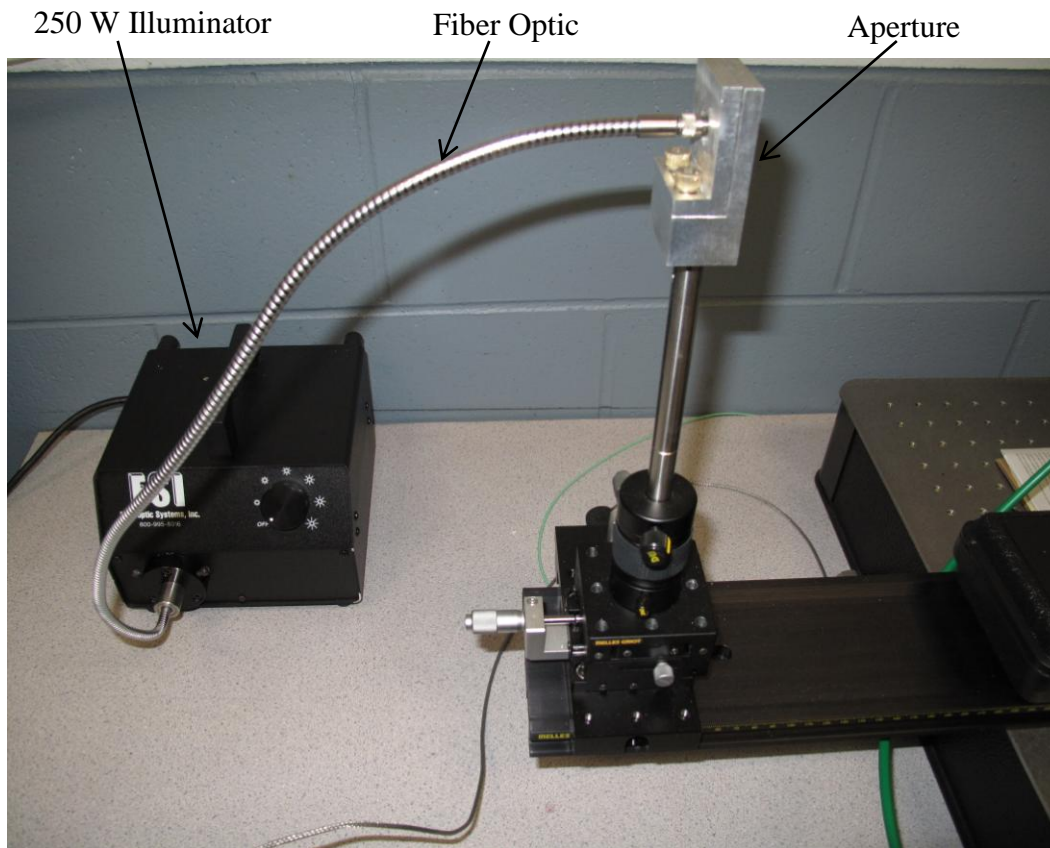


Figure 10. Illuminator and Aperture.

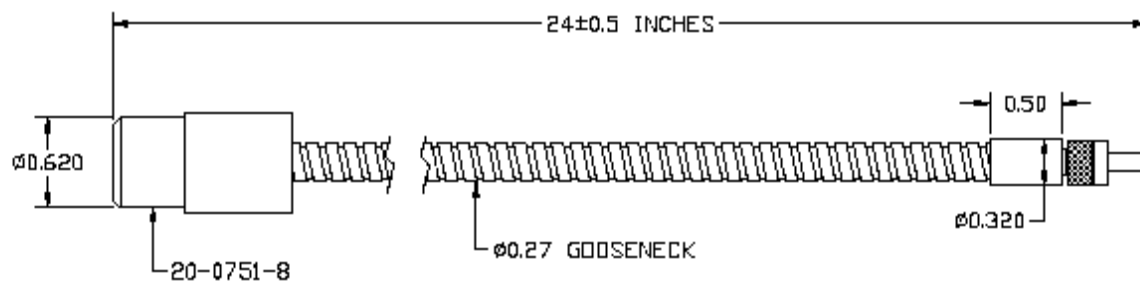


Figure 11. Gooseneck Fiber Optic Cable (Drawing from Fiber Optic Systems, Inc.).

Collimating Lens

Decollimating Lens

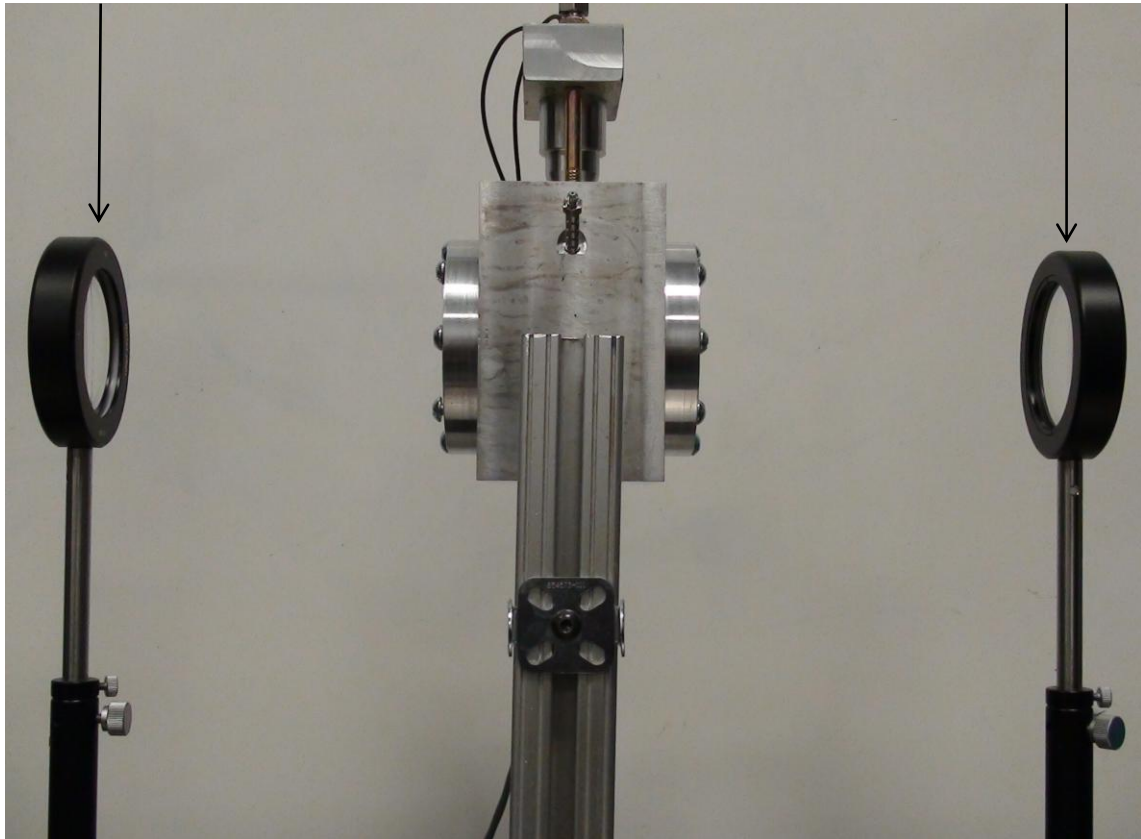


Figure 12. Collimating Lens, Combustion Chamber, and Decollimating Lens.

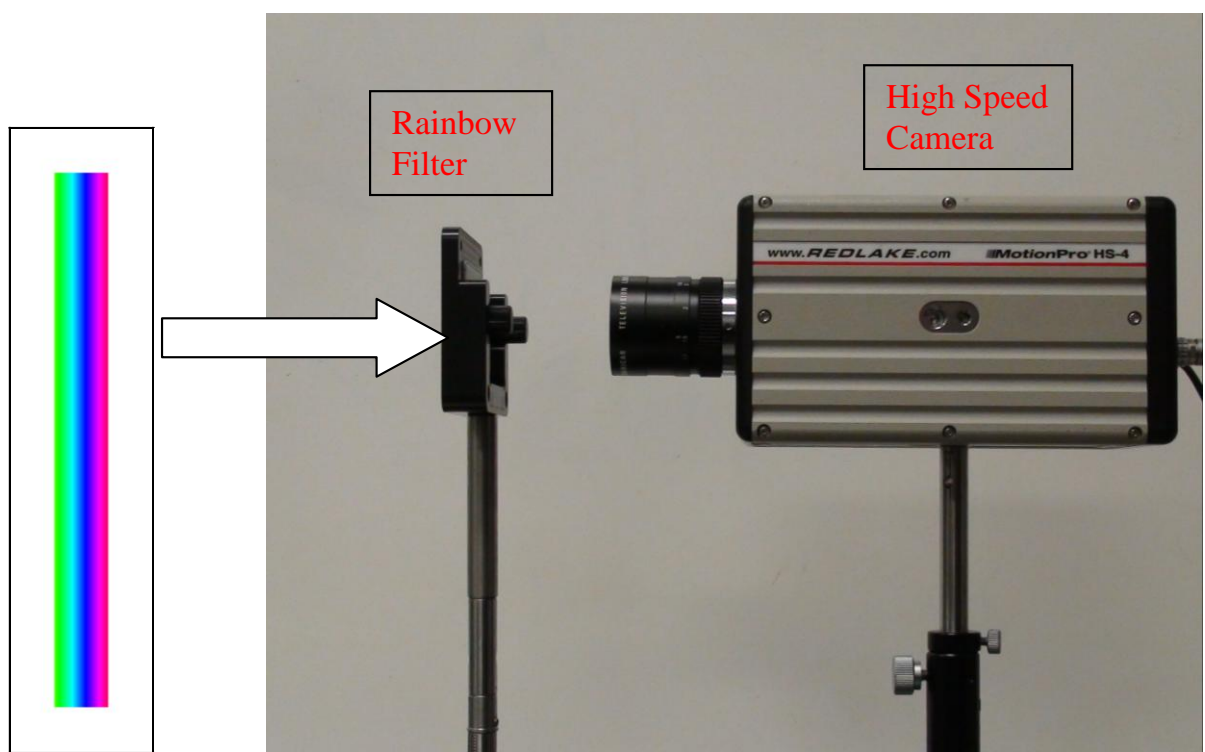


Figure 13. Rainbow Filter and High Speed Camera.

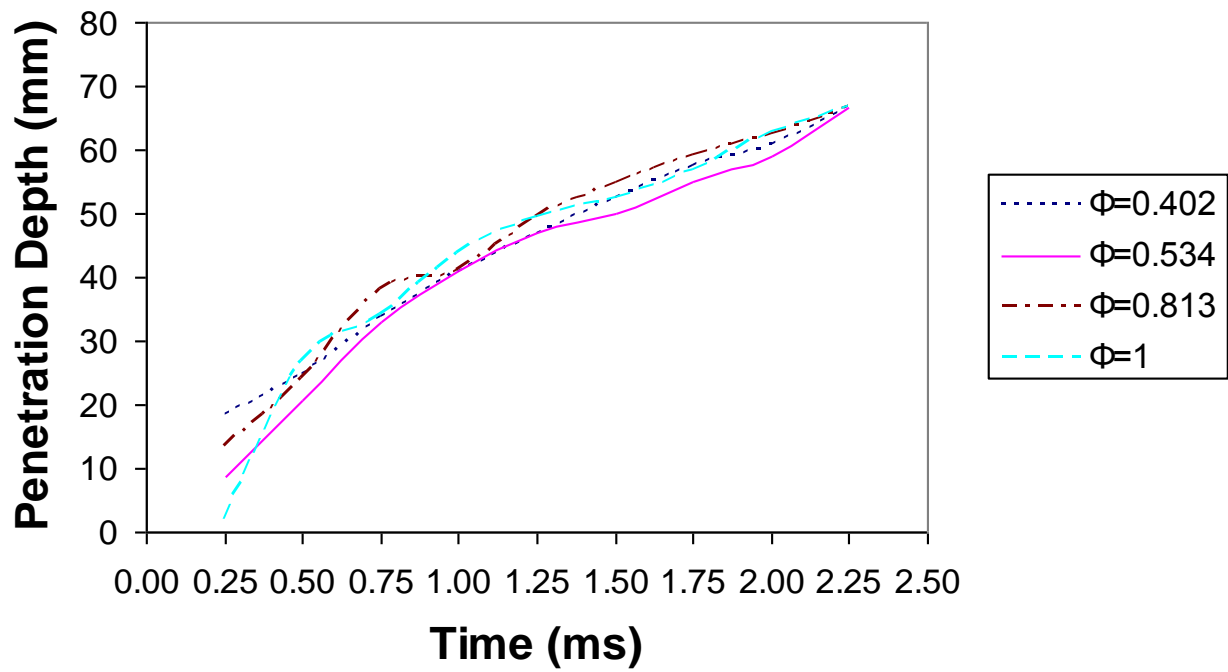


Figure 14. Jet Penetration Distance (L) After Time (t) For Varying Equivalence Ratios, $P_s=275.8$ kPa.

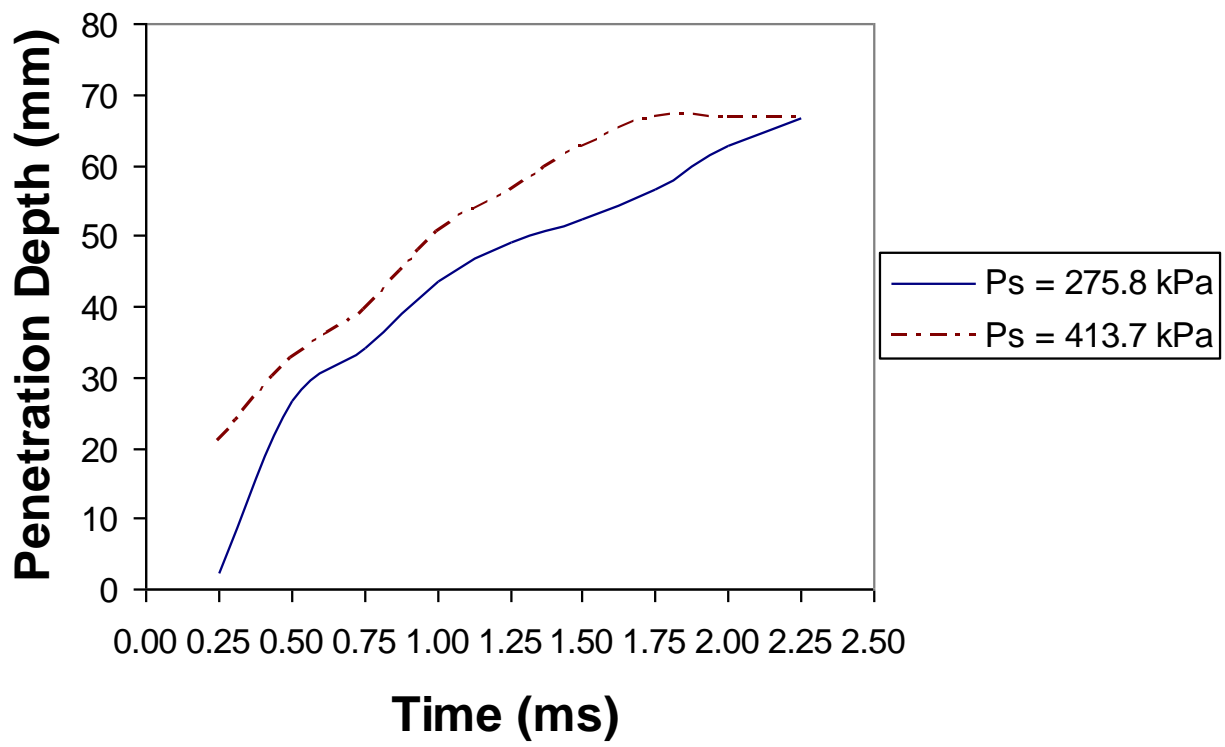


Figure 15. Jet Penetration Distance (L) After Time(t) For Varying Supply Pressures, $\phi = 1$.

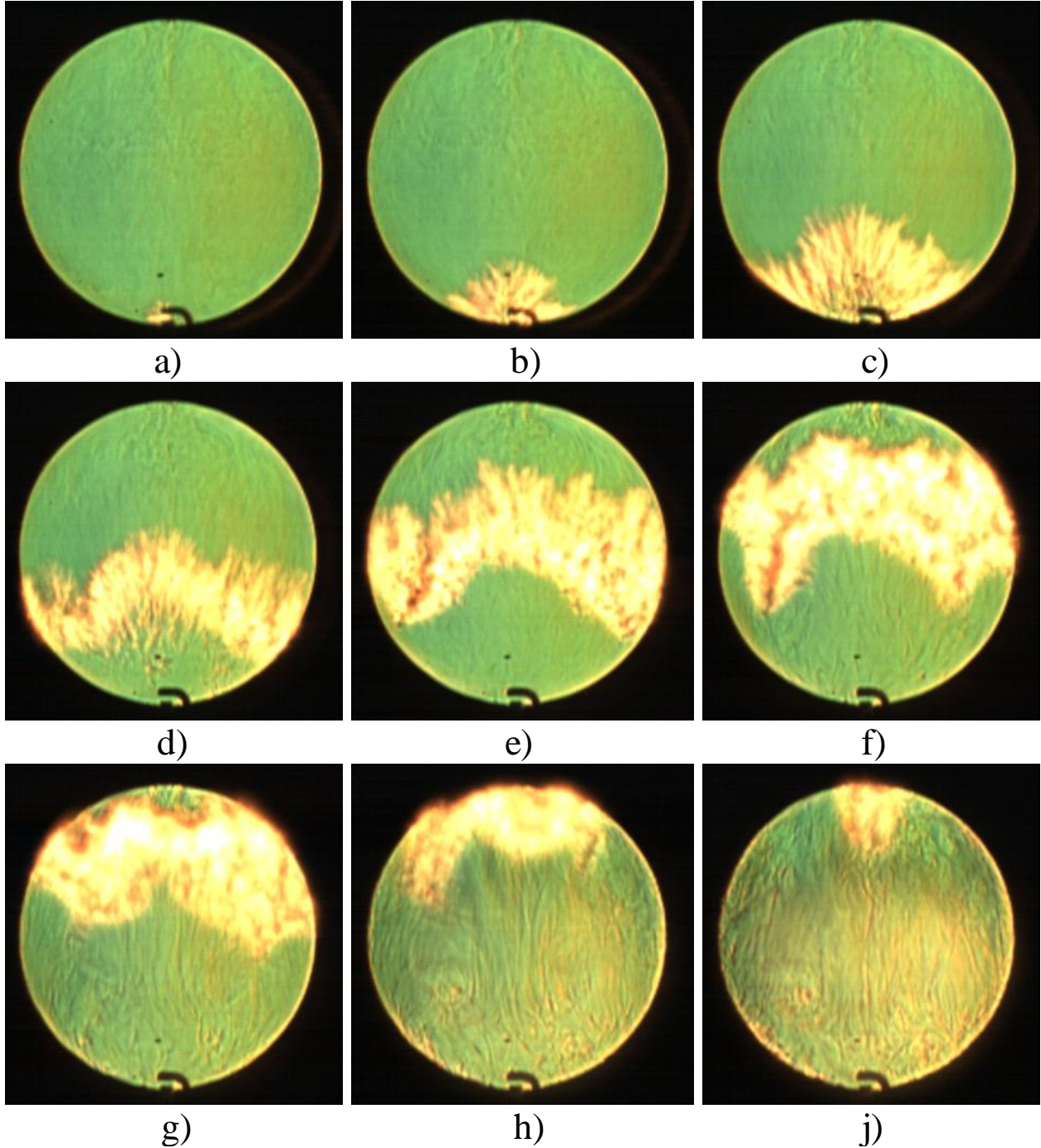


Figure 16. Schlieren Images (250 μ s Intervals) For $P_s=413.7$ kPa and $\phi = 1$.

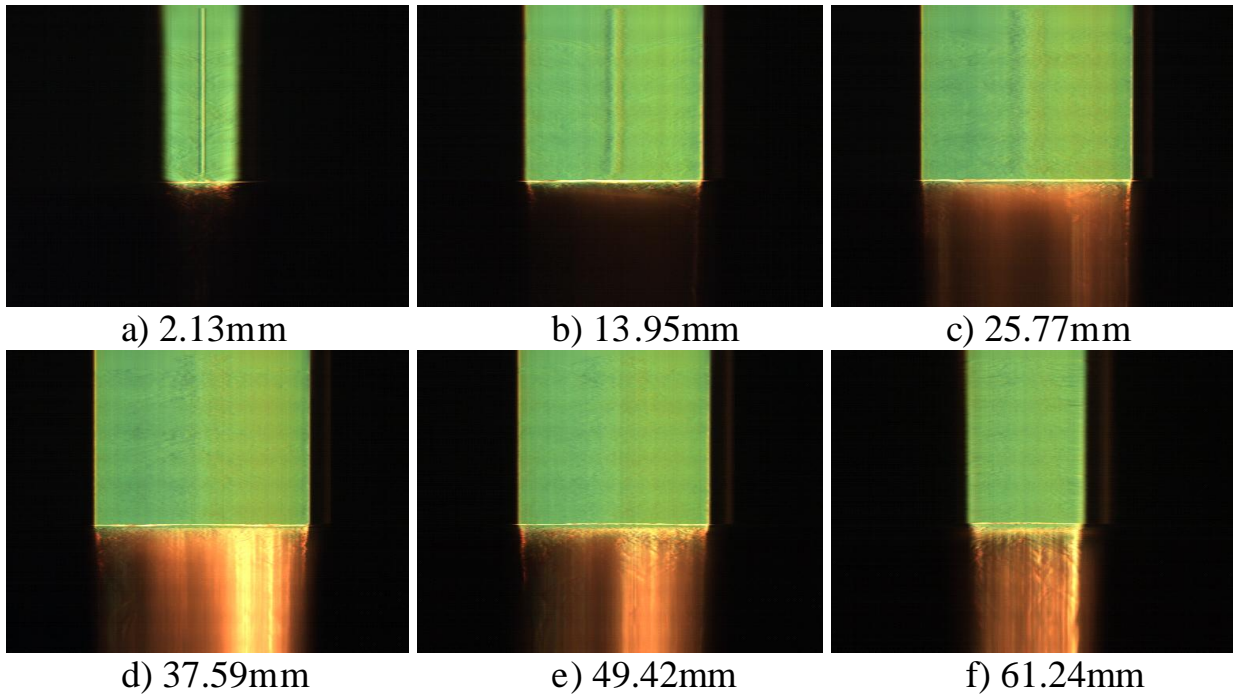


Figure 17. Space-Time Images For $P_s=413.7$ kPa and $\phi = 1$.

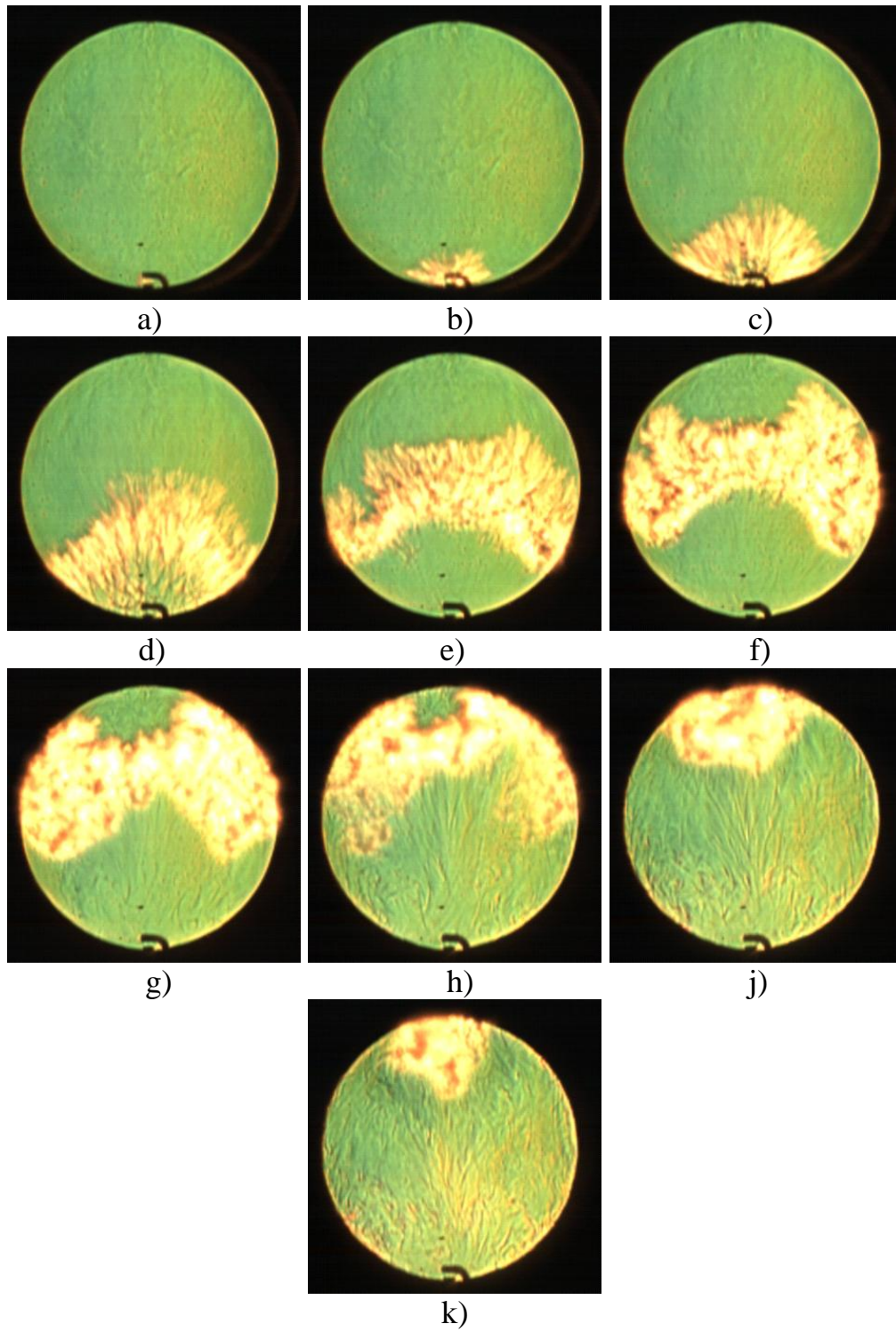


Figure 18. Schlieren Images ($250 \mu\text{s}$ Intervals) For $P_s = 275.8 \text{ kPa}$ and $\phi = 1$.

Table 1. Elapsed Flame Propagation Time for Varying Supply Pressures.

Distance (mm)	Elapsed Time ($P_s=275.8\text{kPa}$)	Elapsed Time ($P_s=413.7\text{kPa}$)
2.13	1.25 ms	1 ms
13.95	1.25 ms	1 ms
25.77	1 ms	1 ms
37.59	1 ms	1.25 ms
49.42	500 μs	750 μs
61.24	750 μs	750 μs

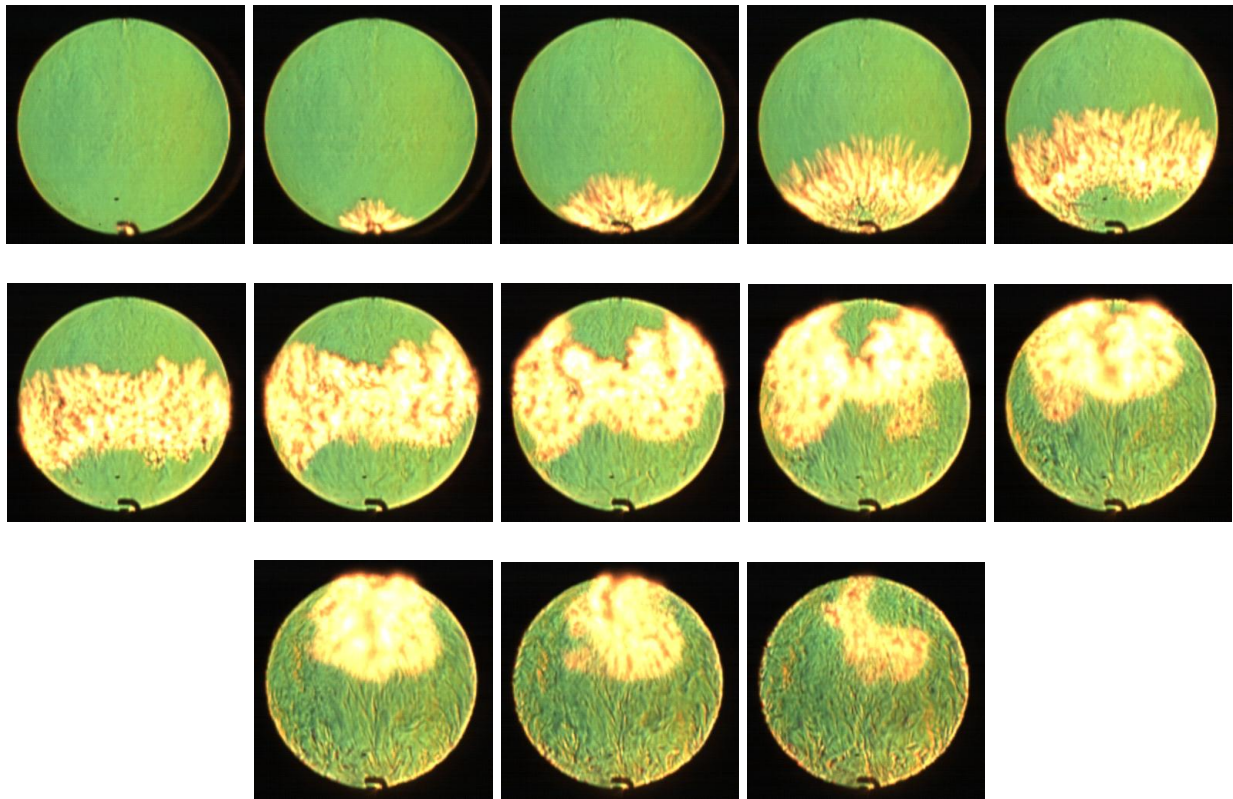


Figure 19. Schlieren Images (250 μ s Intervals) For $P_s=413.7$ kPa and $\phi = 0.804$.

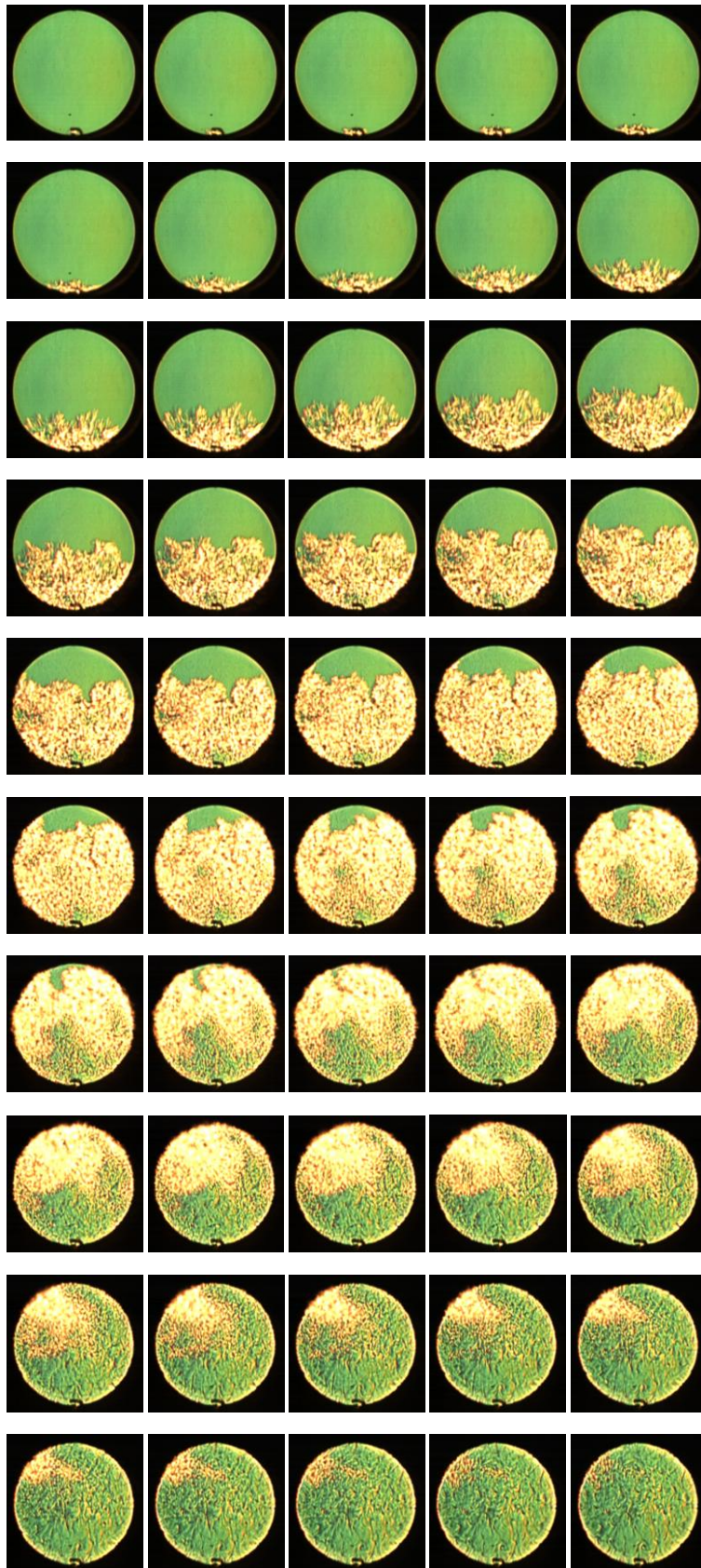


Figure 20. Schlieren Images (250 μ s Intervals) For $P_s=413.7$ kPa and $\phi = 0.318$.

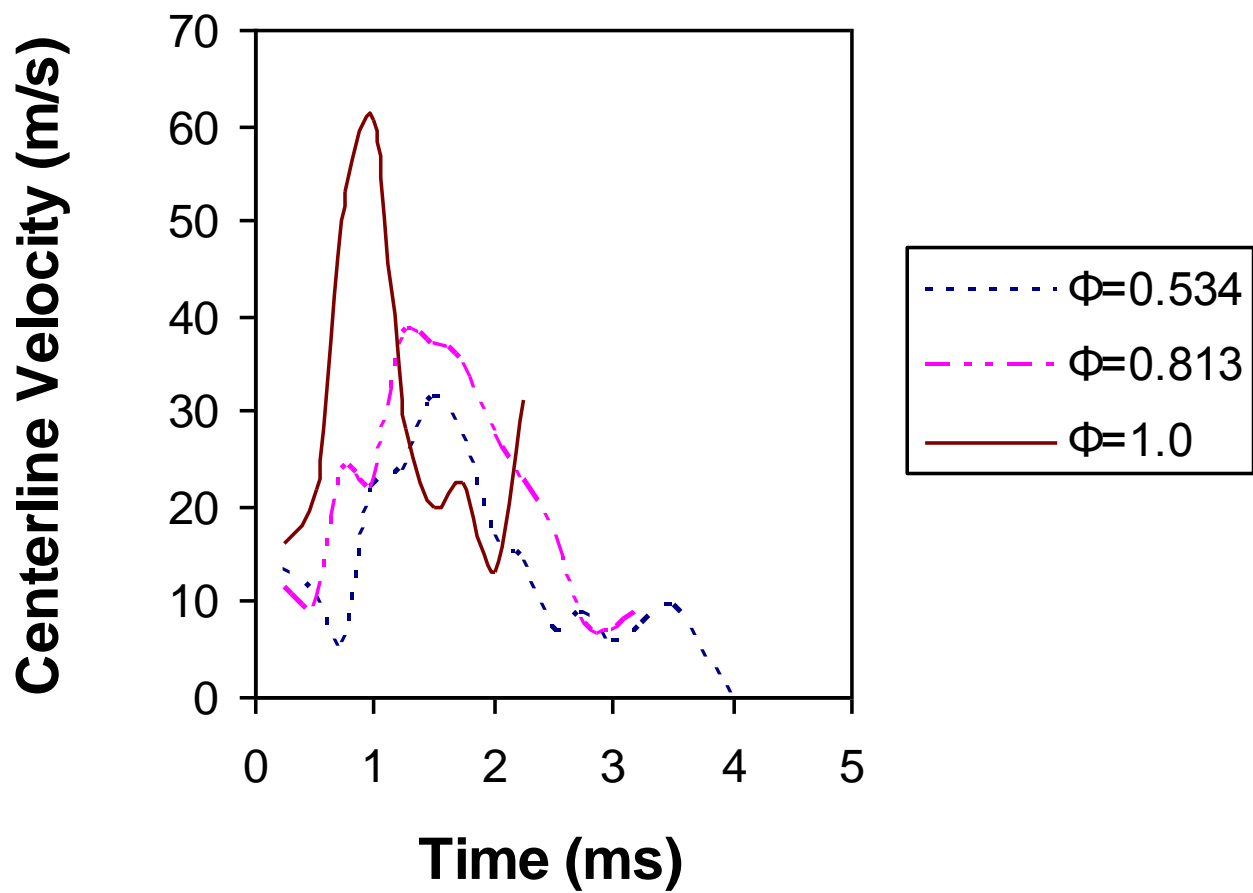


Figure 21. Centerline Flame Velocity For $P_s=275.8$ kPa and Varying Equivalence Ratio.

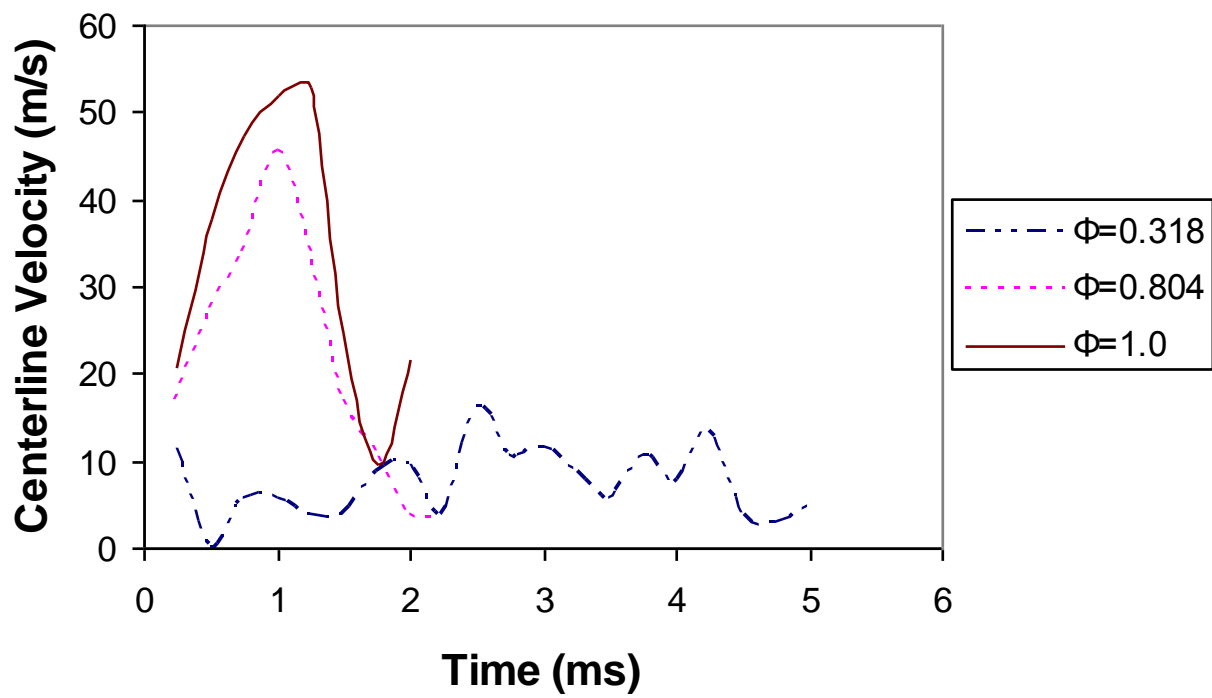


Figure 22. Centerline Flame Velocity For $P_s=413.7$ kPa and Varying Equivalence Ratio.

CHAPTER 3

THE EFFECT OF IGNITION TIME ON COMBUSTION OF STRATIFIED HYDROGEN-AIR MIXTURES IN A CONSTANT VOLUME CHAMBER

Abstract

Hydrogen was directly-injected into a constant volume combustion chamber and turbulently mixed with atmospheric quiescent air. The hydrogen/air mixture was ignited by a spark plug located diametrically opposite the injector. The effect of fuel-air mixing was investigated by varying the ignition time. High-speed Rainbow Schlieren Deflectometry (RSD) technique was used to visualize fuel injection, mixing, and flame propagation processes at 5000 Hz. Color schlieren images were used to calculate flame front propagation speed. Chamber pressure data were collected and used to estimate net heat transfer rates. Ignition times were separated into three groups each producing similar trends. Results show that ignition time has significant effects on flame front propagation, chamber pressure, and net heat transfer rate. Significant variations occur in maximum flame front speeds, maximum chamber pressures, and maximum net heat transfer rates while varying ignition time.

Introduction

Hydrogen as an alternative fuel for use in Internal Combustion Engines (ICE's) has been studied for decades to aid in decreasing our dependence on petroleum fuels. With near zero emissions of carbon monoxide (CO), oxides of nitrogen (NO_x), and unburned hydrocarbons (UHC); potentially zero emissions of carbon dioxide (CO₂); reduced problem of vapor lock, fuel-air mixing, fuel vaporization, and cold wall quenching compared to hydrocarbon fuels (HC); and favorable combustion properties including wide flammability limits lending to lean combustion, hydrogen is a promising fuel.

Disadvantages associated with the use of hydrogen include abnormal combustion such as knock, pre-ignition, and backfire. Compared to conventional petroleum fuels, heat loss through cylinder wall can be higher for hydrogen combustion which negatively affects the thermal efficiency. Recent research on hydrogen has sought to eliminate abnormal combustion, improve thermal efficiency, and increase power output while minimizing heat loss to cylinder wall. ICE's using hydrogen can operate at lean conditions greatly reducing NO_x emissions. In a study on the effect of spark timing on NO emissions in a hydrogen fuelled SI engine, NO production for equivalence ratios up to around 0.5 was shown to be negligible [Subramanian et al., 2007]. Moreover, engines can operate at higher compression ratios without experiencing knock. In particular, implementation of Direct Injected Spark Ignition (DISI) concept in a hydrogen fueled engine is an effective method of controlling abnormal combustion, achieving high thermal efficiency, and high power output [Mohammadi et al., 2007].

Spark timing affects combustion properties such as flame speed, flame propagation, and in-cylinder pressure. These properties have a profound effect on cylinder-wall heat loss and thus, the power output. To achieve stable combustion and desirable combustion properties, the

ignition time must be optimized. Fuel injection and ignition timings have a great effect on engines fueled with hydrogen and ignition should be timed to occur towards the end of the injection process [Zhenzhong et al., 2002]. Fuel injection and ignition times have shown to be a significant factor with other fuels. Research conducted on a methanol fuelled engine showed that fuel injection and ignition timing have significant effects on engine parameters such as cycle to cycle variation, in-cylinder pressure, heat release rate, and engine thermal efficiency. Optimization of injection and ignition timings can improve brake-specific fuel consumption (BSFC) by more than 10% as compared to other times at an engine speed of 1600 rpm [Li et al., 2010]. In a study of a DISI engine fueled with blends of hydrogen and natural gas, turbulence generated by fuel jet in the combustion chamber preserves strong fuel-air mixture stratification [Huang et al., 2007]. Ignition towards the end of injection leads to high and fast burn rates, high BMEP (brake mean effective pressure), short combustion time, and high thermal efficiency [Huang et al., 2007]. NO_x concentrations increase, HC concentrations decrease, and CO concentrations change marginally for advanced ignition timing [Huang et al., 2007]. Ignition timing is a key operating parameter that affects SI engine efficiency and performance at any load [Yousufuddin & Masood, 2009]. At conditions leading to high engine output, late hydrogen injection reduces NO_x emissions since engine operates at lean conditions [Mohammadi et al., 2007]. Injecting hydrogen during the compression stroke prevents knock [Mohammadi et al., 2007]. The present study focuses on the effects of ignition time on hydrogen combustion, flame structure, flame front speed, chamber pressure, and net heat transfer rate.

Experimental Setup

The experimental setup consists of a constant volume combustion chamber (CVCC)

system, a high-speed rainbow schlieren deflectometry (RSD) system, and a data acquisition and control system as described below.

Constant Volume Combustion Chamber System

The test apparatus consisted of a CVCC with a fuel injector attached to a fuel supply system. The combustion chamber, shown photographically in Figure 1, is made from an aluminum block with a cylindrical opening drilled through it. This opening forms the volume of the combustion chamber and it has a diameter of 66.7 mm and a width of 31.8 mm. The combustion space is enclosed by two parallel optical windows located in recessed regions on both ends. Each optical window is a fused silica, single surface $1/10^{\text{th}}$ wave optical flat (Edmund Optics NT01-915) with diameter of 76.2 +/- 1 mm and thickness of 19.05 +/- 1.5 mm. The optical flats are precision polished on the side facing the chamber to ensure accuracy and are pitch polished on the other side. The optical flats are held in place by aluminum collars (Figure 1) bolted to the outer surface of the combustion chamber using eight evenly spaced bolts.

Hydrogen was supplied by a compressed gas cylinder as shown in Figure 2. The hydrogen flowed through a test vessel system and a supply pressure regulator before reaching the fuel injector located at the top center of the CVCC (see Figure 1). The fuel injector is a Hoerbiger high pressure hydrogen direct injector (GV1) connected to a Provebo controller powered by a 13.8 VDC single channel regulated power supply (MG Pro Series PS22). The controller is connected to a solid state relay (SSR1, Opto 22 DC60S3) with a 3-32 VDC control used to ground the power required for injector operation. The spark is created by a spark plug (Champion RV12YC6) fixed at the bottom center of the CVCC, diametrically opposite from the hydrogen injector. The spark plug is fixed in a Honda stick coil that receives 13V from a variable channel of a DC power supply (TekPower HY3003D-3) via a second solid state relay

(SSR2). SSR1 and SSR2 switch sides are connected to two 5V output ports of a Programmable Logic Controller (PLC, Keyence KV-24DTP). A third PLC output port provides 5V power directly to the coil to trigger the spark. The PLC's 24V power requirement is met by the TekPower DC power supply. The third channel of the TekPower DC power supply is a fixed 5V channel connected to the common supply port of the PLC. A 5V signal is sent to the PLC from the Digital I/O ports of a National Instrument's PCI Data Acquisition System (DAQ) with a BNC breakout box to initiate program execution. The fuel injector, coil charging, and spark triggering are sequenced and controlled by a Ladder Logic program downloaded to the PLC. Time constants are changed in the program to vary the ignition time. The DAQ is also connected to a high speed camera, discussed in the following section. The sequencing of the PLC and the high speed camera is controlled by a program written in the LabView software.

A piezoelectric pressure transducer (Kistler Type 6053CC60) calibrated at 0 to 150 bar with a sensitivity of 20.2 pC/bar is mounted on the lateral surface of the CVCC. The pressure transducer collects dynamic pressure data during hydrogen injection and combustion processes. The charge output from the pressure transducer is amplified and converted to voltage output range of 0 to 10 V by a charge amplifier (Kistler Type 5010-Dual Mode). Voltage output from the amplifier is connected to the Labview DAQ where pressure data are acquired and digitized at 10000 Hz.

Rainbow Schlieren Deflectometry System

Rainbow Schlieren Deflectometry (RSD), an optical technique to visualize density gradients in the flow field, was utilized to acquire the necessary data. An inhomogeneous media, for example, hydrogen injected into air, creates density gradients that lead to schlieren effects arising from refraction of light rays traveling through the medium. RSD is an optical technique

to project light ray deflections or displacements in color to a viewing screen. In some cases, the color schlieren images can be quantitatively analyzed to obtain the local distributions of the density field.

Figure 3 illustrates the RSD setup implemented in this study. A beam of light was transmitted from a white LED turn-key light source using a LR-C optical fiber. The 1.0 m fiber optic cable is connected to the source aperture located at the focal point of the collimating lens. The lens is a precision achromatic doublet lens that is 76.2 mm in diameter with a 500 mm focal length. It is coated with a 400-700 nm antireflection coating. The collimated beams or parallel light rays traveled through the test media contained in the CVCC as discussed previously. During experiments, the test media was composed of a non-homogeneous hydrogen-air mixture. After passing through the test media, refracted light rays passed through a de-collimating lens, which refocused light beams onto a rainbow filter. The de-collimating lens has the same properties as the collimating lens, except its focal length is 750 mm. The rainbow filter is fixed at the focal point of the de-collimating lens. The rainbow filter is a 35 mm photo slide with vertical strips of color gradations. Light rays transmitted through the rainbow filter form an inverted image of the test medium captured by a high speed digital camera (Red Lake MotionPro HS-4). The camera acquires color schlieren images for 3.2 s at a rate of 5,000 frames per second (fps) with an exposure time of 95 μ s.

Schlieren images were analyzed to compute the flame front speed along the centerline (the diameter whose ends are the injector and spark plug) of the chamber. The flame front location was identified visually from the images, and then, its speed was computed by dividing the displacement by the time interval of 0.2 ms between the images. Based on the pixel resolution of 245 μ m, the uncertainty in flame front speed is estimated to be 1.2 m/s.

Instantaneous chamber pressure ($P(t)$) measured by the pressure transducer was used to calculate instantaneous chamber temperature ($T(t)$) and instantaneous net heat transfer ($Q(t)$) during the experiment. The instantaneous net heat transfer is the net thermal input in the chamber by heat released in reactions and heat loss from chamber surfaces to the ambient. Thus, the instantaneous net heat transfer will be positive when the heat released is greater than the heat loss, and vice versa. The instantaneous chamber temperature was calculated using the equation of state for an ideal gas with the total mole number of the reactants given as

$$N = N_{H_2} + N_{air}$$

where $N_{H_2} = m_{H_2}(t) / M_{H_2}$ and $N_{air} = m_{air}(t) / M_{air}$.

The instantaneous net heat transfer was calculated using:

$$Q(t) = m(t) C_v (dT/dt) \Delta t$$

where $m(t) = (m_{air} + m_{H_2})$ and the specific heat (C_v) is calculated by first using a third order polynomial to find C_p and then using $C_p/C_v = 1.4$ for air to find C_v [Cengel & Boles, 2002].

Results and Discussions

Hydrogen at a supply pressure of 413.7 kPa (60 psi) was injected into quiescent, atmospheric air in the CVCC to obtain an overall equivalence ratio of 1.0. The hydrogen fuel jet mixed turbulently with the air as it moved through the chamber. The jet reaches the igniter, diametrically opposite the injector, at $t = 2.25$ ms, where $t = 0$ refer to the start of the fuel injection. At a later time, the fuel was ignited and the flame propagated upward toward the fuel injector. The fuel was injected for a period of 40 ms to obtain the desired equivalence ratio. Thus, the fuel injector closed at $t = 40$ ms. Experiments were conducted with ignition at $t = 3, 5, 10, 20, 30, 40, 60, 80, 240,$ and 540 ms. These ignition times were separated into three groups:

early ignition ($t = 3$ to 10 ms), mid ignition ($t = 20$ to 40 ms), and late ignition (60 to 540 ms) groups as shown in Figure 4. Acquired measurements were processed to investigate the effect of ignition time on flame structure, flame front speed, chamber pressure, and heat transfer signifying heat release by reactions and heat loss from chamber walls to the ambient.

When the injector opens, the hydrogen jet, which is initially conically shaped, propagates towards the igniter, located diametrically opposite the injector. As the hydrogen jet penetrates through the chamber it turbulently mixes with the air in the chamber. Once the jet reaches the opposite end of the chamber at $t = 2.25$ ms, it interacts with the chamber wall creating vortical structures that propagate back towards the injector. Early ignition is characterized by fuel-rich regions in the jet core, fuel-air mixing in the jet shear layer, and fuel-air mixing in the vortical structures, constrained by the limited time for fuel injection before ignition. For mid ignition times, the fuel-rich region of the jet core and fuel-air mixing in the jet shear layer are similar to those for early ignition times. However, the increased time for fuel injection before ignition allows for the vortical structures to propagate closer to the fuel injector, which in turn creates a wider fuel-air mixing region. At late ignition times, all of the fuel has been injected into the chamber, the fuel injector is close, fuel has spread throughout the chamber to produce fuel-air mixing regions, a distinct fuel jet is no longer present, and turbulence in the chamber created by the fuel jet is decreasing with increasing time for ignition. Late ignition tends to create a more homogeneous fuel-air mixture throughout the chamber prior to combustion.

Flame Front Propagation

For the early ignition time group, $t = 3$, 5 , and 10 ms, the flame front initially propagates vertically toward the injector and laterally in a symmetric manner, as seen in Figures 5-7. Two distinct features of flame front propagation are identified from the schlieren images. The flame

in the center core region propagates vertically into the perimeter of hydrogen jet, eventually taking on its conical shape. The flame in regions outside the fuel jet travels vertically and laterally to form distinct side lobes reminiscent of the vortical structures formed during the fuel-air mixing process. The initial speed of the central flame front is greater than that of the outer flame front. After the initial transients, the flame structure approaches steady conditions with combustion mainly in diffusion mode as the additional fuel enters the chamber. Thus, the fuel injection and fuel-air mixing rates would constrain the reaction rate. Schlieren images indicated that the combustion ended immediately after the fuel supply was terminated, i.e., when the injector was closed at $t = 40$ ms. Thus, combustion duration for ignition at $t = 3, 5,$ and 10 ms was $37, 35,$ and 30 ms, respectively. Figure 8 presents the central flame front speed for different cases. The flame front accelerates rapidly to attain peak front speed within the first millisecond after ignition. The maximum flame front speed varies from 50 to 70 m/s, which is significantly higher than the laminar flame speed of a stoichiometric hydrogen-air mixture. The high flame front speed is indicative of the high-level of turbulence generated by the fuel jet. After the peak, the flame front decelerates quickly to reach speed of less than 10 m/s within 1.5 ms after ignition as the remaining fuel-air mixture in the chamber is consumed,

For the mid ignition time group, $t = 20, 30,$ and 40 ms, Figures 9-11 show that within the first millisecond of combustion, the flame propagates in same manner as the early ignition group. The lower region forms distinct side lobes, but the central flame front does not propagate into the shear layer of the hydrogen jet indicating inadequate fuel-air mixing near the injector inlet. Instead, combustion occurs in regions outside the fuel jet inlet, where the vortical structures formed by interactions between the jet and chamber wall have produced a combustible fuel-air mixture. For ignition at $t = 20$ and 30 ms, the reactions completed at the end of fuel injection ($t =$

40 ms) and thus, the combustion duration was 20 and 10 ms, respectively. For ignition at $t = 40$ ms, the combustion duration of 3.6 ms was much shorter than the earlier ignition times. In this case, all of the fuel was injected before ignition and thus, diffusion mode combustion limited by fuel injection and fuel-air mixing rates was eliminated. Figure 12 shows the centerline flame front speed for different cases in the mid ignition time group. Results show a rapid increase in the flame front speed followed by a decrease to less than 10 m/s within 1.5 ms after ignition. The peak flame front speed is 75 m/s and 90 m/s for ignition at $t = 20$ and 30 ms, respectively. The peak flame front speed for ignition at $t = 40$ ms is much lower, about 55 m/s, which can be attributed to a decrease in turbulence in the chamber after the fuel injector has closed.

For the late ignition group, $t = 60, 80, 240,$ and 540 ms, the flame front propagation significantly changes as compared to early and mid-ignition groups. A single flame front with hemi-spherical shape is observed throughout the duration of the combustion process, as seen in Figures 13-16. With injector closed at $t = 40$ ms, more time is available for fuel-air mixing to occur throughout the chamber. Increasing the ignition time however decreases the turbulence generated by the fuel jet. The schlieren image in Figure 13 shows initial flame front with turbulent corrugations for ignition at $t = 60$ ms. In contrast, the flame front in Figure 16 for ignition at $t = 540$ ms is initially laminar, and later on, it shows straining resulting from flame generated turbulence, a mechanism different from the fuel jet generated turbulence. Figure 17 shows the gradual increase and decrease in flame front speed after ignition. The maximum flame front speed is much smaller compared to early and mid-ignition groups: 33 m/s, 28 m/s, 21 m/s, and 23 m/s, respectively, for ignition at $t = 60$ ms, 80 ms, 240 ms, and 540 ms. The decrease in the maximum flame front speed is attributed to the decrease in the fuel jet generated turbulence as the ignition time is increased. The combustion duration is 3.2 ms, 3.6 ms, 4.6 ms, and 4.2 ms,

respectively, for ignition at $t = 60$ ms, 80 ms, 240 ms, and 540 m/s. A graph of the combustion duration for all ignition times is provided in Appendix F. These results show that ignition time is an important combustion parameter for direct injected spark ignition systems. The present findings are consistent with previous studies showing higher flames speeds in stratified fuel-air mixtures as compared to homogeneous fuel-air mixtures [Kang & Kyritsis, 2007].

Chamber Pressure

Figures 18-20 present chamber pressure variations for each ignition time group. After the injector opens, the pressure increases gradually because of the added mass of hydrogen in the chamber. After ignition, combustion starts and temperature and pressure increase rapidly. After reaching a peak, the pressure decreases because of the temperature decreasing by heat loss to the ambient. For ignition at $t = 3$ ms (see Figure 18), the pressure rises to its peak value of 478 kPa in two stages; a rapid increase associated with combustion in initially well-mixed and highly turbulent regions of the chamber, which also results in high flame front speed as discussed previously. The gradual increase in pressure can be attributed initially to combustion in regions with limited fuel penetration and thus, lean mixtures with low turbulence. The pressure also increases gradually during combustion in diffusion mode until the peak value is reached. Subsequently, the pressure decreases and then, reaches a steady value for the remaining period of combustion in diffusion mode. The constant pressure indicates that the heat release rate by combustion and rate of heat loss to the ambient are the same. For ignition at $t = 5$ ms, the chamber pressure also increases in two stages. However, the pressure after the first stage is higher than that for ignition at $t = 3$ ms because of the increased fuel supply in the chamber before ignition. As the injected fuel is consumed, the pressure increases gradually during combustion in diffusion mode. For ignition at $t = 10$ ms, more fuel has mixed with air in the

chamber, which results in a greater increase in pressure with peak value of 500 kPa. Subsequently, the pressure decreases to reach a steady value during combustion in diffusion mode with equal heat release and heat loss rates.

For the mid ignition group, $t = 20, 30,$ and 40 ms, fuel is injected into the chamber for 20, 10, and 0 ms, respectively, after ignition. For all three times, pressure rises rapidly after ignition, as seen in Figure 19, until reaching peak at 680 kPa for $t = 20$ ms, 850 kPa for $t = 30$ ms, and 645 kPa for $t = 40$ ms. Increased fuel supply in the chamber before ignition results in higher peak pressure for $t = 30$ ms case compared to that for $t = 20$ ms case and early ignition cases. The peak pressure is lowest for $t = 40$ ms case, evidently because of the decrease in the fuel generated turbulence which also decreased the flame front speed as discussed previously. After reaching the peak, the pressure declines at a rate greater than that for the early ignition group. Moreover, insufficient time is available for the pressure to reach steady value during combustion in diffusion mode for $t = 20$ ms and 30 ms cases.

For the late ignition group, $t = 60, 80, 240,$ and 540 ms, pressure, as seen in Figure 20, rises rapidly until it reaches a peak value of about 1000 kPa. With all of the fuel in the chamber prior to ignition, combustion occurs in premixed mode. Thus, the combustion time is shorter and more heat is retained within the chamber (less heat loss to the ambient) during combustion, which increases the peak pressure (and temperature). After the peak, the pressure declines at a rate much faster than the other ignition groups, presumably because of the higher heat loss rate resulting from the high chamber temperature. Variations in chamber pressure by as much as 670 kPa from the lowest peak pressure in the early ignition group to the highest peak pressure in the late ignition group suggest that ignition time has a significant effect on pressure. As ignition time increases prior to the end of injection, chamber pressure peaks increases.

Net Heat Transfer Rate

Figures 21-23 shows the net heat transfer rate for each ignition group. With low heating value of hydrogen, LHV = 121,000 kJ/kg and total injected mass, $m = 3.89\text{E-}16$ kg, the total heat release by the fuel is 472 J. In the early ignition group, $t = 3, 5,$ and 10 ms, the net heat transfer rate increases until it peaks at 49 kW for $t = 3$ ms, 48 kW for $t = 5$ ms, and 57 kW for $t = 10$ ms as seen in Figure 21. The amount of heat release decreases after these peaks for the duration of the combustion. In the mid-ignition group, the net heat transfer rate increases until it peaks at 89 kW for $t = 20$ ms, 125 kW for $t = 30$ ms, and 72 kW for $t = 40$ ms and decreases after the peaks, as seen in Figure 22. For the late ignition group, the net heat transfer rate increases until it peaks at 106 kW at $t = 60$ ms, 105 kW at $t = 80$ ms, 94 kW at $t = 240$ ms, and 106 kW at $t = 540$ ms, and rapidly decreases after the peak is reached, as seen in Figure 23. Net heat transfer rates for using the number of moles of the products instead of the reactants can be found in Appendix M.

All three ignition time groups have similar heat transfer trends with an initial increasing positive net heat transfer rate signifying that heat released by the fuel during combustion is much greater than the heat loss to the chamber wall ($Q_{\text{rel}} > Q_{\text{loss}}$). After the peak, the net heat transfer rate is initially positive until its sign changes when $Q_{\text{loss}} > Q_{\text{rel}}$. Finally, the net heat transfer rate approaches zero signifying thermal equilibrium, i.e., either $Q_{\text{loss}} = Q_{\text{rel}}$ or $Q_{\text{loss}} = Q_{\text{rel}} = 0$. Again, ignition time has a significant effect on the net heat transfer in the chamber.

Conclusions

In this study, hydrogen was injected in a constant volume combustion chamber to create stratification and turbulent mixing of fuel and air before combustion. Combustion was initiated before, at, and after closing the fuel injector. The key findings of the study are summarized below:

The flame front propagated rapidly with peak speed of up to 70 m/s because of the intense mixing and turbulence generated by the fuel jet when ignition occurred before the injector was closed. Once the injected fuel was consumed, combustion in diffusion mode, constrained by fuel injection rate, was sustained until the end of fuel injection. Turbulence generated by the fuel jet decreased after the injector was closed, which resulted in decrease in the flame front speed with increasing ignition time. The combustion duration decreased with increasing ignition time for ignition before closing the fuel injector, while the reverse was true for ignition after closing the fuel injector. The peak pressure and rate of pressure decay were also affected by the ignition time. Higher peak pressure values and higher pressure decay rates were obtained for ignition after closing the injector. These cases were also accompanied with high net heat transfer rates during the combustion.

Acknowledgements

Tanisha Booker was supported by the Graduate Assistance in Areas of National Need (GAANN) program of the U.S. Department of Education.

References

- Cengel Y., Boles M. Thermodynamics, An Engineering Approach. 4th Ed. (2002), The McGraw Hill Companies, Inc.
- Huang Z., Wang J., Liu B., Zeng K., Yu J., Jiang D. Combustion characteristics of a direct-injection engine fueled with natural gas-hydrogen blends under different ignition timings. Fuel 86 (2007) 381-387.
- Kang T., Kyritsis D. A combined experimental/ computational investigation of stratified combustion in methane-air mixtures. Energy Convers. Manage. 48 (2007) 2769-2774.
- Li J., Gong C., Su Y., Dou H., Liu X. Effect of injection and ignition timings on performance and emissions from a spark-ignition engine fueled with methanol. Fuel 89 (2010) 3919-3925.
- Ma F., Liu H., Wang Y., Li Y., Wang J., Zhao S. Combustion and emission characteristics of a port-injection HCNG engine under various ignition timings. Int. J. Hydrogen Energy 33 (2008) 816-822.

- Mohammadi A., Shioji M., Nakai Y., Ishikura W., Tabo E. Performance and combustion characteristics of a direct injection SI hydrogen engine. *Int. J. Hydrogen Energy* 32 (2007) 296-304.
- Subramanian V., Mallikarjuna J.M., Ramesh A. Effect of water injection and spark timing on the nitric oxide emission and combustion parameters of a hydrogen fuelled spark ignition engine. *Int. J. Hydrogen Energy* 32 (2007) 1159-1173.
- Yousufuddin S., Masood M. Effect of ignition timing and compression ratio on the performance of a hydrogen-ethanol fuelled engine. *Int. J. Hydrogen Energy* 34 (2009) 6945-6950.
- Zhenzhong Y., Jianqin W., Zhuoyi F., Jinding L. An investigation of optimum control of ignition timing and injection system in an in-cylinder injection type hydrogen fueled engine. *Int. J. Hydrogen Energy* 27 (2002) 213-217.

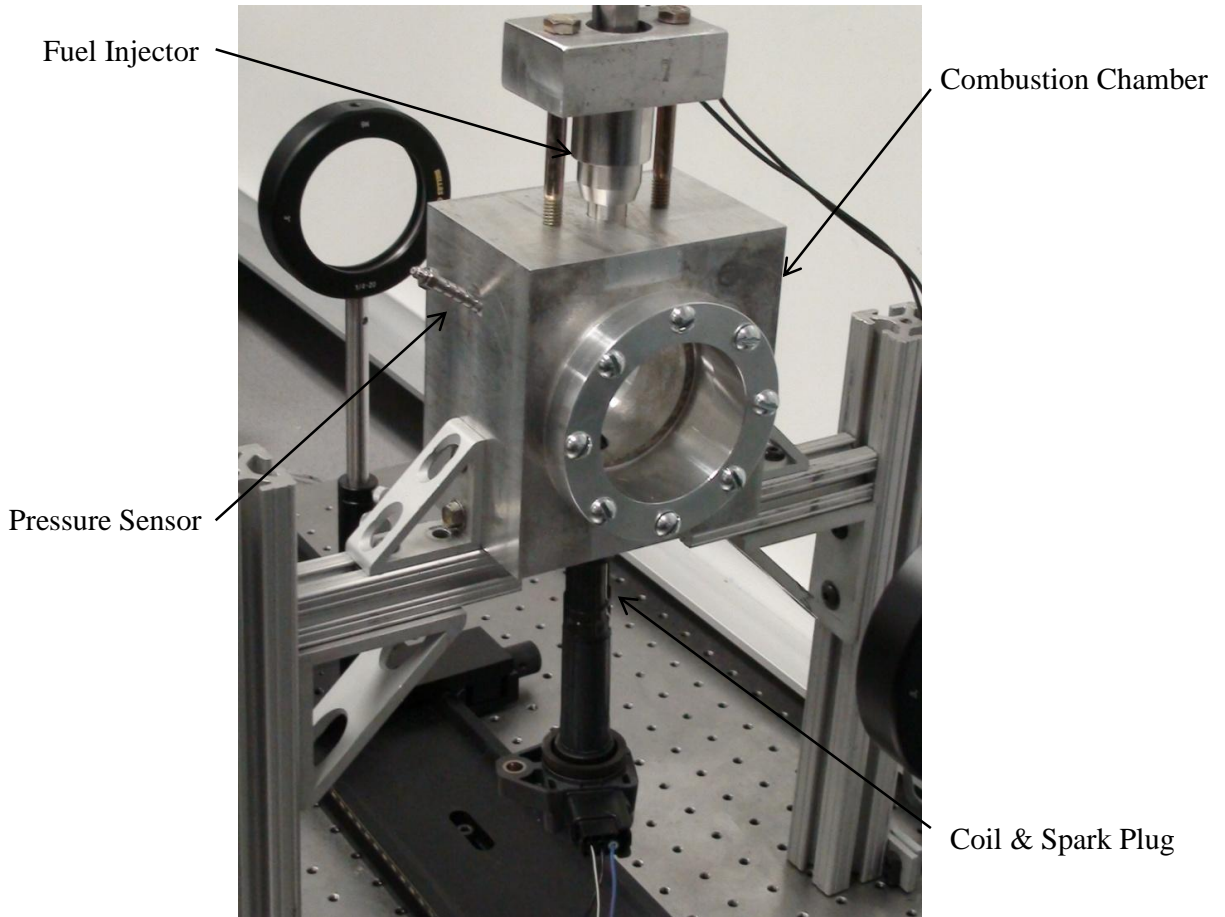


Figure 1. Combustion Chamber.

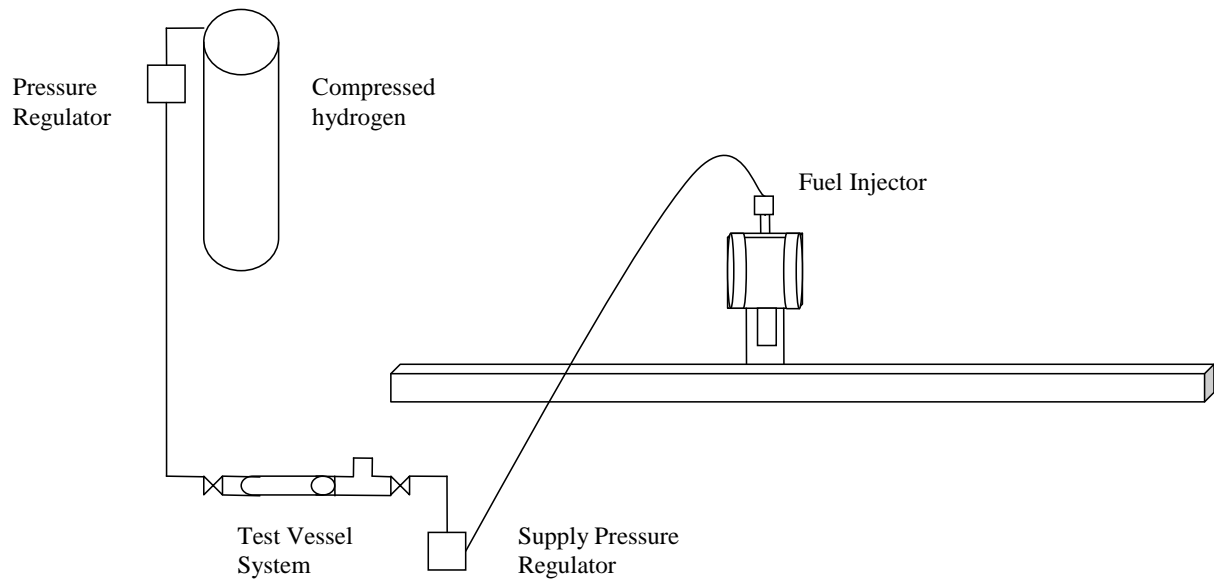


Figure 2. Fuel Flow System.

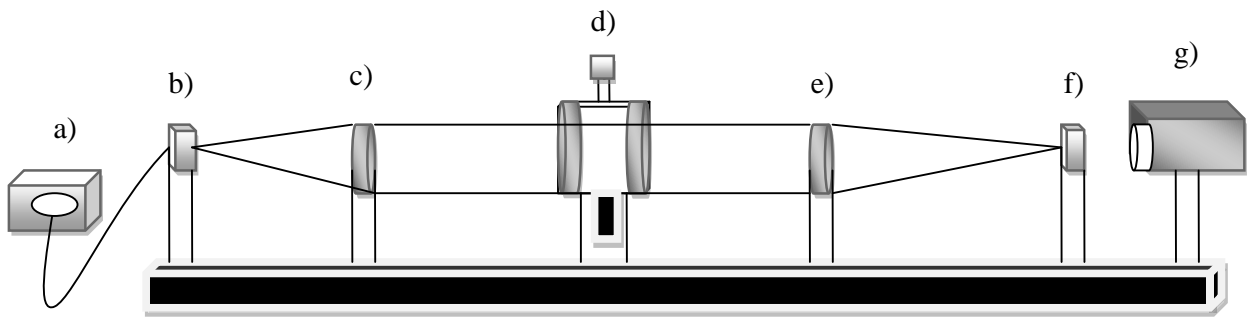


Figure 3. Rainbow Schlieren Deflectometer; a) Illuminator, b) Aperture, c) Collimating Lens, d) Test Media (Combustion Chamber), e) Decollimating Lens, f) Rainbow Filter, and g) High Speed Camera.

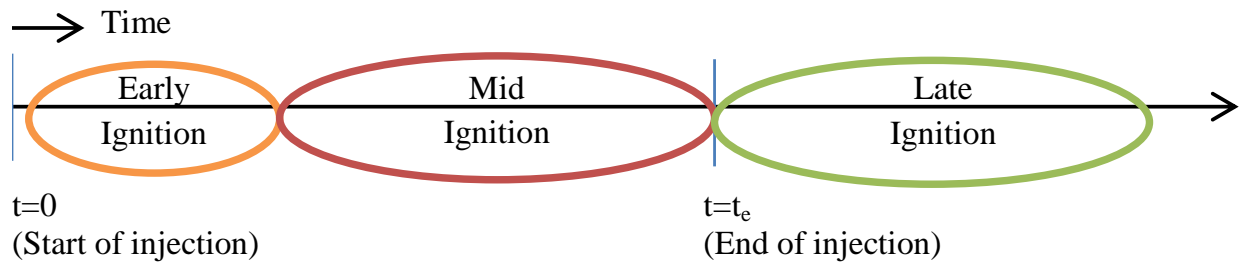


Figure 4. Ignition Time Groups.

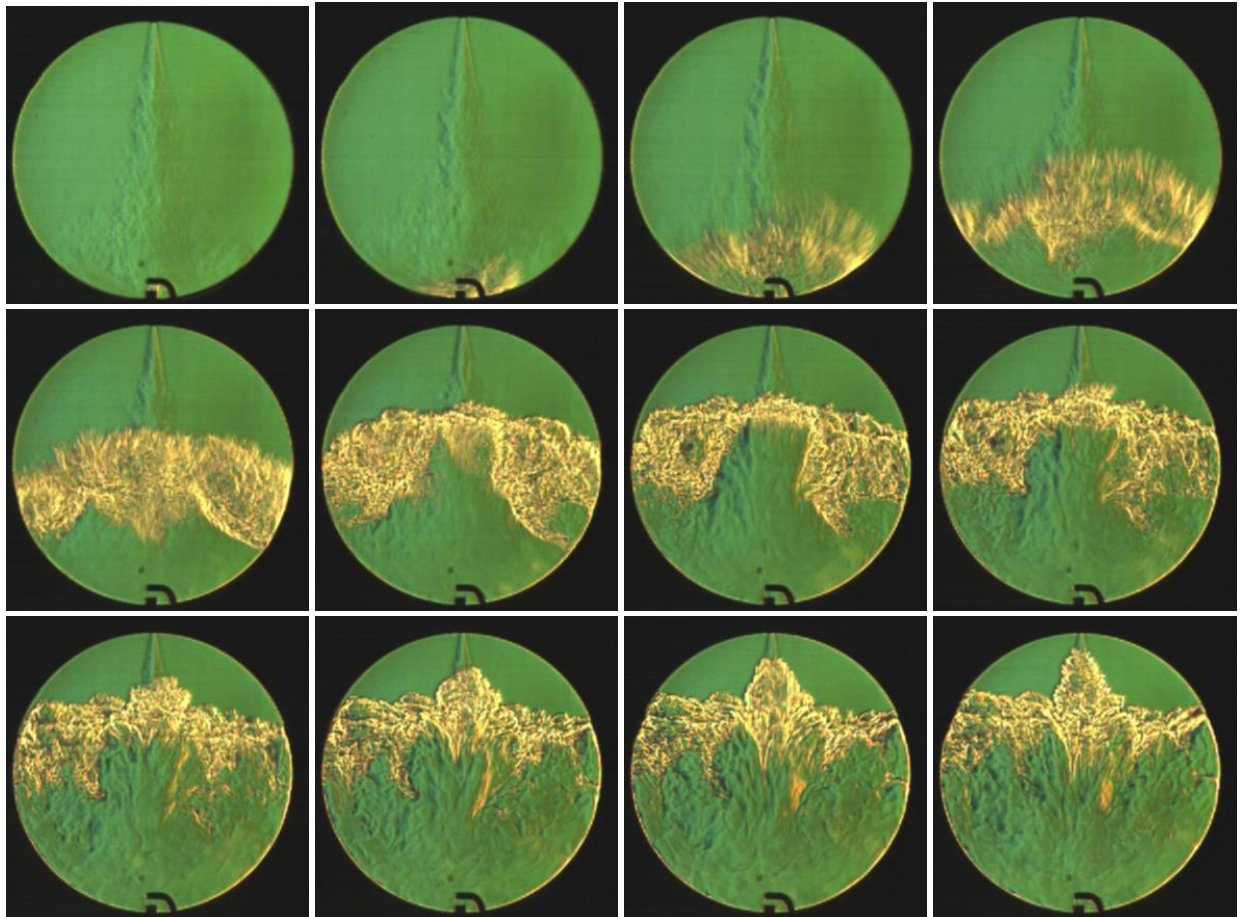


Figure 5. Schlieren Images (200 μ s intervals) for $t = 3$ ms.

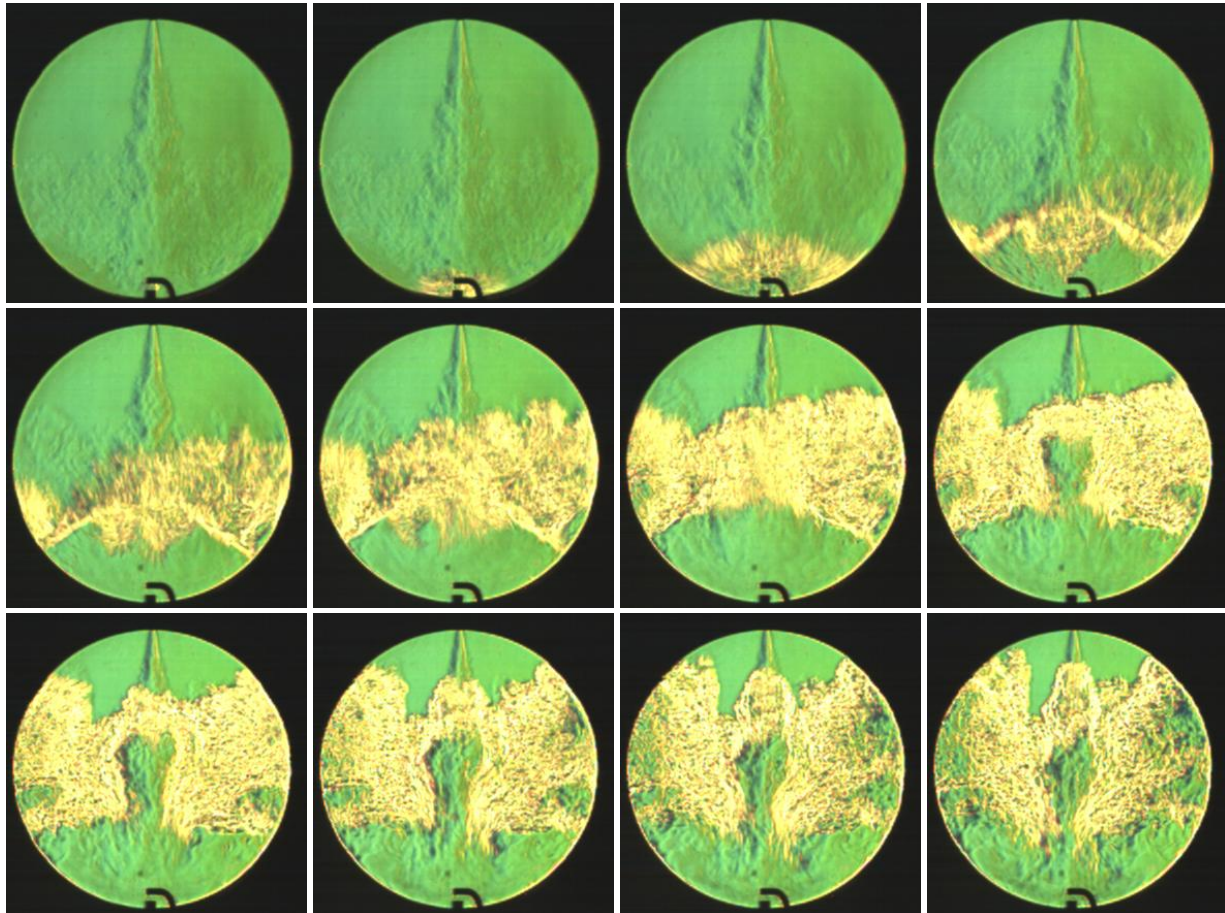


Figure 6. Schlieren Images (200 μ s intervals) for $t = 5$ ms.

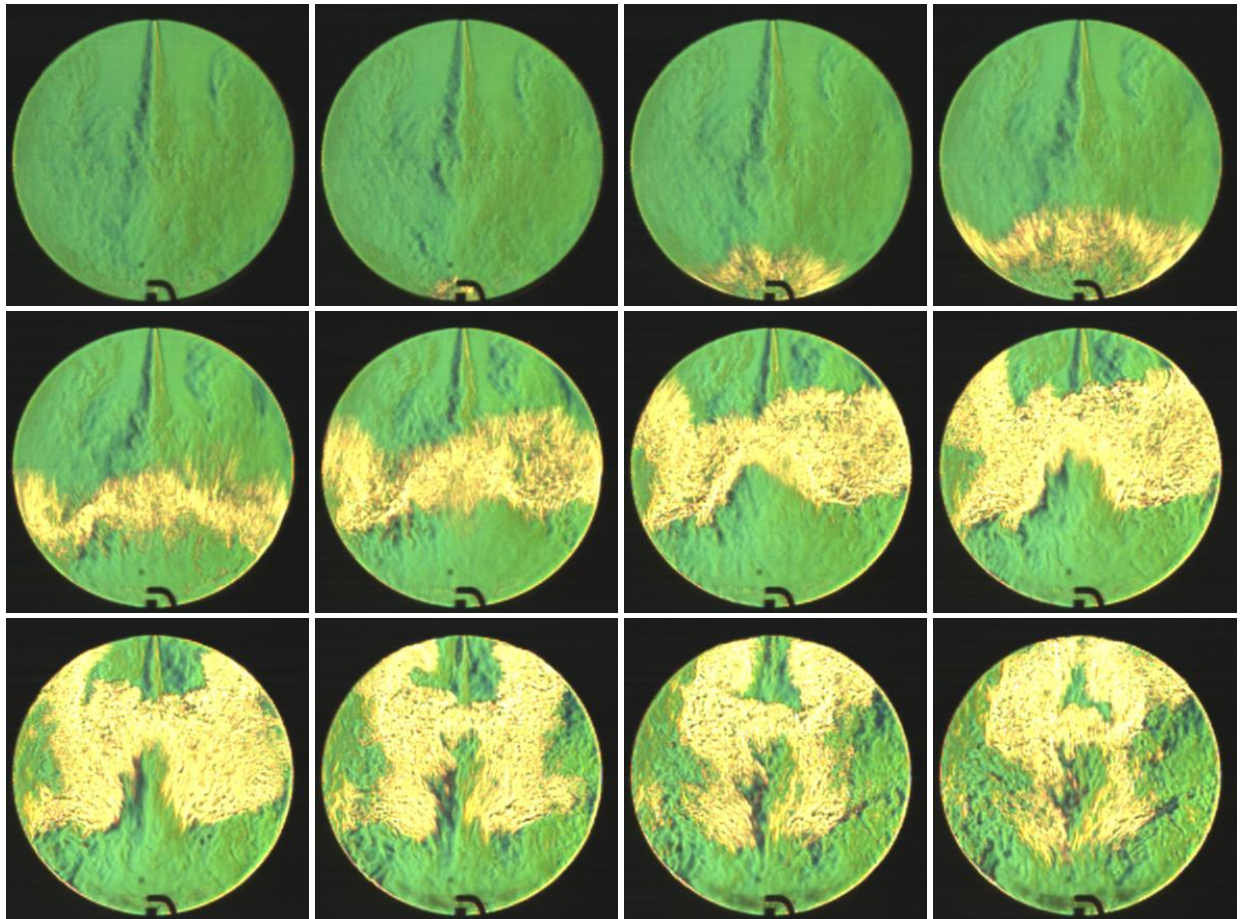


Figure 7. Schlieren Images (200 μ s intervals) for $t = 10$ ms.

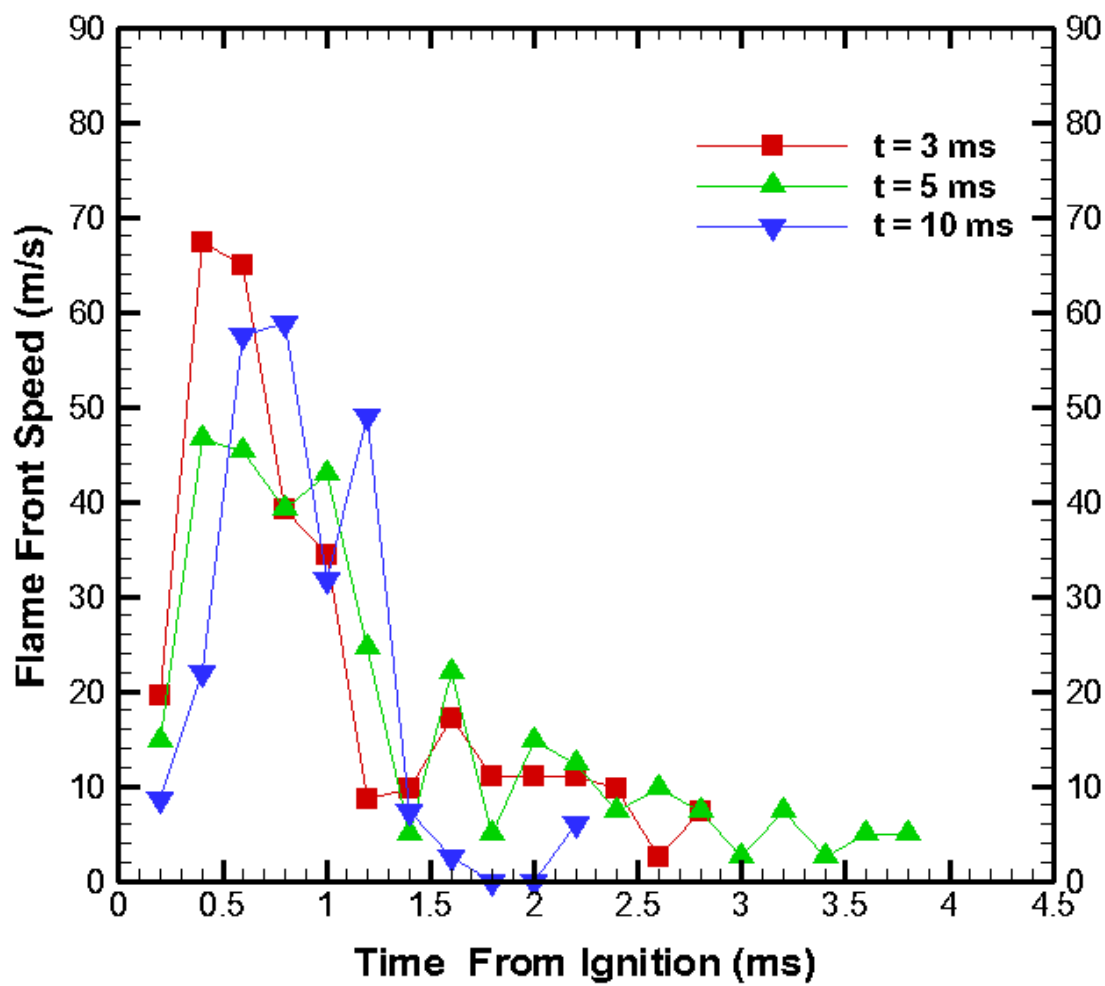


Figure 8. Flame front speed for $t = 3, 5,$ and 10 ms.

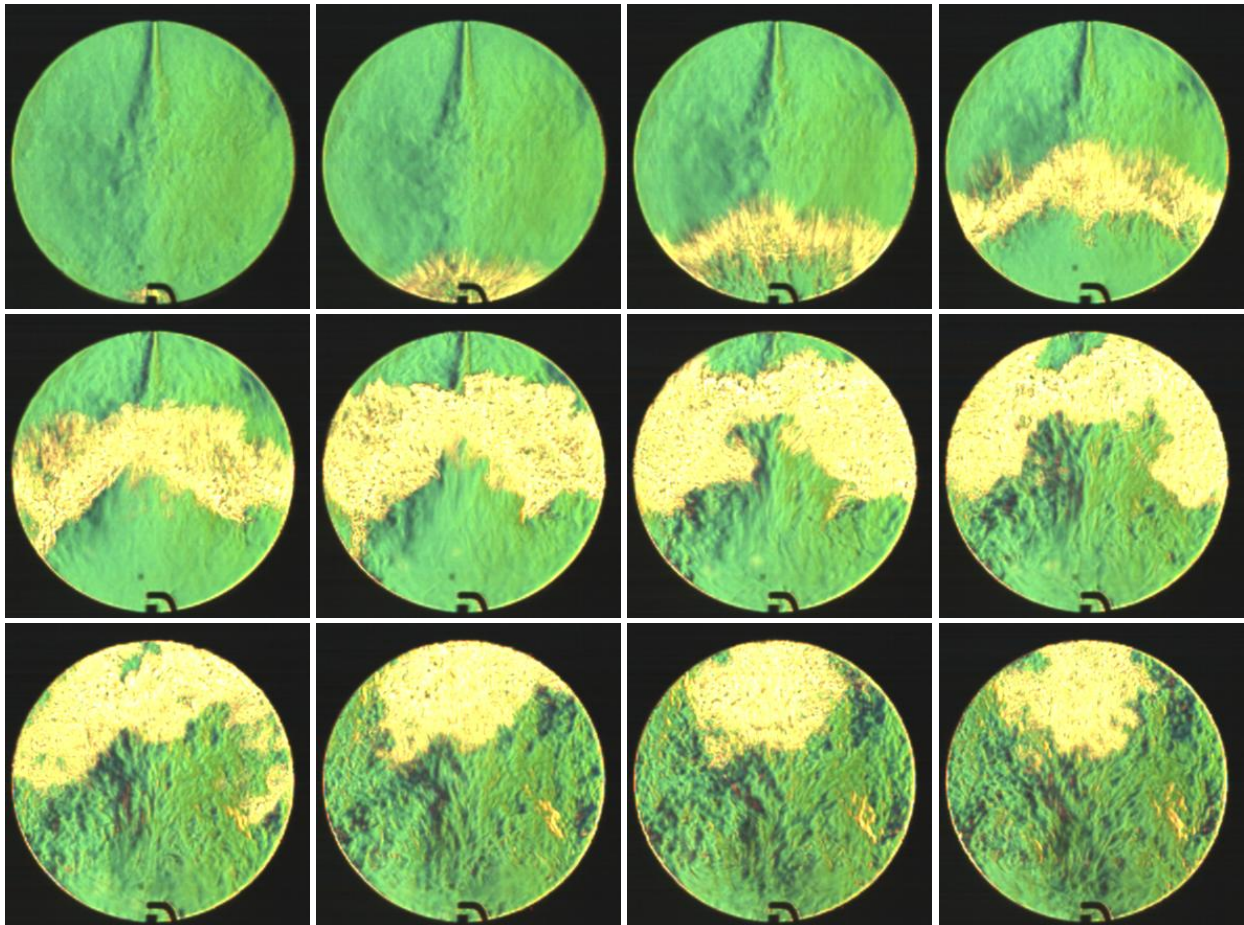


Figure 9. Schlieren Images (200 μ s intervals) for $t = 20$ ms.

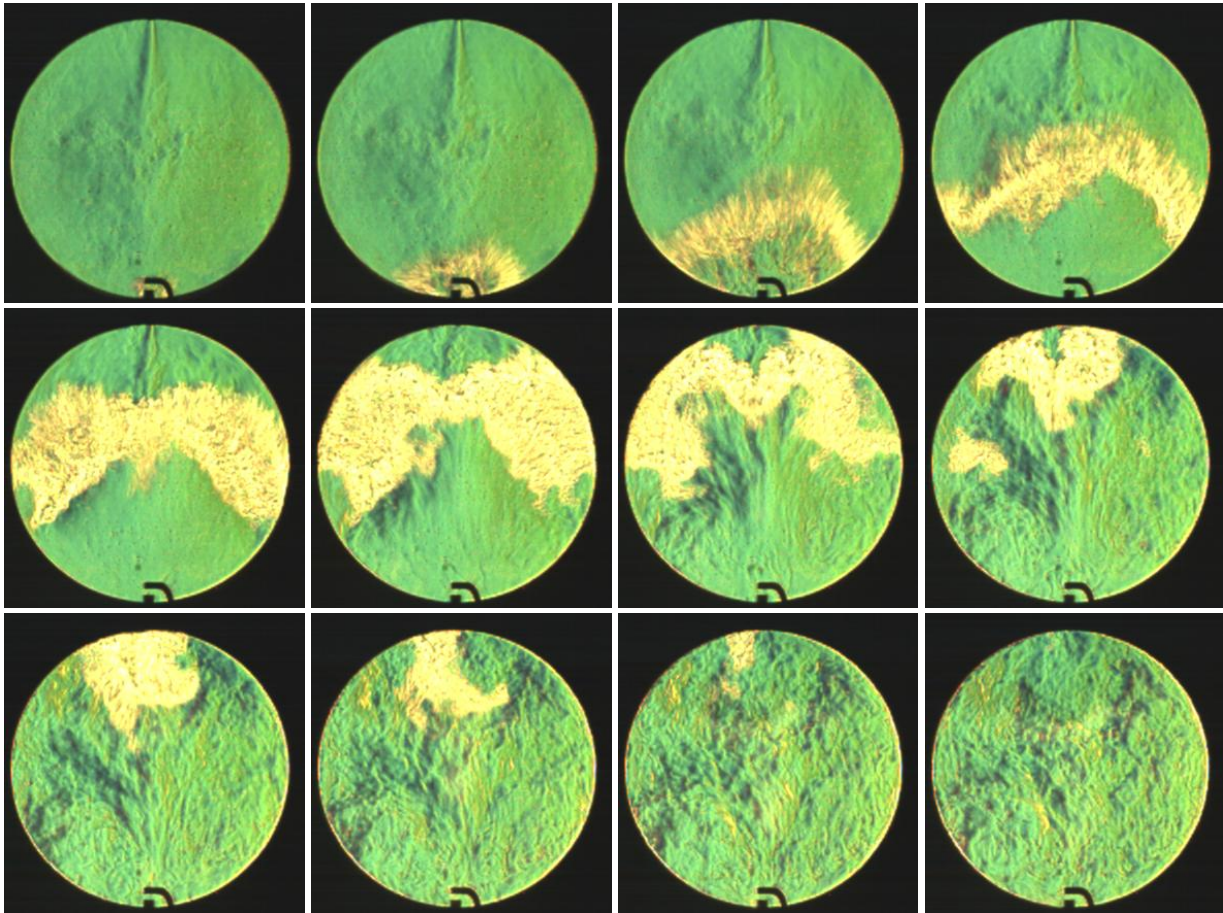


Figure 10. Schlieren Images (200 μ s intervals) for $t = 30$ ms.

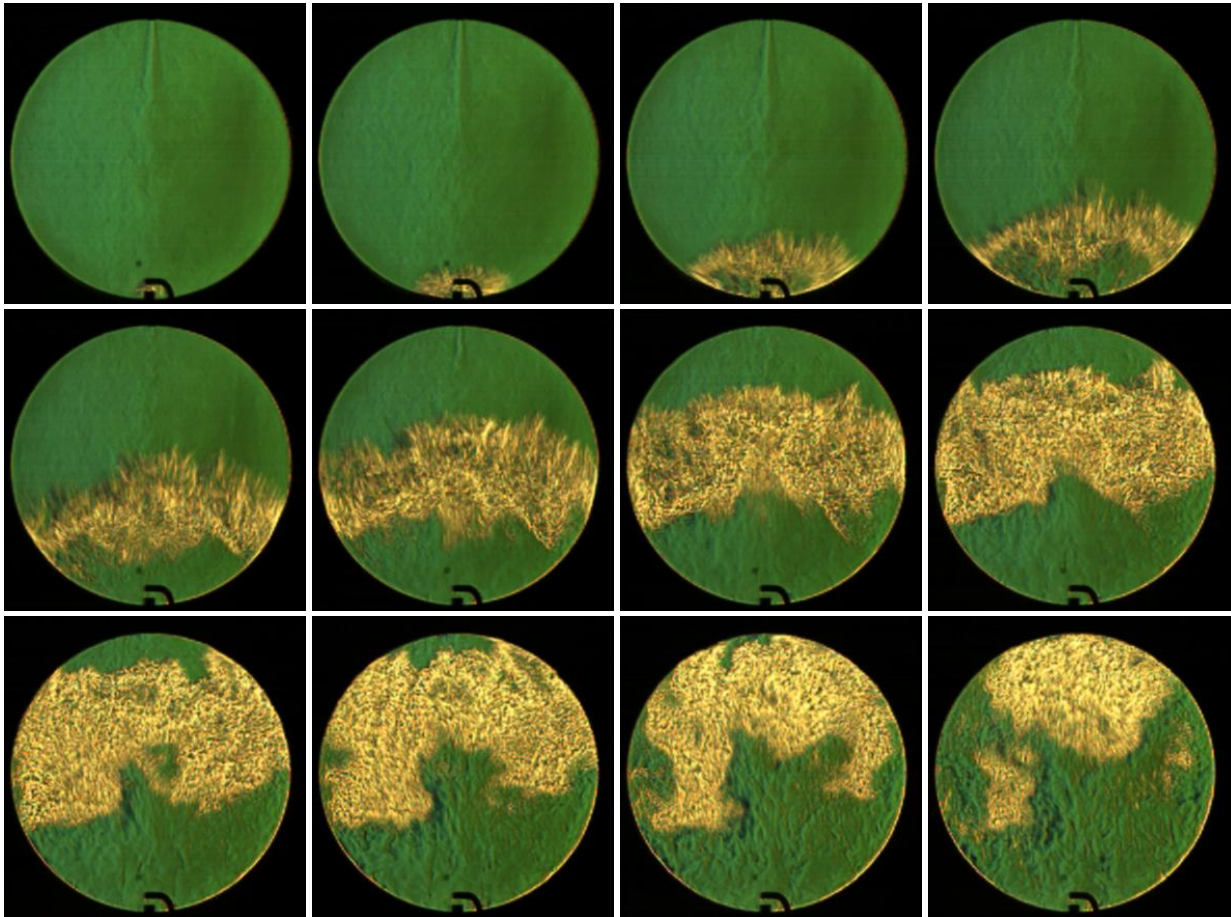


Figure 11. Schlieren Images (200 μ s intervals) for $t = 40$ ms.

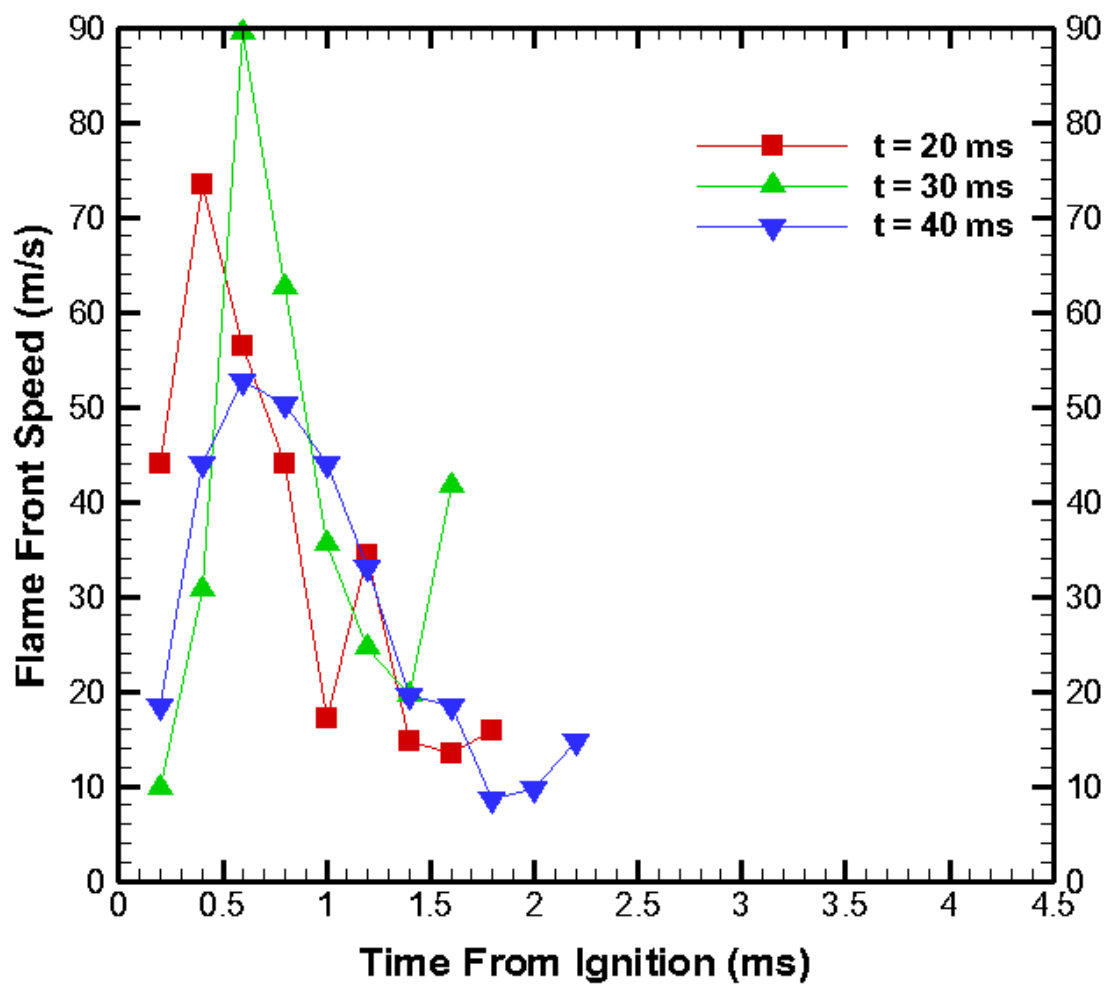


Figure 12. Flame front speed for t = 20, 30, and 40 ms.

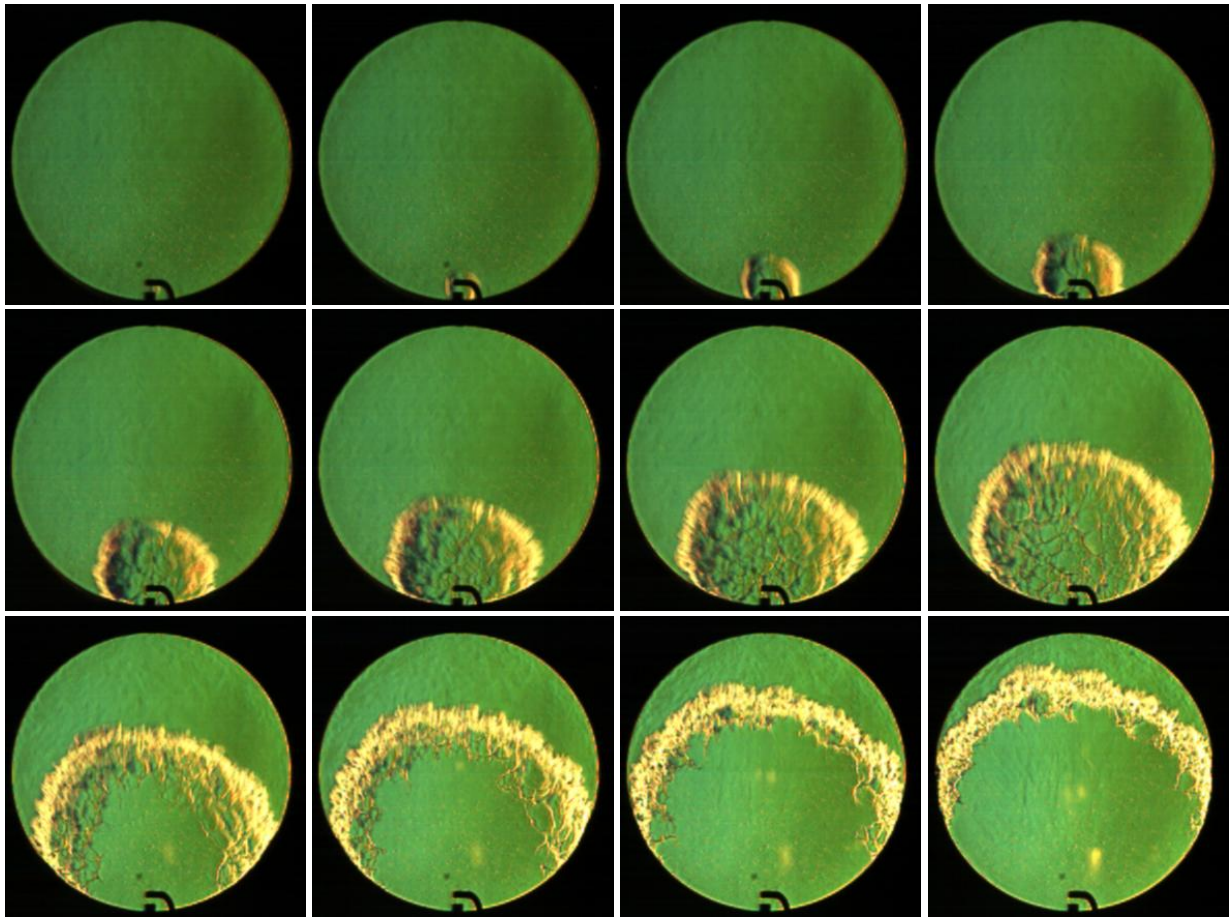


Figure 13. Schlieren Images (200 μ s intervals) for $t = 60$ ms.

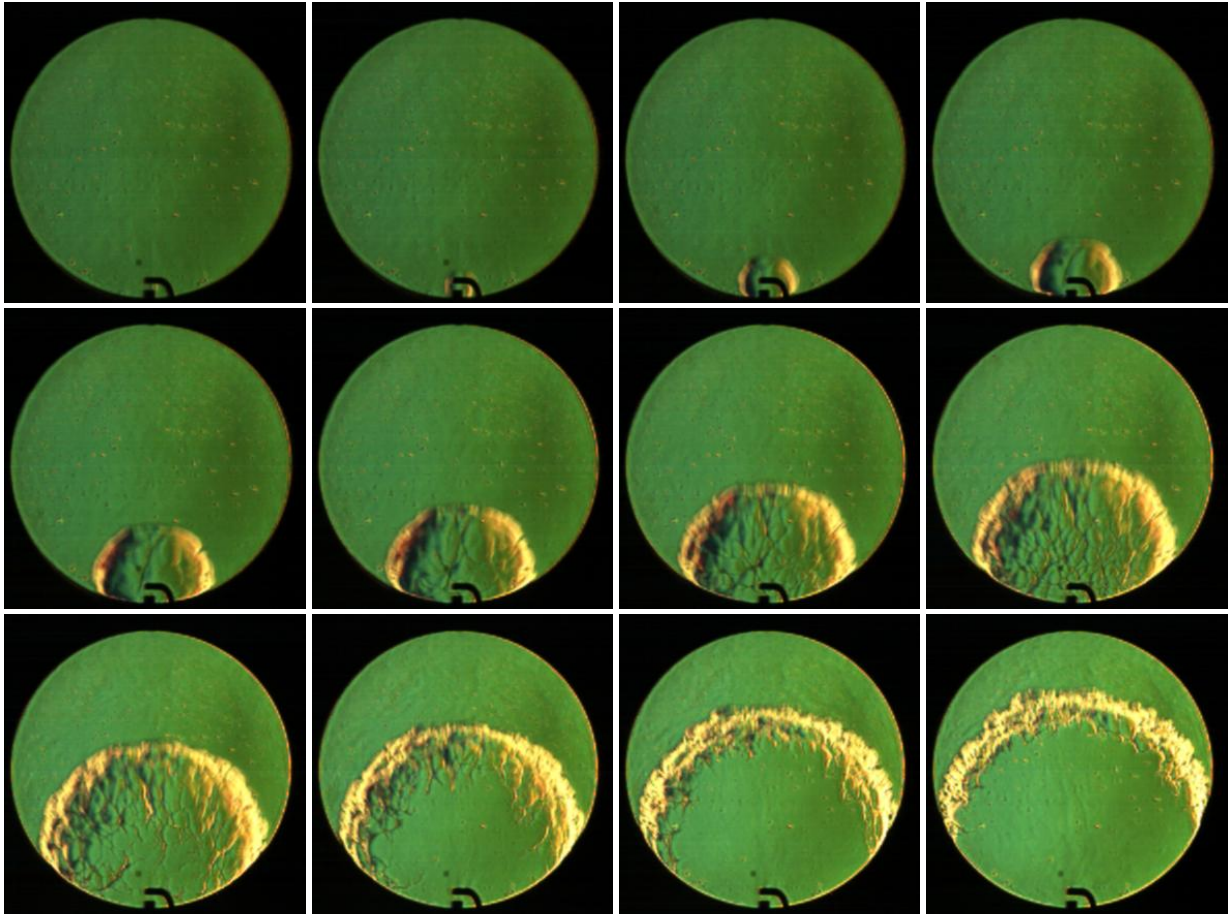


Figure 14. Schlieren Images (200 μ s intervals) for $t = 80$ ms.

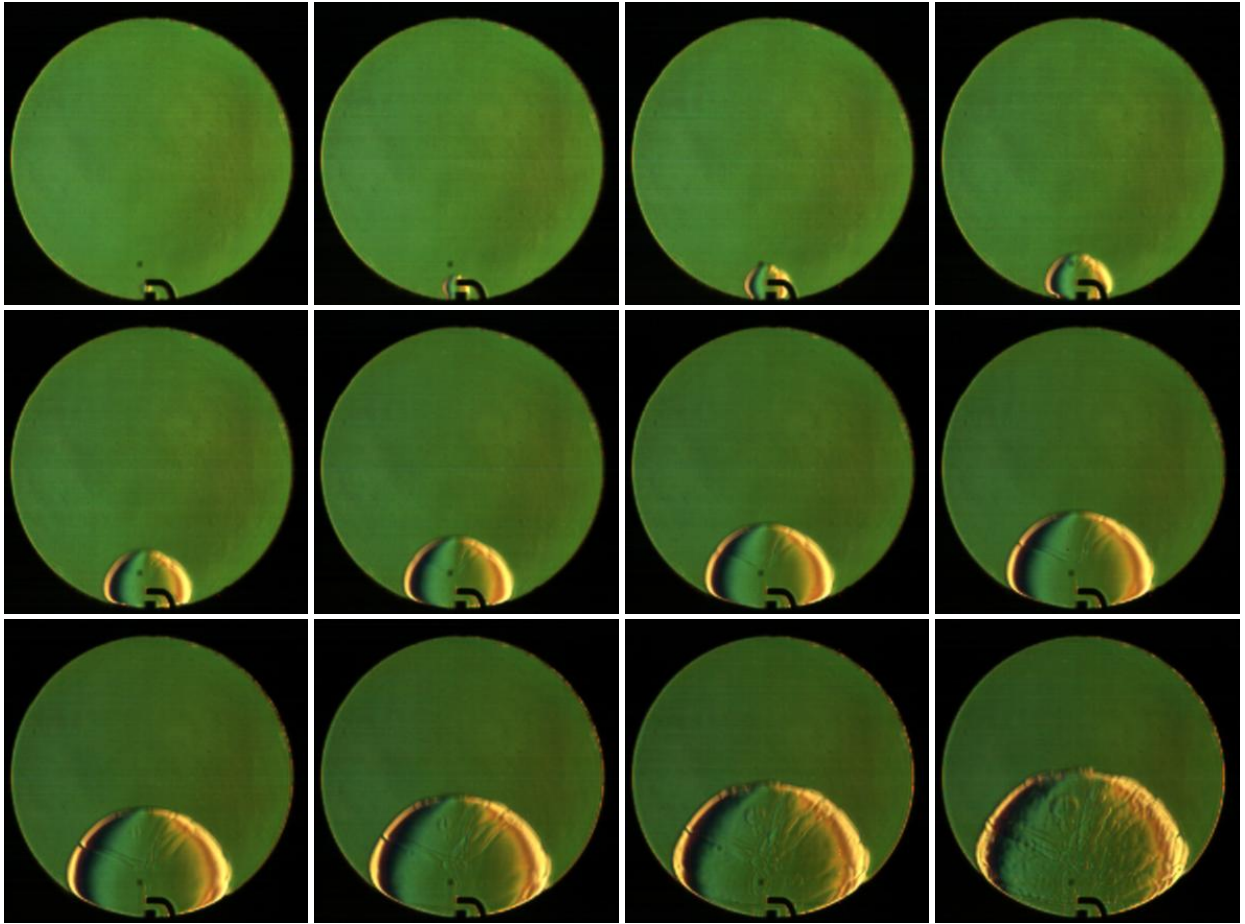


Figure 15. Schlieren Images (200 μ s intervals) for $t = 240$ ms.

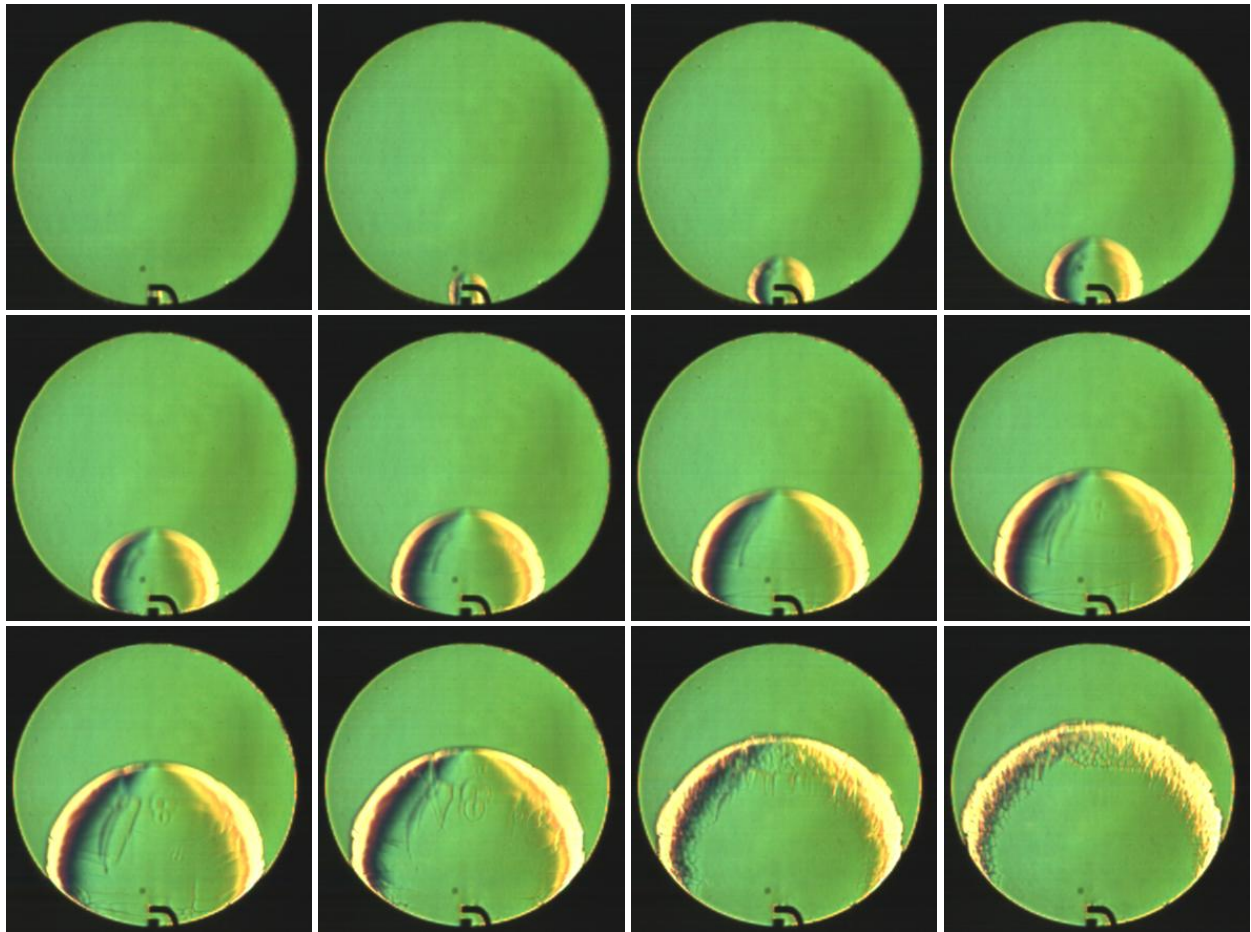


Figure 16. Schlieren Images (200 μ s intervals) for $t = 540$ ms.

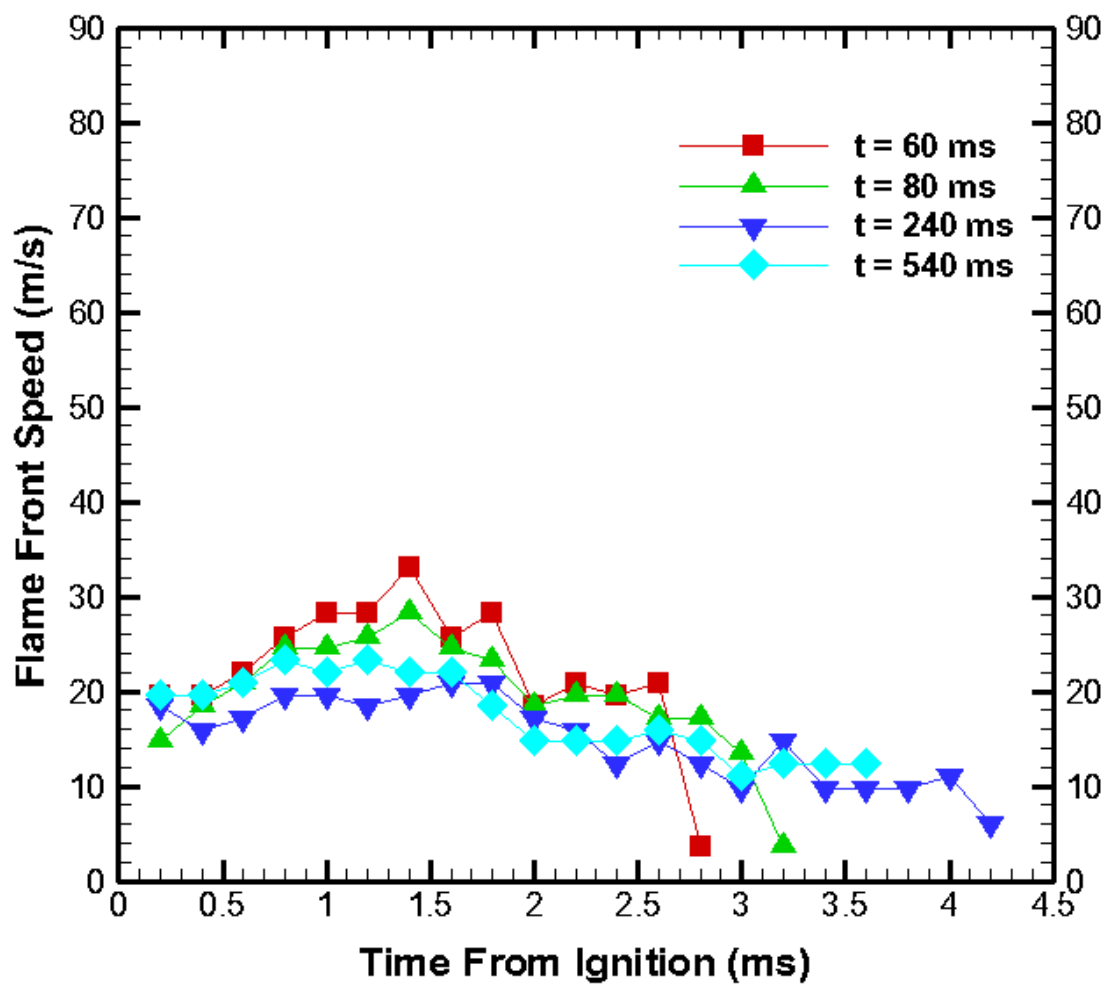


Figure 17. Flame front speed for $t = 60, 80, 240,$ and 540 ms.

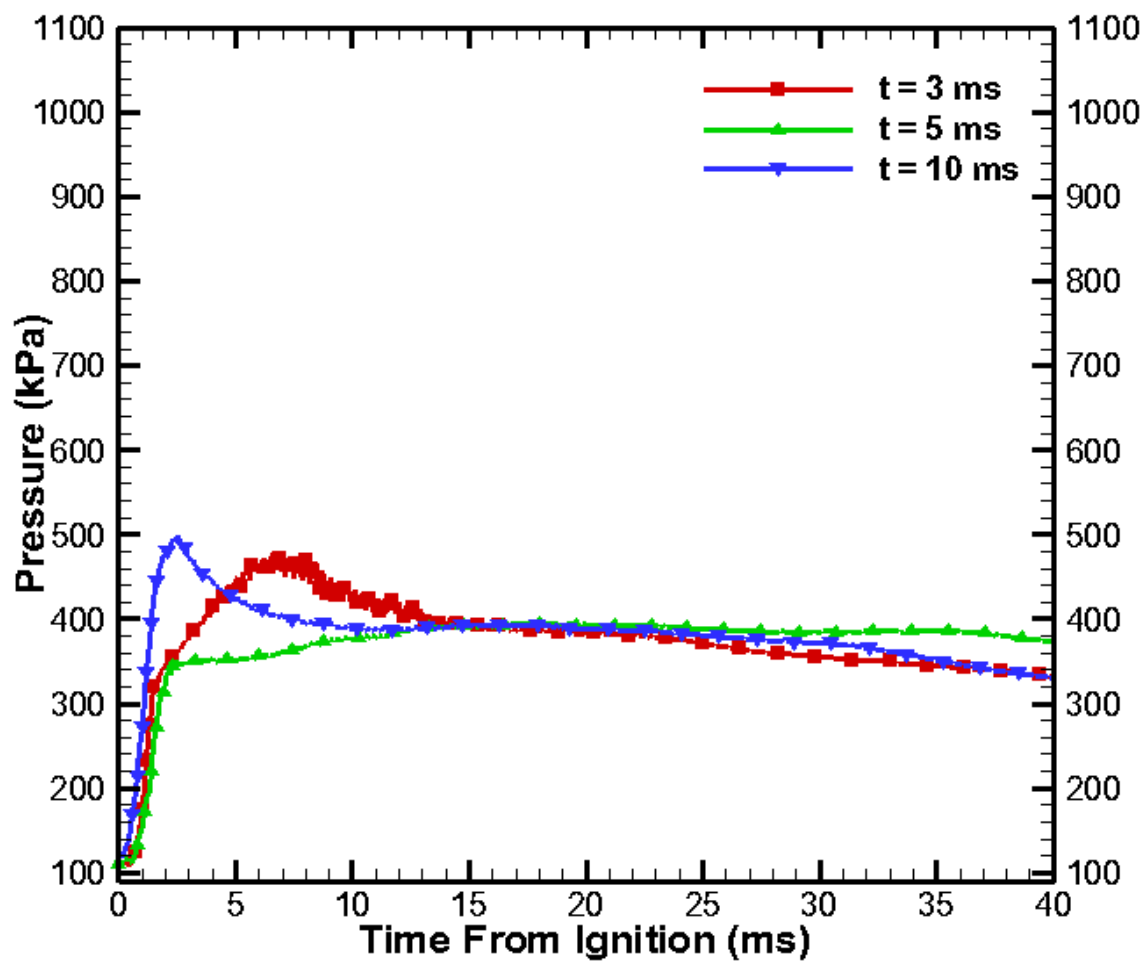


Figure 18. Chamber Pressure for t = 3, 5, and 10 ms.

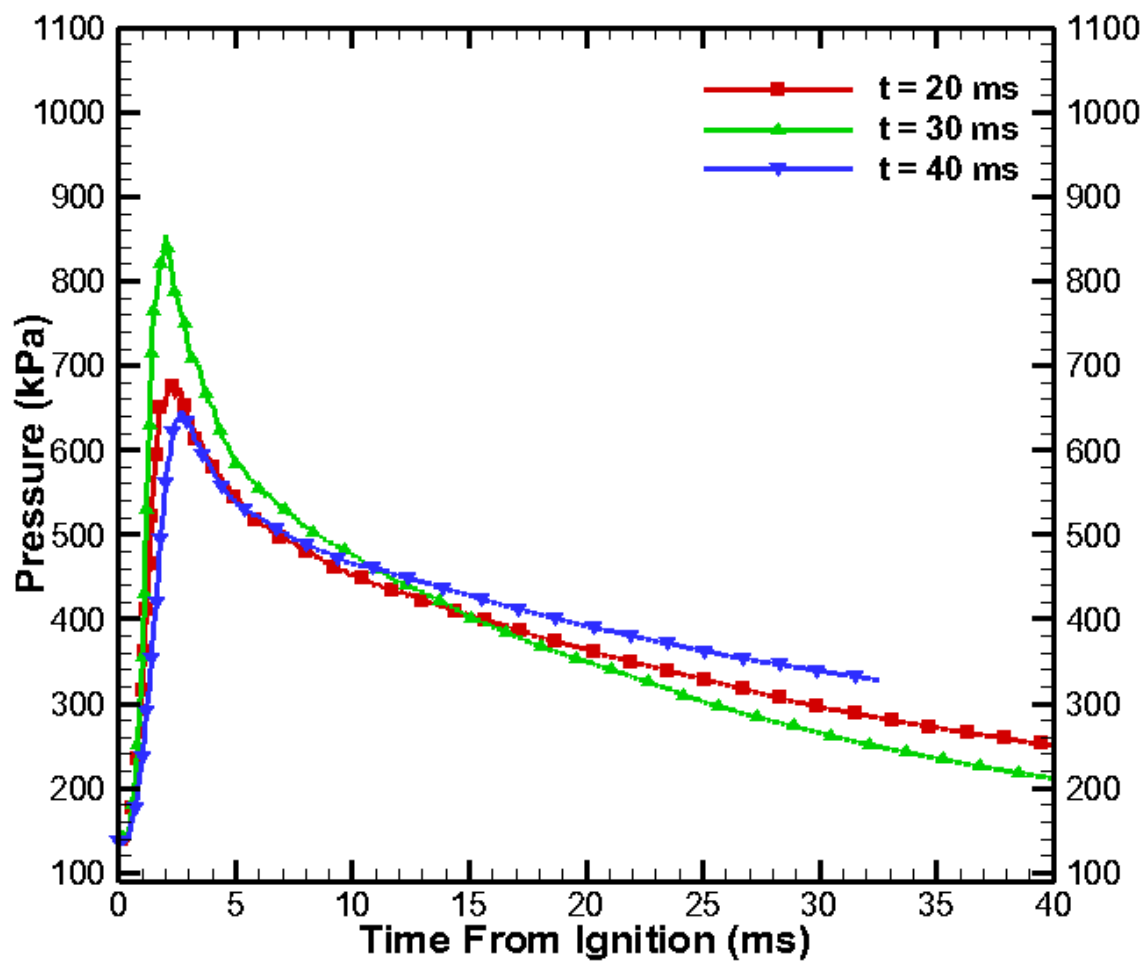


Figure 19. Chamber Pressure for t = 20, 30, and 40 ms.

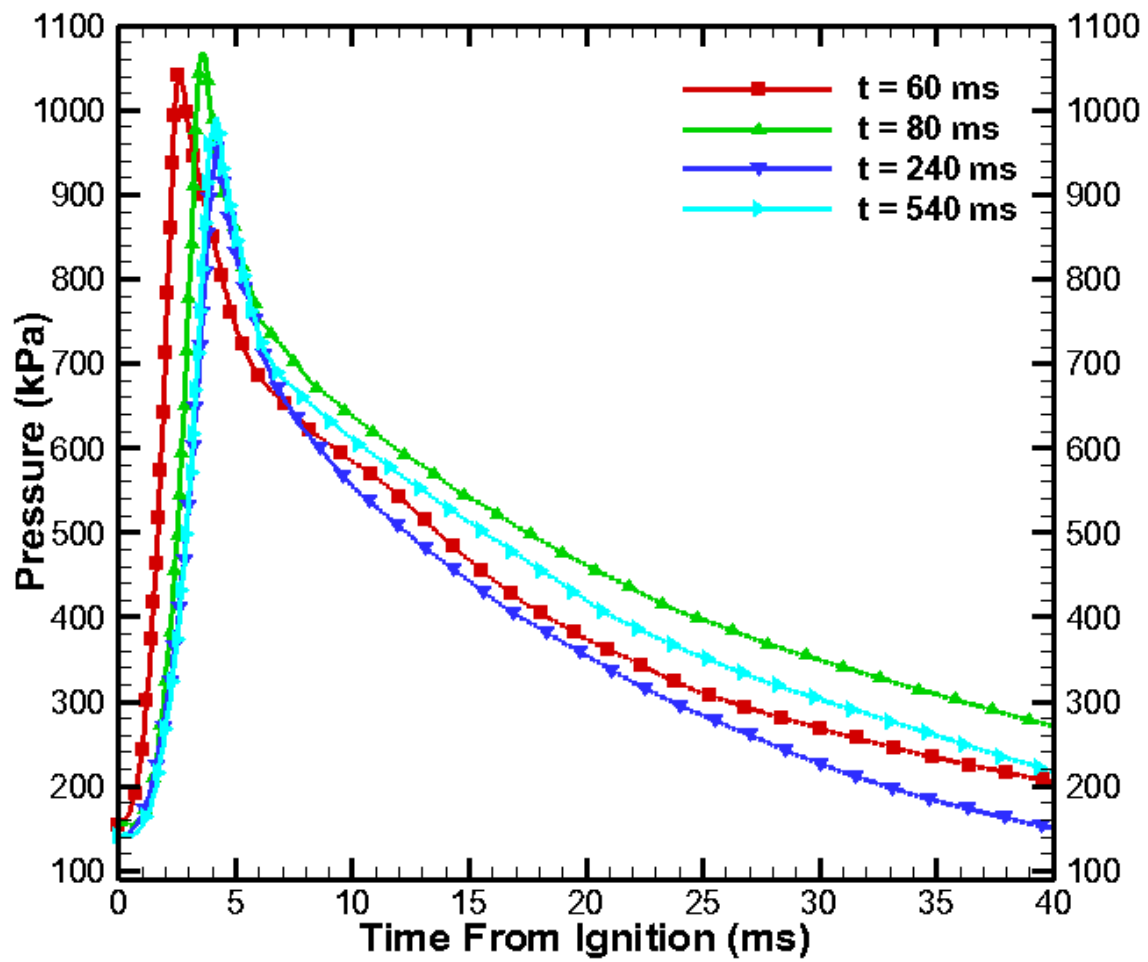


Figure 20. Chamber Pressure for $t = 60, 80, 240,$ and 540 ms.

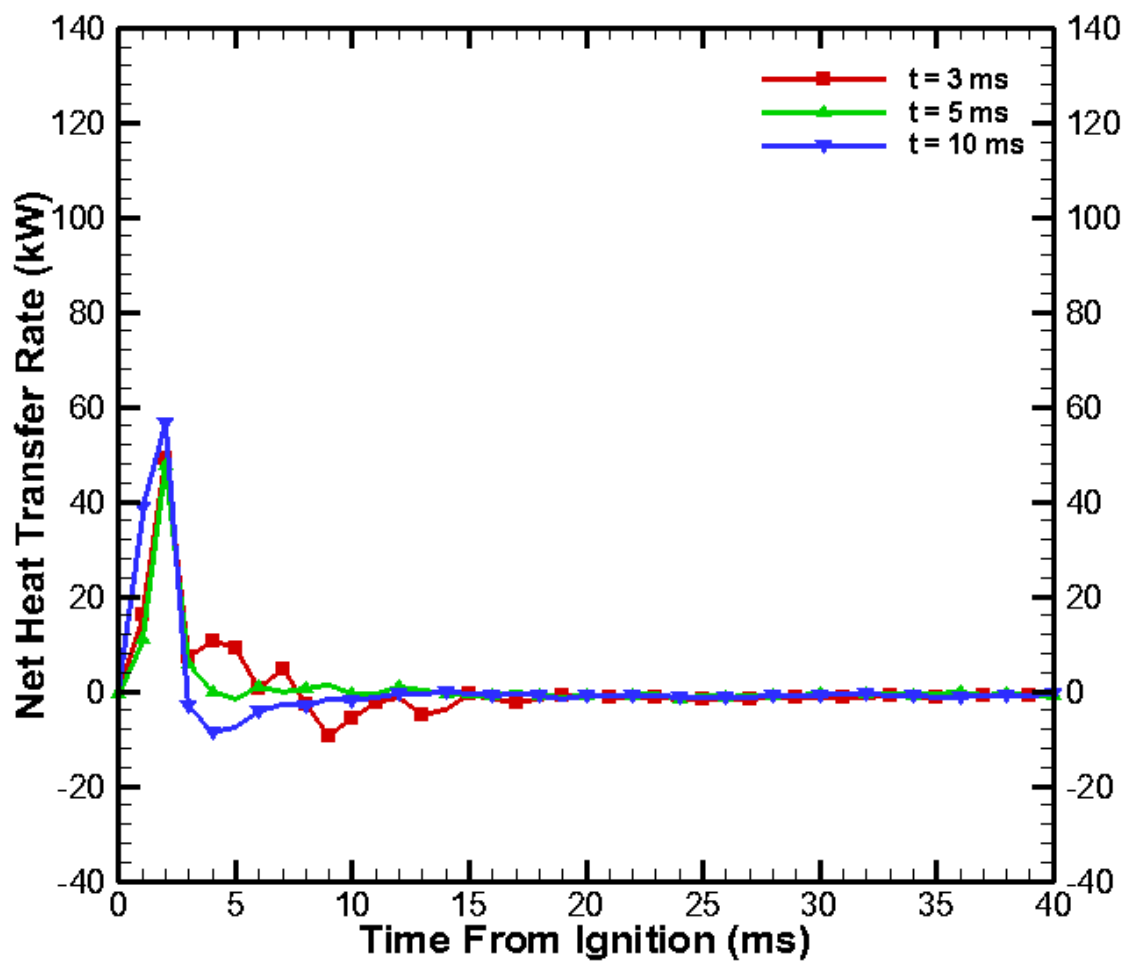


Figure 21. Net heat transfer rates for t = 3, 5, and 10 ms.

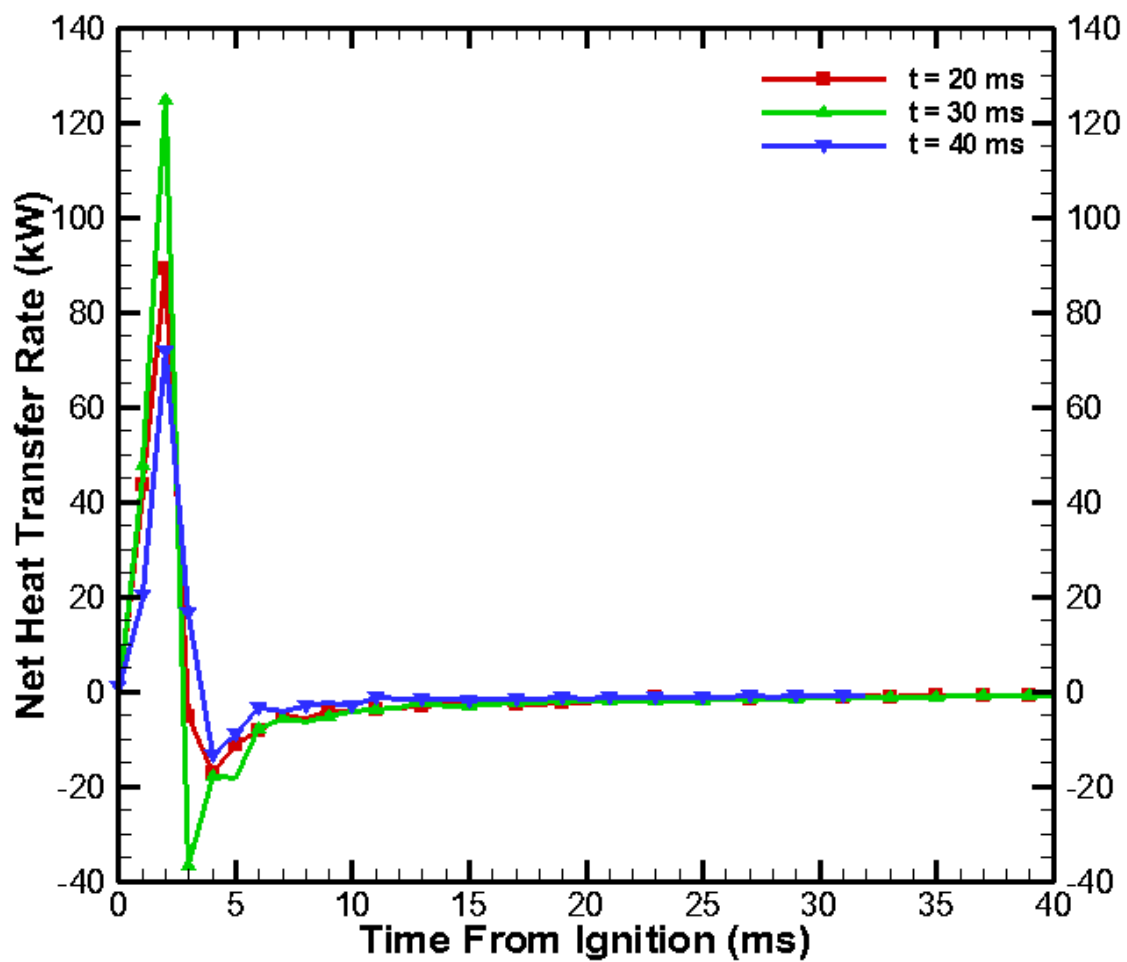


Figure 22. Net heat transfer rates for t = 20, 30, and 40 ms.

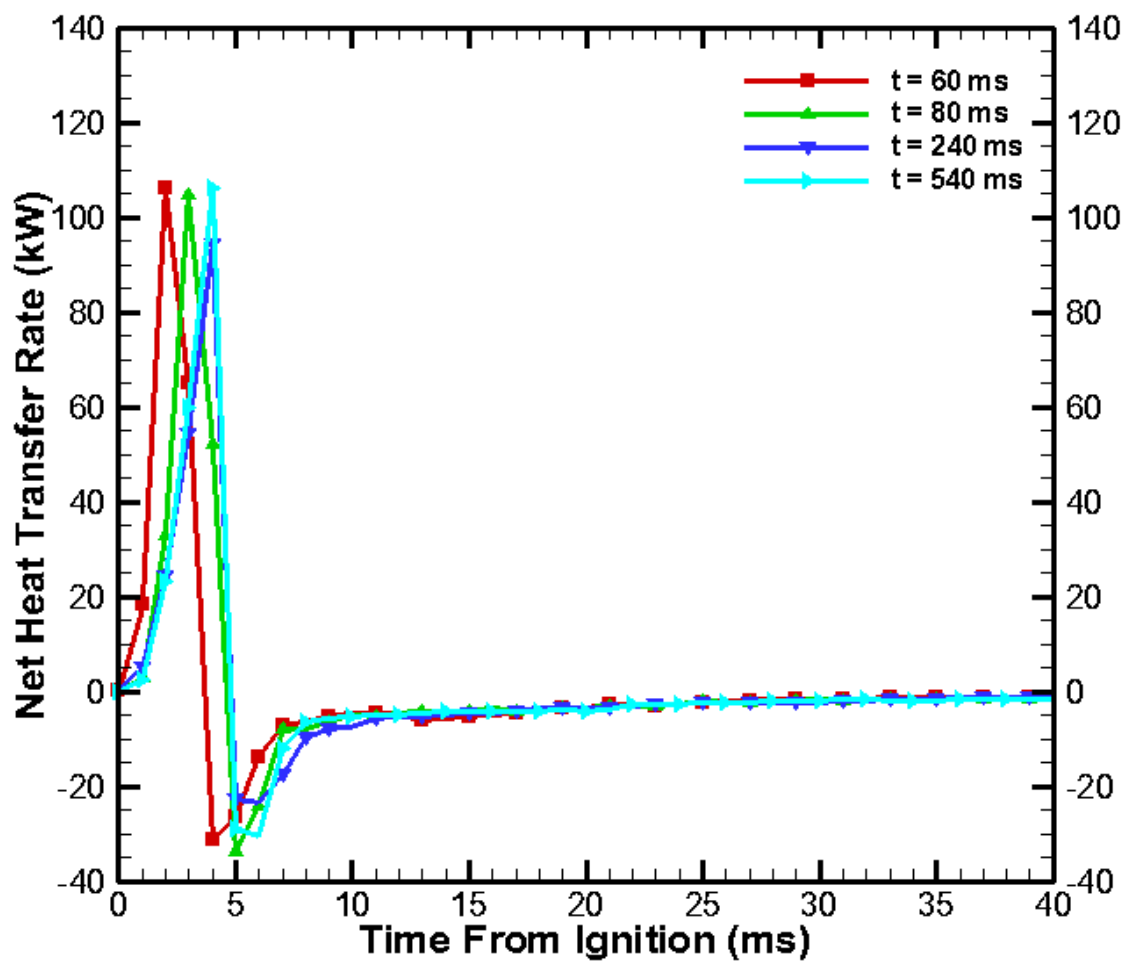


Figure 23. Net heat transfer rates for t = 60, 80, 240 and 540 ms.

CHAPTER 4

HYDROGEN COMBUSTION IN A STRATIFIED CONSTANT VOLUME COMBUSTION CHAMBER USING ULTRA HIGH SPEED IMAGING

Abstract

Hydrogen was directly-injected into a constant volume combustion chamber and turbulently mixed with atmospheric quiescent air. The hydrogen/air mixture was ignited by a spark plug located diametrically opposite the injector. Rainbow Schlieren Deflectometry (RSD) technique was used to acquire schlieren images at a frame rate of 50000 Hz and an exposure time of 19.8 μ s. A cross-correlation approach was used to analyze the schlieren images and to quantify flame front propagation speed. Measurements were acquired to obtain variations in chamber pressure during combustion and to compute the net heat transfer rates. Ignition times and equivalence ratios were varied to study the effects on combustion processes. Three equivalence ratios, $\phi = 0.6, 0.8$ and 1.0 were studied for four ignition times, before, at, and after the end of fuel injection. Results show ignition time has a significant effect on flame structure, flame front speed, chamber pressure, and net heat transfer rate. Equivalence ratio has minor effects on flame structure and flame front speeds for a given ignition time. Equivalence ratio has significant effects on chamber pressure and net heat transfer rate for varying ignition times.

Introduction

Hydrogen as an alternative fuel for use in Internal Combustion Engines (ICEs) has been studied for decades to aid in decreasing the nation's dependency on petroleum fuels. Hydrogen has shown to be a promising fuel due to its desirable combustion properties. Hydrogen's mass diffusion coefficient ($0.61\text{cm}^2/\text{s}$) is about four times that of gasoline ($0.16\text{cm}^2/\text{s}$) which helps improve fuel/air mixing leading to homogeneity in mixtures [Ji et al., 2009]. Hydrogen's adiabatic flame speed at stoichiometric conditions (237 cm/s) is about five times that of gasoline (42 cm/s) which contributes to engine operation stability and higher thermal efficiency. Hydrogen's flammability range in air is 4.1-75% by volume and is therefore wider than gasoline's at 1.5-7.6% by volume. Hydrogen can be used as the sole fuel source in an ICE or as a supplement to engines fueled with other fuels. In a study of hydrogen addition to spark ignition gasoline engines, Ji et al. [2009] concluded that an engine operating under lean conditions experiences an improvement in brake mean effective pressure (BMEP) with the addition of hydrogen. Brake thermal efficiency and excess air ratio for maximum brake thermal efficiency increase with the addition of hydrogen. Maximum cylinder temperatures and pressures also increase with hydrogen addition. Cycle variations are eased especially under lean conditions. Hydrocarbons (HC) and carbon dioxide (CO_2) emissions for lean combustion are reduced with the addition of hydrogen. For hydrogen to be a practical fuel, its combustion characteristics must be identified for optimal operation. Operating conditions include but are not limited to the method of fuel injection, timing of ignition, and fuel-air mixture ratio. Optimization of these parameters can increase engine efficiency and reduce harmful pollutants.

This study pertains to a Direct Injected Spark-Ignition (DISI) concept, which addresses problems with hydrogen use such as abnormal combustion by knock, backfire, and pre-ignition.

According to Green and Glasson, the most satisfactory way to overcome light-back, pre-ignition, and autoignition in a spark-ignition engine using hydrogen is to deliver the fuel late in the compression stroke using a high-pressure direct injection system [Green & Glasson, 1992; Glasson & Green, 1994]. In a DISI system, a high pressure injector delivers the fuel into the cylinder during the compression stroke, and the resulting transient jet is ignited by a spark plug. The flame propagation is affected by the turbulence and stratification created by the fuel jet. Direct injection of fuel into the cylinder prevents formation of a fully premixed charge in the cylinder.

The equivalence ratio of hydrogen-air mixtures has significant effects on combustion processes. The equivalence ratio affects flame propagation through the chamber, combustion temperatures which determine the production of harmful pollutants, and in-cylinder pressures. Knowing the effects of varying equivalence ratios, as stated by Owston et al. [2007] in studying interactions of hydrogen flames with wall, has applications to determining optimum values required for efficiency and to reduce emissions. Previous studies have also shown that equivalence ratio affects engine efficiency. Rakopoulos et al. [2011], reports in a study of thermal processes of hydrogen-fueled spark ignition (SI) engines that as mixtures become leaner, the indicated efficiency is increased significantly. They contribute this increase in efficiency to lower heat loss and specific gas properties. They found rapid NO production for richer mixtures immediately after ignition which follows the rapid increase in the temperature of burned gases. However, for leaner mixtures NO production decreases due to lower burned gas temperatures. Experiment revealed termination in NO production when average burned gas temperatures fell below a certain value. As the equivalence ratio increased, the combustion efficiency also increased [Rakopoulos et al., 2011]. In agreement, Vudumu et al. [2011], in a study predicting

emission characteristics of hydrogen IC engines found that NO_x formation was negligible below an equivalence ratio of 0.5. The brake power and NO_x production increase until a peak value is reached around an equivalence ratio of 0.84.

Extensive research has been conducted to relate ignition timing and injection timing effects on in-cylinder chamber pressure and flame speed, which determine cylinder wall heat loss and power loss. Optimization in ignition timing is necessary to achieve stable combustion and desirable combustion properties. Ignition and injection timings have a great effect on engines fueled with hydrogen and ignition timing should be matched with injection timing [Zhenzhong et al., 2002]. Research conducted on a methanol fuelled engine showed that ignition timing and injection timing affect engine parameters such as cycle to cycle variations, in-cylinder pressure, heat release rate, and thermal efficiency. Optimization in injection and ignition timing can improve brake-specific fuel consumption (BSFC) by more than 10% as compared to other timings at an engine speed of 1600 rpm [Li et al., 2010]. In a study of a DISI engine fueled with blends of hydrogen and natural gas, Huang et al. [2007] reported that turbulence generated by fuel jet in the combustion chamber preserves high and strong mixture stratification when ignition is closer to the end of fuel injection, which leads to high and fast burn rate, high BMEP, short combustion time, and high thermal efficiency. NO_x concentrations increase, HC concentrations decrease, and CO concentrations vary only a little with advanced ignition timing [Huang et al., 2007]. Yousufuddin et al. [2009] concluded that ignition timing is a key operating parameter that affects SI engines efficiency and performance at any load. Mohammadi et al. [2007] reports that at conditions lending to high engine output, late hydrogen injection reduces NO_x emissions since engine operates at lean conditions. Mohammadi et al. also show that injecting hydrogen during the compression stroke prevents knock.

This study is a combined parametric study of the effects of ignition time with varying equivalence ratio for hydrogen/air combustion in a constant-volume combustion chamber. Fuel is delivered by a high pressure fuel injector to simulate the direct-injection concept as discussed earlier. Ignition time and equivalence ratio were varied to observe hydrogen combustion to determine the flame characteristics.

Experimental Setup

The experimental setup consists of a CVCC system and a high-speed RSD system as described below.

Constant Volume Combustion Chamber System. The test apparatus consisted of a CVCC with a high pressure fuel injector attached to a fuel supply system. The combustion chamber, shown photographically in Figure 1, is made of aluminum with a cylindrical hole drilled through it. The cylinder has a diameter of 66.7 mm and a width of 31.8 mm, which forms the volume of the combustion chamber. The combustion space is walled by optical windows located in depressed areas on both ends. Each optical window is a fused silica, single surface 1/10th wave optical flat (NT01-915) with a diameter of 76.2 +/- 1 mm and thickness of 19.05 +/- 1.5 mm. The optical flats are precision polished on one side to ensure accuracy and are pitch polished on the other side. The optical flats are held in place by aluminum collars (Figure 1) tightened to the outer surface of the combustion chamber by eight bolts.

Hydrogen was supplied by a compressed gas cylinder as shown in fuel flow system diagram (in Figure 2). The hydrogen flowed through a test vessel system and a supply pressure regulator before approaching the fuel injector fixed at the top center of the CVCC (see Figure 1). The fuel injector is a Hoerbiger hydrogen direct injector with a maximum intake pressure of 250 bar and an equivalent flow area of 1.0 mm². The fuel injector is connected to a Provebo

Electronic Valve Booster that is powered by a MG Pro Series PS22 13.8V DC single channel regulated power supply. The spark is created by a Champion RV12YC6 spark plug located diametrically opposite the hydrogen injector and sits in a Honda stick coil. A Keyence KV-24DTP Programmable Logic Controller (PLC) controls coil charging, spark triggering, and injector duration. A TekPower HY3003D-3 digital display 3 channel output DC power supply provides 13 V to the Honda stick coil, 24 V for PLC operation, and 5 V to the common port of the PLC. A 5V signal is sent to the PLC from the Digital I/O ports of a National Instrument's PCI Data Acquisition System (DAQ) with a BNC breakout box to initiate program execution. The fuel injector, coil charging, and spark triggering are sequenced by a program written using Ladder Logic Software that is downloaded to the PLC. Time constants are changed in the program to conduct ignition variation testing. The DAQ is also connected to a high speed camera, discussed in the following section. A program written in National Instrument's LabView software controls the sequencing of the PLC and the high speed camera.

A Kistler Type 6053CC60 piezoelectric pressure sensor calibrated at 0...150 bar with a sensitivity of 20.2 pC/bar is mounted along the lateral surface of the CVCC. It is used to collect pressure data during fuel injection into the chamber and during the combustion process. The charge from the pressure sensor is amplified by a Kistler Type 5010 Dual Mode Charge Amplifier which is connected to the DAQ where pressure data is collected.

Rainbow Schlieren Deflectometry System

Rainbow Schlieren Deflectometry, an optical technique to visualize density gradients in the flow field was utilized to acquire the necessary data. An inhomogeneous media, for example, hydrogen injected into air, has density gradients that lead to schlieren effects arising from refraction of light rays traveling through the medium. Schlieren effects can result from

temperature gradients, mixing of gases of different densities, or high velocity flows. The RSD is an experimental technique to project light ray deflections or displacements in color to a viewing screen. The color schlieren images thus acquired can be quantitatively analyzed to obtain the local distributions of the density field.

Figure 3 illustrates the RSD setup implemented in this study. A beam of light was transmitted from a MCWHL2 LED assembly with a 6500K wavelength and an optical beam power range of 650 – 1300mW. The MCWHL2 is powered by a T-Cube (LEDD1B) LED Driver with a maximum output current of 1200 mA that has a single channel controller to vary LED intensity. The MCWHL2 is structurally housed by an aluminum prism located at the focal point of the collimating lens. The lens is a precision achromatic doublet lens that is 76.2 mm in diameter with a 500 mm focal length. It is coated with a 400-700 nm antireflection coating. The collimated beams or parallel light rays traveled through the test media contained in the CVCC as discussed previously. During experiments, the test media was composed of a non-homogeneous hydrogen-air mixture. After passing through the test media, refracted light rays passed through a de-collimating lens, which refocused light beams onto a rainbow filter. The de-collimating lens has the same properties as the collimating lens, except its focal length is 750 mm. The rainbow filter is fixed at the focal point of the de-collimating lens. Light rays transmitted through the rainbow filter form an inverted image of the test medium that is captured by a Photron Fastcam SA5 ultra high speed camera. The camera is set to acquire color schlieren images at 50,000 frames per second with an exposure time of 19.8 μ s.

Results and Discussions

Hydrogen at 413.7 kPa was injected into quiescent, atmospheric air in a CVCC for varying durations to obtain overall equivalence ratios, $\phi = 0.6, 0.8,$ and 1.0 . The hydrogen jet

mixes turbulently with the air in the chamber. The hydrogen jet reaches the igniter, located diametrically opposite the injector at time, $t = 2.25$ ms. The hydrogen/air mixture was ignited at $t = 3$ ms, $t = 10$ ms, $t = t_{\text{end}}$ representing time at the close of the injector, and $t = t_{\text{end}} + 50$ ms. For ignition times $t = 3$ ms and 10 ms, only a fraction of the fuel entered the chamber at ignition and the remainder of the supplied fuel enters with combustion occurring in the chamber. For $t = t_{\text{end}}$ and $t = t_{\text{end}} + 50$ ms all of the supplied fuel has entered the chamber at the time of ignition. For late ignition, additional time for fuel-air mixing is available before combustion. After ignition, the flame propagated towards the top of the chamber where the injector is located.

Flame Front Propagation

Color schlieren images were acquired to analyze flame propagation and calculate flame front speed. For early ignition times, $t = 3$ ms and 10 ms, at the start of combustion, the flame for all varying equivalence ratios propagates towards the injector spreading horizontally, vertically and laterally as shown in Figures 4-9. For $t = 3$ ms, the centerline region of the flame propagates into the perimeter of hydrogen jet forming its conical shape as seen in schlieren images. The flame in the region outside the fuel jet propagates upward at a much lower rate compared to the flame in the perimeter of the fuel jet. Schlieren images show the flame in the fuel jet region reaching the top of the combustion chamber first signifying greater flame front speed. Schlieren images (Figures 4-6) show that for $t = 3$ ms, hydrogen has reached only limited regions outside the fuel jet prior to ignition. For $t = 10$ ms, more fuel has entered the chamber and fuel has dispersed, creating combustable fuel-air mixtures throughout the chamber. In this case, the flame does not propagate into the perimeter of the fuel jet to take on its shape. For both, $t = 3$ ms and 10 ms, the flame in the area outside the fuel jet near the injector propagates upward and along the lateral portion of the chamber until it coincides with the flame in the jet

shear layer near the injector. The lower section of the flame forms distinct side lobes. Comparison of schlieren images in Figures 4-9 shows equivalence ratio does not affect flame propagation for $t = 3$ ms and $t = 10$ ms. Therefore, equivalence ratio has insignificant effects on the method of flame propagation for these early ignition times.

For $t = t_{\text{end}}$, hydrogen, as verified by schlieren images in Figures 10-12, is present in all areas of the chamber and all of the fuel has been supplied to the chamber at ignition. In this case, fuel jet generated turbulence would be high, although the residence time for fuel-air mixing is inadequate to produce homogeneous mixtures throughout the chamber. After the start of combustion, the flame propagates upward while spreading towards the chamber wall. The flame continues to propagate upward with the formation of side lobes in the lower region until it reaches the injector at the top of the chamber. The method of flame propagation is the same for all three equivalence ratios.

For $t = t_{\text{end}} + 50$ ms, as with $t = t_{\text{end}}$, the overall equivalence ratio has been established at ignition. Hydrogen, as verified in Figures 13-15, is present in all areas of the chamber, and increase in ignition time lends towards more homogeneous fuel/air mixing in the chamber. However, fuel jet generated turbulence, which enhances combustion, is dissipating, as seen in schlieren images. After the start of combustion, the flame takes a semi-spherical shape that expands as combustion progresses through the chamber. Flame propagation is more uniform than in the earlier ignition times because of improved fuel-air mixing and lower initial turbulence. Flame generated turbulence can be observed from schlieren images at later times.

Flame Front Speed

Acquired color schlieren images were analyzed using a cross-correlation approach to determine the flame front speed at varying locations in the combustion chamber. The cross-

correlation approach utilizes the Matlab function normxcorr2:

$$\gamma_{u,v} = \frac{\sum_{x,y} f(x,y) - \bar{f}_{u,v} [t(x-u, y-v) - \bar{t}]}{\{\sum_{x,y} f(x,y) - \bar{f}_{u,v}^2 \sum_{x,y} t(x-u, y-v) - \bar{t}^2\}^{0.5}}$$

whereas f = image, t = mean of template (structure)

and $\bar{f}_{u,v}$ = mean of $f(x, y)$ in the region

under the template (structure).

Thus, defined structures are tracked from consecutive schlieren images using patterns of intensity (green) variations. For further explanation see Appendix H.

The cross-correlation technique was validated using synthetic images with pre-defined structures and pathlines. Then images were analyzed using the cross-correlation technique to determine structure locations and pathline plots. Next, consecutive schlieren images from the start to the end of combustion for each experiment were analyzed to obtain pathline and flame front speed for initially defined structures in the chamber.

Pathlines for initially defined structures at varying locations in the combustion chamber are shown in Figures 16-24. The flame front speeds of the corresponding pathlines are shown in Figures 16a-24a. Pathline pertains to path of structures in the flame front at varying locations in the chamber. The time interval between schlieren images at a frame rate of 50000 frames per second is 20 μ s. Thus, with a pixel resolution of 310 μ m/pixel, the uncertainty of flame front speed is 15.5 m/s. The flame front speed uncertainty was decreased to 3.1 m/s by correlating every fifth image. The spark igniter location is the reference point for flame front distance.

Flame front speeds at $t = 3$ ms for $\phi = 0.6, 0.8,$ and 1.0 are shown in Figures 16, 17, and 18. Maximum flame front speed is 44 m/s for $\phi = 0.6,$ 38 m/s for $\phi = 0.8$ and 40 m/s for $\phi = 1.0.$ All three figures show higher initial flame front speeds with flame speeds decreasing as the

flame front distance increases. This decrease occurs when the flame front has propagated about half the distance of the combustion chamber and the flame front along the centerline is beginning to propagate into the fuel jet. The higher flame front speeds are also observed in the areas outside the fuel jet (pathlines a and e). The lower flame front speeds in the center of the combustion chamber are due to the flames interaction with the fuel jet. Flame front speeds for varying equivalence ratios are comparable due to the mass of fuel being constant at ignitions.

Flame front speeds at $t = t_{\text{end}}$ are shown in Figures 19, 20, and 21. Maximum flame front speeds are $s_{\text{max}} = 64$ m/s for $\phi = 0.6$, $s_{\text{max}} = 58$ m/s for $\phi = 0.8$ and $s_{\text{max}} = 60$ m/s for $\phi = 1.0$. Again initial flame front speeds are the highest followed by a decrease in flame front speeds as the flame front distance increases. Trends are similar to the $t = 3$ ms cases, however, maximum flame front speeds at $t = t_{\text{end}}$ are much higher than the $t = 3$ ms cases. Maximum flame front speeds are higher due to high turbulence and higher overall equivalence ratio at the time of ignition.

Flame front speeds at $t = t_{\text{end}} + 50$ ms are shown in Figures 22, 23, and 24. The maximum flame front speeds are $s_{\text{max}} = 22$ m/s for $\phi = 0.6$, $s_{\text{max}} = 29$ m/s for $\phi = 0.8$, and $s_{\text{max}} = 35$ m/s at $\phi = 1.0$. Flame front speeds are more constant and maximum flame front speeds are much lower than at the earlier ignition times. At $t = t_{\text{end}} + 50$ ms fuel-jet generated turbulence has decreased and fuel-air mixture in the chamber is more homogeneous.

Flame front speeds are variable for $t = 3$ ms and for $t = t_{\text{end}}$. Flame front speed variations are due to variations in localized fuel/air ratio that result from improper mixing, the presence of the hydrogen jet for $t = 3$ ms, and the amount of fuel present in the chamber at early ignition. Maximum flame front speeds for $t = t_{\text{end}}$ are higher than flame front speeds at other ignition times and combustion duration is therefore the lowest. See Appendix G for combustion durations for

varying ignition times at the three equivalence ratios. This is due to higher overall equivalence ratio at the start of combustion as compared to $t = 3$ ms and greater turbulent activity as compared to $t = t_{\text{end}} + 50$ ms. Total combustion time is affected by varying equivalence ratios. The time that it takes the flame front to reach the top of the chamber is 0.8 ms less for $\phi = 1.0$ than for $\phi = 0.8$, which is significant for processes that takes no more than 2.3 ms.

Chamber Pressure

Chamber pressures for early ignition times, $t = 3$ ms and $t = 10$ ms are shown in Figures 25 and 26 respectively. A rapid pressure rise is seen from the start of combustion until the flame front has propagated over half the diameter of the chamber and flame front speeds have peaked. For $t = 3$ ms, pressure peaks occur when the flame front is just beginning to propagate into the fuel jet region to acquire its shape. For $t = 10$ ms the flame along the centerline is propagating at slower speeds than the flame along the wall of the chamber. Rapid pressure rise is followed by a slower rise to a peak value. For $t = 10$ ms, and $\phi = 1.0$, there is only one region of pressure rise. After reaching the peak, pressure decreases at a much lower rate, as shown in Figure 26. Pressure peaks at $P_{\text{max}} = 377$ kPa, 328 kPa, and 335 kPa for $\phi = 0.6, 0.8,$ and 1.0 respectively for $t = 3$ ms. Pressure peaks at $P_{\text{max}} = 386$ kPa, 324 kPa, and 400 kPa for $\phi = 0.6, 0.8$ and 1.0 respectively for $t = 10$ ms. Similarities in peak pressures are due to equivalent amounts of fuel present in the chamber at the start of combustion for $t = 3$ ms and for $t = 10$ ms regardless of the overall equivalence ratio. Thus, overall equivalence ratio has a minor effect on chamber pressure. Pressure trends for $t = 3$ ms and 10 ms agree with those from the previous chapter.

Chamber pressures for $t = t_{\text{end}}$ are shown in Figure 27. Pressure rises rapidly during combustion, with only one positive slope that is greater than that of the earlier ignition times. The rate of pressure rise increases as equivalence ratio increases. With combustion durations of

3.1 ms, 3.0 ms, and 1.9 ms for $\phi = 0.6$, 0.8, and 1.0 respectively, pressure peaks, as seen in Figure 27, occur just prior to the end of combustion. Following peak pressures, pressure decrease in two phases. The first phase last for about 4 ms and occurs at a rate lower than pressure increase, as seen by their slopes, but higher than the second phase. Peak pressures at $P_{\max} = 757$ kPa, 696 kPa, and 1058 kPa for $\phi = 0.6$, 0.8, and 1.0 respectively. Peak pressure for stoichiometric combustion, $\phi = 1$ is at least 300 kPa greater than peak pressures at lower equivalence ratios. At the end of injection, the total mass of supplied hydrogen is in the chamber for all equivalence ratios and significant fuel-jet generated turbulence is still present. Pressure rises rapidly and peaks much higher than with $t = 3$ ms and 10 ms due to more hydrogen present at the start of combustion. Without the presence of the fuel jet delivering hydrogen at the start of combustion, differing from early ignition times, combustion occurs in premixed mode.

Chamber pressures for $t = t_{\text{end}} + 50$ ms are shown in Figure 28. Pressure rises rapidly during combustion. The rates of pressure rise is higher than the rates for $t = 3$ ms and $t = 10$ ms due to more fuel in the chamber at the start of combustion, but is slightly lower than the rates for $t = t_{\text{end}}$ due to lower turbulent activity. With combustion durations of 6.2 ms, 5.4 ms, and 3.3 ms for $\phi = 0.6$, 0.8, and 1.0 respectively, pressure peaks, as seen in Figure 28, occur also just prior to the end of combustion. Pressure decrease, as with $t = t_{\text{end}}$, occurs in two phases with the duration of the first phase being about 4 ms and decreasing at a rate greater than that of the second phase. Pressure peaks at $P_{\max} = 830$ kPa, 831 kPa, and 1015 kPa for $\phi = 0.6$, 0.8, and 1.0 respectively. There is at least a 184 kPa peak pressure difference between stoichiometric and non-stoichiometric conditions. Again all hydrogen is present in the chamber and equivalence ratio effects are seen in the pressure differences. Pressure trends are similar to those at $t = t_{\text{end}}$

with a rapid increase in pressure followed by a rapid decrease but different from those at early ignition times, which, as explained earlier, is attributed to ignition time.

Net Heat Transfer Rate

The net heat transfer rate was calculated from chamber pressure data. Average chamber temperature (T) was found using the ideal gas law. The molar specific volume (v) was found using $v = V / N$ whereas V is the chamber volume and N is the total mole number of the reactants. Net heat transfer rate (Q) was found from $Q = m \times C_v \times \frac{dT}{dt}$ where the specific heat, C_v , is determined by first calculating C_p using a third order polynomial and then using $\frac{C_p}{C_v} = 1.4$ for air to find C_v . Net heat transfer rates were graphed to show how heat release/loss occurred in the chamber. Positive net heat transfer indicates that heat generated by the fuel during combustion is greater than heat lost to the ambient, with negative net heat transfer rates indicating the opposite. Figures 29-32 represent the net heat transfer rates for varying ignition times.

Net heat transfer rate for $t = 3$ ms and 10 ms are shown in Figures 29 and 30. For $t = 3$ ms, net heat transfer rate peaks within 5 ms after of the opening of the injector and peaks at $Q_{max} = 20$ kW, 17 kW, and 15 kW for $\phi = 0.6$, 0.8, and 1.0 respectively. This peak occurs within 2 ms after the start of combustion and the flame front has propagated to about half the diameter of the chamber. Flame front speed increases prior to the net heat transfer rate peak and decrease afterwards as the flame front propagates into the perimeter of the fuel jet. As flame front speed decreases, heat is being generated at a lower rate and this rate must be lower than the heat being loss to the chamber as net heat transfer rates decreases afterwards. Pressure does increase after the net heat transfer rate peak is reached, however it increases at a lower rate. Net heat transfer

rate peaks with the first 13 ms after the injector opens (within 3 ms after the start of combustion) for $t = 10$ ms with $Q_{max} = 17$ kW, 17 kW, and 38 kW for $\phi = 0.6$, 0.8, and 1.0 respectively. With the exception of $Q_{max} = 38$ kW, net heat transfer rates for both of these ignition times are comparable. When the net heat transfer rates for $t = 10$ ms peaks, the flame front has propagated over half the chamber and the flame front speed near the centerline, diameter whose endpoints are the fuel injector and spark plug, is decreasing. After the peak is reached, the flame front along the lateral surface of the chamber propagates upward and toward the fuel injector until it eventually interacts with the flame along the centerline. Pressure at this net heat transfer rate peak continues to increase, but at a lower rate; positive pressure slope decreases. For $t = 3$ ms and 10 ms, after net heat transfer rate peaks, although heat is continually being generated in the chamber from the combustion of fuel that is continually added at early ignition, heat is transferred to the chamber wall and causes an overall decline in net heat transfer rate. After combustion, heat addition by the fuel goes to zero but heat transfer to the chamber wall continues until chamber temperatures reach ambient air temperature. Net heat transfer rate becomes negative when heat transfer to the chamber wall, because of high chamber temperatures, is greater than heat generation.

Net heat transfer rate for $t = t_{end}$ for varying equivalence ratios are shown in Figure 31. In the first 2 ms after combustion net heat transfer rate peaks at $Q_{max} = 119$ kW, 76 kW, and 110 kW for $\phi = 0.6$, 0.8, and 1.0 respectively. Net heat transfer rate peaks at the time that pressure peaks, which is a different trend from $t = 3$ ms and $t = 10$ ms. This difference is attributed to ignition time where fuel is no longer added after combustion starts. The flame front, at the peak, has just reached the top of the combustion chamber and flame front speed is zero. Peak net heat transfer rates at this ignition time is greater than those at $t = 3$ ms and $t = 10$ ms due to the higher

overall equivalence ratio with the presence of all supplied fuel in the chamber at the start of combustion. Combustion time is less which means that the net heat transfer rate is much greater than for earlier ignition times.

Net heat transfer rate for $t = t_{\text{end}} + 50$ ms is shown in Figure 32. Net heat transfer rate peaks at $Q_{\text{max}} = 81$ kW, 70 kW, and 92 kW for $\phi = 0.6$, 0.8, and 1.0 respectively and occur with 5 ms of the start of combustion. Pressure peaks, as with $t = t_{\text{end}}$, when net heat transfer rate peaks. The flame front is near the top of the chamber and flame front speeds are ceasing.

Observing variations in peak net heat transfer rates for varying ignition times show that ignition time has a significant effect on heat transfer rates. Net heat transfer rate varies by as much as 102 kW for $\phi = 0.6$, 59 kW for $\phi = 0.8$, and 95 kW for $\phi = 1.0$ for varying ignition times. These significant variations are due to variations in overall equivalence ratios at the start of combustion. Net heat transfer rates for using the number of moles of the products instead of the reactants can be found in Appendix M.

Conclusions

Equivalence ratios were varied with varying ignition times. Flame propagation, flame front speed, chamber pressure, and heat transfer were studied.

Flame front speeds at varying equivalence ratios are similar for each ignition time. Flame front speeds are higher when ignition occurs at the end of combustion where overall equivalence ratio is established and turbulence is present. Ignition time has a significant effect on flame propagation while the effect of equivalence ratio is less significant. Equivalence ratio has significant effect on chamber pressure when all hydrogen has entered the chamber, thus when ignition occurs at the end of injection and 50ms after the end of injection. Ignition time has a significant effect on chamber pressure at any equivalence ratio. Chamber pressure trends

are similar for varying equivalence ratios at the same ignition time. Chamber pressure trends are different for varying ignition times. Net heat transfer rates are greater at $t = t_{\text{end}}$ and $t = t_{\text{end}} + 50$ ms than at earlier ignition times. Net heat transfer trends are similar for varying equivalence ratios at the same ignition time.

References

- Glasson N.D., Green R.K. Performance Of A Spark-Ignition Engine Fuelled With Hydrogen Using A High-Pressure Injector. *Int. J. Hydrogen Energy* 19 (1994) 917-923.
- Green R.K., Glasson N.D. High-Pressure Hydrogen Injection For Internal Combustion Engines. *Int. J. Hydrogen Energy* 17 (1992) 895-901.
- Huang Z., Wang J., Liu B., Zeng K., Yu J., Jiang D. Combustion characteristics of a direct-injection engine fueled with natural gas-hydrogen blends under different ignition timings. *Fuel* 86 (2007) 381-387.
- Ji C., Wang S. Effect of hydrogen addition on combustion and emissions performance of a spark ignition gasoline engine at lean conditions. *Int. J. Hydrogen Energy* 34 (2009) 7823-7834.
- Li J., Gong C., Su Y., Dou H., Liu X. Effect of injection and ignition timings on performance and emissions from a spark-ignition engine fueled with methanol. *Fuel* 89 (2010) 3919-3925.
- Mohammadi A., Shioji M., Nakai Y., Ishikura W., Tabo E. Performance and combustion characteristics of a direct injection SI hydrogen engine. *Int. J. Hydrogen Energy* 32 (2007) 296-304.
- Owston R., Magi V., Abraham J. Interactions of hydrogen flames with walls: Influence of wall temperature, pressure, equivalence ratio, and diluents. *Int. J. Hydrogen Energy* 32 (2007) 2094-2104.
- Rakopoulos C., Kosmadakis G., Demuyneck J., De Paepe M., Verhelst S. A combined experimental and numerical study of thermal processes, performance and nitric oxide emissions in a hydrogen-fueled spark-ignition engine. *Int. J. Hydrogen Energy* 36 (2011) 5163-5180.
- Vudumu S., Koylu U. Computational modeling, validation, and utilization for predicting the performance, combustion and emission characteristics of hydrogen IC engines. *Energy* 36 (2011) 647-655.

Yousufuddin S., Masood M. Effect of ignition timing and compression ratio on the performance of a hydrogen-ethanol fuelled engine. *Int. J. Hydrogen Energy* 34 (2009) 6945-6950.

Zhenzhong Y., Jianqin W., Zhuoyi F., Jinding L. An investigation of optimum control of ignition timing and injection system in an in-cylinder injection type hydrogen fueled engine. *Int. J. Hydrogen Energy* 27 (2002) 213-217.

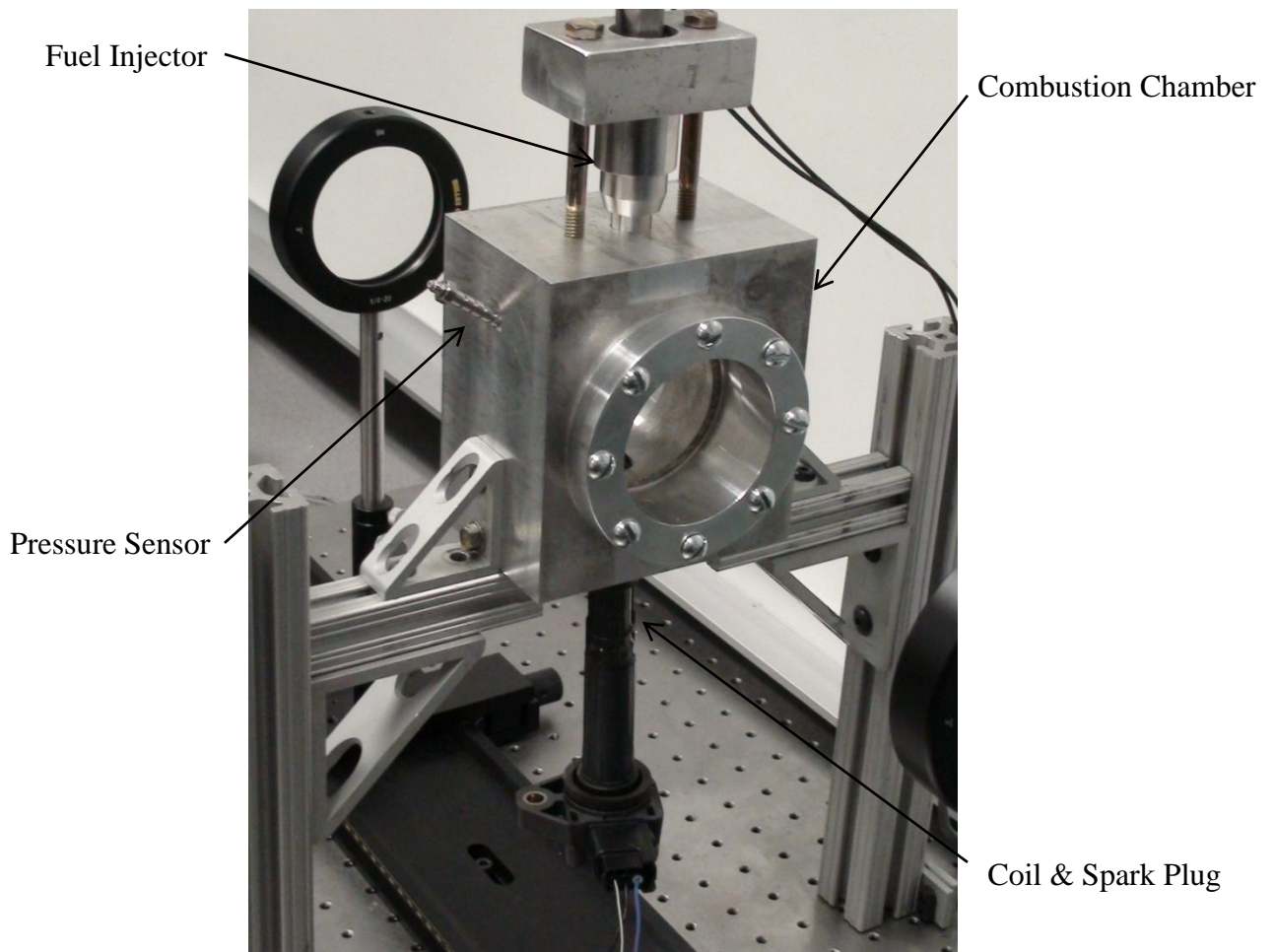


Figure 1. Combustion Vessel.

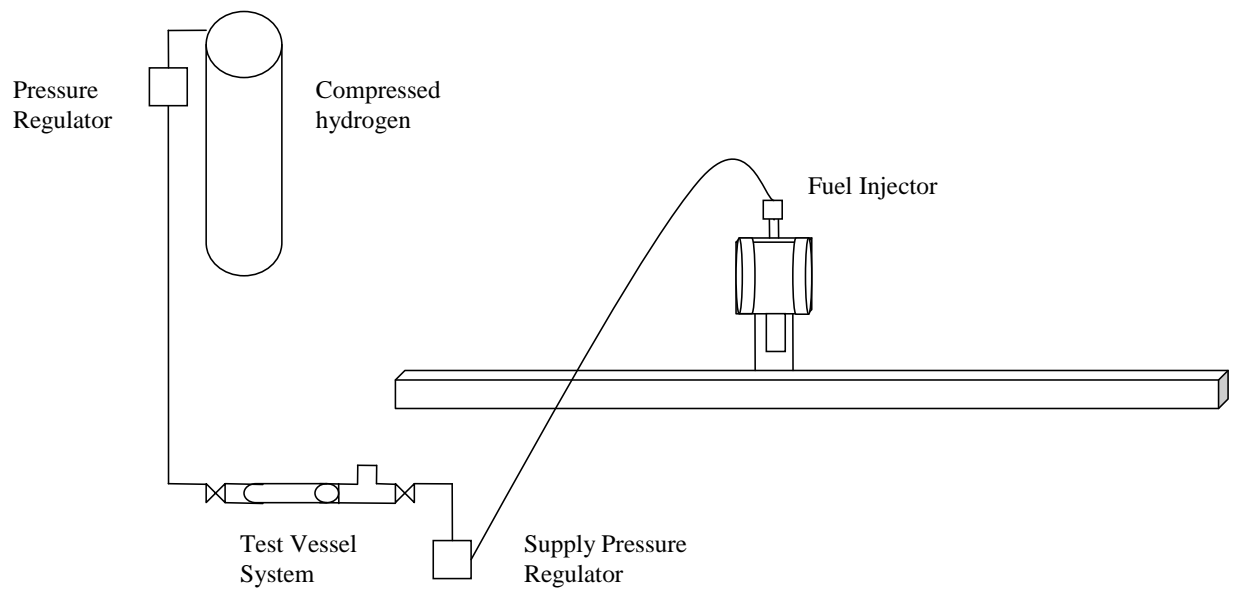


Figure 2. Fuel Flow System.

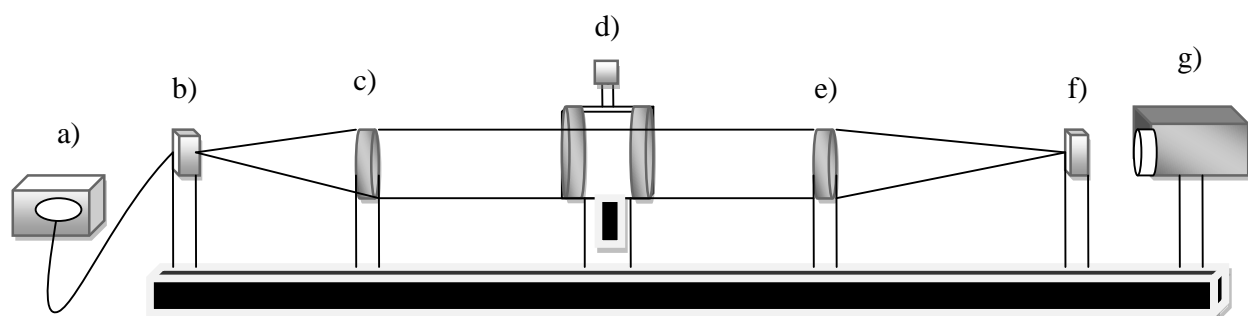


Figure 3. Rainbow Schlieren Deflectometer; a) Illuminator, b) Aperture, c) Collimating Lens, d) Test Media (Combustion Chamber), e) Decollimating Lens, f) Rainbow Filter, and g) High Speed Camera.

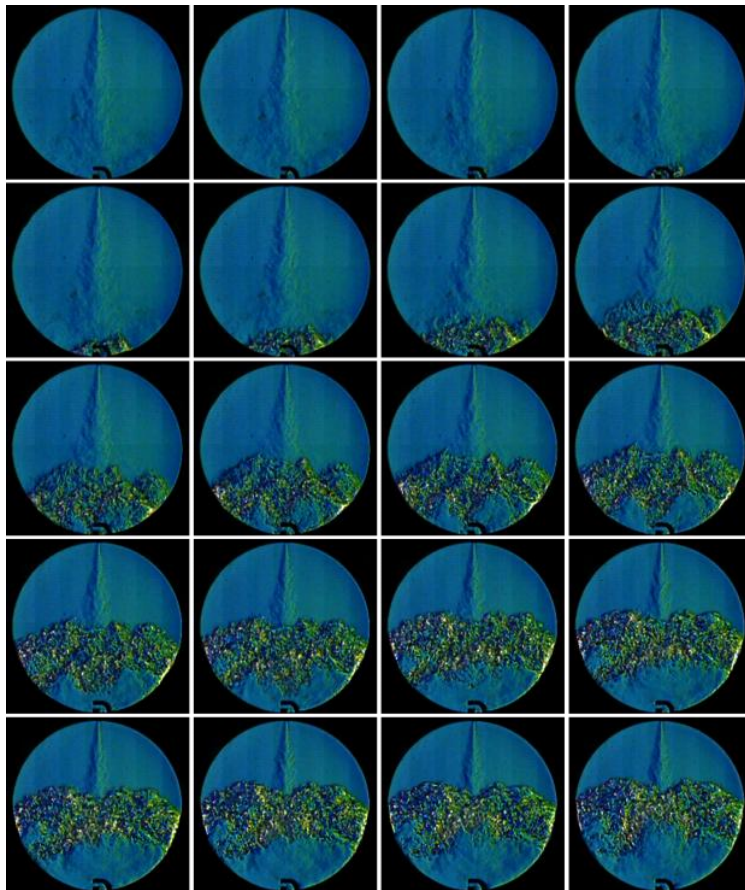


Figure 4. Schlieren Images (100 μ s intervals) for $\phi = 0.6$ and $t = 3$ ms.

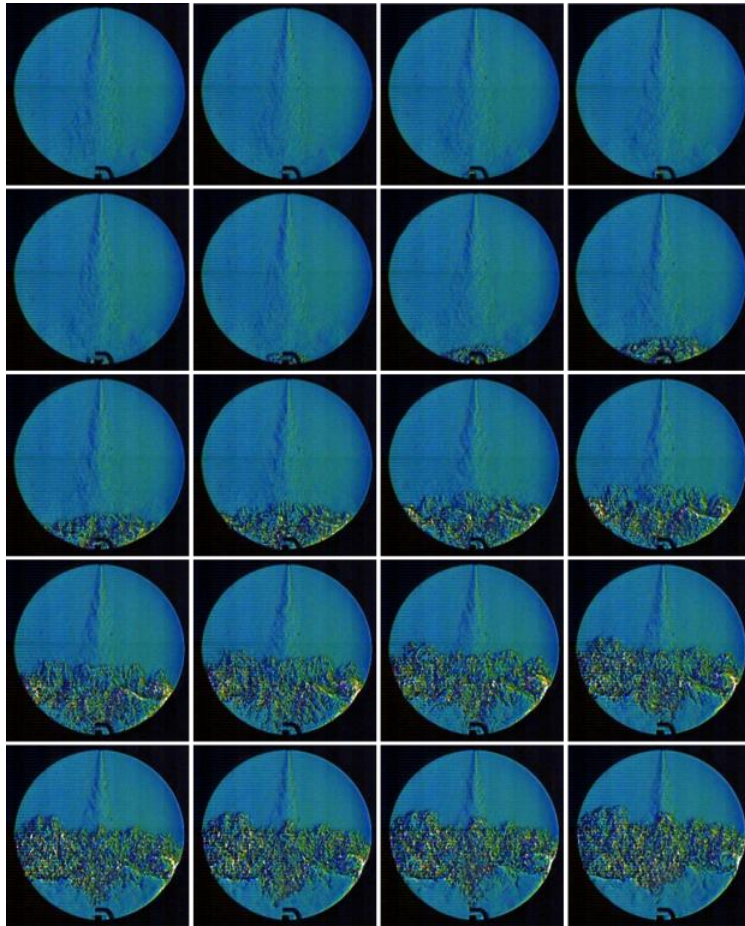


Figure 5. Schlieren images (100 μ s intervals) for $\phi = 0.8$ and $t = 3$ ms.

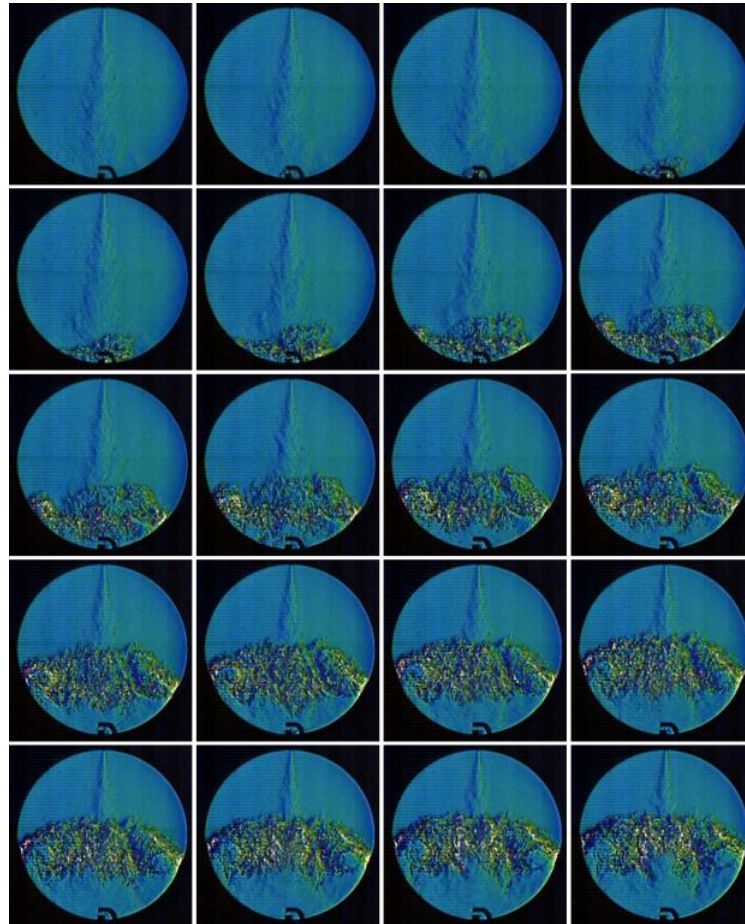


Figure 6. Schlieren images (100 μ s intervals) for $\phi = 1.0$ and $t = 3$ ms.

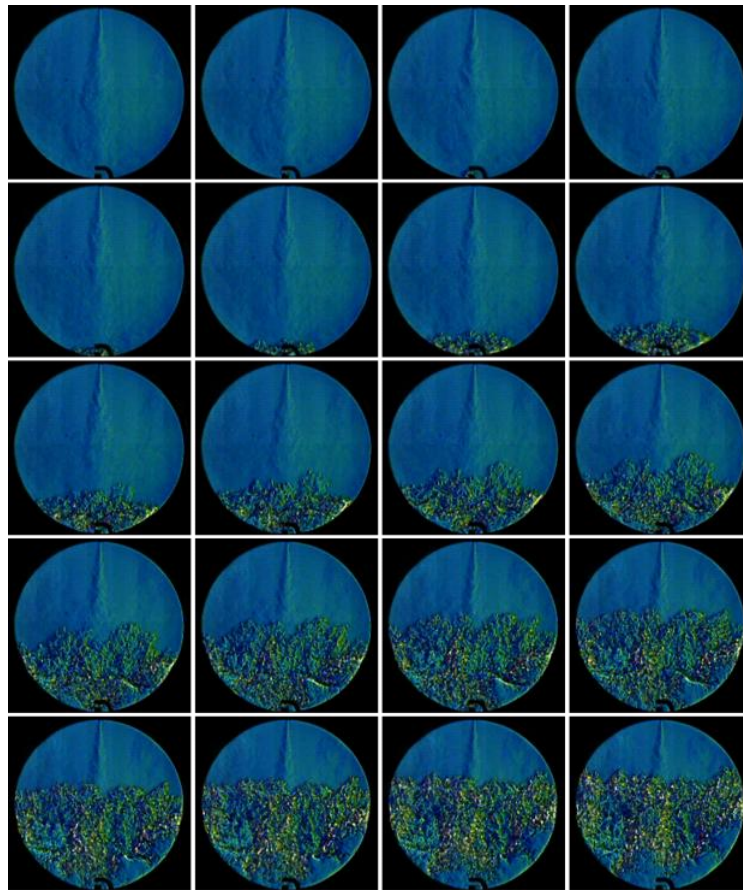


Figure 7. Schlieren images (100 μ s intervals) for $\varphi = 0.6$ and $t = 10$ ms.

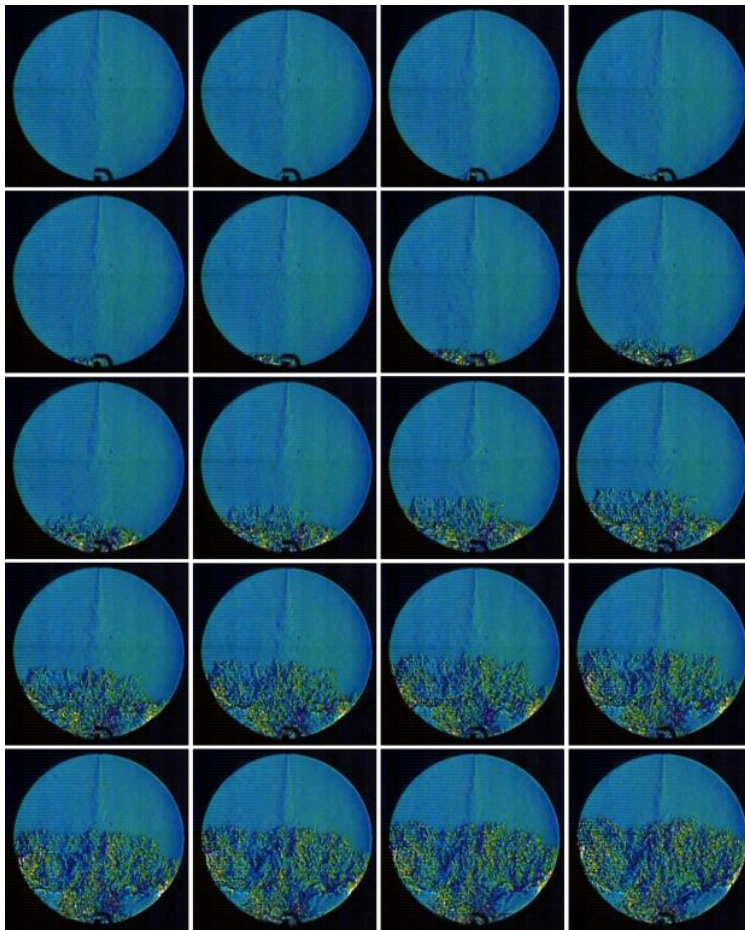


Figure 8. Schlieren images (100 μ s intervals) for $\phi = 0.8$ and $t = 10$ ms.

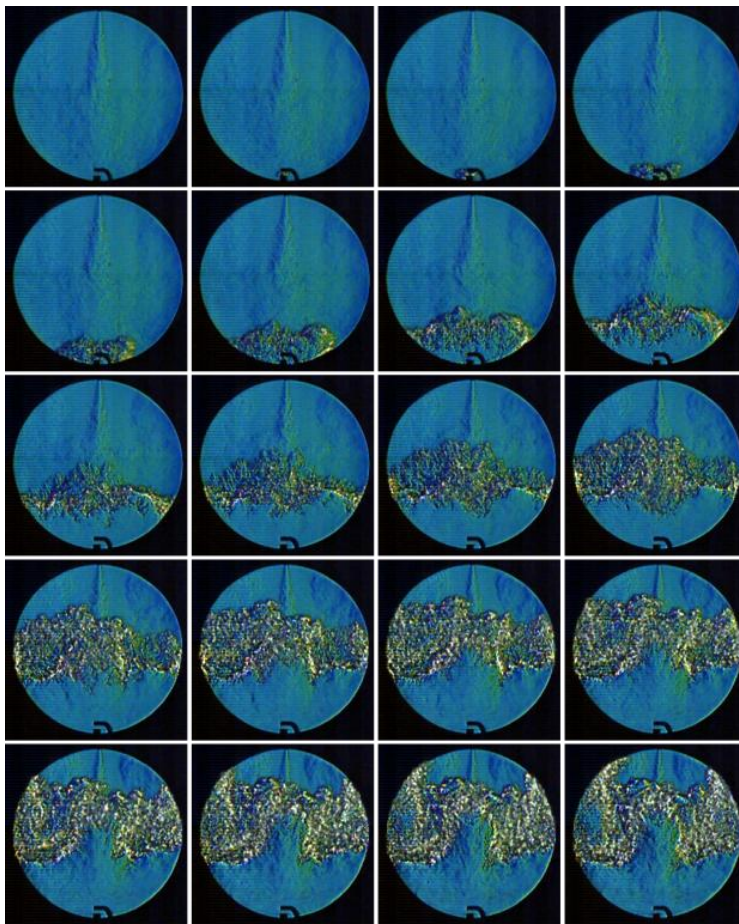


Figure 9. Schlieren images (100 μ s intervals) for $\phi = 1.0$ and $t = 10$ ms.

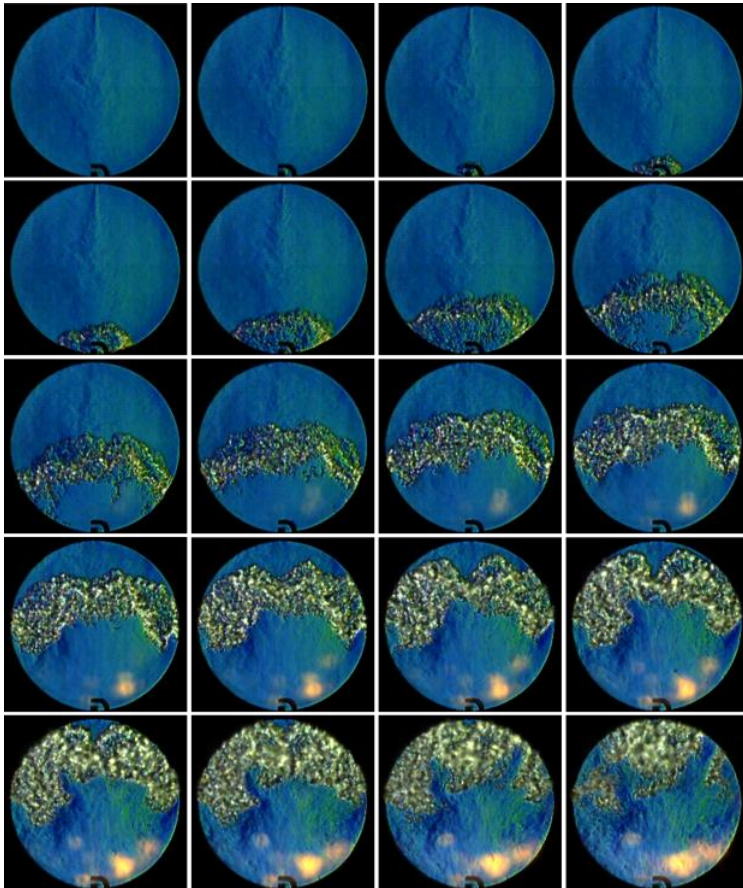


Figure 10. Schlieren images (100 μ s intervals) for $\varphi = 0.6$ and $t = t_{\text{end}}$.

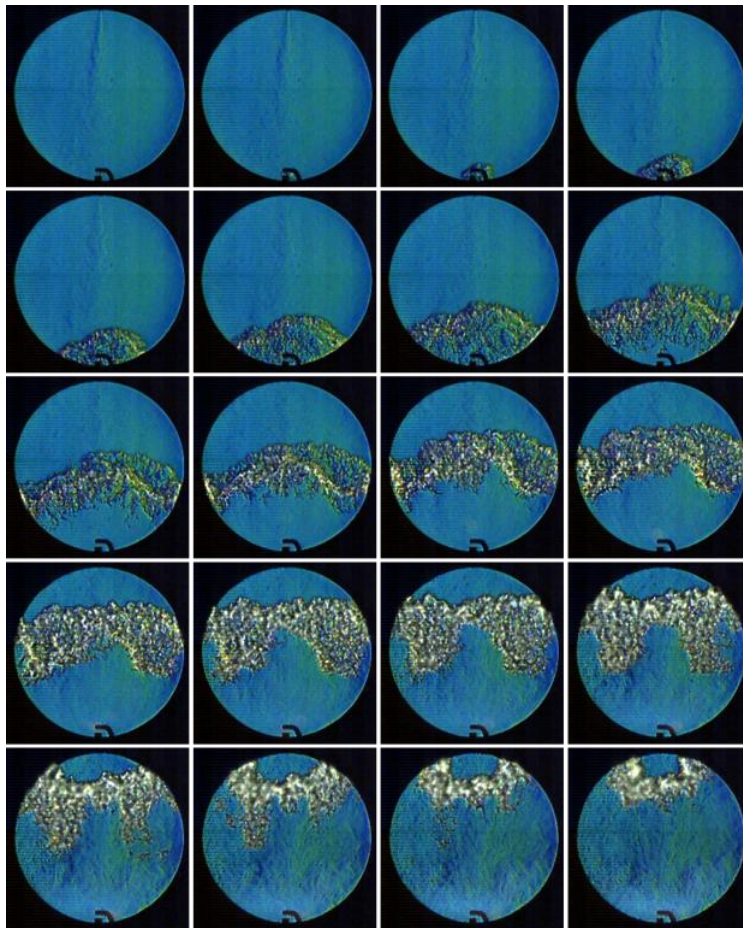


Figure 11. Schlieren images (100 μ s intervals) for $\varphi = 0.8$ and $t = t_{\text{end}}$.

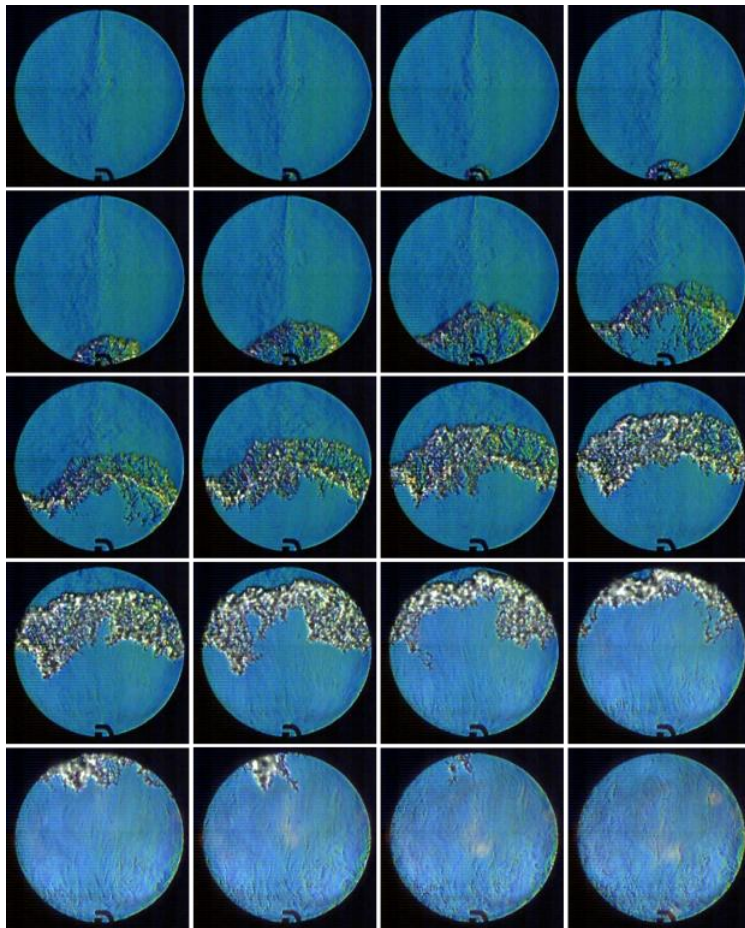


Figure 12. Schlieren images (100 μs intervals) for $\varphi = 1.0$ and $t = t_{\text{end}}$.

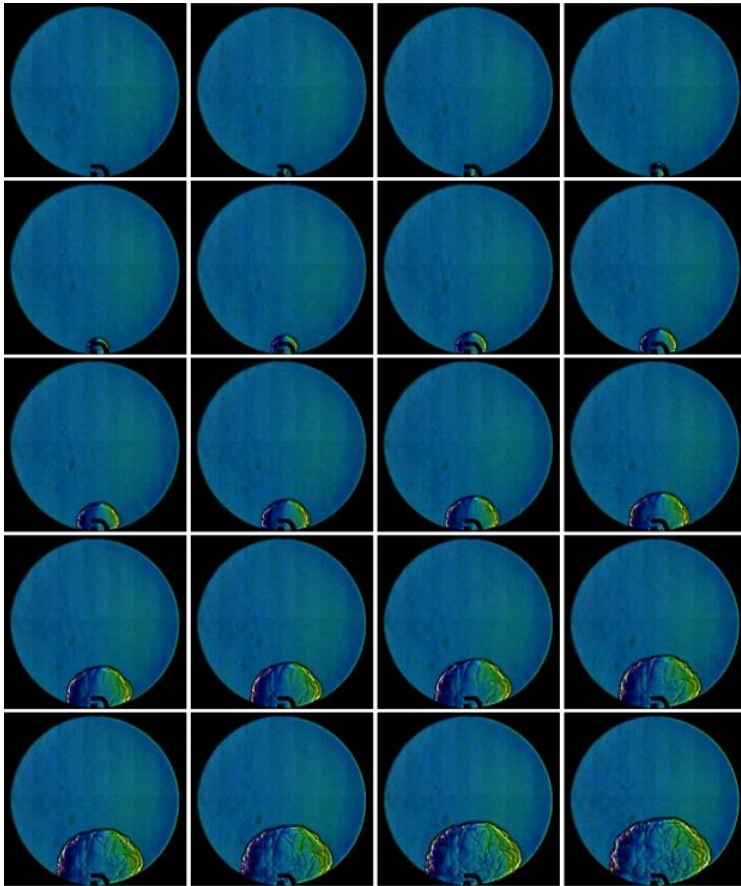


Figure 13. Schlieren images (100 μ s intervals) for $\varphi = 0.6$ and $t = t_{\text{end}} + 50$ ms.

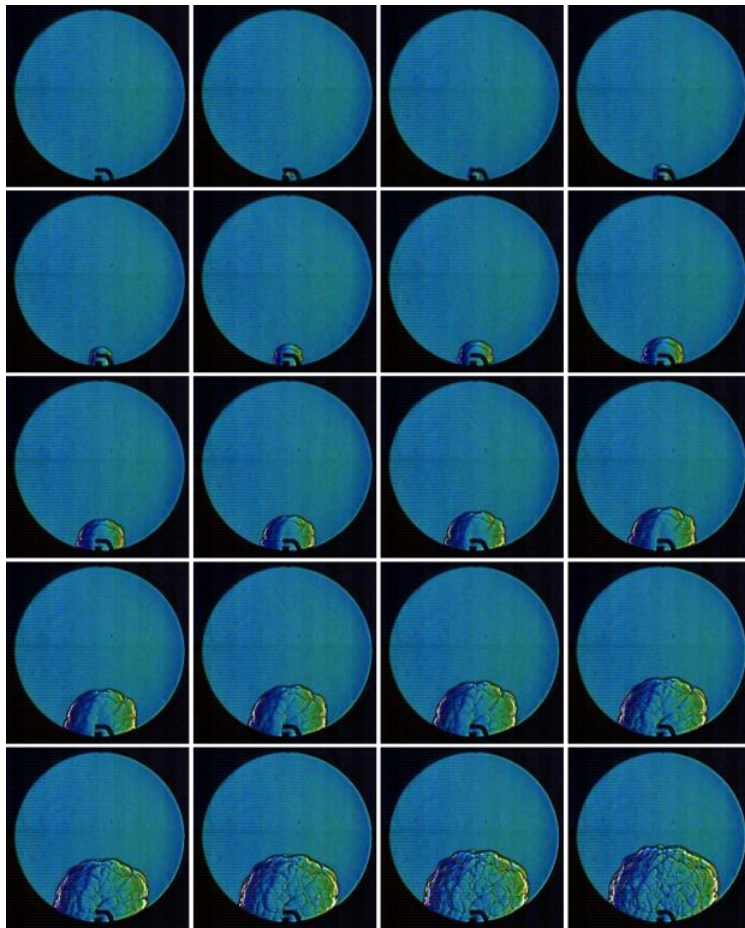


Figure 14. Schlieren images (100 μ s intervals) for $\phi = 0.8$ and $t = t_{\text{end}} + 50$ ms.

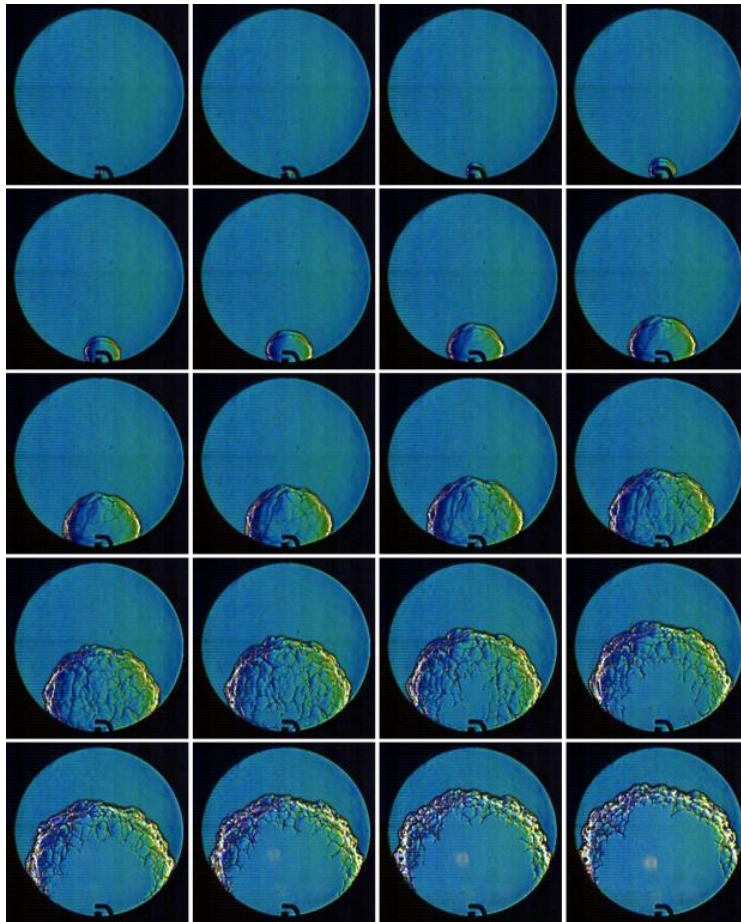


Figure 15. Schlieren images (100 μ s intervals) for $\phi = 1.0$ and $t = t_{\text{end}} + 50$ ms.

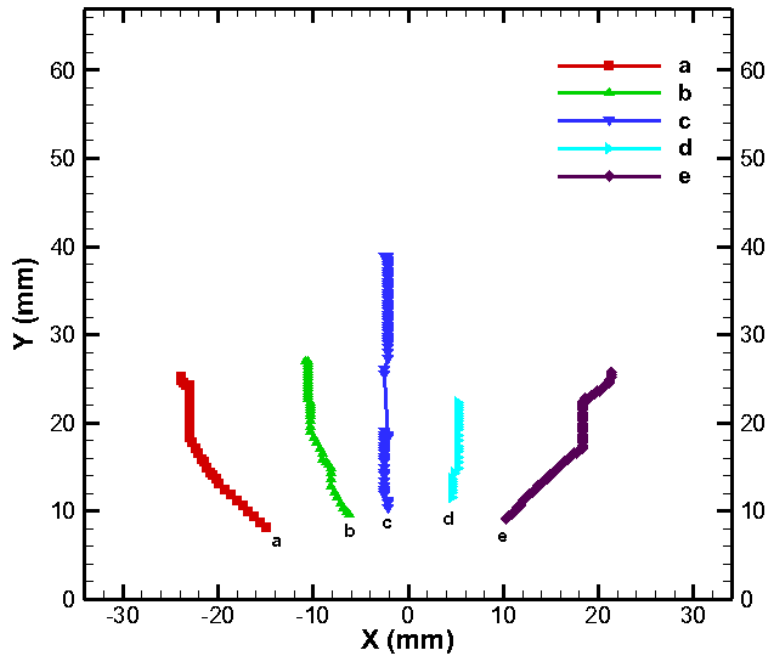


Figure 16. Pathlines of specified structures for $t = 3$ ms and $\phi = 0.6$.

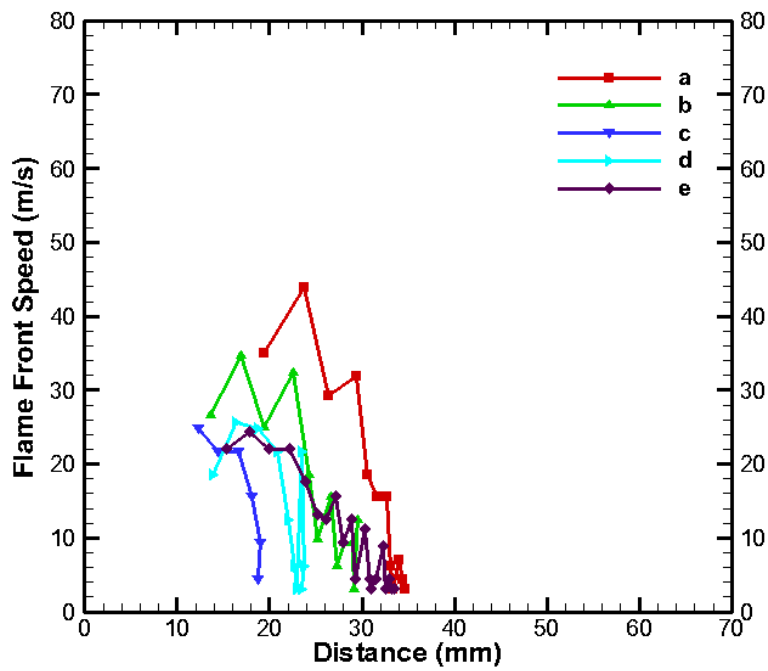


Figure 16a. Flame front speeds for corresponding pathlines for $t = 3$ ms and $\phi = 0.6$.

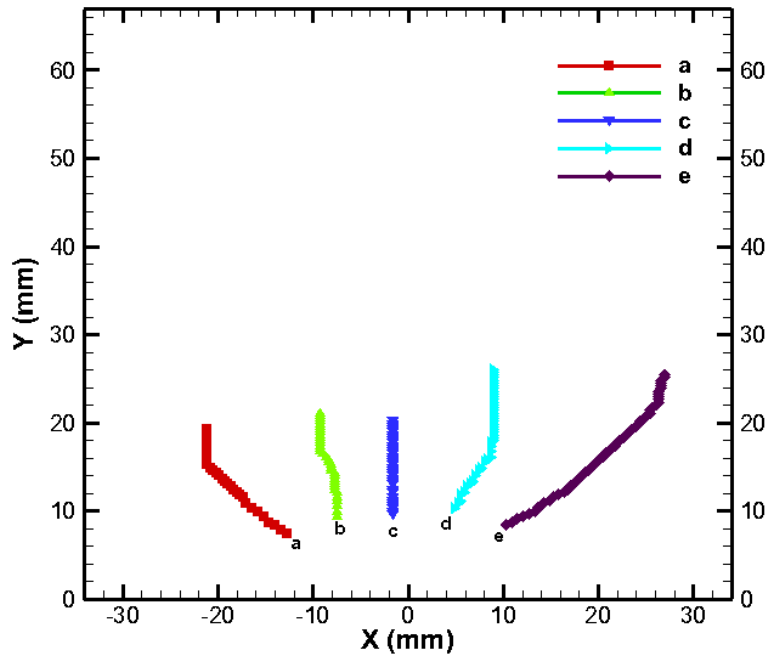


Figure 17. Pathlines of specified structures for $t = 3$ ms and $\phi = 0.8$.

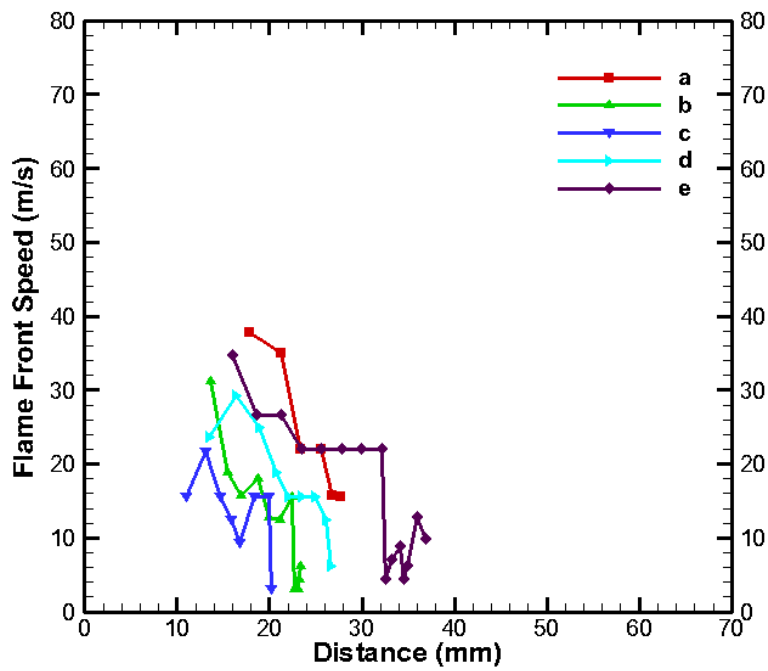


Figure 17a. Flame front speeds for corresponding pathlines for $t = 3$ ms and $\phi = 0.8$.

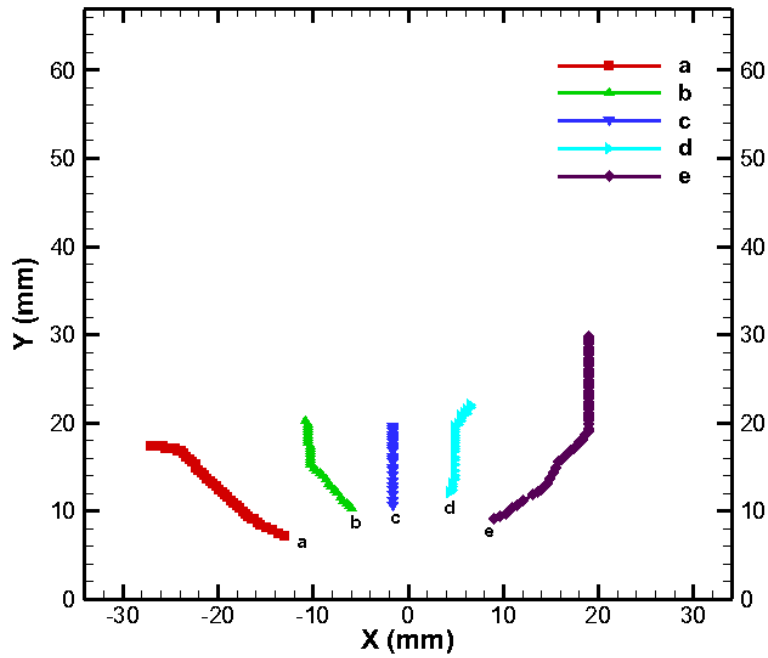


Figure 18. Pathlines of specified structures for $t = 3$ ms and $\phi = 1.0$.

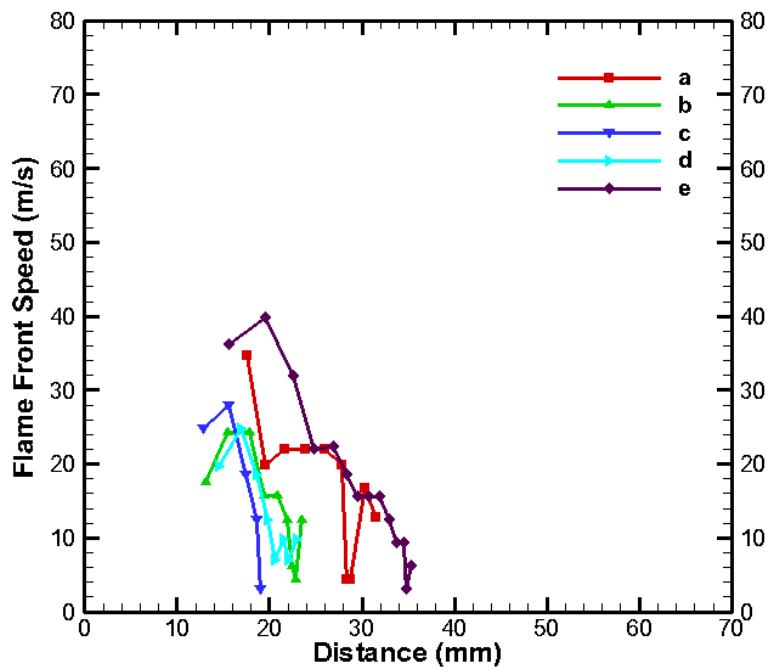


Figure 18a. Flame front speeds for corresponding pathlines for $t = 3$ ms and $\phi = 1.0$.

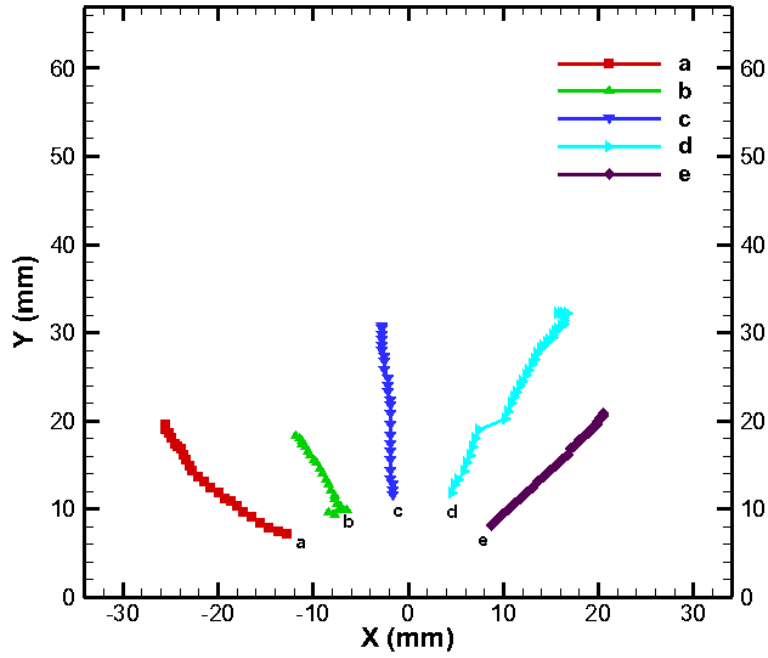


Figure 19. Pathlines of specified structures for $t = t_{\text{end}}$ and $\phi = 0.6$.

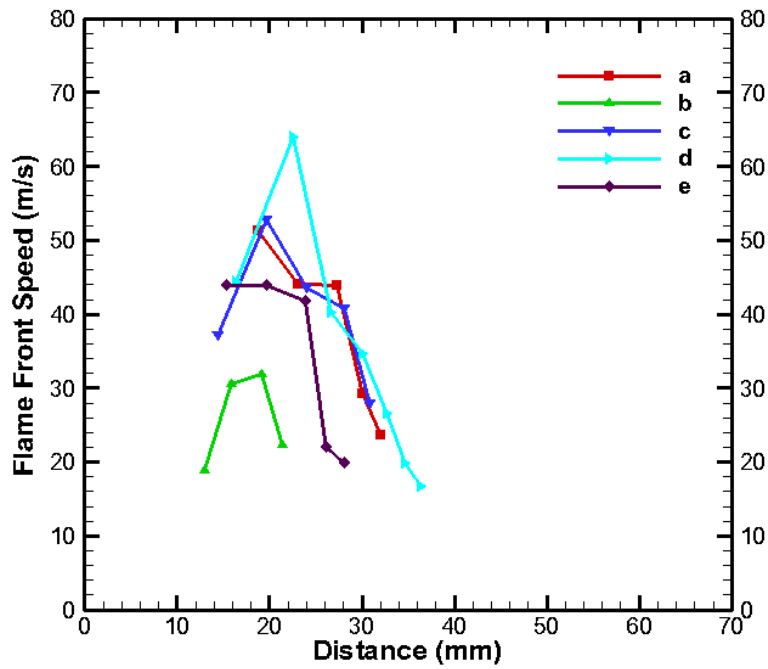


Figure 19a. Flame front speeds for corresponding pathlines for $t = t_{\text{end}}$ and $\phi = 0.6$.

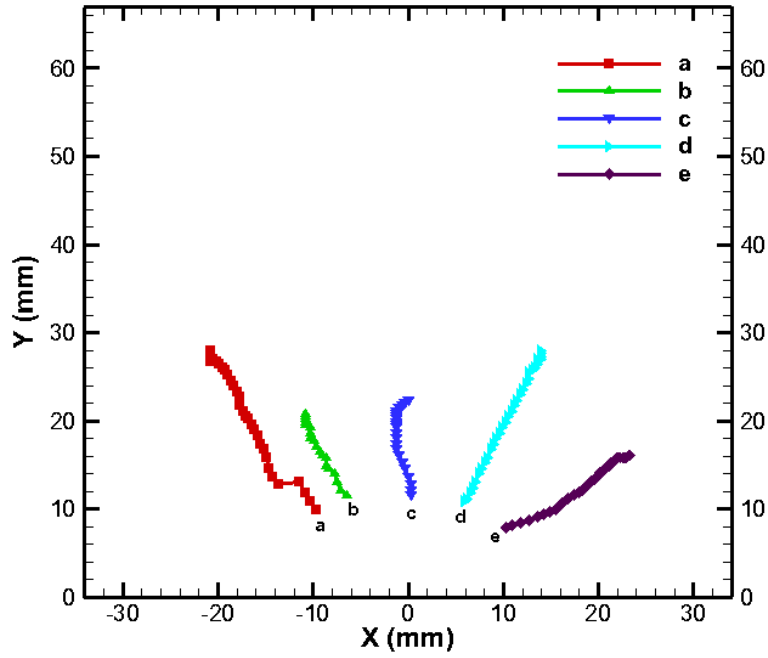


Figure 20. Pathlines of specified structures for $t = t_{\text{end}}$ and $\phi = 0.8$.

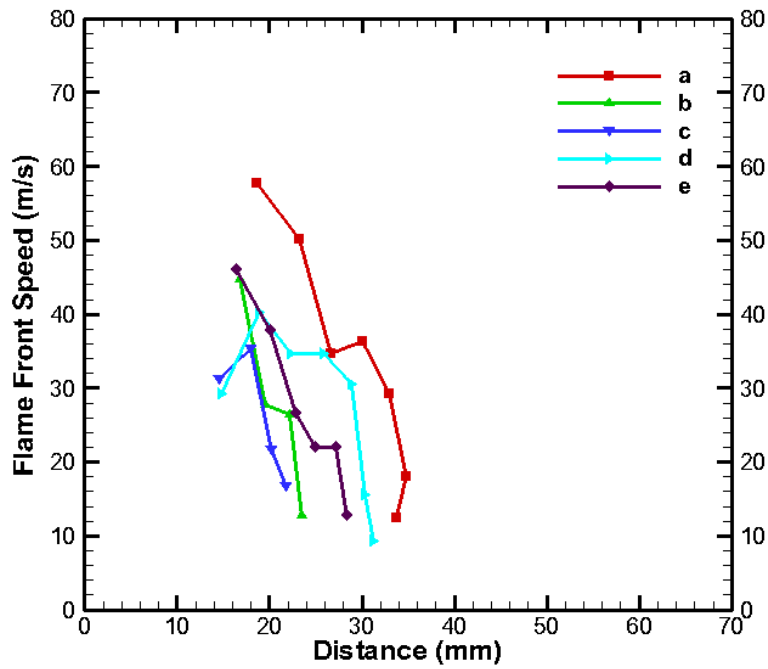


Figure 20a. Flame front speeds for corresponding pathlines for $t = t_{\text{end}}$ and $\phi = 0.8$.

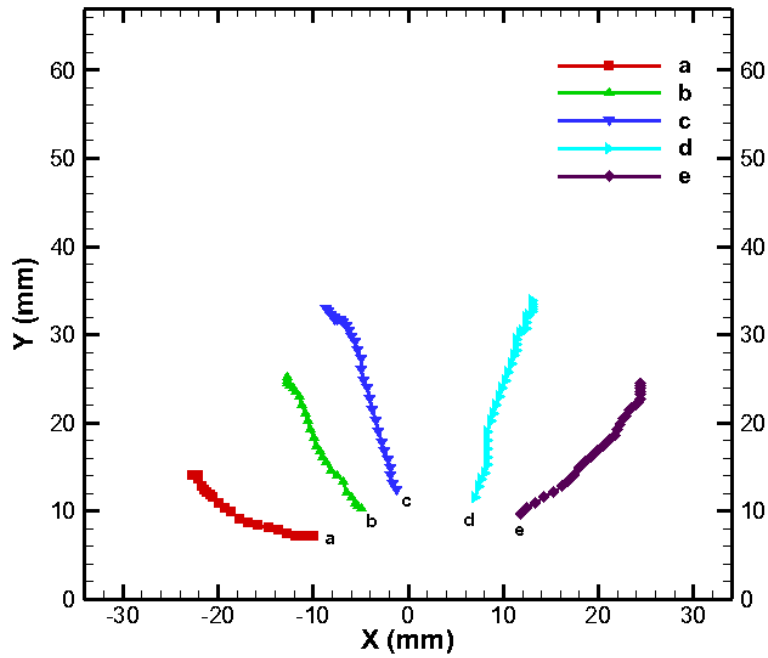


Figure 21. Pathlines of specified structures for $t = t_{\text{end}}$ and $\phi = 1.0$.

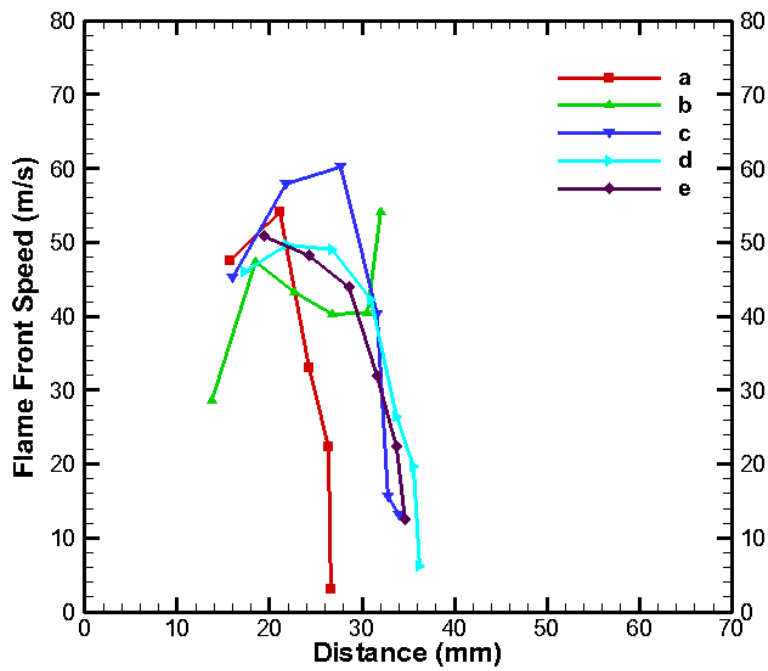


Figure 21a. Flame front speeds for corresponding pathlines for $t = t_{\text{end}}$ and $\phi = 1.0$.

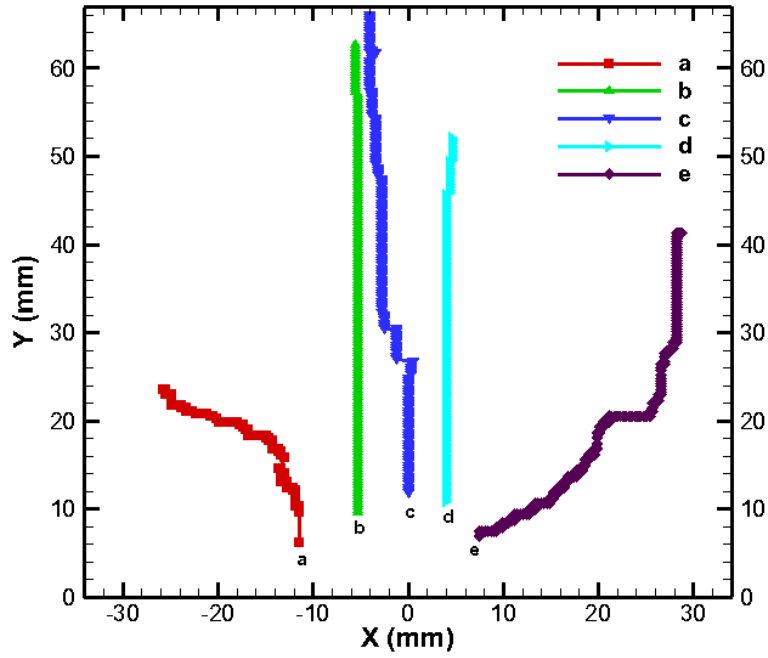


Figure 22. Pathlines of specified structures for $t = t_{\text{end}} + 50 \text{ ms}$ and $\phi = 0.6$.

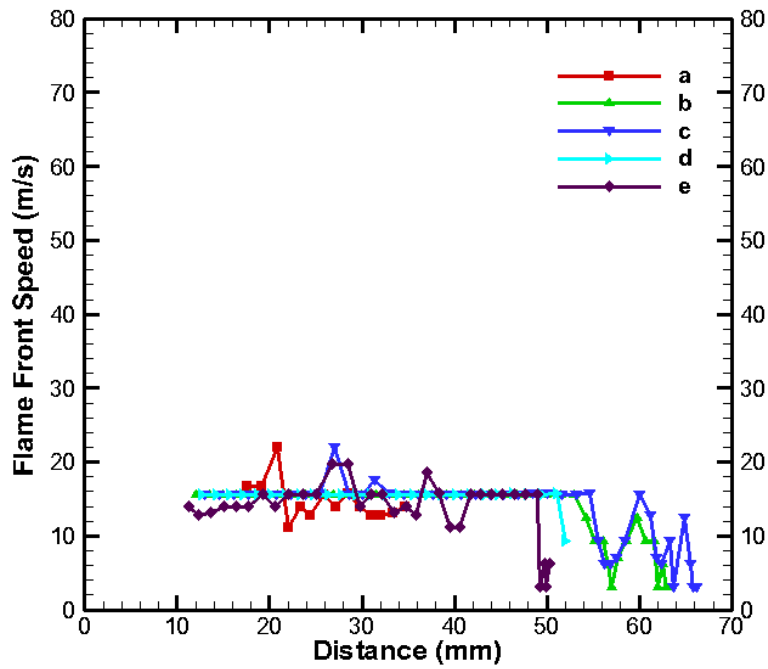


Figure 22a. Flame front speeds for corresponding pathlines for $t = t_{\text{end}} + 50 \text{ ms}$ and $\phi = 0.6$.

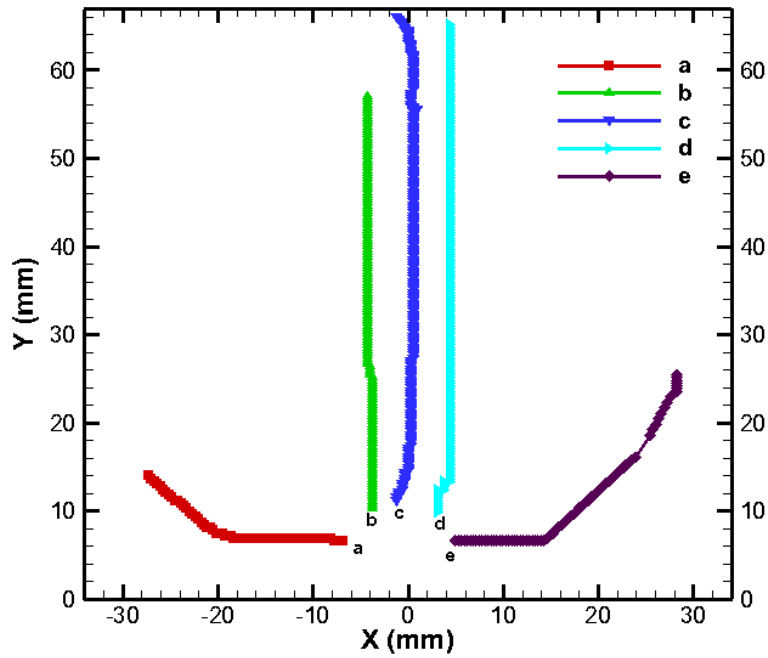


Figure 23. Pathlines of specified structures for $t = t_{\text{end}} + 50$ ms and $\phi = 0.8$.

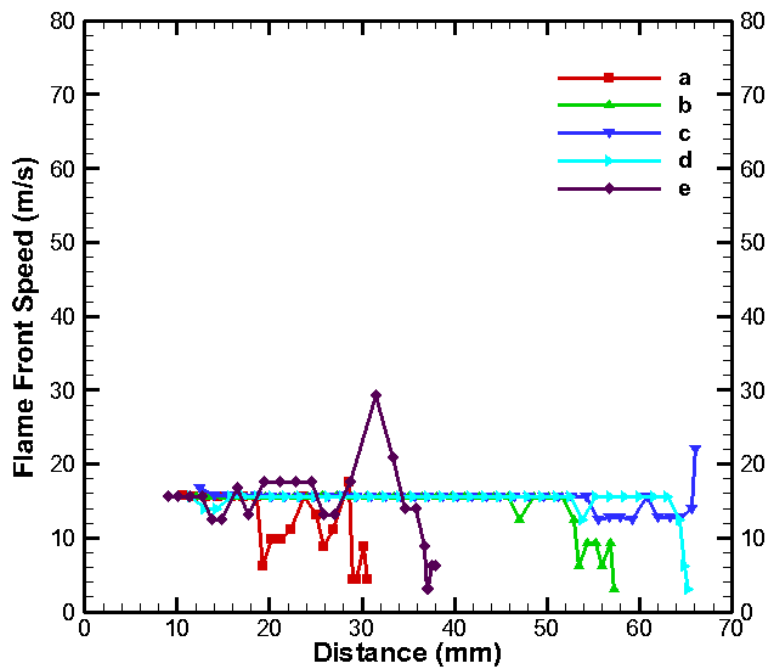


Figure 23a. Flame front speeds for corresponding pathlines for $t = t_{\text{end}} + 50$ ms and $\phi = 0.8$.

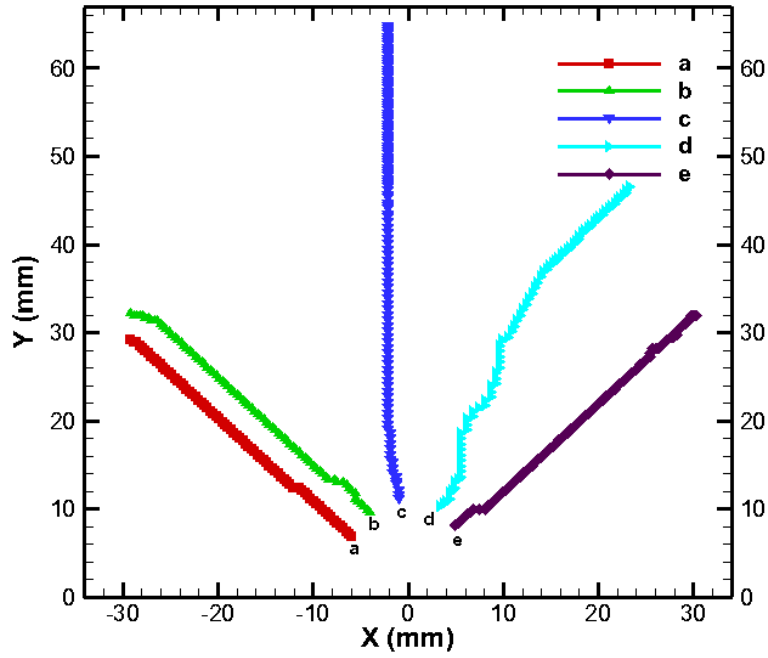


Figure 24. Pathlines of specified structures for $t = t_{\text{end}} + 50 \text{ ms}$ and $\phi = 1.0$.

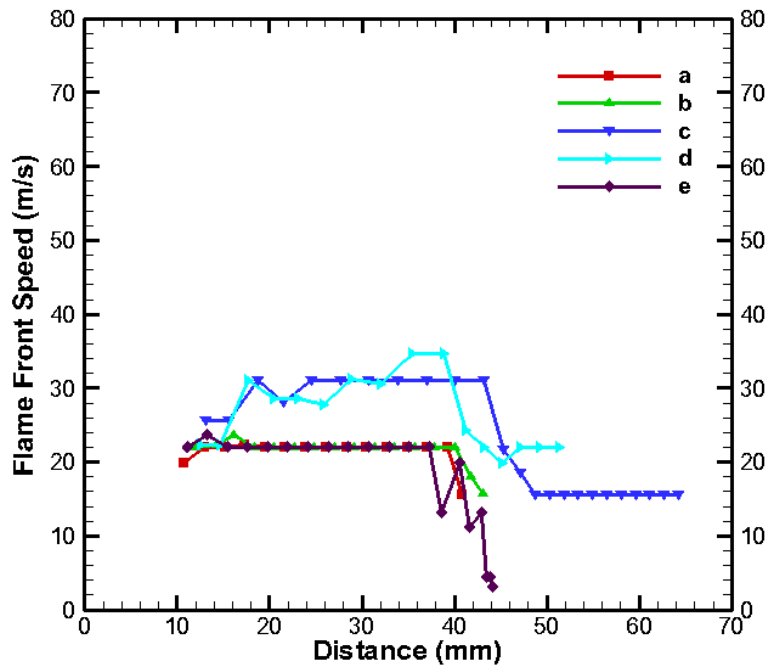


Figure 24a. Flame front speeds for corresponding pathlines for $t = t_{\text{end}} + 50 \text{ ms}$ and $\phi = 1.0$.

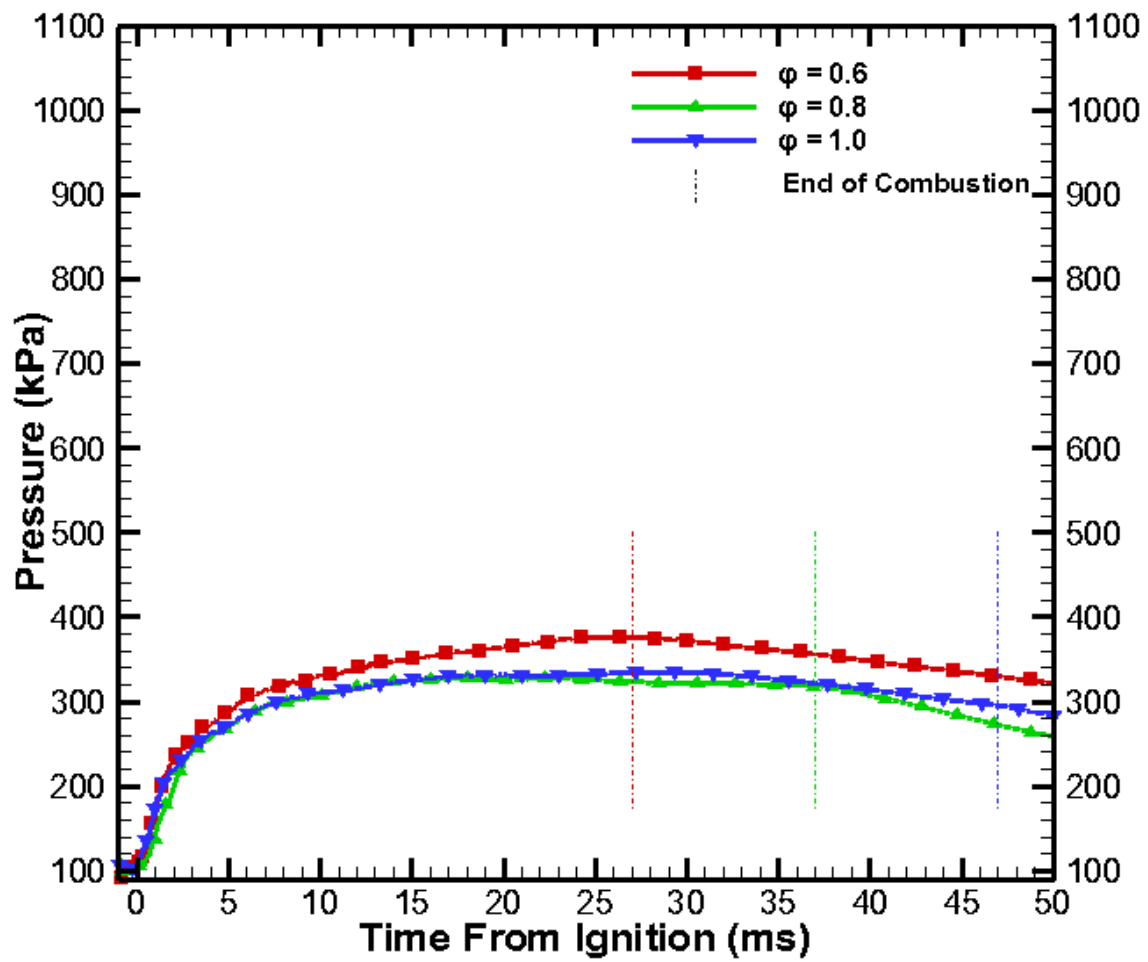


Figure 25. Chamber pressure at varying equivalence ratios for $t = 3$ ms.

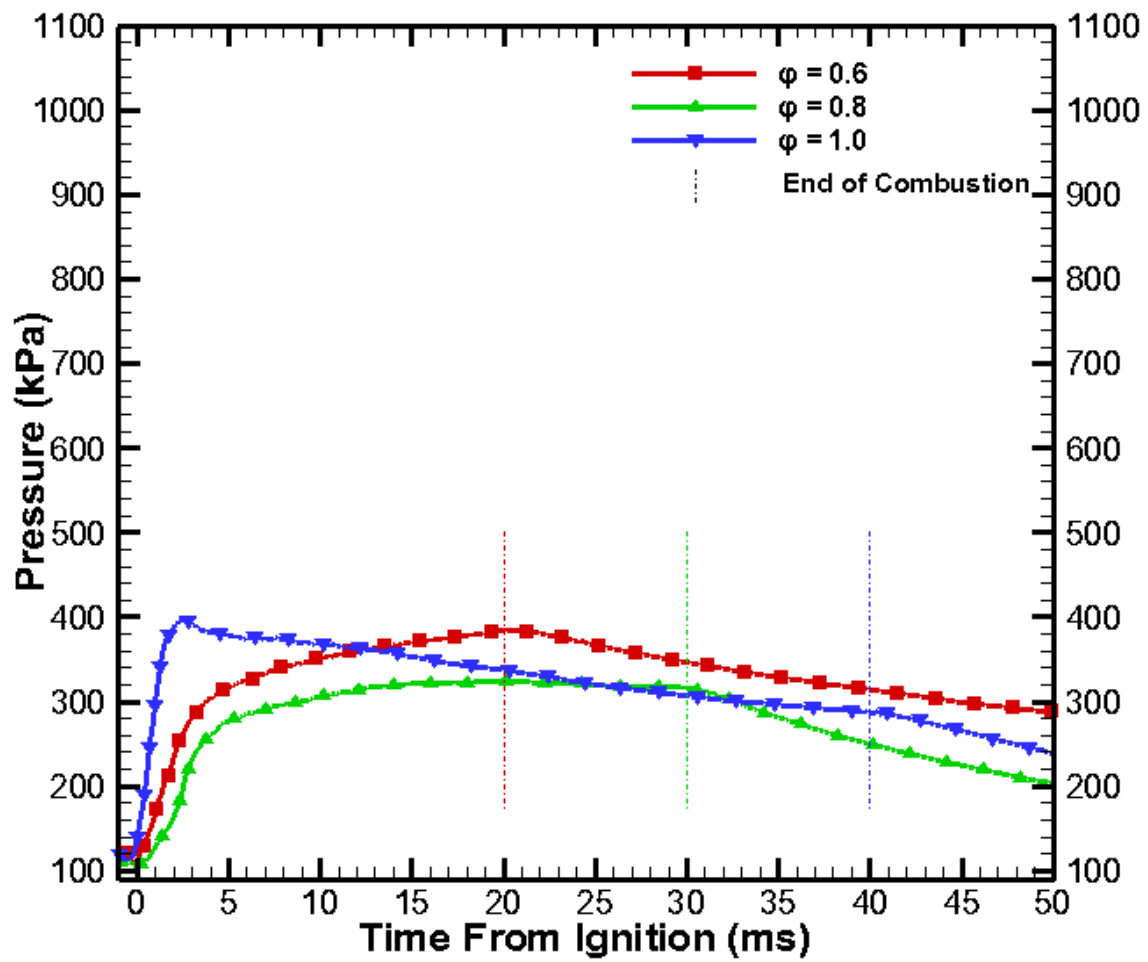


Figure 26. Chamber pressure at varying equivalence ratios for $t = 10$ ms.

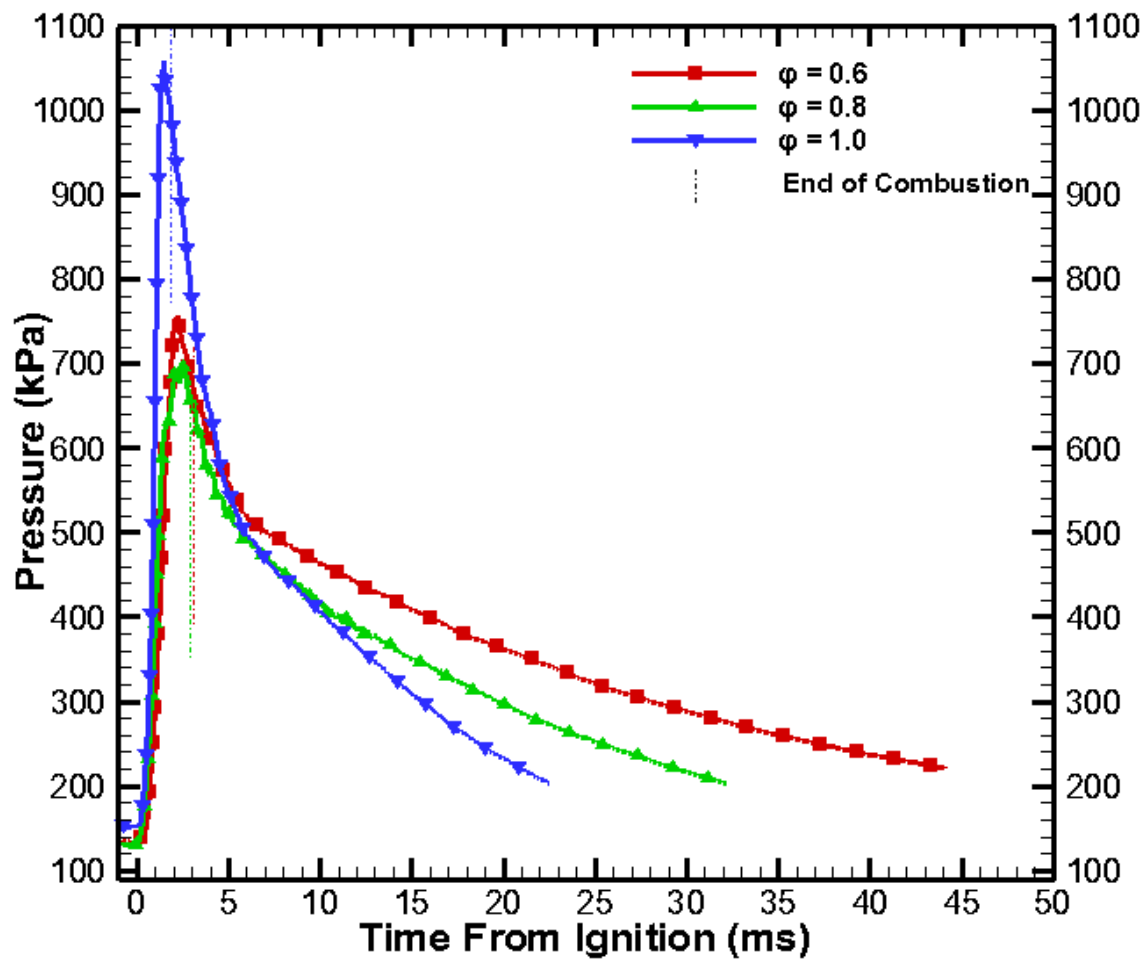


Figure 27. Chamber pressure at varying equivalence ratios for $t = t_{\text{end}}$.

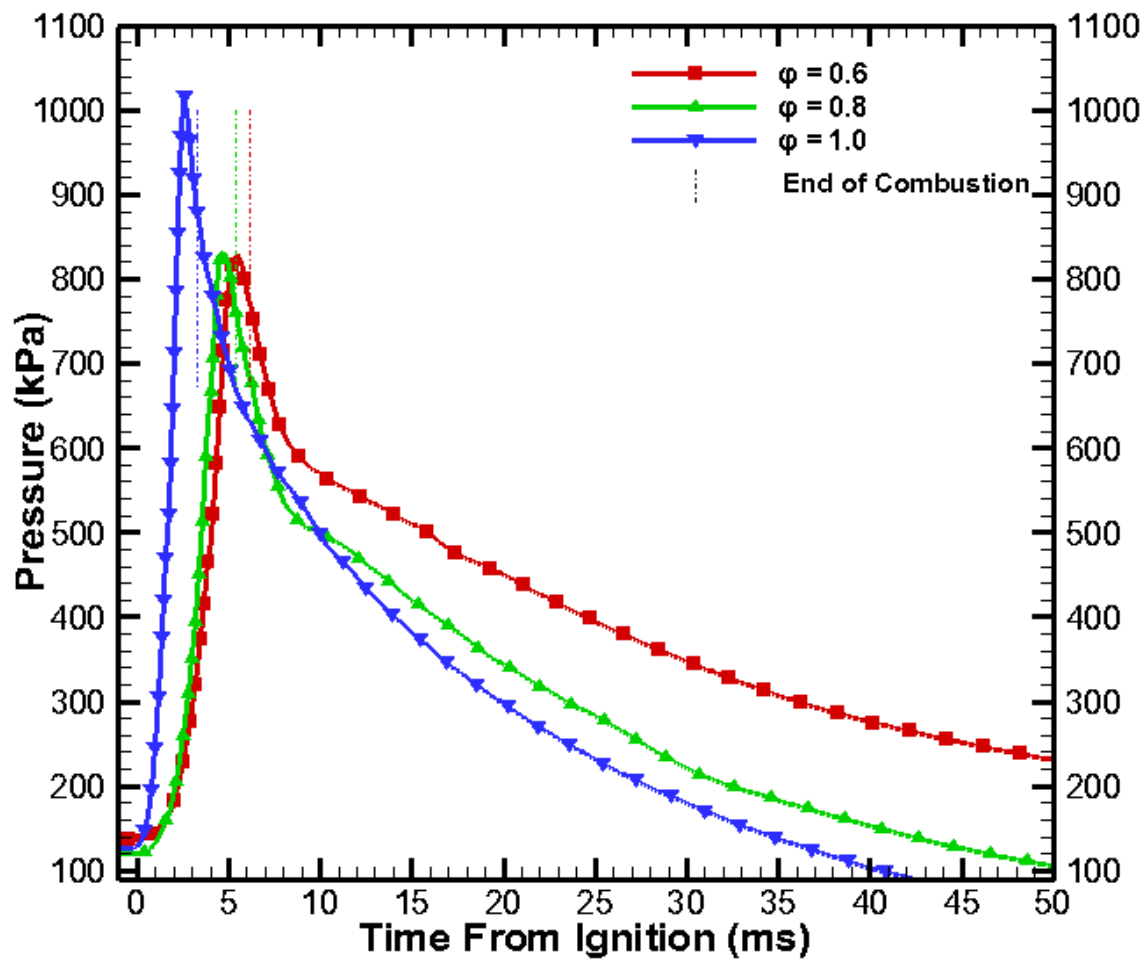


Figure 28. Chamber pressure at varying equivalence ratios for $t = t_{\text{end}} + 50$ ms.

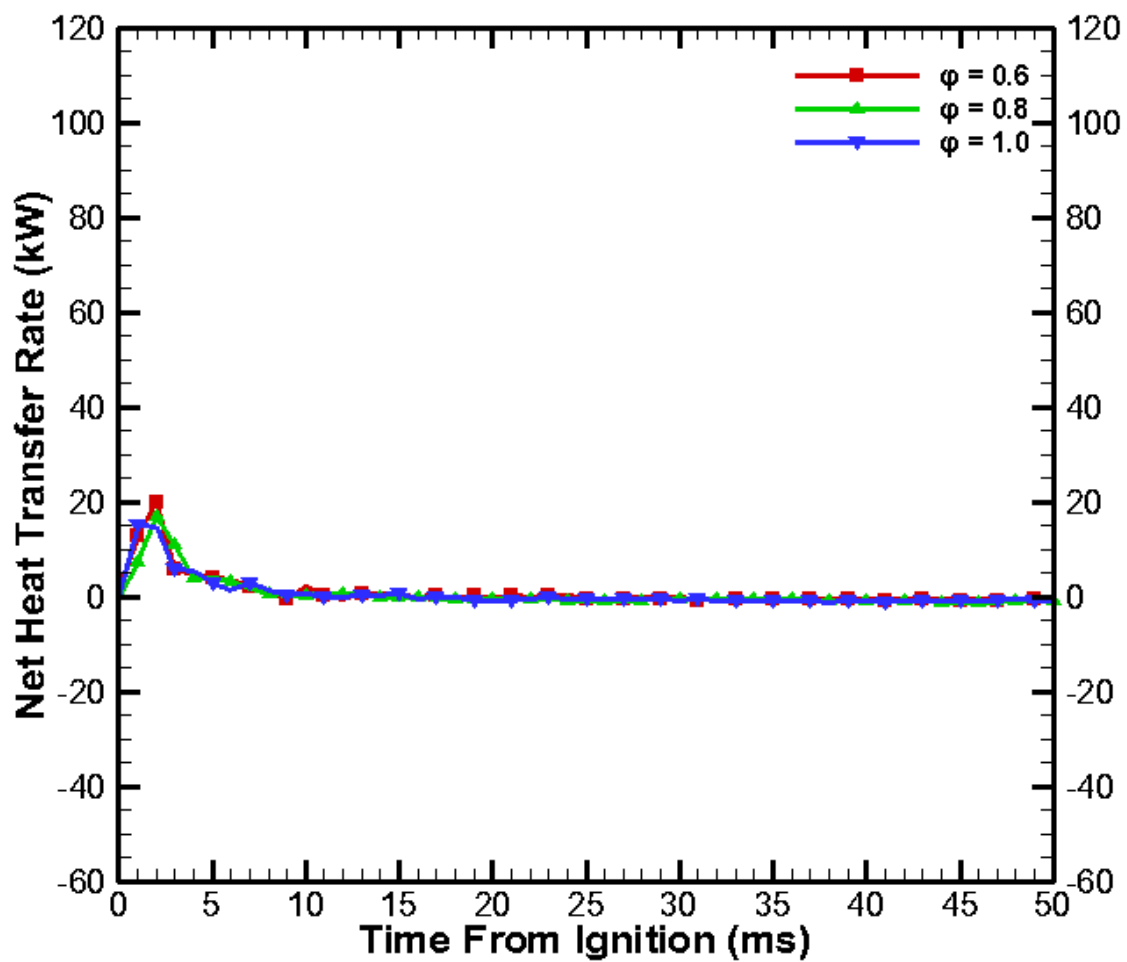


Figure 29. Net heat transfer rates at varying equivalence ratios for $t = 3$ ms.

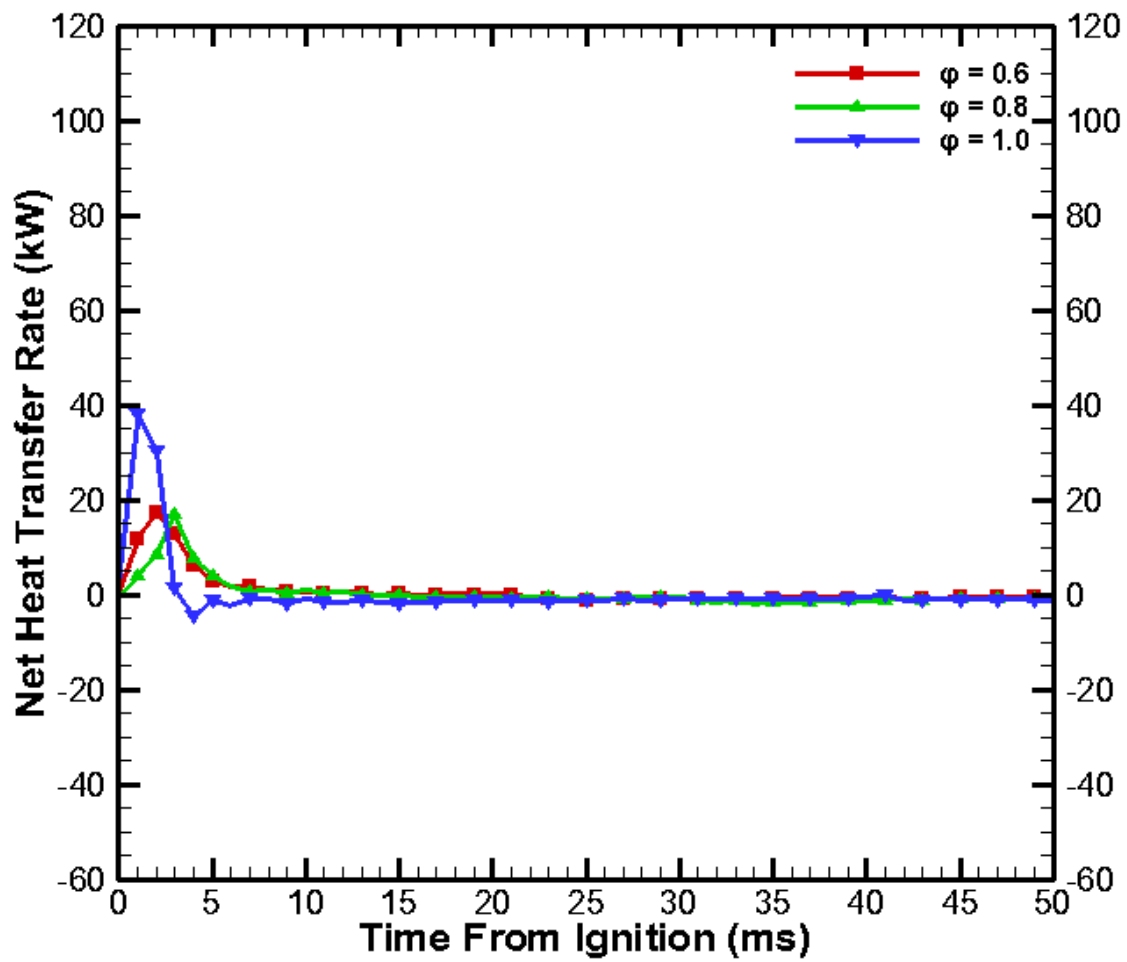


Figure 30. Net heat transfer rates at varying equivalence ratios for $t = 10$ ms.

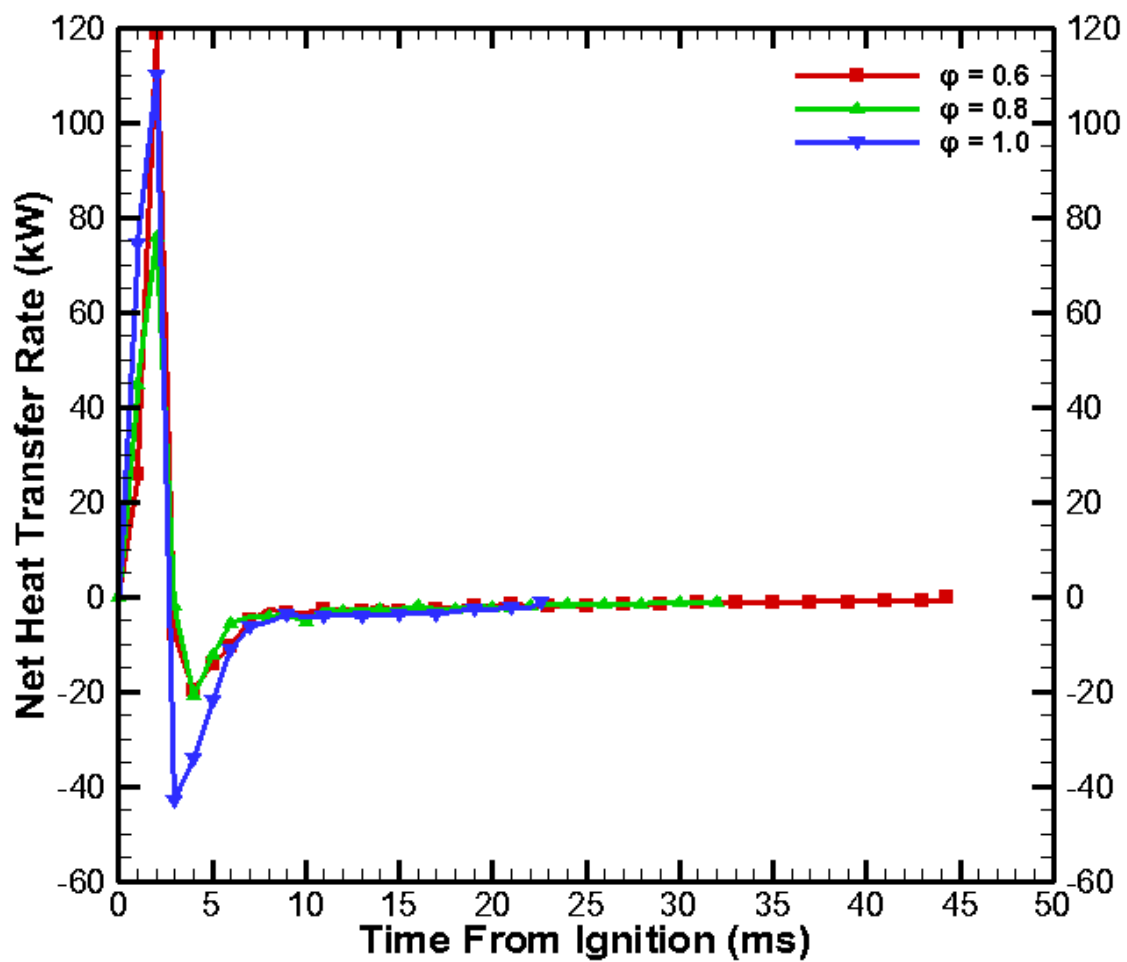


Figure 31. Net heat transfer rates at varying equivalence ratios for $t = t_{\text{end}}$.

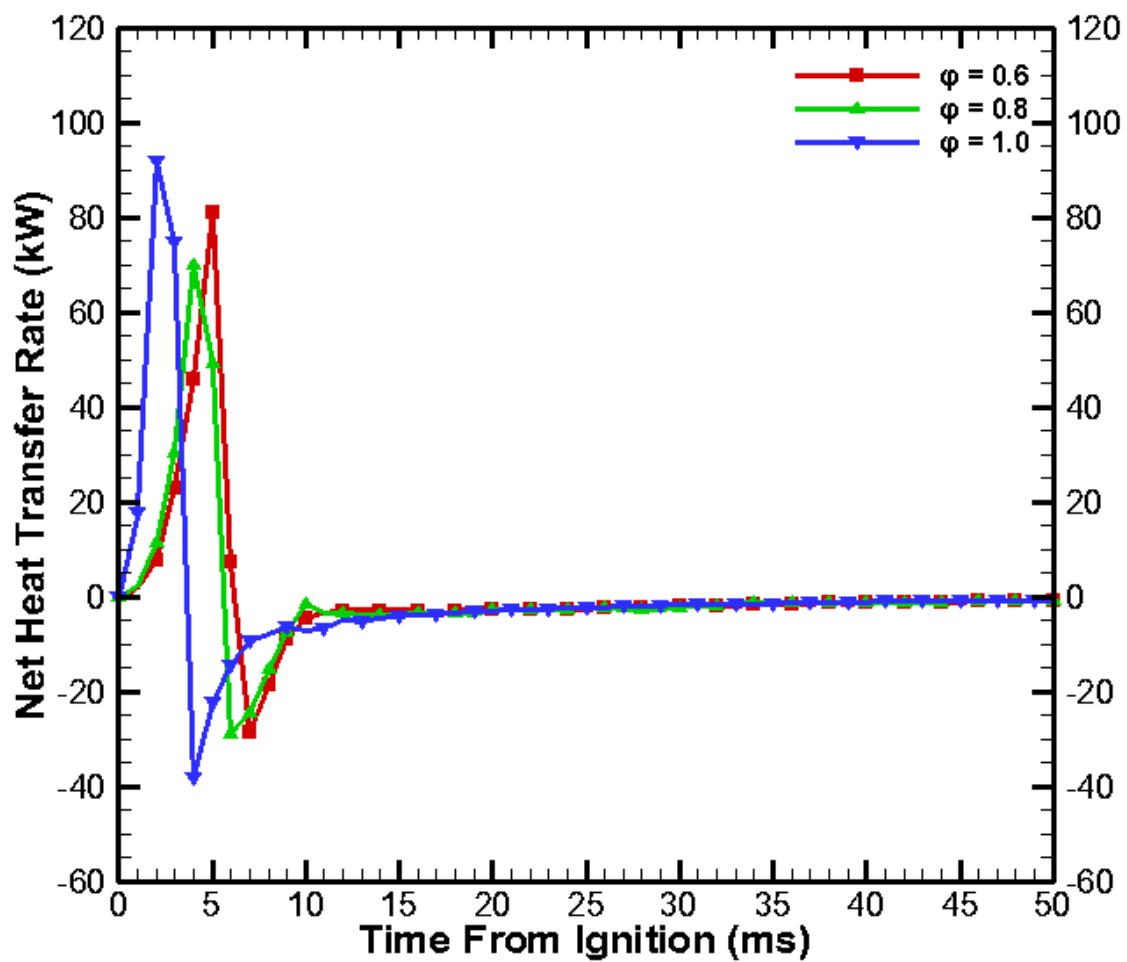


Figure 32. Net heat transfer rates at varying equivalence ratios for $t = t_{\text{end}} + 50$ ms.

CHAPTER 5

THE EFFECT OF METHANE/HYDROGEN FRACTIONS AND IGNITION TIME ON COMBUSTION IN A CONSTANT VOLUME COMBUSTION CHAMBER

Abstract

Methane and hydrogen at varying fractions were directly injected, separately, in a constant volume combustion chamber (CVCC) and turbulently mixed with quiescent air at atmospheric pressure. A spark plug, located diametrically opposite the methane injector, was used to ignite the methane/hydrogen/air mixture. Hydrogen fractions in the fuel and ignition times were varied to study the effects on flame structure, combustion time, flame front speed, chamber pressure, and net heat transfer rate. Rainbow Schlieren Deflectometry (RSD) technique was used to visualize the combustion processes. Color schlieren images were acquired at a frame rate of 50000 Hz and an exposure time of 19.8 μ s. Five fuels with 23% CH₄ – 77% H₂, 33% CH₄ – 67% H₂, 43% CH₄ – 57% H₂, 53% CH₄ – 47% H₂, and 63% CH₄ – 37% H₂, were investigated at two ignition times, ignition at the end of fuel injection and ignition 50 ms after the end of fuel injection. Results show that the fraction of hydrogen in the fuel and the time of ignition have significant effects on combustion properties. Increasing hydrogen fraction in fuel increased the flame front speed and decreased the combustion time. The peak chamber pressure and net heat transfer rate decreased when delaying ignition for a given fuel.

Introduction

Hydrogen has been studied for many decades for use as an alternative fuel source in internal combustion engines (ICEs) due to its desirable combustion properties. With water as its main product, other than the production of nitric oxides at higher equivalence ratios, hydrogen can be a clean fuel for the environment. Factors to consider when using hydrogen as an alternative fuel include whether to use it as a sole fuel source or in dual fuel mode, the method of injection, injection and ignition timing, the equivalence ratio, and other engine operation conditions.

Majority of hydrogen combustion research has focused on its use both as a primary fuel and more recently as a dual fuel for spark-ignited (SI) internal combustion engines. When using hydrogen in dual fuel mode, it has been used as an enrichment fuel to improve combustion. Hydrogen has been studied in dual fuel mode with fuels such as methane. The performance of a SI engine operating with methane can be improved significantly with the addition of small amounts of hydrogen [Karim et al., 1996; Bade Shrestha & Karim, 1999; Akansu S.O. et al., 2007; Ceper et al., 2009]. In a study of hydrogen addition on methane combustion in a quartz reactor by Zhao et al. [2008], hydrogen decreased ignition and burn off temperatures of methane at wide concentration ranges. The ignition and burn off temperatures could decrease to 45°C and 42°C respectively when the H₂/CH₄ ratio was 0.05 for 1 volume percent methane combustion and to 170°C and 180°C when the ratio was 2.5. Thurnheer et al. [2009] in a study using a naturally aspirated spark ignited engine with port fuel injection of methane with varying (5%, 10%, and 15%) percentages of hydrogen by volume found that increasing hydrogen percentages in this dual fuel blend decreases overall burn duration, particularly during the flame development, and leads to an increase in fuel conversion efficiency. The addition of 15%

hydrogen shortens the combustion duration during flame development by more than 15% compared to methane alone at a spark time that provides the best efficiency. Fuel conversion efficiencies increased by 0.7%, 1.6%, and 2.0% for hydrogen additions of 5%, 10%, and 15% respectively. Rao et al. [1983] reports an increase in thermal efficiency at full load using hydrogen/diesel fuels in a single cylinder, manifold injection, compression-ignition engine. The increase in efficiency was attributed to the high diffusion rate of hydrogen and higher flame propagation speeds which results in faster energy release rates. Results also show an increase in the maximum pressure and a decrease in exhaust temperature. At partial loads, the flame front did not propagate into all regions of the chamber leaving unburnt hydrogen which reduced thermal efficiency. Emissions of nitrogen oxide increased while hydrocarbon emissions decreased at all loads.

Recently, studies have been conducted on hydrogen use in compression-ignition (CI) internal combustion engines. In compression-ignition engines, hydrogen cannot be used as a sole fuel source due to its higher self-ignition temperature, 858K, and must be used in dual fuel mode. Hydrogen can be injected into a CI engine by different methods such as conventional port injection or by direct injection. CI engines enriched with hydrogen can produce higher thermal efficiency compared to a CI engine using diesel as a sole fuel source. Saravanan et al. [2008] conducted a study of a hydrogen-enriched diesel engine with varying hydrogen percentages (10%, 20%, 30%, 50%, 70% and 90%). Hydrogen was used to enrich the air and diesel to ignite the mixture in a stationary diesel engine. The hydrogen and air were mixed using a gas carburetor and then entered the inlet manifold. Conclusions were that 30% hydrogen addition is best for increasing brake thermal efficiency (BTE). BTE increased by 27.9 % for 30% hydrogen over the entire engine load range. BTE increased by 29.1% for 90% hydrogen addition but

engine knock occurred. As the hydrogen addition increased, the specific energy consumption (SEC) decreased. Particulate matter and smoke intensity decreased with an increase in hydrogen enrichment. Oxides of nitrogen decreased with leaner mixtures of hydrogen. Bari et al. [2010] added an H₂/O₂ mixture, by water electrolysis, to a conventional four-cylinder, direct injection diesel engine at varying total diesel equivalences. A load cell applied three power levels, 19kW, 22kW, and 28kW, to the engine which was running at constant rpm of 1500 rpm. Results show that hydrogen, due to its higher flame speed, enhances overall combustion and produces higher peak pressures near top dead center (TDC), thus increasing work. BTE increases were 2.6% (19kW), 2.9% (22kW), and 1.6% (28kW) for 6.1% H₂/O₂ total diesel equivalence addition, which resulted in fuel savings of 15.07%, 15.161%, and 14.96% respectively. Brake specific fuel consumption (BSFC) reduced by 7.3% (19kW), 8.1% (22kW), and 4.8% (28kW) for this 6.1% addition. Saravanan et al. [2009] report in a study of hydrogen addition in a hydrogen diesel engine that BTE at full load increases by 6% for port injection and 2% for manifold injection when compared to using diesel as a sole fuel source. BTE with hydrogen addition at 75% load increases to 21% for port injection and 18% for manifold injection. Results also show reductions in NO_x emissions at full load, reductions in smoke emissions at 75% load, and a reduction in carbon monoxide (CO) for the entire load spectrum. HC emissions, however, did increase for both injection methods at full loads.

Direct injection has been shown to aid in eliminating the abnormal combustion that occurs with the use hydrogen in spark-ignited systems. Direct injection, according to Antunes et al. [2009], is the preferred over port-injection when using hydrogen in CI engines as it allows better control over engine operation conditions. Antunes et al. also reports that hydrogen

addition by direct injection gives higher power to weight ratio, peaking at 14% higher than typical diesel-fuelled engines.

The objective of this research is to study combustion properties of methane/hydrogen combustion using air as the oxidizer in a constant volume combustion chamber. Fuels with varying hydrogen ratios were injected and ignited in the chamber by a spark-ignition system. Combustion time, flame front speed, chamber pressure, and net heat transfer rate were analyzed.

Experimental Setup

The experimental setup consists of a CVCC system and a high-speed RSD system as described below.

Constant Volume Combustion Chamber System

The test apparatus consisted of a CVCC with fuel injectors attached to a fuel supply system. The combustion chamber, shown photographically in Figure 1, is made from an aluminum block with a cylindrical opening drilled through it. This opening forms the volume of the combustion chamber and it has a diameter of 66.7 mm and a width of 31.8 mm. The combustion space is enclosed by optical windows located in recessed areas on both ends. Each optical window is a fused silica, single surface 1/10th wave optical flat (NT01-915) with a diameter of 76.2 +/- 1 mm and thickness of 19.05 +/- 1.5 mm. The optical flats are precision polished on one side to ensure accuracy and are pitch polished on the other side. The optical flats are held in place by aluminum collars (Figure 1) that are bolted by eight evenly spaced bolts to the outer surface of the combustion chamber.

Hydrogen and methane were supplied by compressed gas cylinders as shown in Figure 2. The hydrogen flowed through a test vessel system and a supply pressure regulator before reaching a fuel injector fixed along the side of the CVCC (see Figure 1). The methane flowed

through a supply pressure regulator before reaching a second fuel injector fixed at the top of the CVCC (see Figure 1). The fuel injectors are Hoerbiger hydrogen direct injectors that were calibrated prior to experimentation using the test vessel system. The fuel injectors are controlled by an electronic valve booster (Provebo) that is powered by a 13.8V DC single channel regulated power supply (MG Pro Series PS22). The Provebo's input signals are connected to two solid state relays that are used to ground power necessary for injector operation. The spark is created by a spark plug (Champion RV12YC6) fixed at the bottom center of the CVCC, diametrically opposite from the injector used for methane. The spark plug is fixed in a stick coil (Honda) that receives 13V from a DC power supply (TekPower). The two injectors, coil charging system, and spark triggering are connected to 5V output ports of a programmable logic controller (PLC) that is used to control the instruments and sequence events. The PLC (Keyence KV-24DTP) 24V power requirement is received from the TekPower DC power supply. A third channel of the TekPower DC power supply is a fixed 5V channel and is connected to the common supply port of the PLC. A 5V signal is sent to the PLC from the Digital I/O ports of a National Instrument's PCI Data Acquisition System (DAQ) with a BNC breakout box to initiate program execution. The fuel injector, coil charging, and spark triggering are sequenced and controlled by a program written using Ladder Logic Software that is downloaded to the PLC. Time constants are changed in the program to conduct ignition variation testing. The DAQ is also connected to a high speed camera, discussed in the following section. A program written in National Instrument's LabView software controls the sequencing of the PLC and the high speed camera.

A Kistler Type 6053CC60 piezoelectric pressure transducer calibrated for 0 to 150 bar with a sensitivity of 20.2 pC/bar is mounted along the lateral surface of the CVCC. It is used to collect pressure data while methane and hydrogen is injected into the chamber and during the

combustion process. The charge from the pressure transducer is amplified by a Kistler Type 5010 Dual Mode Charge Amplifier which is connected to the DAQ where pressure data is obtained.

Rainbow Schlieren Deflectometry System

Rainbow Schlieren Deflectometry, an optical technique to visualize density gradients in the flow field was utilized to acquire the necessary data. An inhomogeneous media, for example, hydrogen injected into air, has density gradients that lead to schlieren effects arising from refraction of light rays traveling through the medium. Schlieren effects can result from temperature gradients, mixing of gases of different densities, or high velocity flows. The RSD is an experimental technique to project light ray deflections or displacements in color to a viewing screen. The color schlieren images thus acquired can be quantitatively analyzed to obtain the local distributions of the density field.

Figure 3 illustrates the RSD setup implemented in this study. A beam of light was transmitted from a MCWHL2 LED assembly with a 6500K wavelength and an optical beam power range of 650 – 1300mW. The MCWHL2 is powered by a T-Cube (LEDD1B) LED Driver with a maximum output current of 1200 mA that has a single channel controller to vary LED intensity. The MCWHL2 is structurally housed by an aluminum prism located at the focal point of the collimating lens. The lens is a precision achromatic doublet lens that is 76.2 mm in diameter with a 500 mm focal length. It is coated with a 400-700 nm antireflection coating. The collimated beams or parallel light rays traveled through the test media contained in the CVCC as discussed previously. During experiments, the test media was composed of a non-homogeneous hydrogen-air mixture. After passing through the test media, refracted light rays passed through a

de-collimating lens, which refocused light beams onto a rainbow filter. The de-collimating lens has the same properties as the collimating lens, except its focal length is 750 mm. The rainbow filter is fixed at the focal point of the de-collimating lens. Light rays transmitted through the rainbow filter form an inverted image of the test medium captured by a Photron Fastcam SA5 ultra high speed camera. The camera is set to acquire color schlieren images at 50,000 frames per second with an exposure time of 19.8 microseconds.

Results and Discussions

The initial objective of this study was to combust methane in a constant volume combustion chamber with air enriched with hydrogen at varying ignition times with an equivalence ratio of 0.8. Hydrogen has a wide flammability range, 4% to 75% by volume, and low minimum ignition energy, 0.017 mJ in air. After enriching the air with hydrogen, even at lower fractions as compared to methane, combustion would occur in the chamber and the flame would quench before all of the methane could enter the chamber for ignition times before closing the methane injector. Thus, early ignition times, i.e. $t = 3$ ms, resulted in large fractions of unburned methane in the chamber as evidenced by acquired schlieren images. Igniting the mixture with ignition occurring after all of the supplied methane was in the chamber was also problematic. With the methane injector located diametrically opposite the spark plug, the methane jet would saturate the region around the spark plug and form ultra fuel-rich mixtures at the ignition source that could not sustain a flame. The flame would initiate and blow off. This problem occurred for varying methane/hydrogen fractions. Relocating the methane injector to the side of the combustion chamber did not solve the problem because methane, injected last, still created fuel rich inflammable mixtures near the spark plug. Delaying ignition to increase time for fuel/air mixing resulted in combustion. Thus, any ignitable hydrogen/air mixture would result in unburned methane if ignition occurred at a time prior to all supplied methane entering

the chamber and flame propagation throughout the chamber. For methane, which has a narrow flammability range of only 5 – 15% by volume in air, ultra fuel-rich mixtures formed around the ignition source causes an unsustainable flame.

Experimental procedure, due to these findings, was altered to inject methane into the chamber first and hydrogen injected second to eliminate the problem of flame quenching. With previous research focused on hydrogen/air combustion, the results from those studies will be used as a comparative basis.

Methane was directly injected at the top of the combustion chamber using a high pressure injector. The conically shaped methane jet flowed toward the spark plug, located diametrically opposite the injector, while turbulently mixing with the quiescent air in the chamber. After reaching the opposite end, the methane interacted with the lateral surface of the chamber and flowed upward, outside the fuel jet, turbulently mixing with the air in all areas of the chamber. Injector durations were set for varying methane percentages to acquire the desired mass for each experiment. At the close of the methane injector, the hydrogen injector, located on the side of the combustion chamber opened to supply hydrogen into the chamber. As the conically shaped hydrogen jet flowed horizontally to the opposite side of the chamber, it turbulently mixed with the methane/air mixture in the chamber. After reaching the opposite side, the hydrogen flowed back toward the hydrogen injector, outside the hydrogen jet region, while continually mixing with the methane/air mixture.

Methane and hydrogen were supplied to the combustion chamber at varying fractions to achieve an overall equivalence ratio, ϕ , of 0.8. Experiments were conducted for five cases: 23% CH₄ – 77% H₂, 33% CH₄ – 67% H₂, 43% CH₄ – 57% H₂, 53% CH₄ – 47% H₂, and 63% CH₄ – 37% H₂. Methane/hydrogen fractions were varied to determine the effects on combustion time,

flame front speed, chamber pressure, and heat transfer rates. Table 1 list the mass and injector duration for each fuel for the varying methane/hydrogen fractions.

CH ₄ /H ₂ Percent (by volume)	Mass of CH ₄ (kg)	Mass of H ₂ (kg)	Inj.Duration CH ₄ (ms)	Inj.Duration H ₂ (ms)
23/77	3.31E-06	1.38E-06	14	25
33/67	4.03E-06	1.02E-06	16	21
43/57	4.56E-06	7.56E-07	18	18
53/47	4.97E-06	5.51E-07	19	15
63/37	5.30E-06	3.89E-07	20	13

Table 1. Mass and injector duration for varying methane/hydrogen fractions.

Two ignition times, t , were experimented, one at the close of the hydrogen injector ($t = t_{\text{end}}$) and the other 50 ms after the close of the hydrogen injector ($t = t_{\text{end}} + 50$ ms). For both cases, all of the supplied fuels are in the chamber and thus, the overall equivalence ratio in the chamber is constant. However, the local equivalence ratio and fuel-jet generated turbulence vary differently for each case. Ignition at $t = t_{\text{end}}$ is characterized by greater turbulent activity and greater variations in localized air/fuel ratios as compared to ignition at $t = t_{\text{end}} + 50$ ms. The late ignition allows more time for fuel/air mixing leading towards a homogenized mixture, while dissipating the turbulence.

Flame Structure

For $t = t_{\text{end}}$, the flame structured and propagation is influenced by fuel-jet generated turbulence. For varying fuels, flame structure and propagation varies greatly. In Figure 4 for 23% CH₄ – 77% H₂, the flame propagated upward and expanding as the flame front distance

from the spark plug increased. However, as seen in Figure 6 for 63% CH₄ – 37% H₂, the flame propagated for some time towards the lateral surface of the chamber to the right of the spark plug. After propagating along half the right surface of the chamber, the flame propagates to the left and upward until reaching the opposite surface of the combustion chamber.

For $t = t_{\text{end}} + 50$ ms, the flame propagated upward in the combustion chamber in an expanding semi-spherical shape as seen in Figures 5 and 7. As the flame front approached the center of the combustion chamber, large combustion-generated turbulent structures can be seen in and following the flame. As the flame front distance from the spark plug increase further, combustion-generated turbulence is present only in the flame itself.

Combustion Duration and Flame Front Speed

Combustion duration shown in Figure 8 is the time from spark until there is no flame present in the chamber. As the hydrogen percentage of the fuel increases, the combustion time decreases. This result can be explained by the higher flame speed of hydrogen compared to methane. For ignition at $t = t_{\text{end}}$, combustion duration of 9 ms for 37% H₂ in fuel decreased to 4 ms for 77% H₂ in fuel. Huang et al. [2007], in a study of natural gas/hydrogen/air premixed combustion in a constant volume bomb, found that at a given equivalence ratio, combustion duration decreases as hydrogen fraction in the fuel blend increases. Wang et al. [2008] also concluded that combustion duration decreases as hydrogen fraction increases for homogeneous mixtures and fuel direct injection for under lean conditions. Combustion duration increased for late ignition times. For 37% H₂ in fuel, combustion duration of 9 ms at $t = t_{\text{end}}$ increased to 15 ms at $t = t_{\text{end}} + 50$ ms. Wang et al. also agrees as they found high turbulence in early ignition shortens combustion duration.

Pre-defined structures in schlieren images were used to compute streamlines and flame front speed. The analysis utilizes a cross-correlation technique where patterns of intensity variations are used to track initially defined flame structures in consecutive images. See Appendix H for further explanation. For each pathline defined, the flame front speed was calculated. Pathline examples for 4 cases are given in Figures 9-10 for 23% CH₄ – 77% H₂ and Figures 11-12 for 63% CH₄ – 37% H₂ at both ignition times. The flame front speeds for each pathline for the 4 test cases are also shown in the Figures 9-12. For the time interval between images of 20 μs and a pixel resolution of 3.1E-04 m/pixel, the flame front speed resolution was limited to 15.5 m/s per pixel. Thus, the flame front speed was computed by analyzing every fifth image which improved the resolution to 3.1 m/s. Flame front speeds are higher at $t = t_{\text{end}}$ than for $t = t_{\text{end}} + 50$ ms as shown in comparing flame front speed plots for the two ignition times at the same methane/hydrogen fraction. For example, flame front speeds in Figure 9a which average at 22 m/s are higher than flame front speeds in Figure 10a which average at 12 m/s where initial structures are in similar regions of the combustion chamber. This result agrees with combustion time, which is longer at the $t = t_{\text{end}} + 50$ ms for all methane/hydrogen fractions. The decrease in flame front speed for the delayed ignition times is due to the decrease in jet-generated turbulence as evident in schlieren images. Flame front speed also increases as the hydrogen fraction increases. Comparing Figures 9(a-e) to Figures 11(a-e) shows that flame front speeds at the higher hydrogen fraction (77% H₂) are greater than those at the lower hydrogen fraction (37% H₂). Again result agrees with the decrease in combustion time as the hydrogen fraction increase for each ignition time as verified in Figure 8.

Chamber Pressure

Chamber pressure for varying fractions at $t = t_{\text{end}}$ are the first graphs shown in Figures 13-

17. Pressure rapidly increases and peaks to $P_{\max} = 847$ kPa, 963 kPa, 982 kPa, 954 kPa, and 919 kPa for 77% H_2 , 67% H_2 , 57% H_2 , 47% H_2 , and 37% H_2 respectively within 5 ms after ignition. Chamber pressure for varying fractions at $t = t_{\text{end}} + 50$ ms are shown in Figures 13-17. Pressure, as with the $t = t_{\text{end}}$ cases, rises rapidly and peak at $P_{\max} = 835$ kPa, 869 kPa, 838 kPa, 832 kPa, and 798 kPa for 77% H_2 , 67% H_2 , 57% H_2 , 47% H_2 , and 37% H_2 respectively within 10 ms after spark. Peak pressure is followed by a decrease in pressure as heat is transferred to the chamber wall. Rates of pressure drop are lower than rates of pressure rise, as shown in the figures, as slopes of pressure drop is lower than slopes of pressure rise. Similar peak pressures suggest that varying hydrogen fractions at $\phi = 0.8$ have minor effects on pressure.

Similar pressure peaks can be attributed to similar adiabatic flame temperatures for the two fuels, $T_{\text{adiabatic}} = 2483$ K for H_2 , and $T_{\text{adiabatic}} = 2223$ K for CH_4 for stoichiometric combustion. Variations in the total amount of heat released inside the chamber, assuming complete combustion, by the fuels is comparable for all cases. Using the lower heating value, LHV, of each fuel, $LHV_{H_2} = 121000$ kJ/kg and $LHV_{CH_4} = 50000$ kJ/kg, and the masses of each fuel, the total amount of heat released during combustion is 333 J for 77% H_2 , 326 J for 67% H_2 , 320 J for 57% H_2 , 316 J for 47% H_2 , and 312 J for 37% H_2 . Huang et al. [2007] found small differences in maximum pressure at varying hydrogen fractions at $\phi = 1.0$. Huang et al. attributed the small differences to similar volumetric heat releases by natural gas (3132 kJ/m³) and hydrogen (3022 kJ/m³) at $\phi = 1.0$. They also found that the time in which the peak pressure is reached is delayed as the hydrogen fraction in the fuel blend is decreased. This indicated that increasing the hydrogen fraction in the fuel blend increases the flame propagation speed. Huang et al. also showed that as equivalence ratios vary from 1.0, differences in peak pressures increase. However, at $\phi = 0.8$, peak pressures in their test varied from near 600 kPa to near 700 kPa. The

difference in peak pressures for their experiments is similar to the differences in peak pressures for these experiments.

Observing pressure curves for the two ignition time for a given hydrogen fraction shows that the rate of pressure rise is greater for $t = t_{\text{end}}$ than for $t = t_{\text{end}} + 50$ ms. This results in the increase in time for peak pressure to occur after spark for $t = t_{\text{end}} + 50$ ms that was mentioned earlier and is due to the decrease in turbulent activity in the chamber which also results in lower flame front speeds. This result is consistent with Wang et al. [2008], as they concluded that advancing ignition timing increases maximum cylinder pressure, rate of pressure rise, mean gas temperature, and heat release rate. Comparing peak pressures at a given hydrogen fraction for the two ignition times suggest that a decrease in turbulence, which is the major difference between the two times, leads to a decrease in peak pressure. This difference is especially notable at lower hydrogen fractions where a pressure difference by as much as 144 kPa is observed at identical hydrogen fractions. This result is consistent with Wang et al. [2008], as their results showed that high turbulence in early ignition increases the rate of pressure rise and that turbulence from fuel direct injection gets higher peak pressures.

Net Heat Transfer Rate

The net heat transfer rate was calculated from chamber pressure data. Average chamber temperature (T) was found using the ideal gas law. Chamber net heat transfer rate (Q) was found using $Q = m \times C_v \times \frac{dT}{dt}$ and the specific heat, C_v , was calculated by first using a third order polynomial to calculate C_p and then using $\frac{C_p}{C_v} = 1.4$ for air to find C_v . Figures 18-22 represent the net heat transfer rates for varying fractions at the two ignition times.

Net heat transfer rates for varying methane/hydrogen fractions for $t = t_{\text{end}}$ are the first graphs shown in Figures 18-22. Net heat transfer rate is characterized by a rapid increase to a

peak value followed by a decrease at a rate greater than that of the increase as evident in slopes. Peak net heat transfer rates are $Q_{\max} = 139$ kW, 212 kW, 219 kW, 183 kW, and 138 kW for 77% H₂, 67% H₂, 57% H₂, 47% H₂, and 37% H₂ respectively. When net heat transfer rates become negative near the end of combustion, the flame front has propagated, for the higher hydrogen percentages (77%, 67%, and 57%), to the top of the combustion chamber. For the lower hydrogen percentages (47% and 37%) the flame front has propagated over half the distance of the combustion chamber. Lower percentages of hydrogen have lower flame front speeds which contribute to the flame front propagation distance being lower than that for the higher percentages. For all methane/hydrogen percentages, maximum net heat transfer occurs at the same time as maximum chamber pressure.

Net heat transfer rates for varying methane/hydrogen fractions for $t = t_{\text{end}} + 50$ ms are shown in Figures 18-22. Peak amounts are $Q_{\max} = 81$ kW, 85 kW, 77 kW, 60 kW, and 45 kW for 77% H₂, 67% H₂, 57% H₂, 47% H₂, and 37% H₂ respectively. Flame front propagation is similar to that of $t = t_{\text{end}}$ whereas the flame front has reached the top of the chamber for 77% H₂, 67% H₂, and 57% H₂ but has not reached the top of the chamber for 47% H₂ and 37% H₂ at the time the net heat transfer rates drops to negative values. This is again due to lower flame front speeds at the lower hydrogen fractions. For both times, combustion continues after peak net heat transfer rates are reached, however, heat transfer to the chamber wall dominates heat generation by the fuel and net heat transfer rates are negative. Maximum net heat transfer rates occur at the same time as maximum chamber pressure. Net heat transfer rates for $t = t_{\text{end}} + 50$ ms are significantly lower than $t = t_{\text{end}}$ for each methane/hydrogen fraction and follows the trend of peak pressures. This is attributable to the decrease in fuel-jet turbulence for the later ignition time.

Conclusions

Methane and hydrogen at varying fractions were directly injected at separate times into a constant volume combustion chamber and ignited at two ignition times, at the end of fuel injection, and 50 ms after the end of fuel injection to study the effect of varying percentages on combustion processes including combustion time, flame front speed, chamber pressure, and net heat transfer rate.

Combustion durations increased significantly from ignition at the end of fuel injection to ignition 50 ms after the end of fuel injection for the same methane/hydrogen fractions. Combustion duration was significantly affected by the hydrogen fractions in the fuel for the same ignition time. Flame front speed increases as the hydrogen fraction in the fuel increases. Ignition time has a significant effect on chamber pressure and peak pressures decreased significantly at a given methane/hydrogen fraction from $t = t_{\text{end}}$ to $t = t_{\text{end}} + 50$ ms. Hydrogen fractions as well as ignition times have significant effects on rates of net heat transfer as evident by significant variations in net heat transfer for varying hydrogen fractions and varying ignition times.

Acknowledgments

Tanisha Booker was supported by the Graduate Assistance in Areas of National Need (GAANN) program of the U.S. Department of Education.

References

- Akansu S.O., Kahraman N., Ceper B. Experimental study on a spark ignition engine fuelled by methane-hydrogen mixtures. *Int. J. Hydrogen Energy* 32 (2007) 4279-4284.
- Antunes J., Mikalsen R., Roskilly A. An experimental study of a direct injection compression ignition hydrogen engine. *Int. J. Hydrogen Energy* 34 (2009) 6516-6522.
- Bade Shrestha S.O., Karim G.A. Hydrogen as an additive to methane for spark ignition engine applications. *Int. J. Hydrogen Energy* 24 (1999) 577-586.

- Bari S., Esmaeil M. Effect of H₂/O₂ addition in increasing thermal efficiency of a diesel engine. *Fuel* 89 (2010) 378-383.
- Ceper B.A., Akansu S.O., Kahraman N. Investigation of cylinder pressure for H₂/CH₄ mixtures at different loads. *Int. J. Hydrogen Energy* 34 (2009) 4855-4861.
- Huang Z., Zhang Y., Zeng K., Liu B., Wang Q., Jiang D. Natural Gas-Hydrogen-Air Premixed Mixture Combustion with a Constant Volume Bomb. *Energy Fuels* 21 (2007) 692-698.
- Karim G.A., Wierzba I., Al-Alousi Y. Methane-Hydrogen Mixtures As Fuels. *Int. J. Hydrogen Energy* 21 (1996) 625-631.
- Rao B., Shrivastava K., and Bhakta H. Hydrogen For Dual Fuel Engine Operation. *Int. J. Hydrogen Energy* 8 (1983) 381-384.
- Saravanan N., Nagarajan G. An experimental investigation of hydrogen-enriched air induction in a diesel engine system. *Int. J. Hydrogen Energy* 33 (2008) 1769-1775.
- Saravanan N., Nagarajan G. Experimental Investigation in Optimizing the Hydrogen Fuel on a Hydrogen Diesel Dual-Fuel Engine. *Energy Fuels* 23 (2009) 2646-2657.
- Thurnheer T., Soltic P., Eggenschwiler D. S.I. engine fuelled with gasoline, methane and methane/hydrogen blends: Heat release and loss analysis. *Int. J. Hydrogen Energy* 34 (2009) 2494-2503.
- Wang, J., Huang Z., Liu B., Zeng K., Yu J., Jiang D. Effect of ignition timing and hydrogen fraction on combustion and emission characteristics of natural gas direct-injection engine. *Front. Energy Power Eng. Chin.* 2 (2008) 194-201.
- Wang, J., Huang Z., Miao H., Wang X., Jiang D. Characteristics of direct injection combustion fuelled by natural gas-hydrogen mixtures using a constant volume vessel. *Int. J. Hydrogen Energy* 33 (2008) 1947-1956.
- Zhao K., Cui D., Xu T., Zhou Q., Hui S., Hu H. Effects of hydrogen addition on methane combustion. *Fuel Process. Technol.* 89 (2008) 1142-1147.

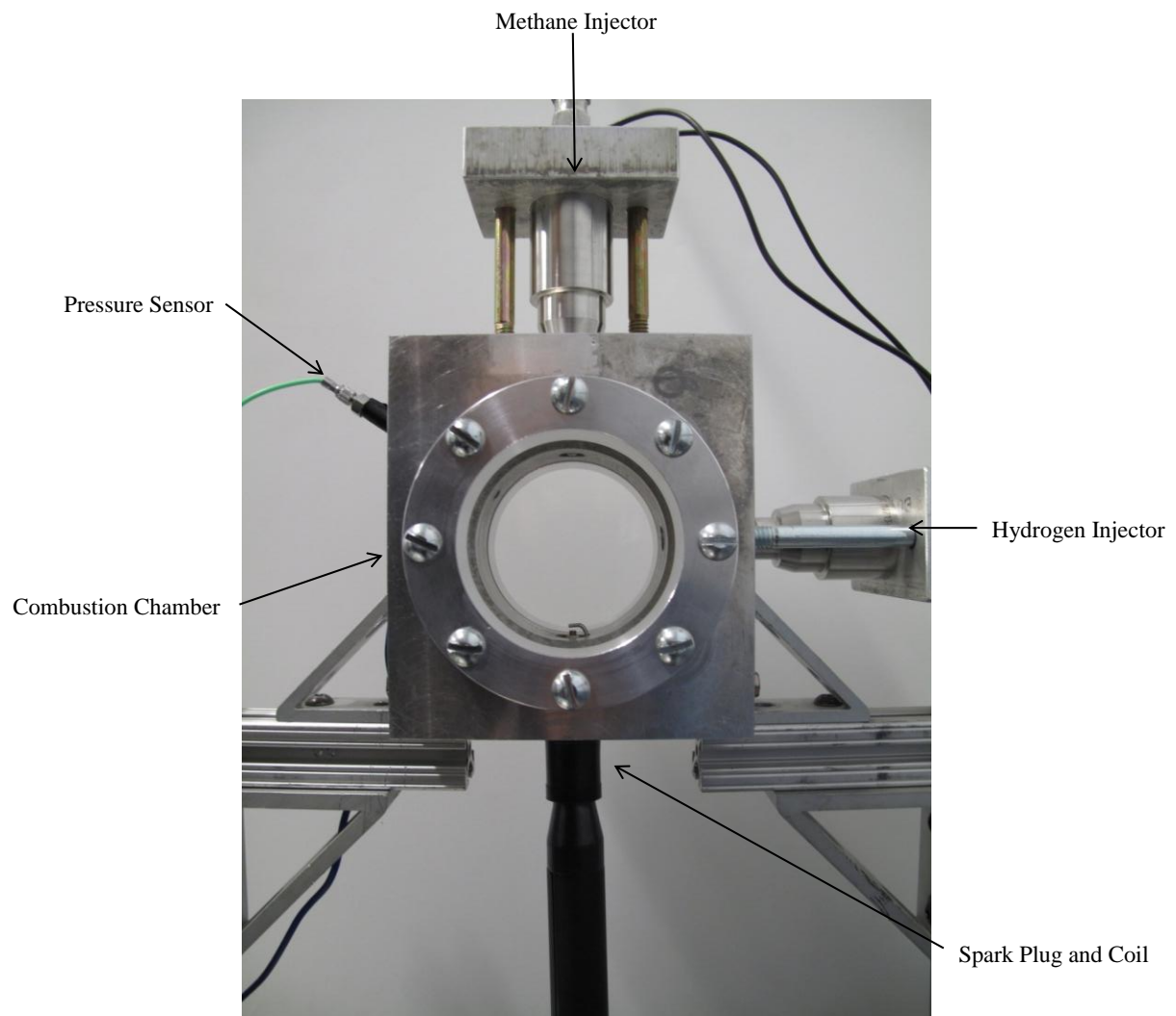


Figure 1. Combustion Vessel.

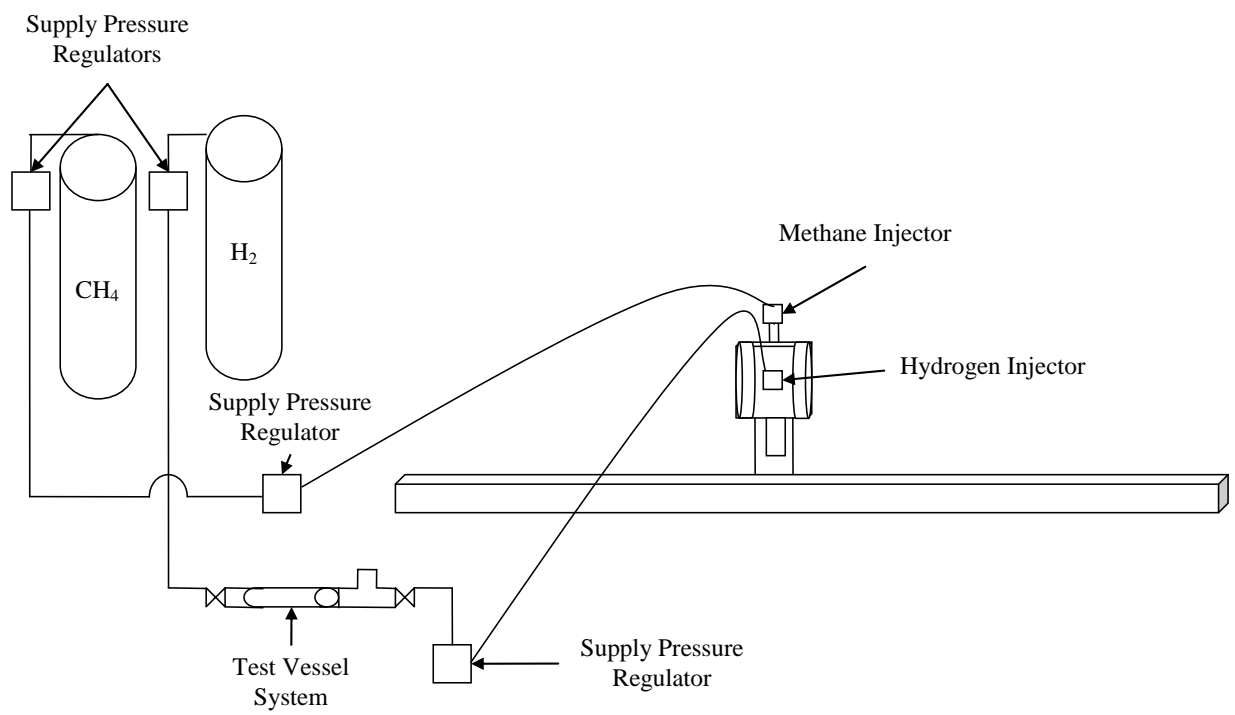


Figure 2. Fuel Flow System.

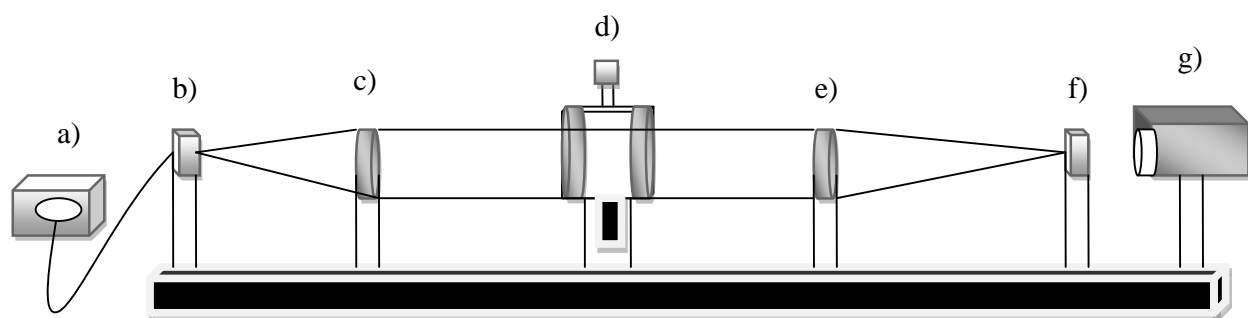


Figure 3. Rainbow Schlieren Deflectometer; a) Illuminator, b) Aperture, c) Collimating Lens, d) Test Media (Combustion Chamber), e) Decollimating Lens, f) Rainbow Filter, and g) High Speed Camera.

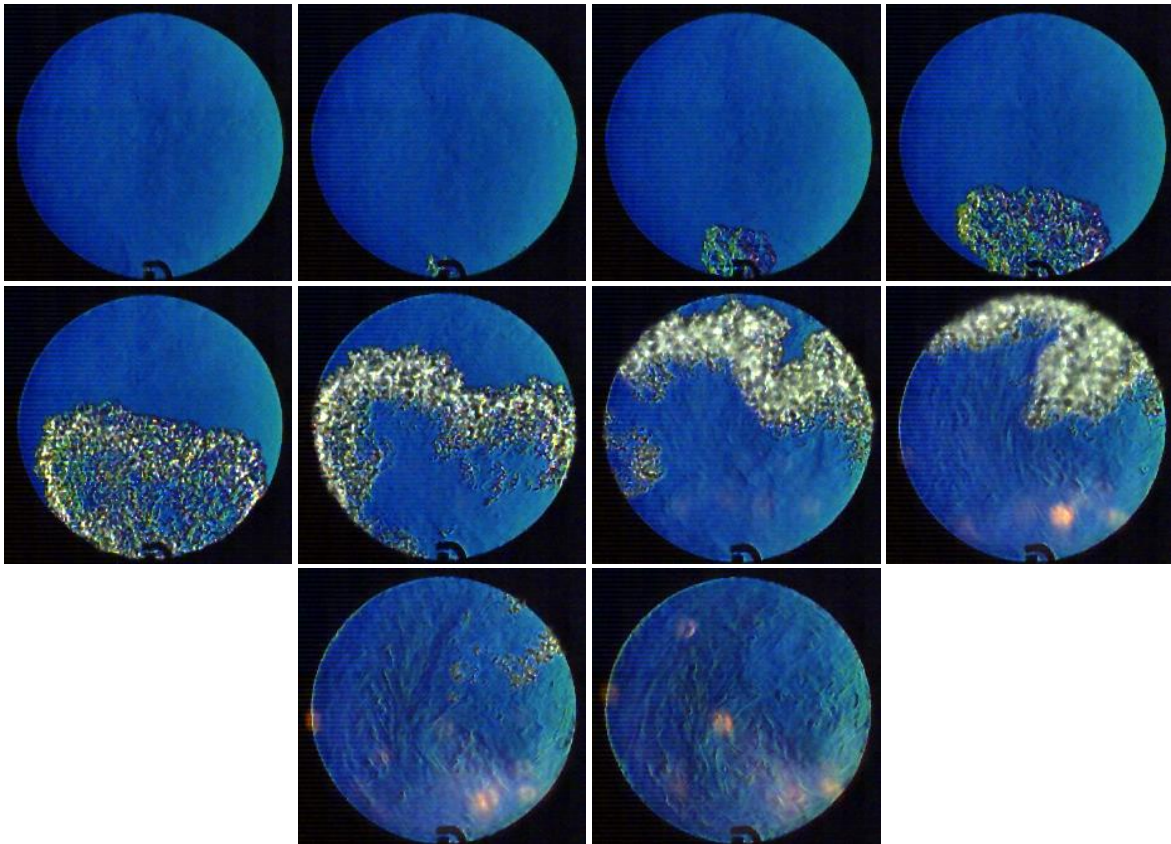


Figure 4. Schlieren images (500 μ s intervals) for 23% CH₄ – 77% H₂ for $t = t_{\text{end}}$.

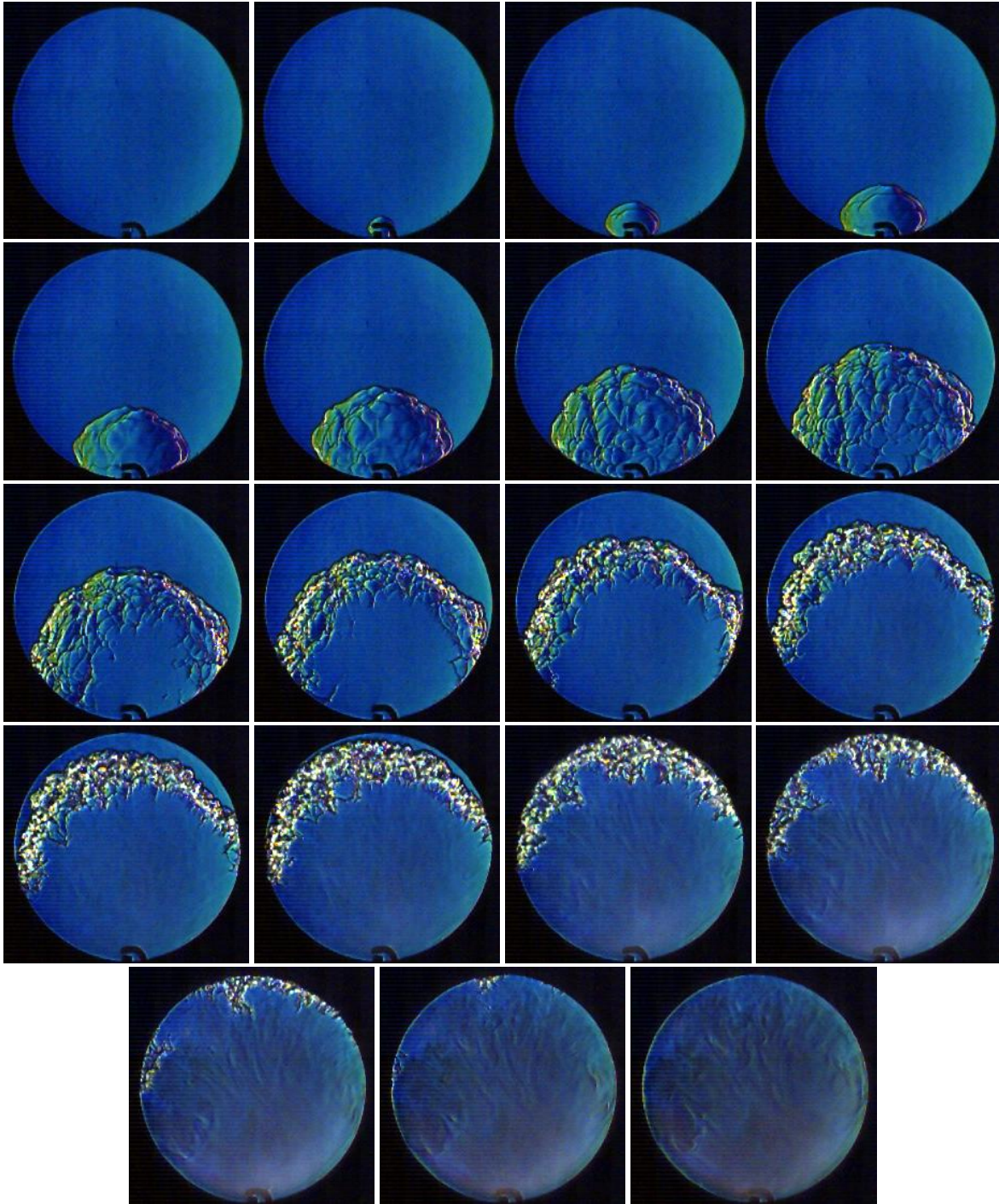


Figure 5. Schlieren images (500 μ s intervals) for 23% CH₄ - 77% H₂ for $t = t_{\text{end}} + 50$ ms.

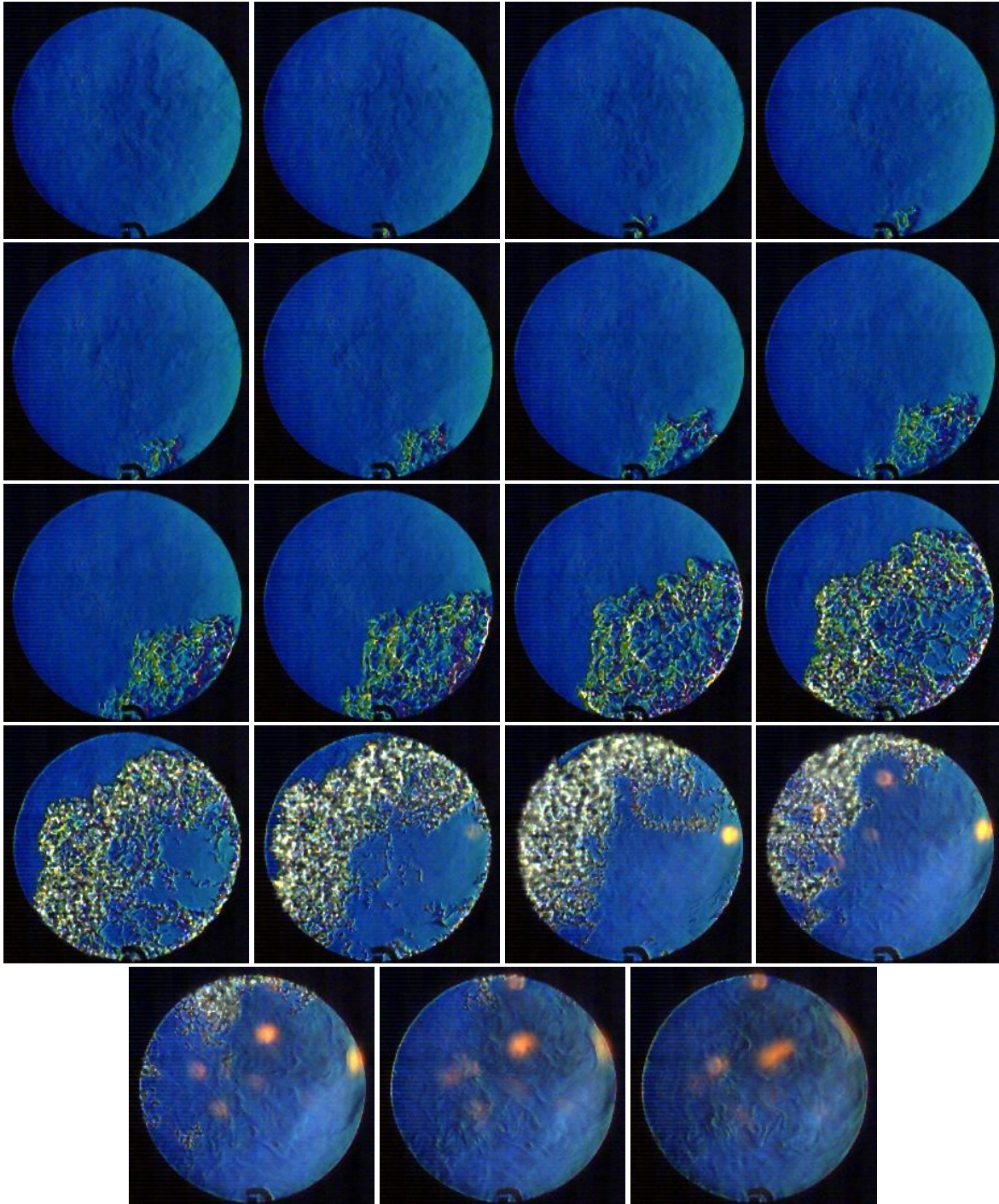


Figure 6. Schlieren images ($500 \mu\text{s}$ intervals) for $63\% \text{CH}_4 - 37\% \text{H}_2$ for $t = t_{\text{end}}$.

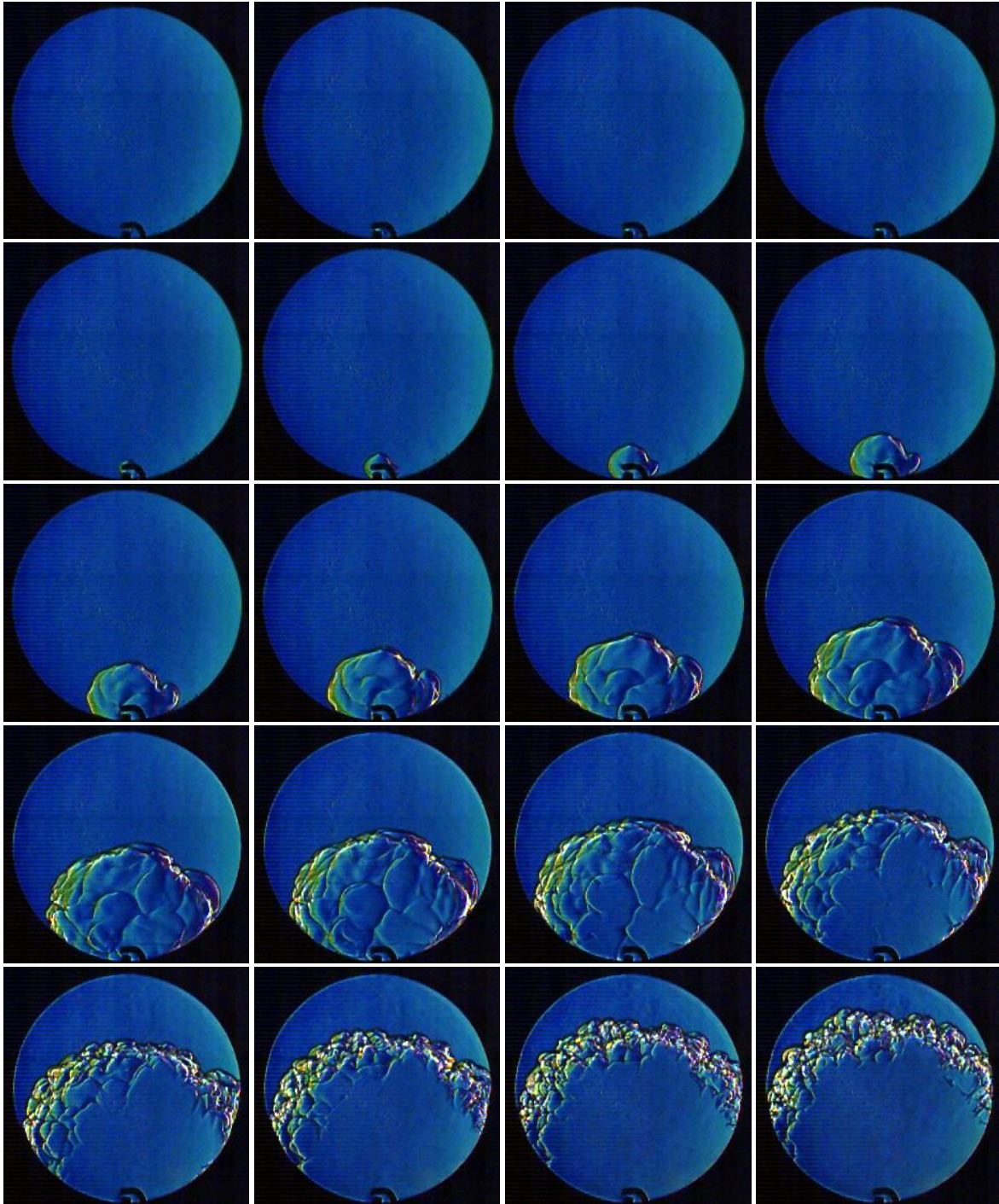


Figure 7. Schlieren images ($500 \mu\text{s}$ intervals) for 63% CH_4 – 37% H_2 for $t = t_{\text{end}} + 50 \text{ ms}$.

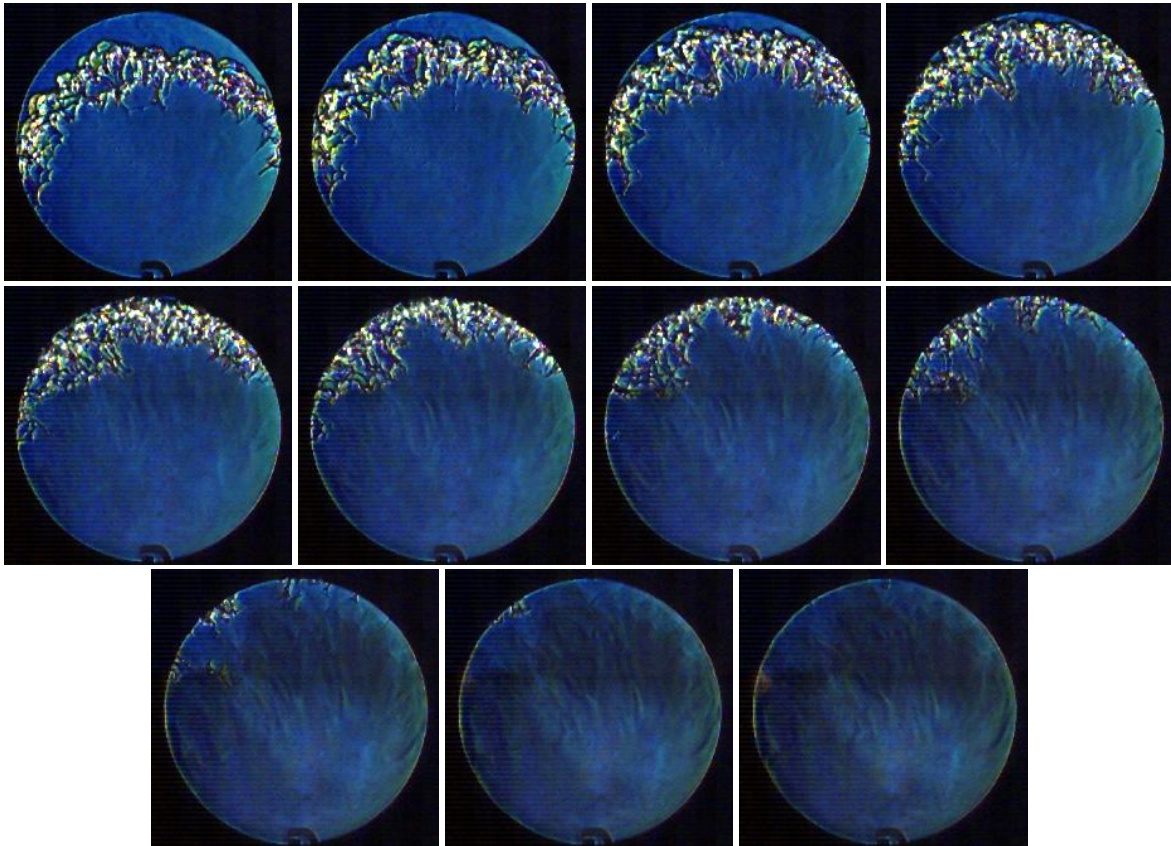


Figure 7. Schlieren images (500 μ s intervals) for 63% CH₄ – 37% H₂ for $t = t_{\text{end}} + 50$ ms (continued).

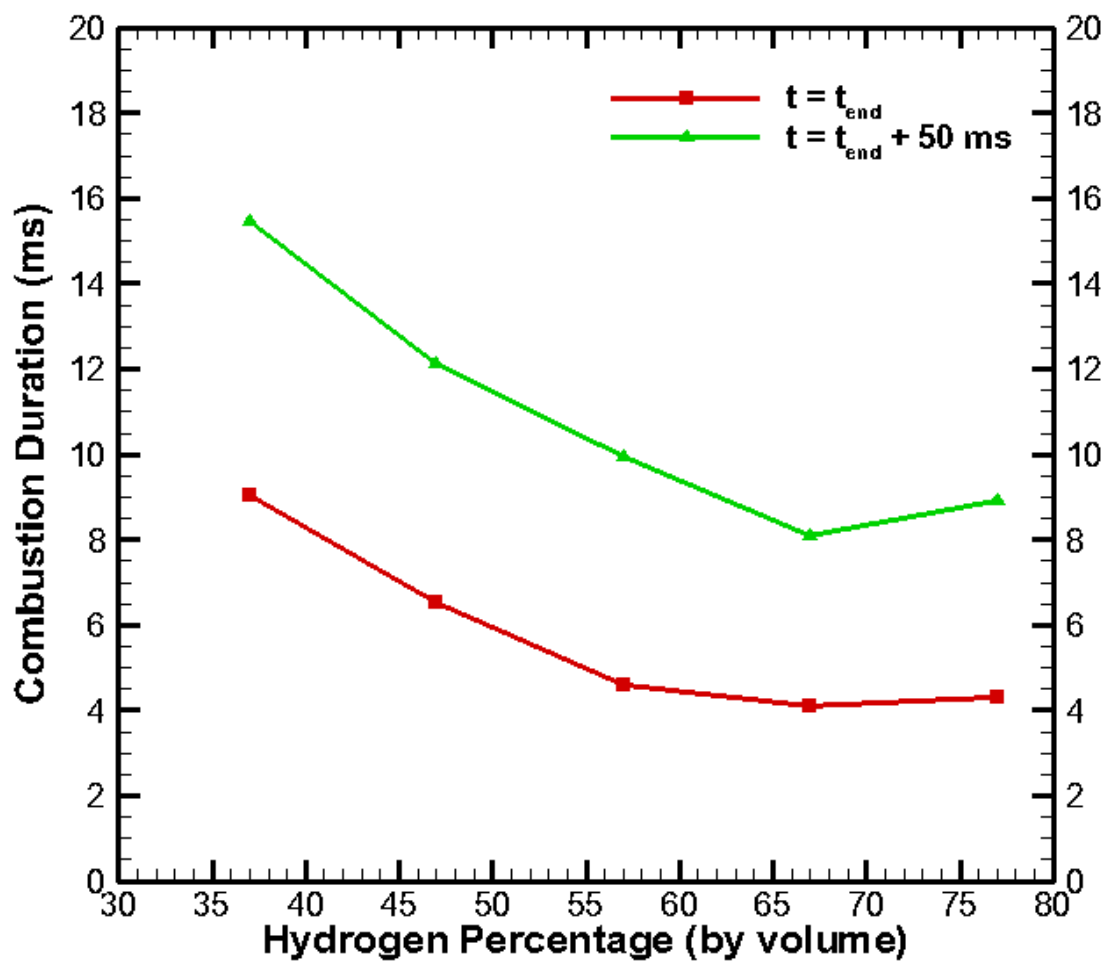


Figure 8. Combustion Duration For Varying Ignition Times.

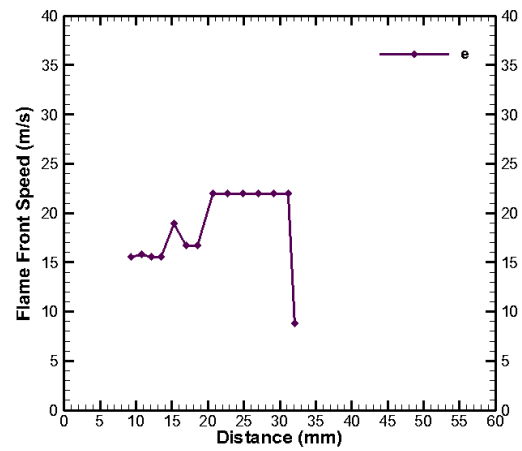
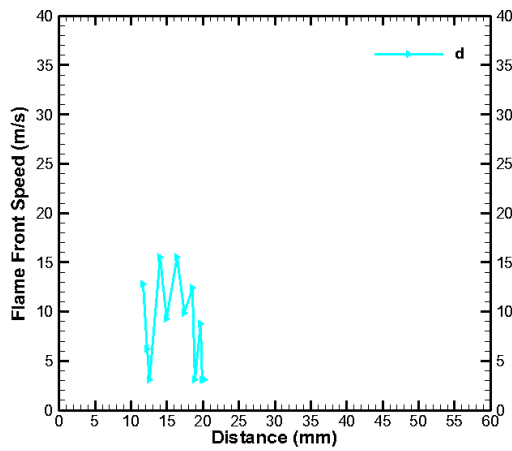
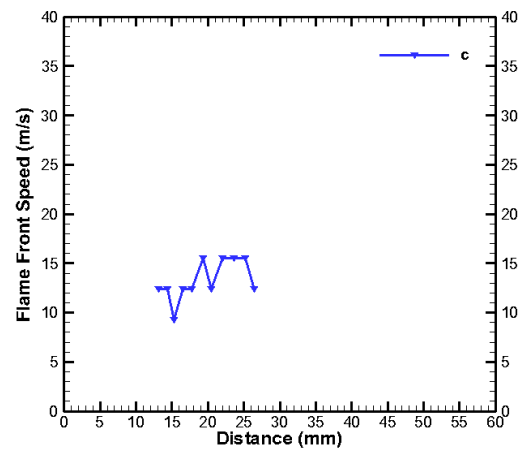
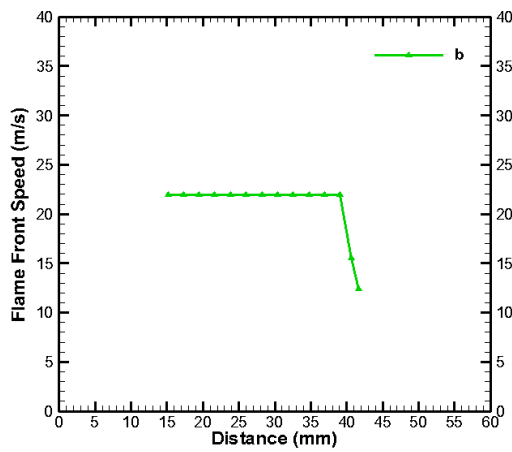
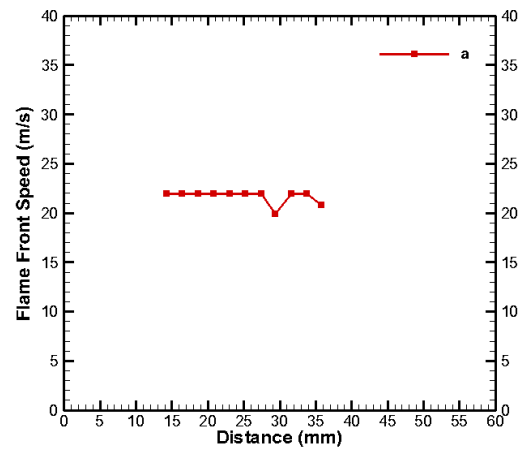
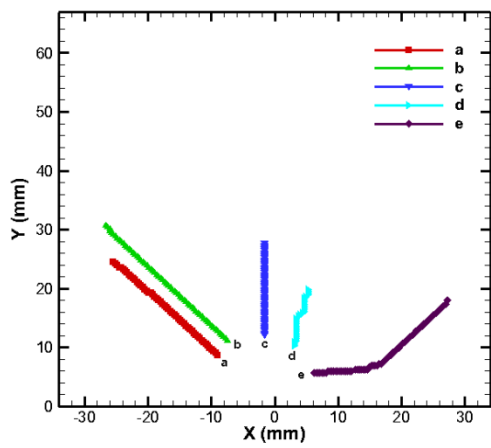


Figure 9. Pathlines at 23% CH₄ – 77% H₂ for $t = t_{end}$.

Figures 9 a – e. Flame front speed for each pathline in Figure 9.

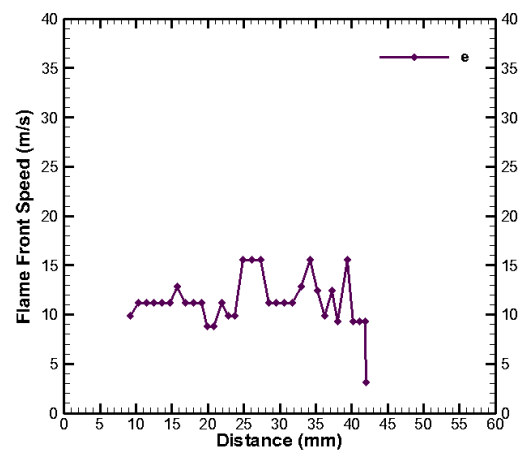
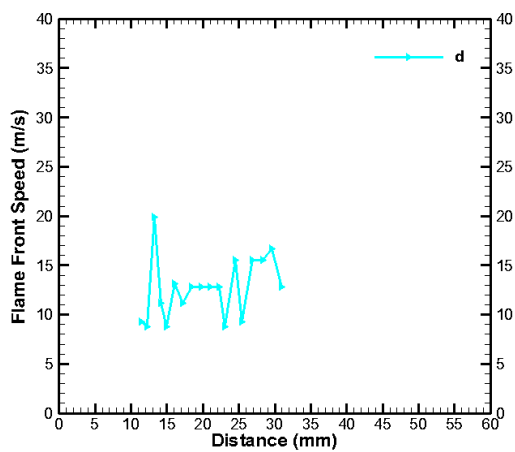
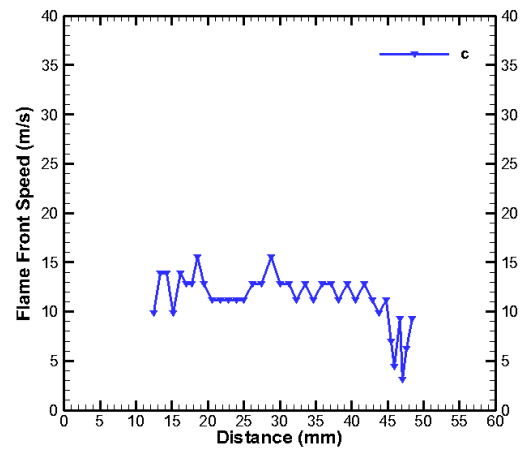
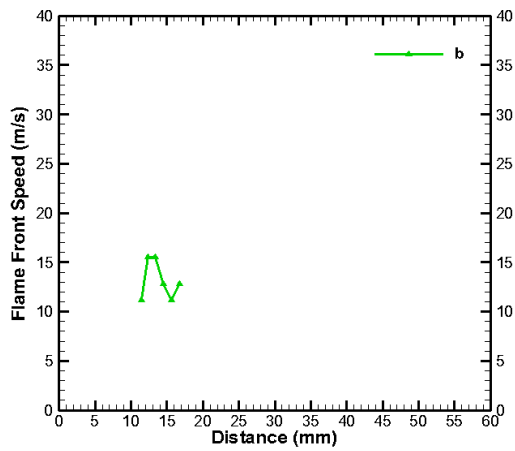
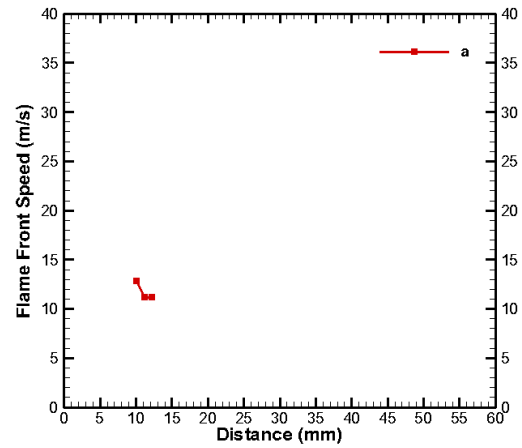
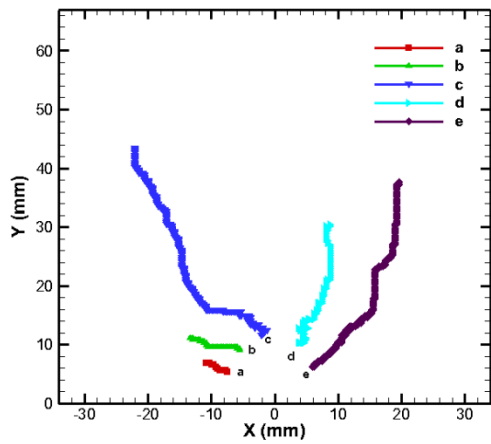


Figure 10. Pathlines at 23% CH₄ – 77% H₂ for $t = t_{\text{end}} + 50$ ms.

Figures 10 a – e. Flame front speed for each pathline in Figure 10.

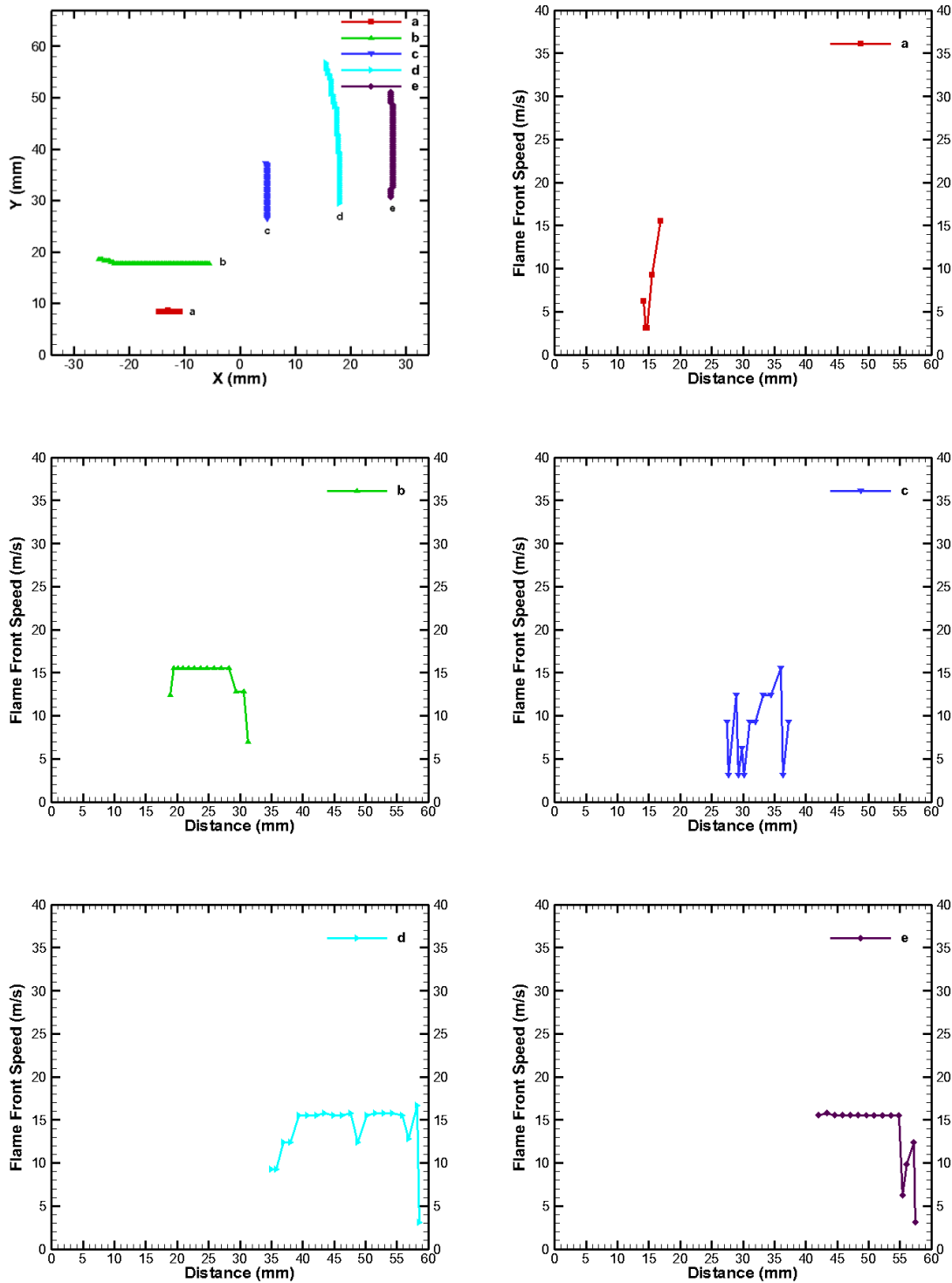


Figure 11. Pathlines at 63% CH₄ – 37% H₂ for $t = t_{\text{end}}$.

Figures 11 a – e. Flame front speed for each pathline in Figure 11.

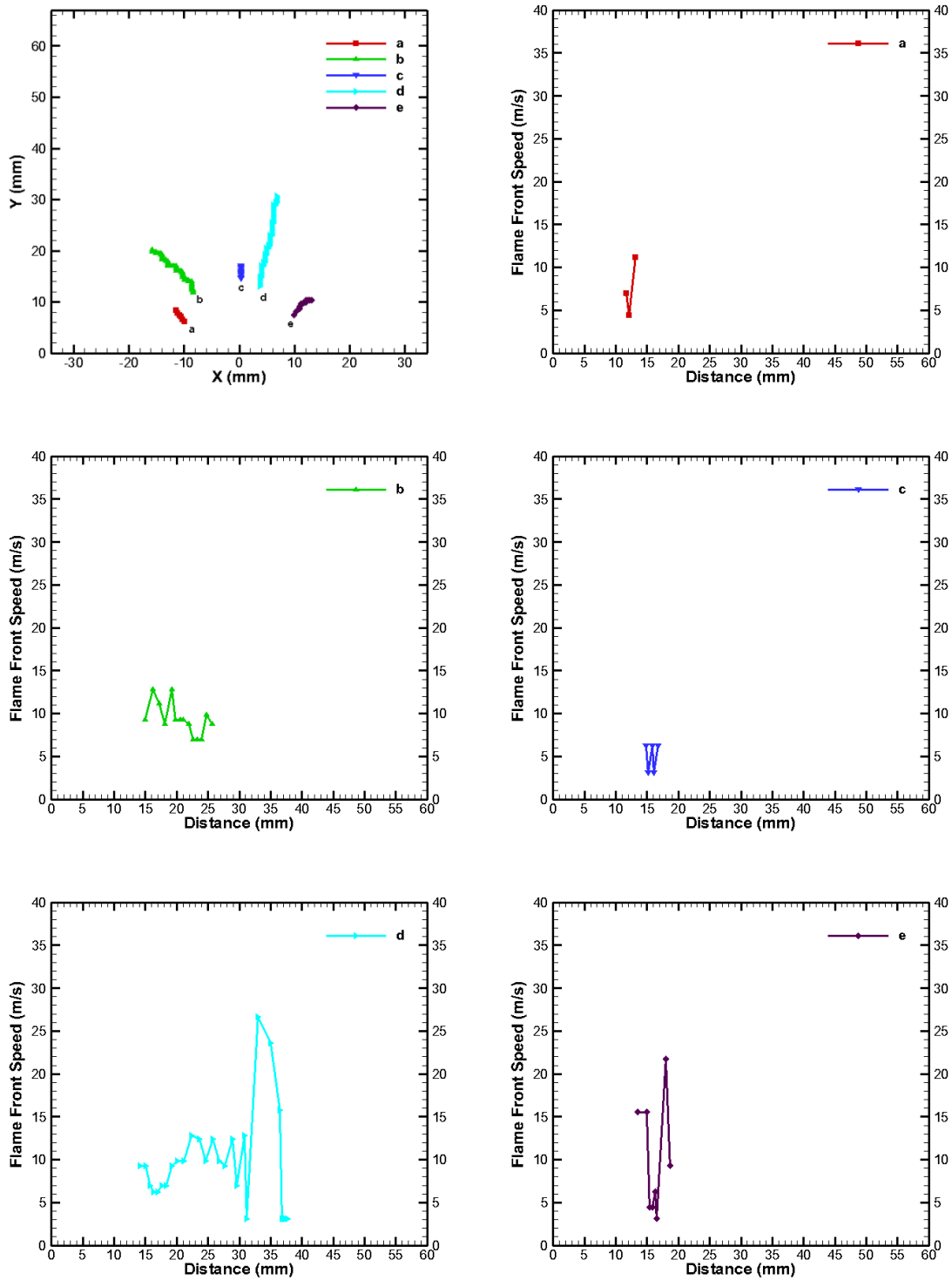


Figure 12. Pathlines at 63% CH₄ – 37% H₂ for $t = t_{\text{end}} + 50$ ms.

Figures 12 a – e. Flame front speed for each pathline in Figure 12.

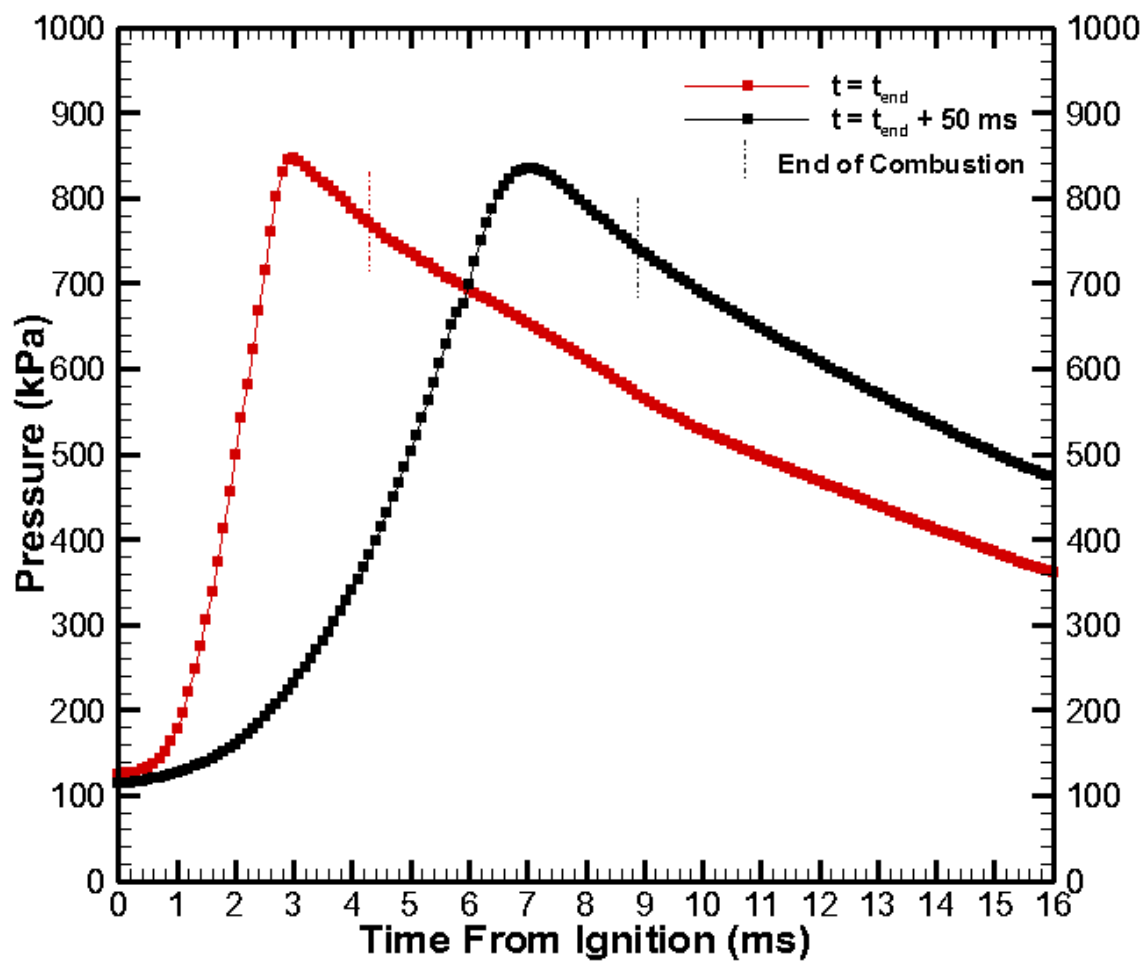


Figure 13. Pressure at 23% CH₄ – 77% H₂ for varying ignition times.

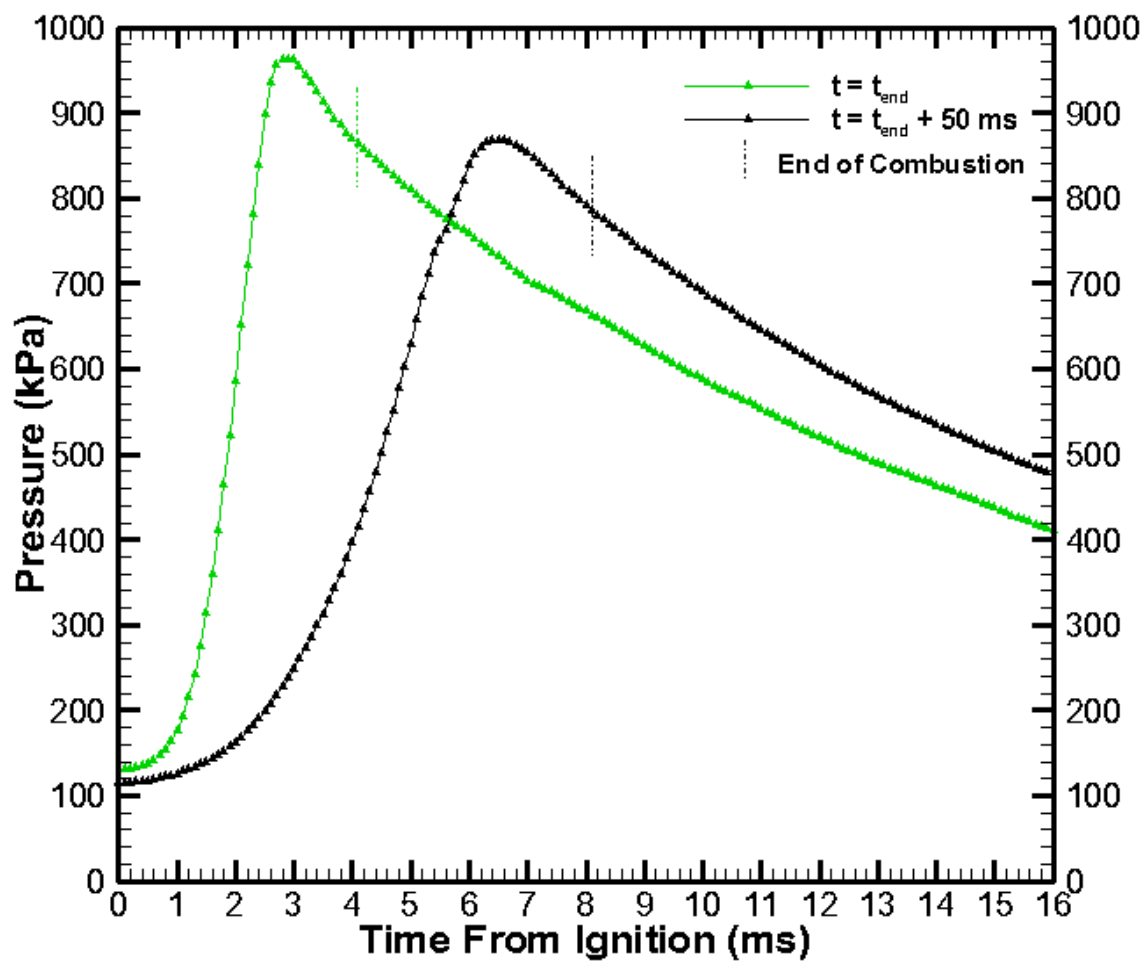


Figure 14. Pressure at 33% CH₄ – 67% H₂ for varying ignition times.

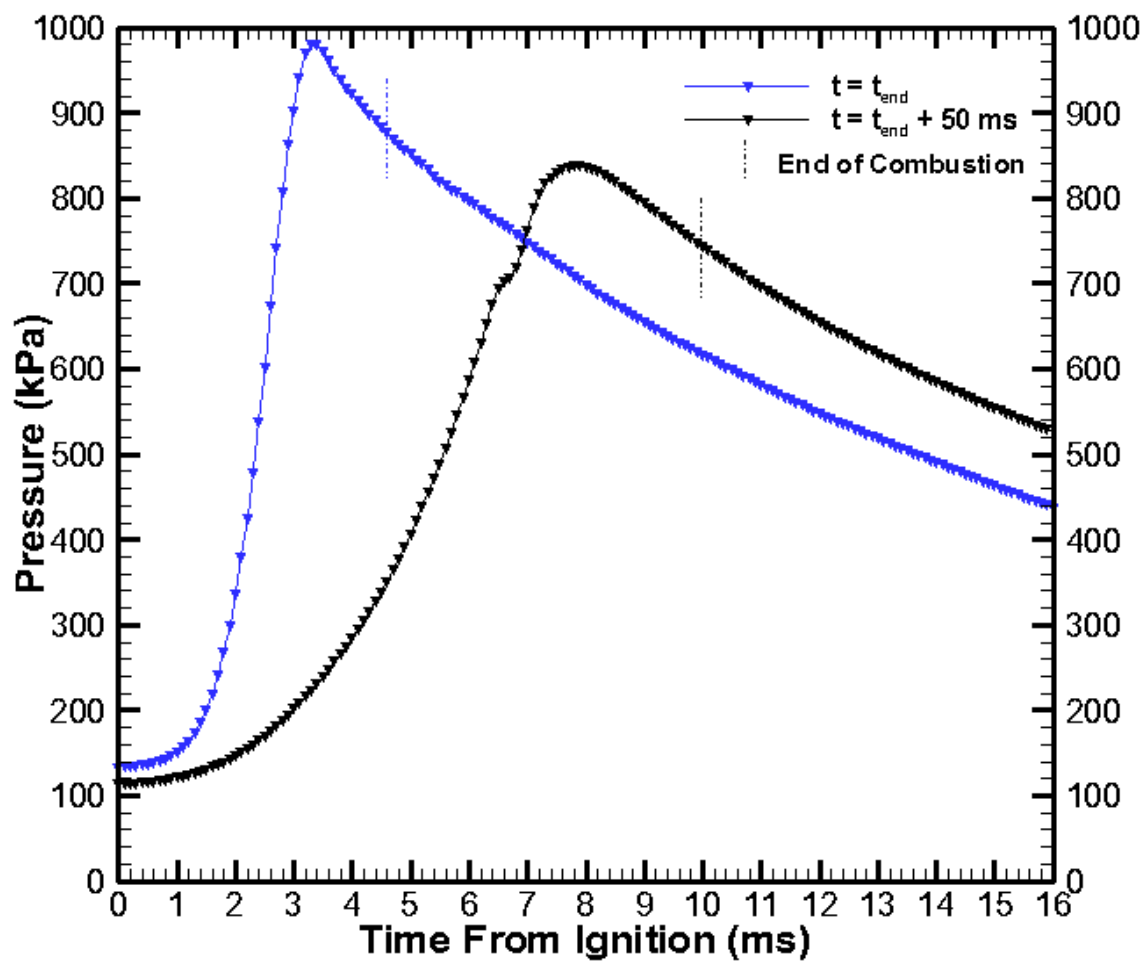


Figure 15. Pressure at 43% CH₄ – 57% H₂ for varying ignition times.

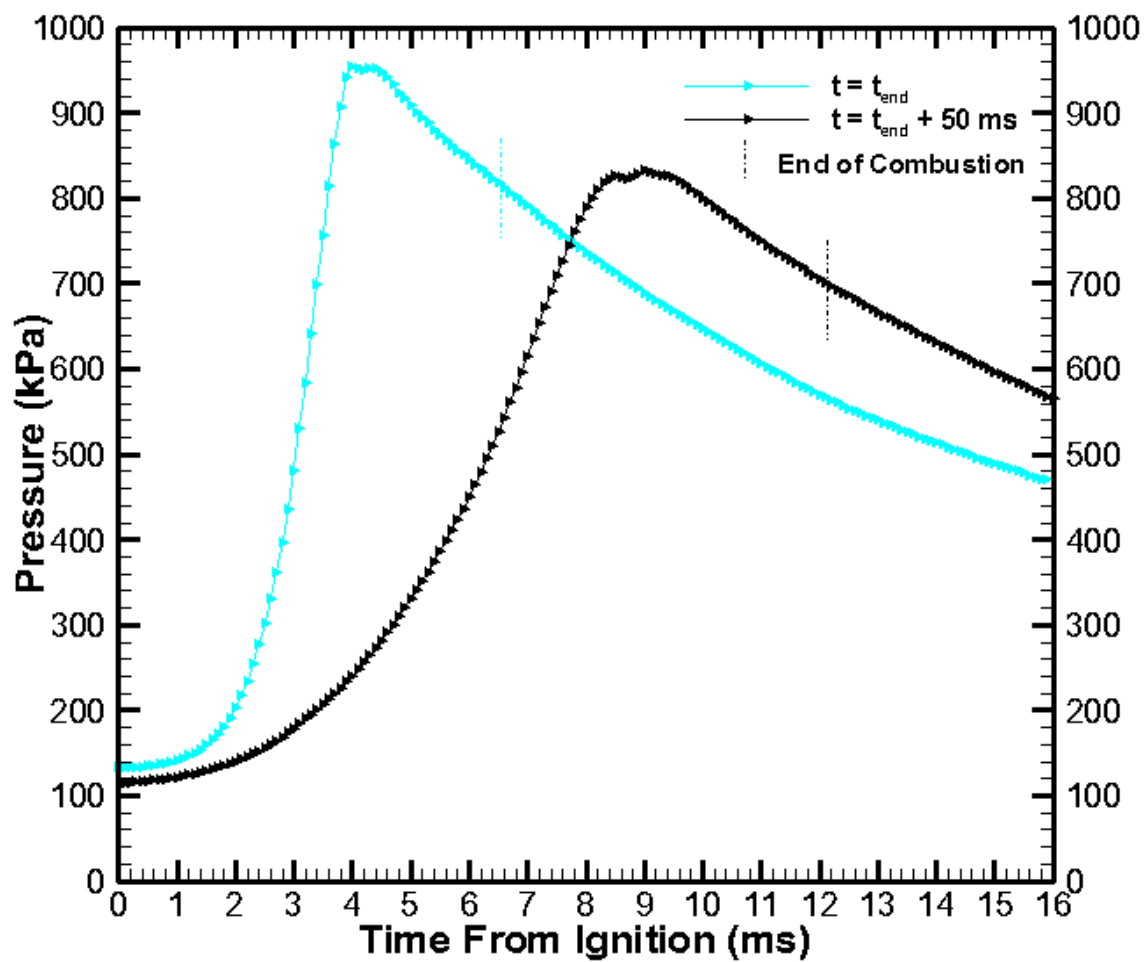


Figure 16. Pressure at 53% CH₄ – 47% H₂ for varying ignition times.

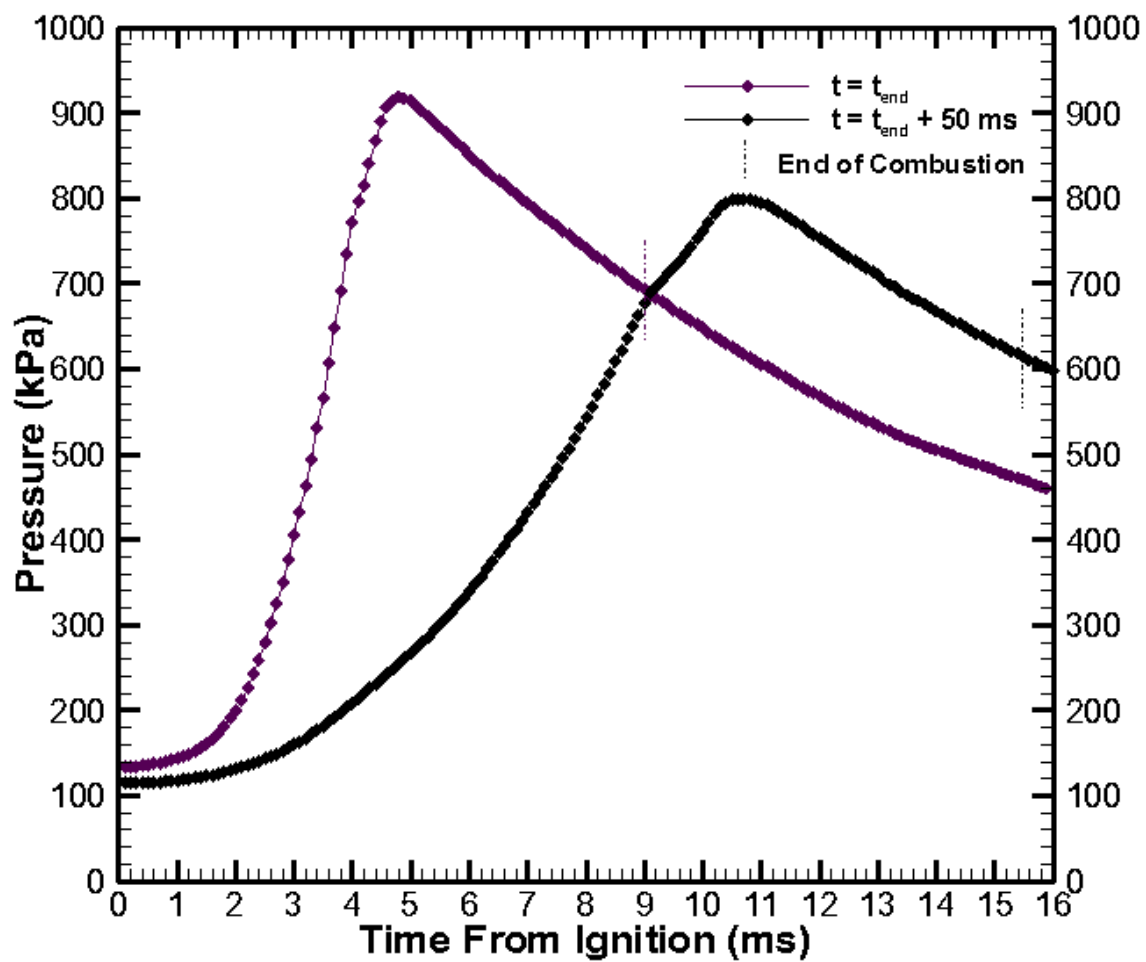


Figure 17. Pressure at 63% CH₄ – 37% H₂ for varying ignition times.

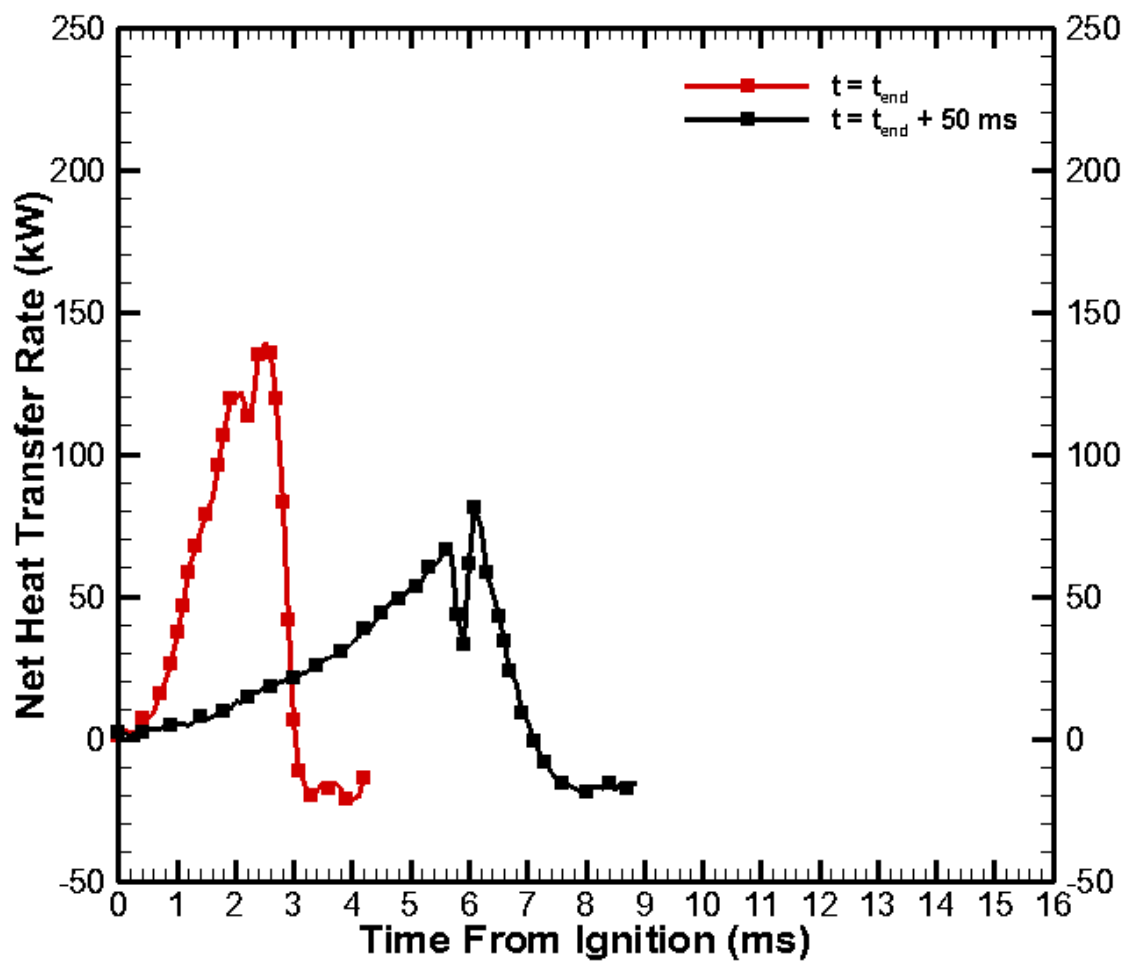


Figure 18. Net heat transfer rates at 23% CH₄ – 77% H₂ for varying ignition times.

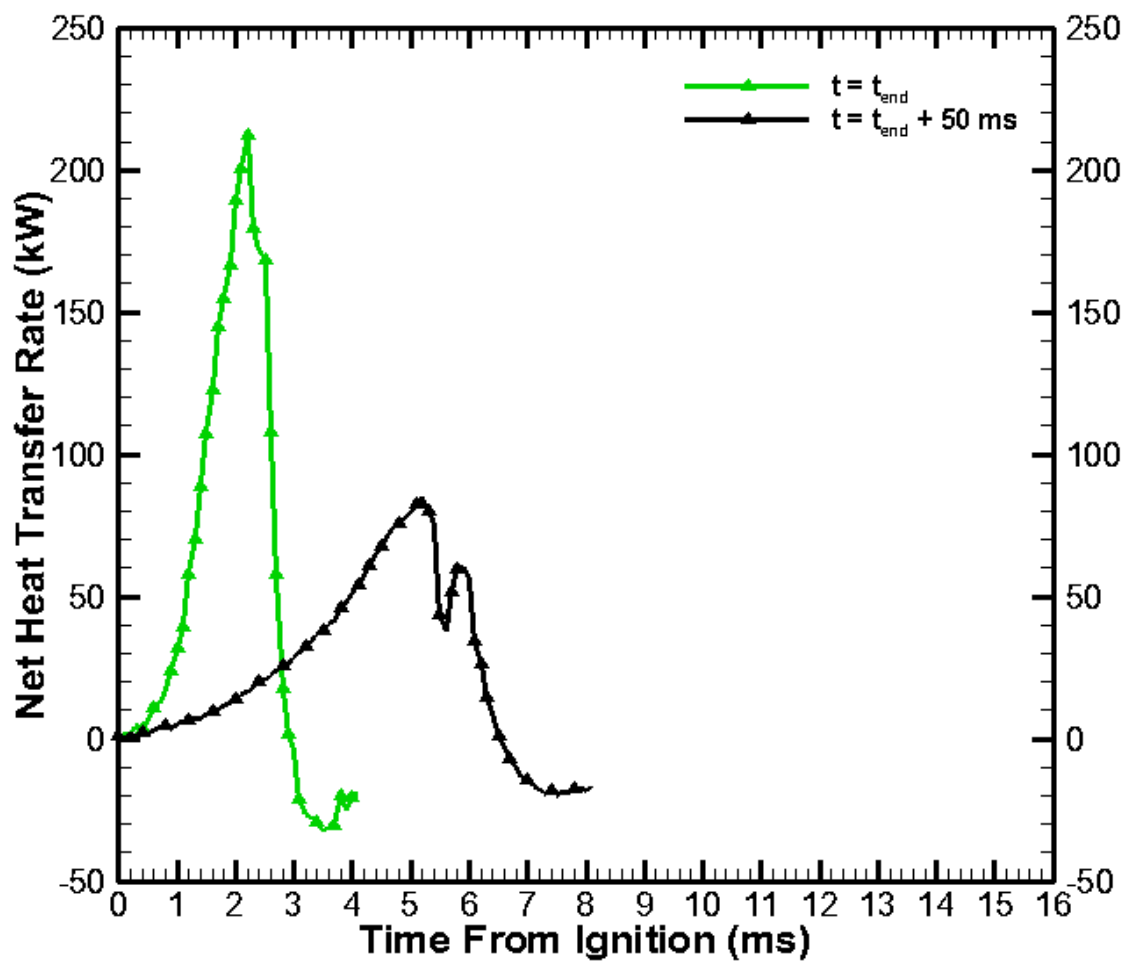


Figure 19. Net heat transfer rates at 33% CH₄ – 67% H₂ for varying ignition times.

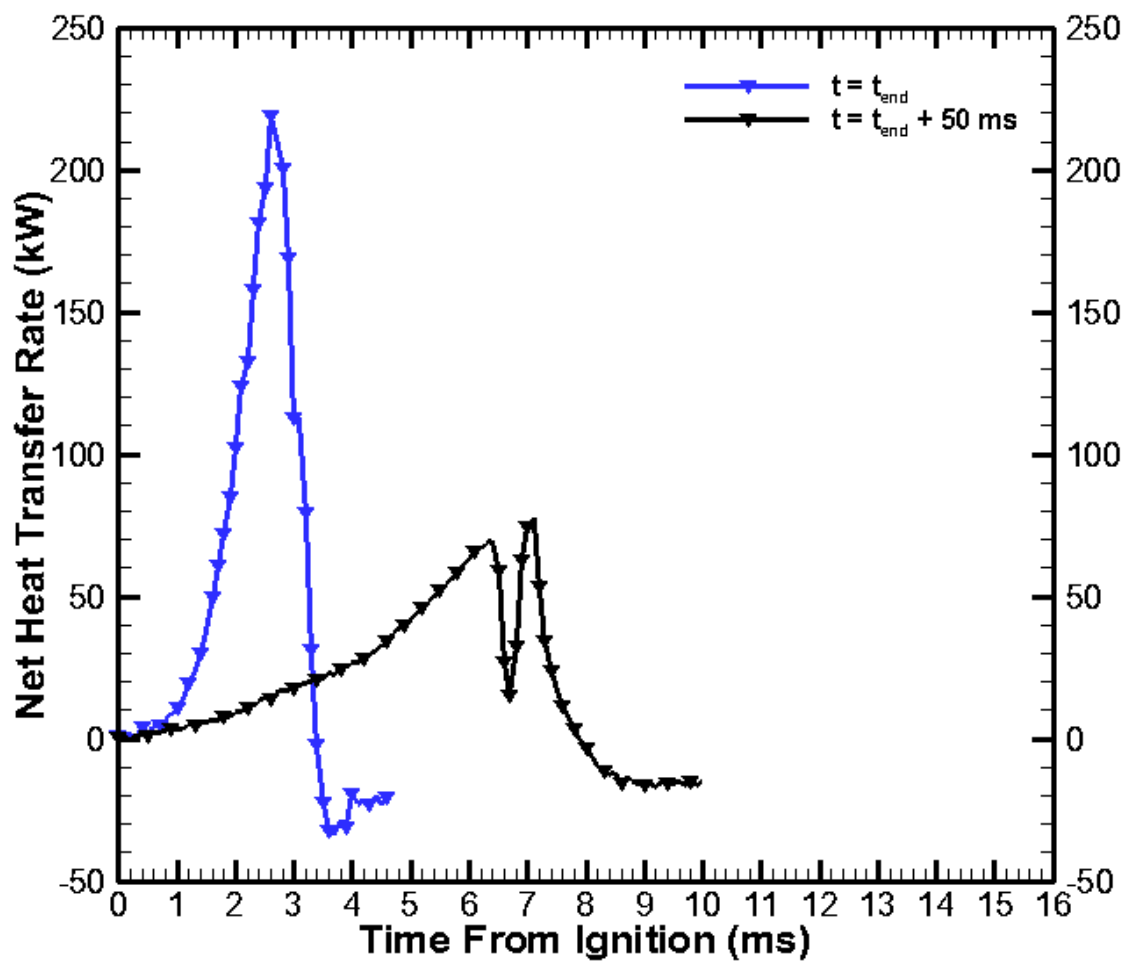


Figure 20. Net heat transfer rates at 43% CH₄ – 57% H₂ for varying ignition times.

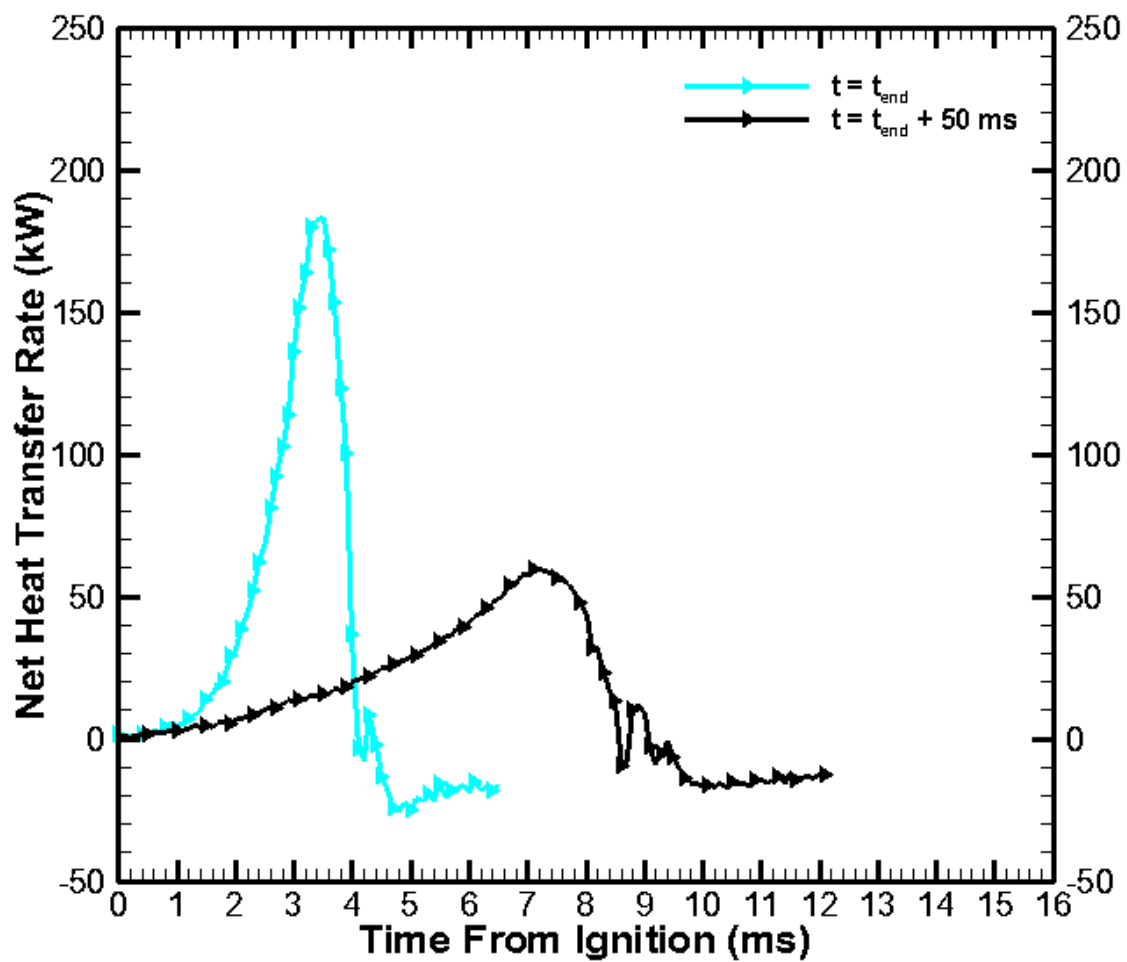


Figure 21. Net heat transfer rates at 53% CH₄ – 47% H₂ for varying ignition times.

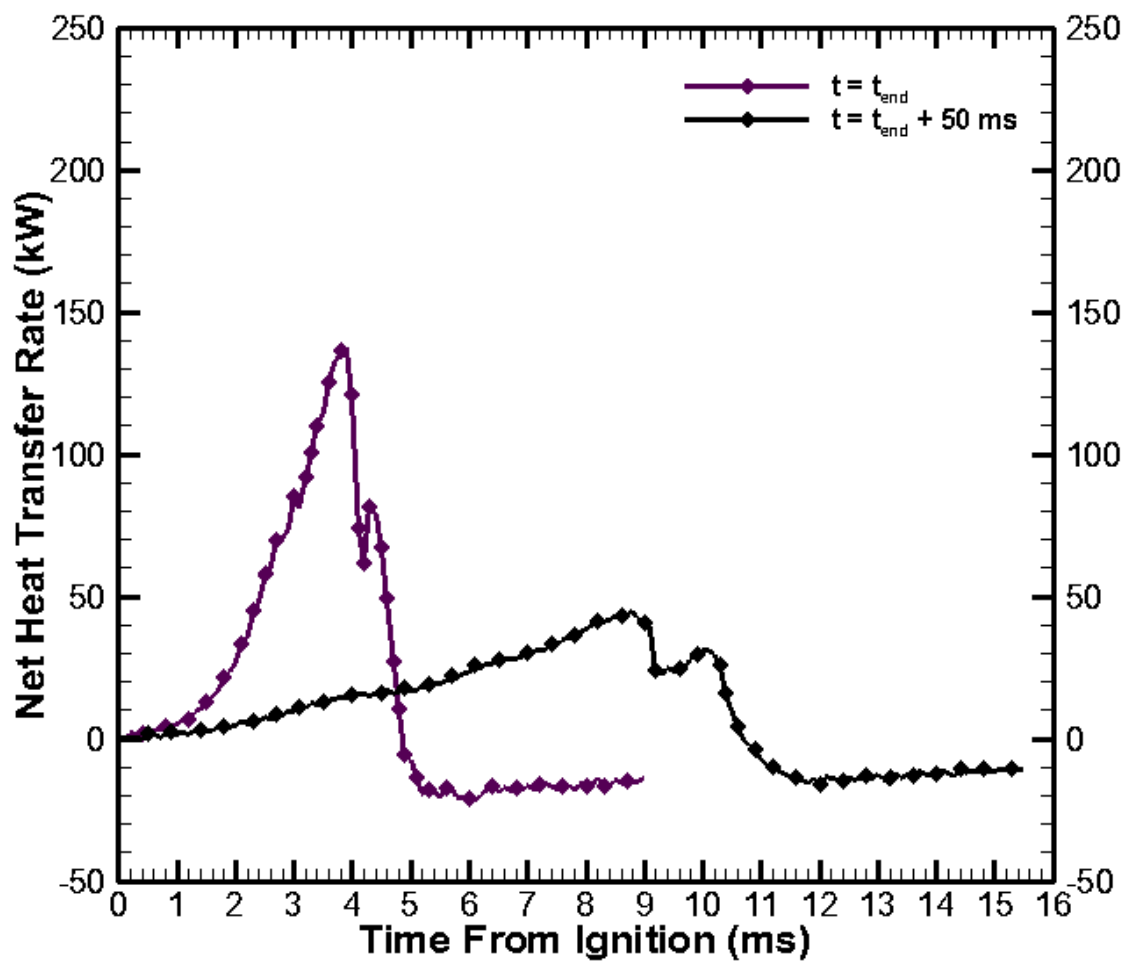


Figure 22. Net heat transfer rates at 63% CH₄ – 37% H₂ for varying ignition times.

CHAPTER 6

CONCLUSIONS AND RECOMMENDATIONS

6.1 Conclusions

The combustion performance of hydrogen directly injected into a constant volume combustion chamber was investigated in this study using an optical technique, Rainbow Schlieren Deflectometry. Air at atmospheric pressure was used as an oxidizer. The fuel/air mixture was ignited using a spark plug. Schlieren images and pressure data were analyzed to characterize fuel jet propagation, flame structure, and flame propagation, determine combustion time, compute flame front speed, determine peak pressures, compare rates of pressure rise and fall, and compute net heat transfer rates. The following results were made:

- Fuel jet penetration is not affected by fuel supply pressure.
- Fuel jet creates turbulence in the chamber that significantly affects the combustion process.
- As the equivalence ratio increase, the flame front speed increase and combustion time decrease.
- At early ignition times, equivalence ratio has minor effects on pressure and net heat transfer rates.
- Ignition time significantly affects flame structure and flame propagation.
- At early ignition times, prior to the close of the injector, flame front speeds are high due to fuel-jet generated turbulence.

- After the close of the injector, as ignition time is increased, flame front speed decrease and are nearly constant due to dissipating fuel-jet generated turbulence.
- Ignition time has a significant effect on rates of pressure rise and fall, peak chamber pressure, and peak net heat transfer rates.
- Increasing hydrogen percentages in methane/hydrogen/air mixtures decreases combustion time at a given ignition time.
- Late ignition results in a decrease in flame front speed and an increase in combustion time.
- Peak chamber pressure and peak net heat transfer rate decreases for the late ignition time at fixed hydrogen percentages.

6.2 Recommendations

- Further improvements on the RSD lighting source should be investigated.
- Reduce the camera frame rate to 20,000 frames per second which will also allow the use of a smaller slit (100 micron).
- Generate different filters to accommodate the smaller slit.
- Due to the ease of wear on high pressure hydrogen injectors, acquire additional hydrogen injectors.
- Conduct high pressure chamber experiments: pressurize the air in the combustion chamber to 2 and 3 atmospheres prior to injecting fuel.
- Conduct laser ignition experiments at varying locations.

REFERENCES

- Agrawal A.K., Gollahalli S.R., Griffin D.W. Fourth International Microgravity Combustion Workshop, NASA CP10194 (1997) 117-122.
- Agrawal A.K., Butuk N.K., Gollahalli S.R., Griffin D.W. Three-dimensional rainbow schlieren tomography of a temperature field in gas flows. *Appl. Opt.* 37 (1998) 479-485.
- Agrawal A.K., Cherry S.M., Gollahalli S.R. Effects of Buoyancy on Steady Hydrogen Gas-Jet Diffusion Flames. *Combust. Sci. Technol.* 140 (1999) 51-68.
- Al-Ammar K., Agrawal A.K., Gollahalli S.R., Griffin D. Applications of rainbow schlieren deflectometry for concentration measurements in an axisymmetric helium jet. *Exp. Fluids* 25 (1998) 89-95.
- Albers B.W., Agrawal A.K. Schlieren Analysis of an Oscillating Gas-Jet Diffusion Flame. *Combust. Flame* 119 (1999) 84-94.
- Das L.M. Fuel Induction Techniques For A Hydrogen Operated Engine. *Int. J. Hydrogen Energy* 15 (1990) 833-842.
- Das L.M. Hydrogen Engines: A View Of The Past And A Look Into The Future. *Int. J. Hydrogen Energy* 15 (1990) 425-443.
- Das L.M., Gulati R., Gupta P.K. A comparative evaluation of the performance characteristics of a spark ignition engine using hydrogen and compressed natural gas as alternative fuels. *Int. J. Hydrogen Energy* 25 (2000) 783-793.
- Heywood J.B. Internal combustion engine fundamentals. New York, NY: McGraw-Hill; 1988.
- Maher A.R., Al-Baghdadi S. Effect of compression ratio, equivalence ratio and engine speed on the performance and emission characteristics of a spark ignition engine using hydrogen as a fuel. *Renewable Energy* 29 (2004) 2245-2260.
- Shenoy A.K., Agrawal A.K., Gollahalli S.R. Quantitative Evaluation of Flow Computations by Rainbow Schlieren Deflectometry. *AIAA J.* 36 (1998) 1953-1960.
- Srivastva D.K., Agarwal A.K. Laser Ignition of Hydrogen-Air Mixture in a Combustion Bomb. *SAE Int.* 2008-28-0033.
- Szwaja S., Bhandary K., Naber J. Comparisons of hydrogen and gasoline combustion knock in a spark ignition engine. *Int. J. Hydrogen Energy* 32 (2007) 5076-5087.
- Verhelst S., Sierens R. A quasi-dimensional model for the power cycle of a hydrogen-fuelled ICE. *Int. J. Hydrogen Energy* 32 (2007) 3545-3554.
- Verhelst S., Sierens R., Verstraeten S. A Critical Review of Experimental Research on Hydrogen Fueled SI Engines. *SAE Int.* 2006-01-0430.

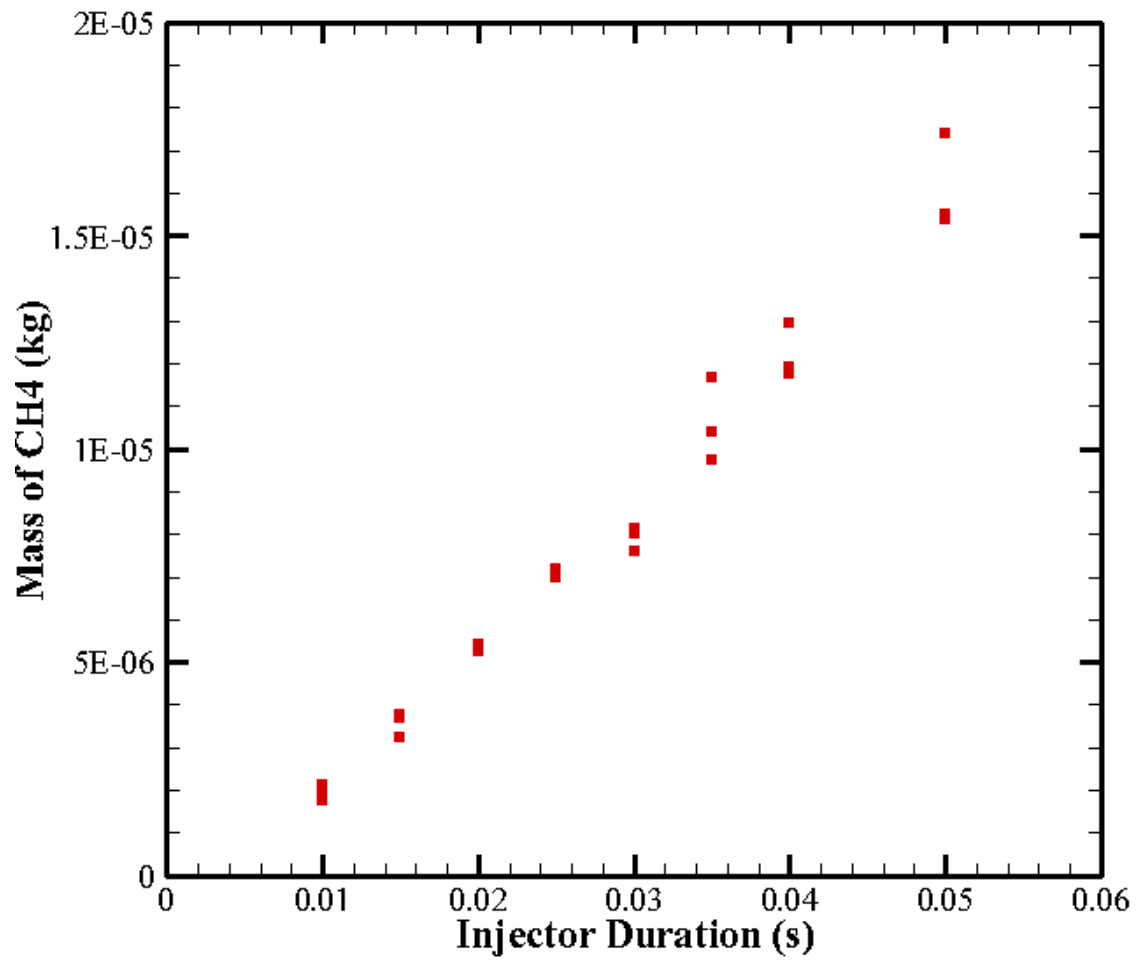
Wallner T., Lohse-Busch H. Performance, Efficiency, and Emissions Evaluation of a Supercharged, Hydrogen-Powered, 4-Cylinder Engine. SAE Int. 2007-01-0016.

Wimmer A., Wallner T. H₂-Direct Injection-A Highly Promising Combustion Concept. SAE Int. 2005-04-0108.

APPENDIX B
PROGRAMMABLE LOGIC CONTROLLER (PLC)

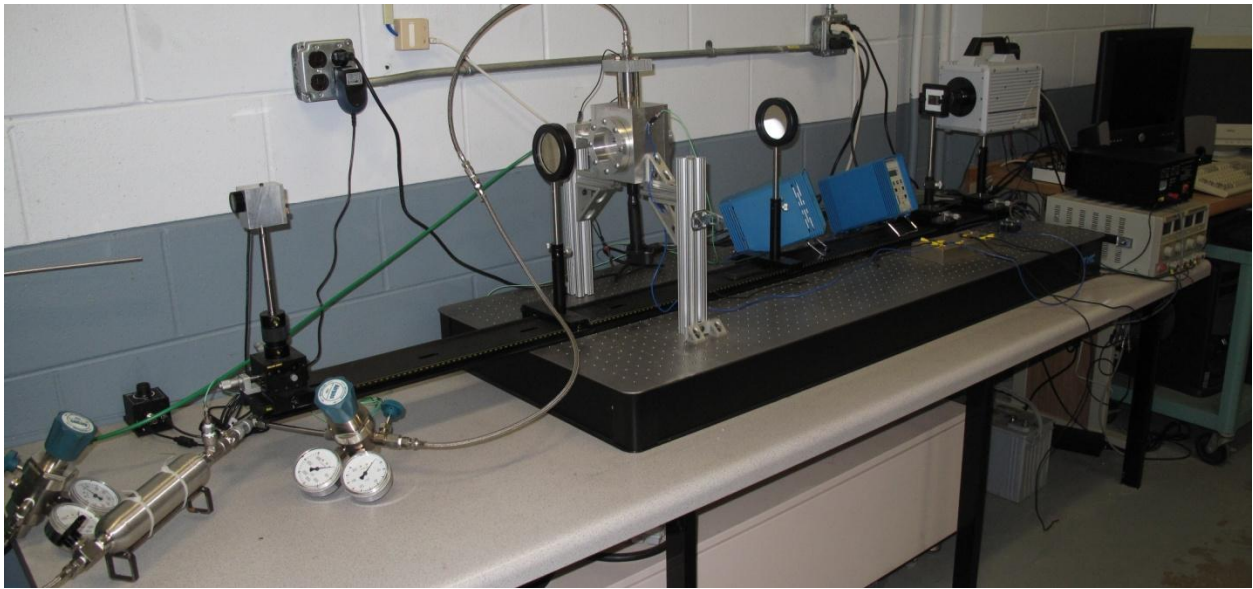


APPENDIX D
METHANE CALIBRATION CURVE



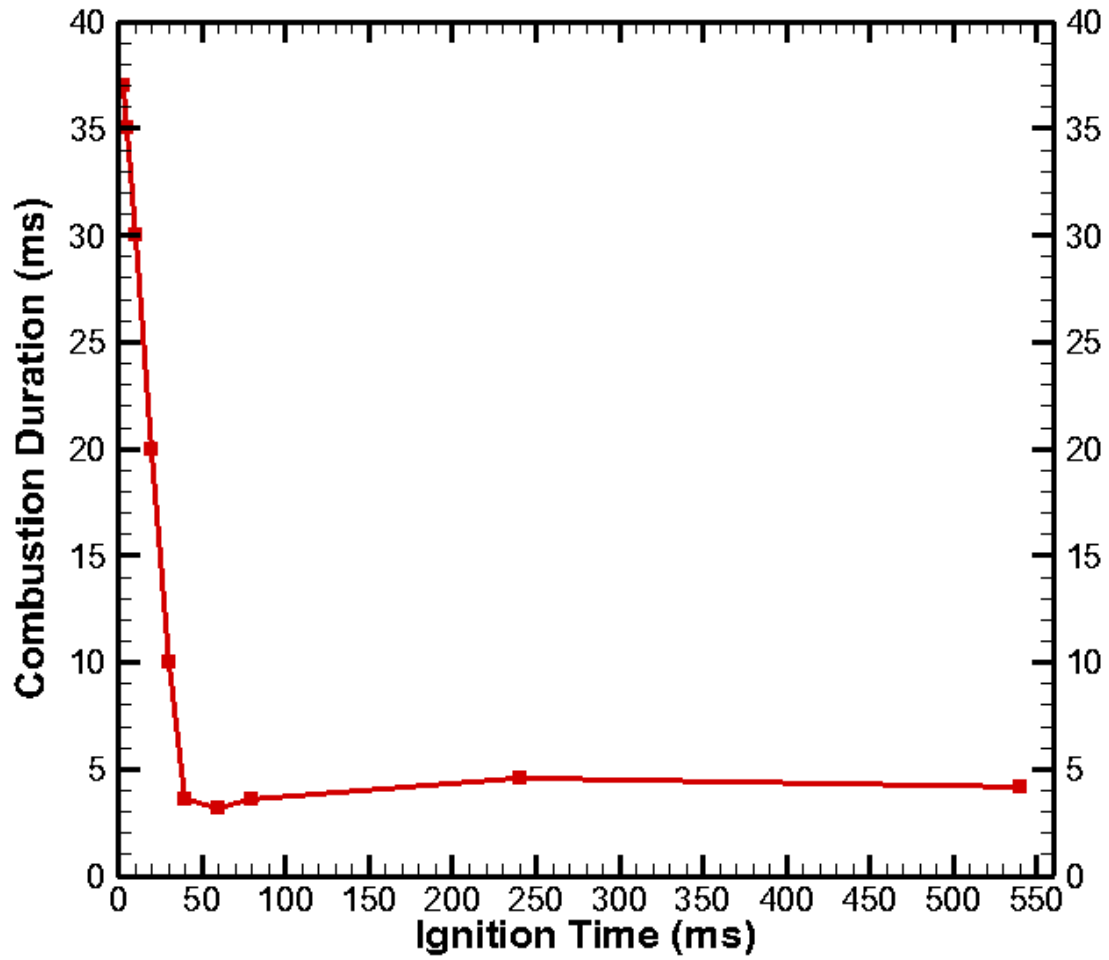
APPENDIX E

EXPERIMENTAL SETUP INCLUDING METHANE INJECTOR, LED ASSEMBLY, AND PHOTRON SA5 CAMERA



APPENDIX F

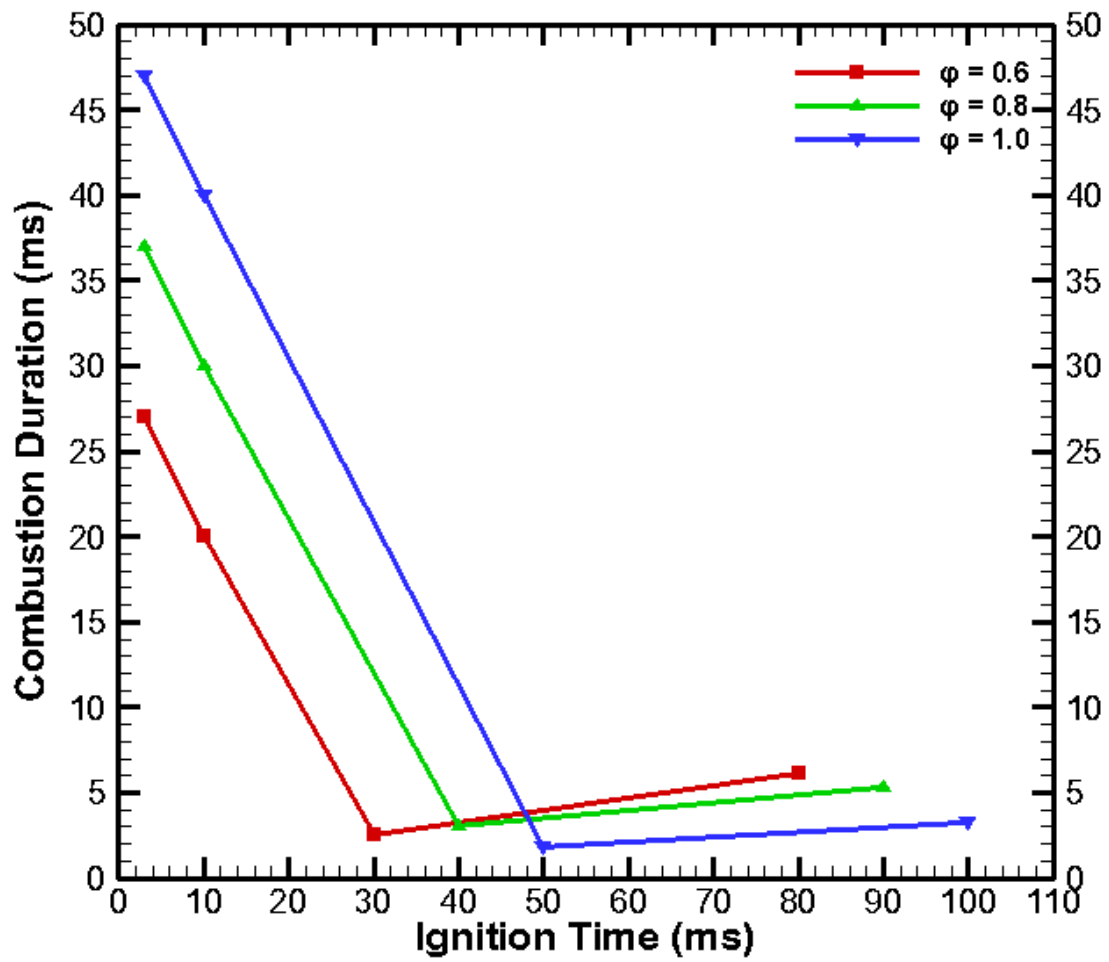
IGNITION TIME COMBUSTION DURATION



Combustion duration for $t = 3, 5, 10, 20, 30, 40, 60, 80, 240,$ and 540 ms (Chapter 3).

APPENDIX G

VARYING IGNITION TIME AND EQUIVALENCE RATIO
COMBUSTION DURATION

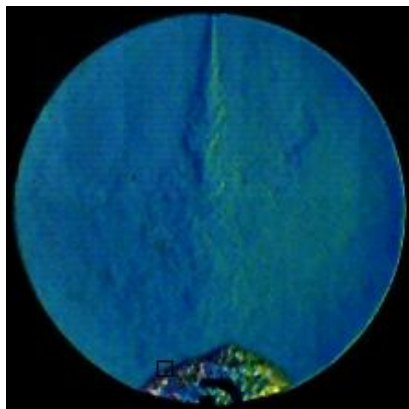


Combustion duration for varying ignition times at $\phi = 0.6, 0.8,$ and 1.0 (Chapter 4).

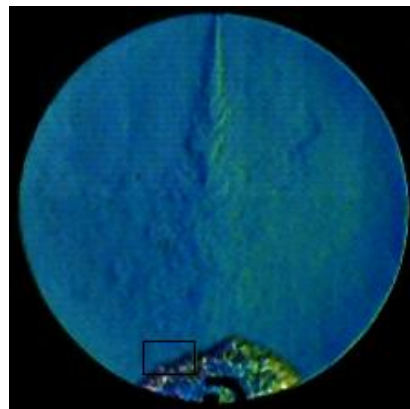
APPENDIX H

CROSS CORRELATION TECHNIQUE

To calculate the flame front speed and define flame pathlines at varying locations, a cross correlation approach was utilized. To use this approach, a very high speed camera was used to acquire images at a high rate, 50,000 frames per second, so that only minute structural changes in the flame had occurred. Schlieren images were acquired for each test conducted containing structural changes in the flame as it propagated through the combustion chamber. A range of consecutive schlieren images containing the flame as it propagated were selected for analysis. In the first of these schlieren images, termed the initial image, five structures that are defined by windows at varying locations along the flame front were selected to track the movement of the flame starting from that location until the flame front has reached the top of the combustion chamber. The second or next consecutive image is termed the delayed image. In the delayed image, a window large enough to contain the corresponding structure defined in the initial image is defined for each of the five structures defined in the initial image.



Initial Image



Delayed Image

Each of the five structures in the initial image is correlated within the corresponding window of the delayed image and a cross-correlation coefficient is calculated using

$$\gamma_{u,v} = \frac{\sum_{x,y} f(x,y) - \bar{f}_{u,v} [t(x-u, y-v) - \bar{t}]}{\{\sum_{x,y} f(x,y) - \bar{f}_{u,v}^2 \sum_{x,y} t(x-u, y-v) - \bar{t}^2\}^{0.5}}$$

whereas $f(x, y)$ = the matrix containing the color intensities of the window in the delayed image, $\bar{f}_{u,v}$ = mean of $f(x, y)$ in the region under the window from the initial image, $t(x - u, y - v)$ = the matrix containing the color intensities of the window in the initial image, and \bar{t} = the mean of the color intensities of the window in the initial image.

The maximum element of cross-correlation coefficient matrix $\gamma(u, v)$ represents the best correlation for the structure between the corresponding windows in the initial and delayed images. The coordinates (u, v) represents the values of the pixel offsets, the right lower corner of the identified structure in the delayed image. The structure displacement is found in reference to its location in the initial image. Once the structure's displacement is determined, the flame front speed can be calculated. The delayed image with the determined structure locations become the initial image. The next consecutive schlieren image becomes the delayed image and the process is repeated until all selected schlieren images are analyzed. Pathlines are defined as the lines connecting the structure locations as they are determined from the initial image to the delayed image.

APPENDIX J

CROSS-CORRELATION CODE FOR CALCULATING PATHLINES AND FLAME FRONT SPEED

```
function[] = image_processing()
clear all
clc
fid = fopen('inp.m');
ns = fscanf(fid, '%d', [1]); % starting image count number
ne = fscanf(fid, '%d', [1]); % ending image count number
wn = fscanf(fid, '%d', [1]); % number of windows(structures) specified
tlcx = fscanf(fid, '%d', [1, wn]); % left column index of window
brcx = fscanf(fid, '%d', [1, wn]); % Right column index of window
tlcy = fscanf(fid, '%d', [1, wn]); % top row index of window
brcy = fscanf(fid, '%d', [1, wn]); % bottom row index of window
ncolumn = fscanf(fid, '%d', [1]); % no. of columns in the image
nrow = fscanf(fid, '%d', [1]); % no. of rows in the image
pixel_resolution = fscanf(fid, '%g', [1]);
delta_t = fscanf(fid, '%g\n', [1]); % time lag between two successive images
name = fgetl(fid); % Name of the image excluding image count number
ext = fgetl(fid); % file extension type
fclose(fid);
% [tlcx' tlcy' brcx' brcy']
tlcxn = tlcx-10; tlcyn = tlcy-15; brcxn = brcx+10; brcyn = brcy;
for wi = 1:wn
    if(tlcxn(wi)<1)
        tlcxn(wi) = 1;
    end
    if(tlcyn(wi)<1);
        tlcyn(wi) = 1;
    end
    if(brcxn(wi)>ncolumn)
        brcxn(wi) = ncolumn;
    end
    if(brcyn(wi)>nrow);
        brcyn(wi) = nrow;
    end
end
end

% [w1 w2 w3 w4 h1 h2 h3 h4]
W = zeros(wn, (ne-ns)); H = W; W(:,1) = tlcx(:); H(:,1) = tlcy(:);
count = 0;
for ifile = ns:ne-1
    count = count+1;
    if (ifile< 10)
        filename1 = strcat(name, '0000', int2str(ifile), '.', ext);
        filename2 = strcat(name, '0000', int2str(ifile+1), '.', ext);
    elseif (ifile>=10) & (ifile<100)
```

```

        filename1 = strcat(name, '0000', int2str(ifile), '.', ext);
        filename2 = strcat(name, '0000', int2str(ifile+1), '.', ext);
elseif (ifile>=100) & (ifile<1000)
    filename1 = strcat(name, '000', int2str(ifile), '.', ext);
    filename2 = strcat(name, '000', int2str(ifile+1), '.', ext);
elseif (ifile>=1000) & (ifile<10000)
    filename1 = strcat(name, '00', int2str(ifile), '.', ext);
    filename2 = strcat(name, '00', int2str(ifile+1), '.', ext);
elseif (ifile>=10000) & (ifile<100000)
    filename1 = strcat(name, '0', int2str(ifile), '.', ext);
    filename2 = strcat(name, '0', int2str(ifile+1), '.', ext);
elseif (ifile>=100000)
    filename1 = strcat(name, int2str(ifile), '.', ext);
    filename2 = strcat(name, int2str(ifile+1), '.', ext);
end
for wi = 1:wn
    h1 = tlcx(wi); h2 = brcx(wi); h3 = tlcyn(wi); h4 = brcyn(wi);
    w1 = tlcx(wi); w2 = brcx(wi); w3 = tlcxn(wi); w4 = brcxn(wi);
    X1 = imread(filename1, ext); %X1 = rgb2hsv(X1);
    Hue1 = X1(h1:h2, w1:w2, 2);
    X2 = imread(filename2, ext); %X2 = rgb2hsv(X2);
    Hue2 = X2(h3:h4, w3:w4, 2);
    % figure(1); contourf(X2(:, :, 3)-X1(:, :, 3));
    [total_offset, max_C] = cross_correlation(w1, w2, w3, w4, h1, h2, h3, ...
        h4, Hue1, Hue2);
    w1 = w1+total_offset(2); h1 = h1+total_offset(1);
    w2 = w2+total_offset(2); h2 = h2+total_offset(1);
    w3 = w1-10; h3 = h1-15; w4 = w2+10; h4 = h2;
    if(w3<1)
        w3 = 1;
    end
    if(h3<1);
        h3 = 1;
    end
    if(w4>ncolumn)
        w4 = ncolumn;
    end
    if(h4>nrow);
        h4 = nrow;
    end
    % [w1 w2 w3 w4 h1 h2 h3 h4];
    tlcx(wi) = h1; brcx(wi) = h2; tlcyn(wi) = h3; brcyn(wi) = h4;
    tlcx(wi) = w1; brcx(wi) = w2; tlcxn(wi) = w3; brcxn(wi) = w4;
    W(wi, count) = w1; H(wi, count) = h1; cv(wi, count) = max_C;
    vx(wi, count) = pixel_resolution*total_offset(2)/delta_t;
    vy(wi, count) = pixel_resolution*total_offset(1)/delta_t;
    v(wi, count) = sqrt((vx(count))^2+(vy(count))^2);
end
end
save('results.mat', 'vx', 'vy', 'v', 'W', 'H');
[W(:) H(:) v(:) cv(:)]
figure(1); plot(W(1,:), H(1,:), '-r. '); hold on
plot(W(2,:), H(2,:), '-b. '); hold on
plot(W(3,:), H(3,:), '-g. '); hold on
plot(W(4,:), H(4,:), '-m. '); hold on
plot(W(5,:), H(5,:), '-k. '); hold on
hold off

```

```

%%%%%%%%%%%%%%%%%%%%%%%%%%%%%%%%%%%%%%%%%%%%%%%%%%%%%%%%%%%%%%%%%%%%%%%%
function [total_offset, max_C] = cross_correlation(w1,w2,w3,w4,h1,h2,h3,...
    h4,Hue1,Hue2)
C = normxcorr2(Hue1,Hue2);
% [(size(Hue1))' (size(Hue2))' (size(C))']
[max_C, imax] = max(abs(C(:)));
[ypeak, xpeak] = ind2sub(size(C),imax(1));
corr_offset = [ (ypeak-size(Hue1,1)) (xpeak-size(Hue1,2)) ];
window_offset = [(h3-h1) (w3-w1)];
total_offset = corr_offset + window_offset;
%%%%%%%%%%%%%%%%%%%%%%%%%%%%%%%%%%%%%%%%%%%%%%%%%%%%%%%%%%%%%%%%%%%%%%%%

```

APPENDIX K

VALIDATION CODE FOR CROSS-CORRELATION TECHNIQUE

```
function[] = validation_cross_correlation_images()
clear all
clc

fid = fopen('parameters.m');
ni = fscanf(fid, '%d', [1]); % number of images to be generated for validation
ns = fscanf(fid, '%d\n', [1]); % number of structures in an image (odd 3-9)
name = fgetl(fid); % Name of the image excluding image count number
ext = fgetl(fid); % file extension type
fclose(fid);

[X,Y]=meshgrid(-256:256, -256:256);
R = sqrt(X.^2+Y.^2);
R = (R>=150);
z = zeros(512,512,3);
i = 1:512; j = 1:512; z(i,j,1)= 0.05*(R(i,j)==0);
z(i,j,2)= 1*(R(i,j)==0); z(i,j,3)= 1*(R(i,j)==0);
clear X Y R i j

% Structures would be arranged on the chord 140 points away from center on
% one side to the chord 140 points away from center on other side.
% Generally from bottom chord to top chord movement of strcutres. This
% chord length is roughly around 106 points so 10 sructures with width of 5
% points can esily be fitted. Based on number of images the vertical
% movement would be finalized although randomly. The sideways movement
% would be governed by ratio of chord lengths when moving from bottom to
% top.

y = 396*ones(ni,ns);
str = rand(5,5,ns);
dy = rand(ni,ns); dy1 = sum(dy);
for i = 2:ni
    for j = 1:ns;
        dy(i,j) = fix(280*dy(i,j)/dy1(j));
        dy(i,j) = dy(i,j) + (dy(i,j)==0);
        y(i,j) = y(i-1,j) - dy(i,j);
    end
end
x = ones(ni,ns); cen = round(1+(ns-1)/2); x(:,cen) = 0;
for i = 1:ni
    for j = 1:ns
        delx = round(2*(sqrt(150^2-(y(i,j)-256)^2)-3))/(ns-1);
        x(i,j) = 256 + (j-cen)*delx;
    end
end
```

```

figure(1); plot(x,y); title('Predefined streamlines'); pause(1);
for i = 1:ni
    if (i < 10)
        filename = strcat(name, '00000', int2str(i), '.', ext);
    elseif (i >= 10) & (i < 100)
        filename = strcat(name, '0000', int2str(i), '.', ext);
    elseif (i >= 100) & (i < 1000)
        filename = strcat(name, '000', int2str(i), '.', ext);
    elseif (i >= 1000) & (i < 10000)
        filename = strcat(name, '00', int2str(i), '.', ext);
    elseif (i >= 10000) & (i < 100000)
        filename = strcat(name, '0', int2str(i), '.', ext);
    elseif (i >= 100000)
        filename = strcat(name, int2str(i), '.', ext);
    end
    z1 = z;
    for j = 1:ns
        a = x(i,j)-2; b = y(i,j)-2;
        z1(b:(b+4), a:(a+4), 1) = str(:, :, j);
    end
    z1 = hsv2rgb(z1);
    f(i) = im2frame(z1);
    imwrite(z1, filename, ext);
end
movie2avi(f, 'Validation-images.avi', 'fps', 5)
save('streamline_input.mat', 'x', 'y', 'ni', 'ns');
clear all

```

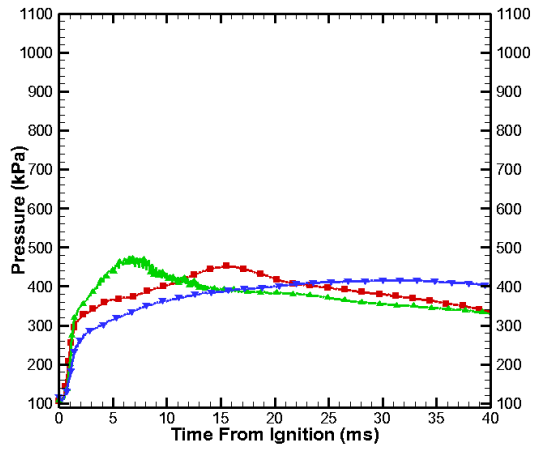
APPENDIX L

UNCERTAINTY ANALYSIS

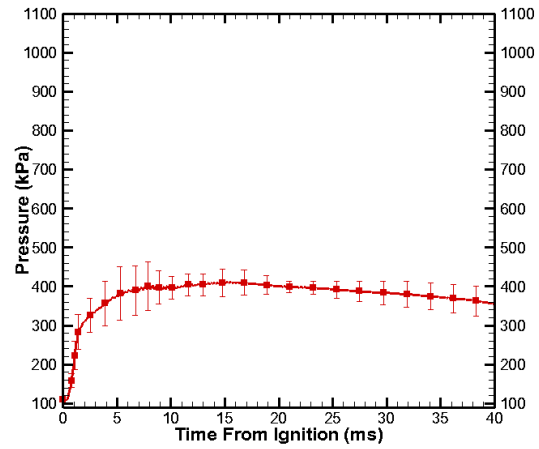
To determine the error associated with the chamber pressure in ignition time experiments, three test were conducted for each ignition time, $t = 3, 5, 10, 20, 30, 40, 60, 80, 240,$ and 540 ms. The standard deviation of the sample for the three sets of pressure data for each ignition time was calculated at each time interval using:

$$\frac{\overline{x-x^2}}{n-1}$$

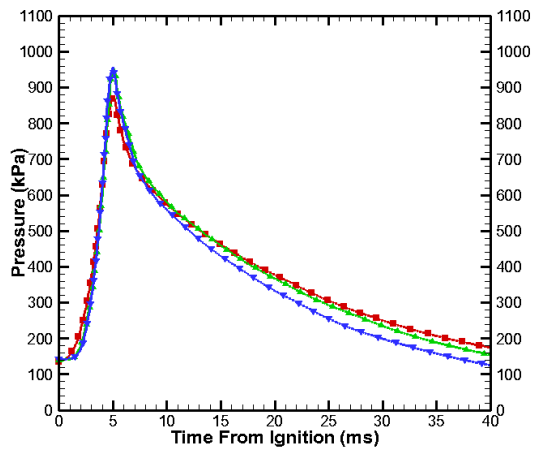
The pressure sensor is a Kistler 6053CC60 piezoelectric sensor with a maximum sensitivity drift of +/- 0.5%. The uncertainty of pressure instrumentation was found by calculating the product of the average pressure of the three tests at each time interval and the maximum sensitivity drift. The error in pressure measurements was then found by taking the square root of the sum of the squares of the standard deviation of the sample and the uncertainty of pressure instrumentation. Examples for two ignition times, $t = 3$ ms and $t = 240$ ms, are given below. To determine the error associated with the chamber pressure in methane/hydrogen experiments, two tests were conducted for the experiments. The error was determined using the same procedure for the ignition time experiments with the exception of two sets of data instead of three. An example is given below for experiments conducted at 53% $\text{CH}_4 - 47\%$ H_2 .



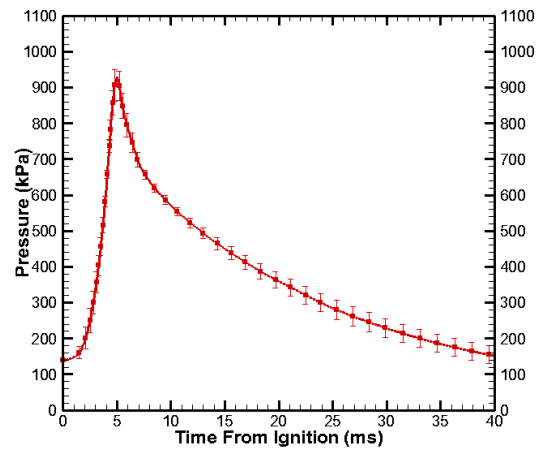
a) Three pressure tests for $t = 3$ ms.



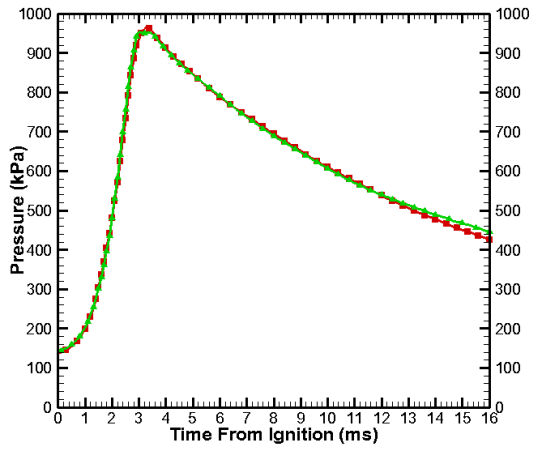
b) Average pressure for $t = 3$ ms with errors.



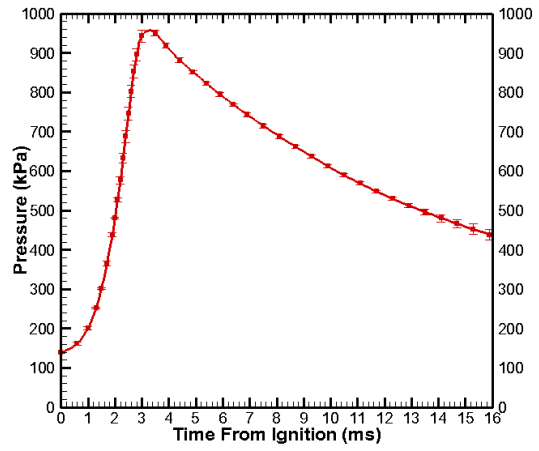
c) Three pressure tests for $t = 240$ ms.



d) Average pressure for $t = 240$ ms with errors.



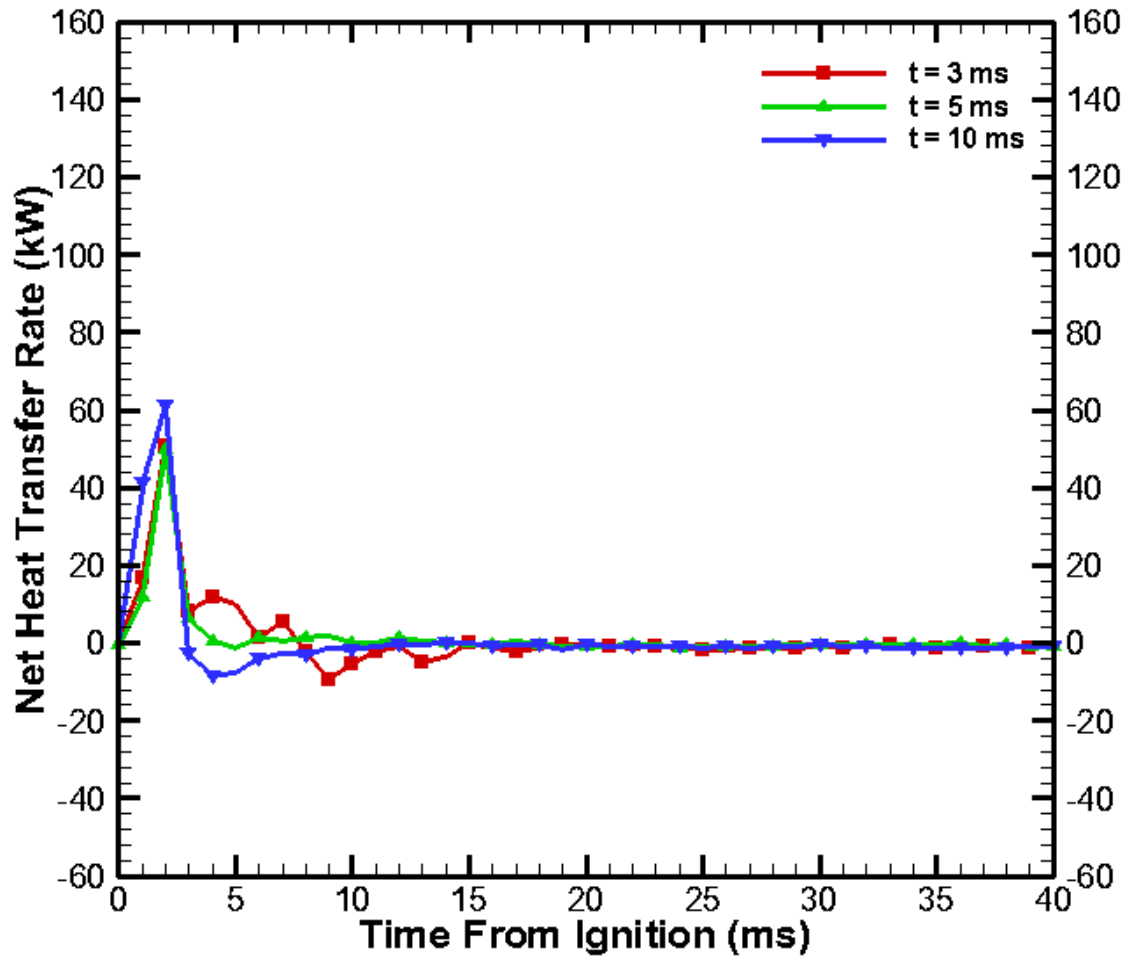
e) Two pressure tests for 53% CH₄ – 47% H₂.



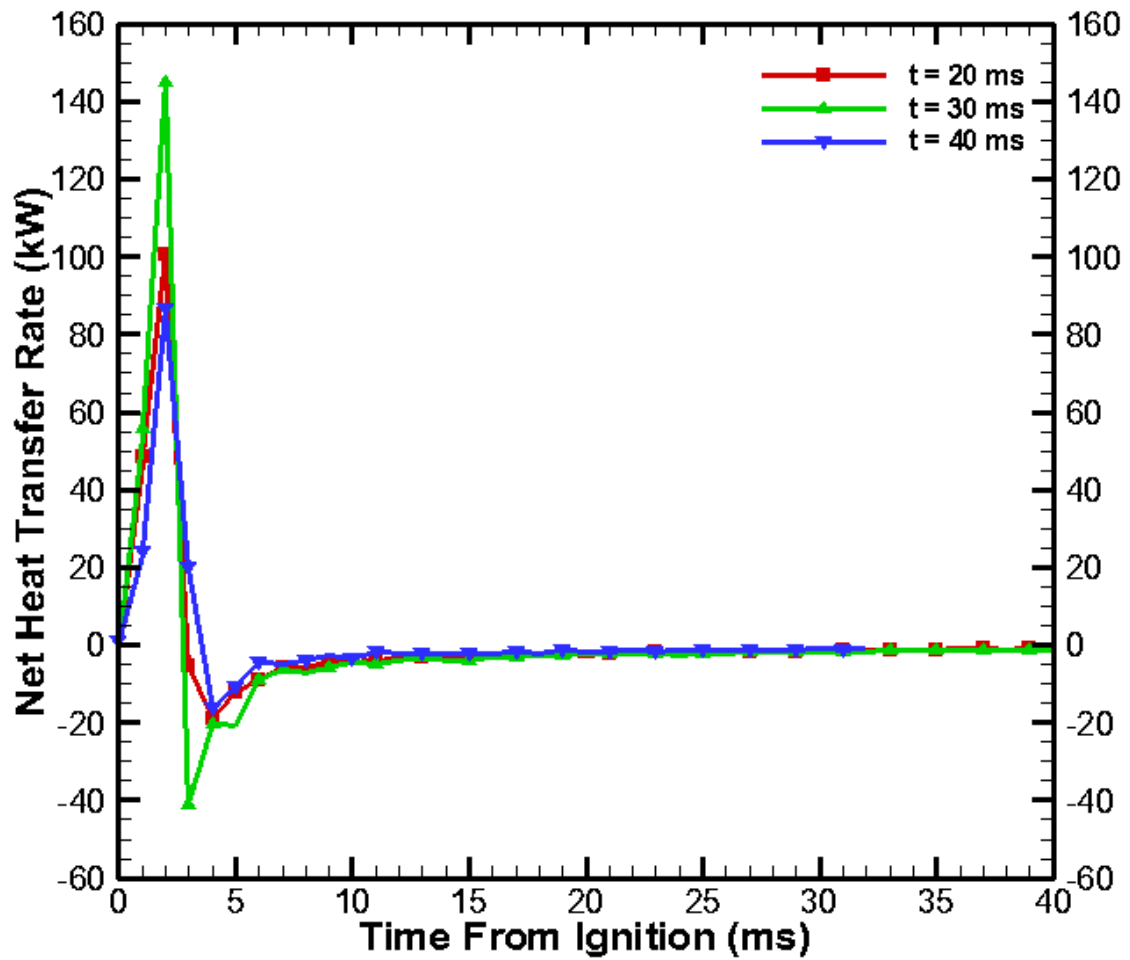
f) Average pressure for 53% CH₄ - 47% H₂ with errors.

APPENDIX M

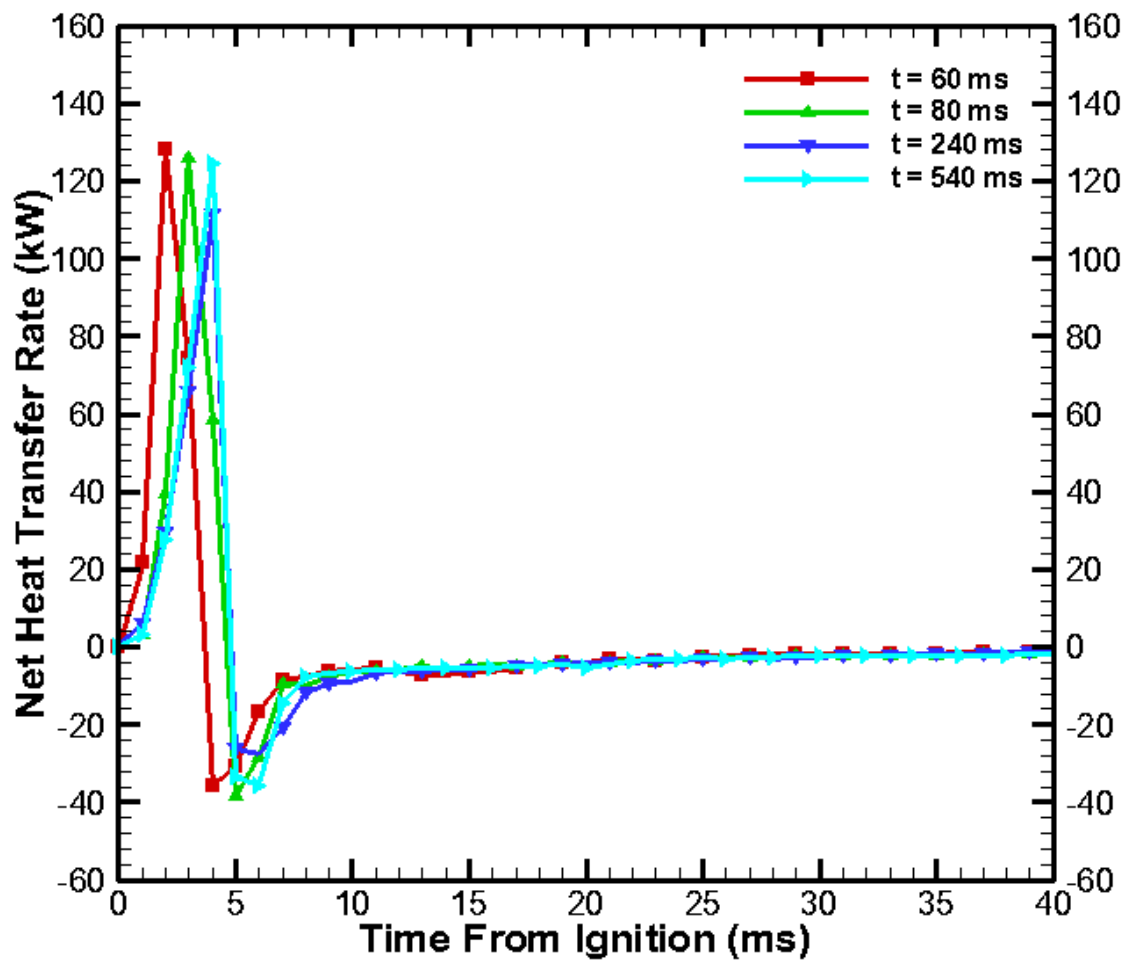
NET HEAT TRANSFER RATES USING N_{PRODUCTS}



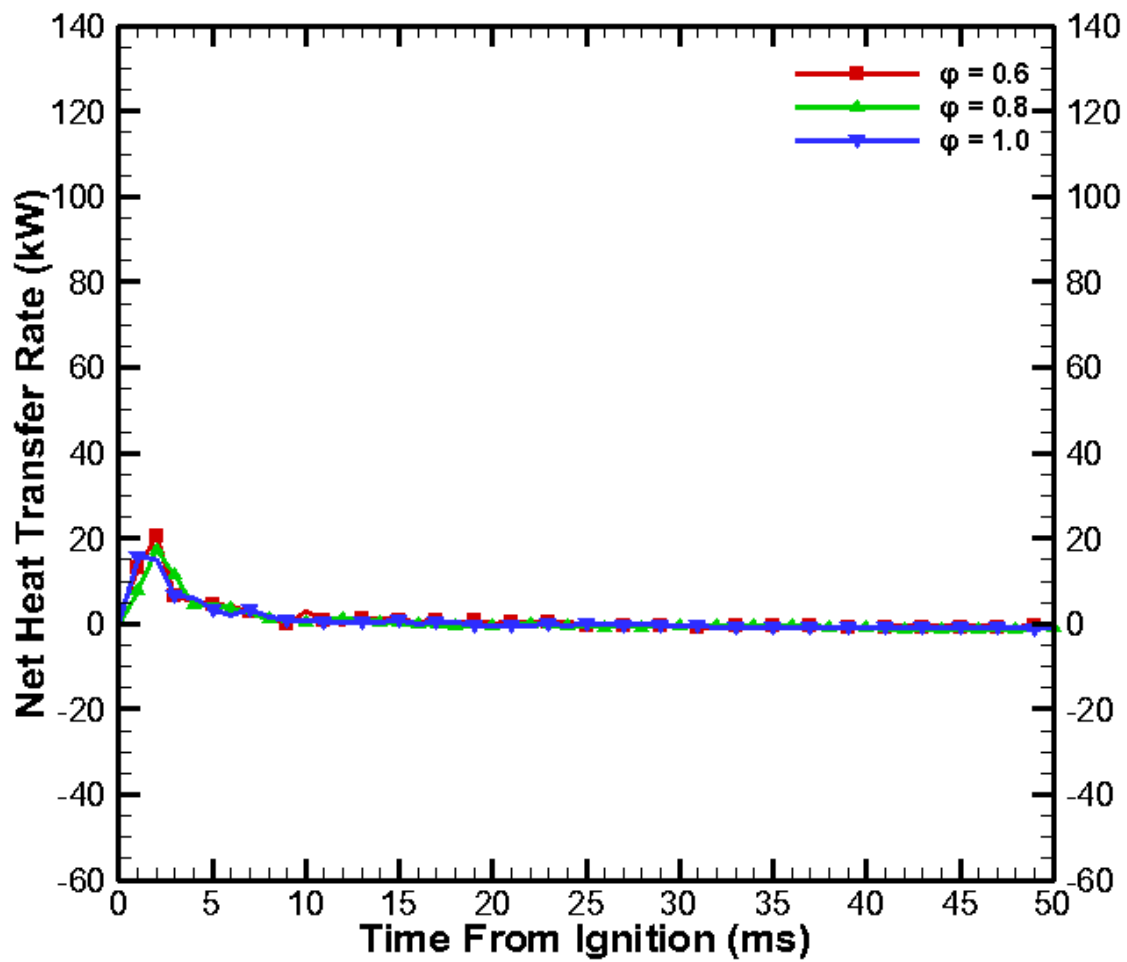
a) Net heat transfer rates for t = 3, 5, and 10 ms (Chapter 3).



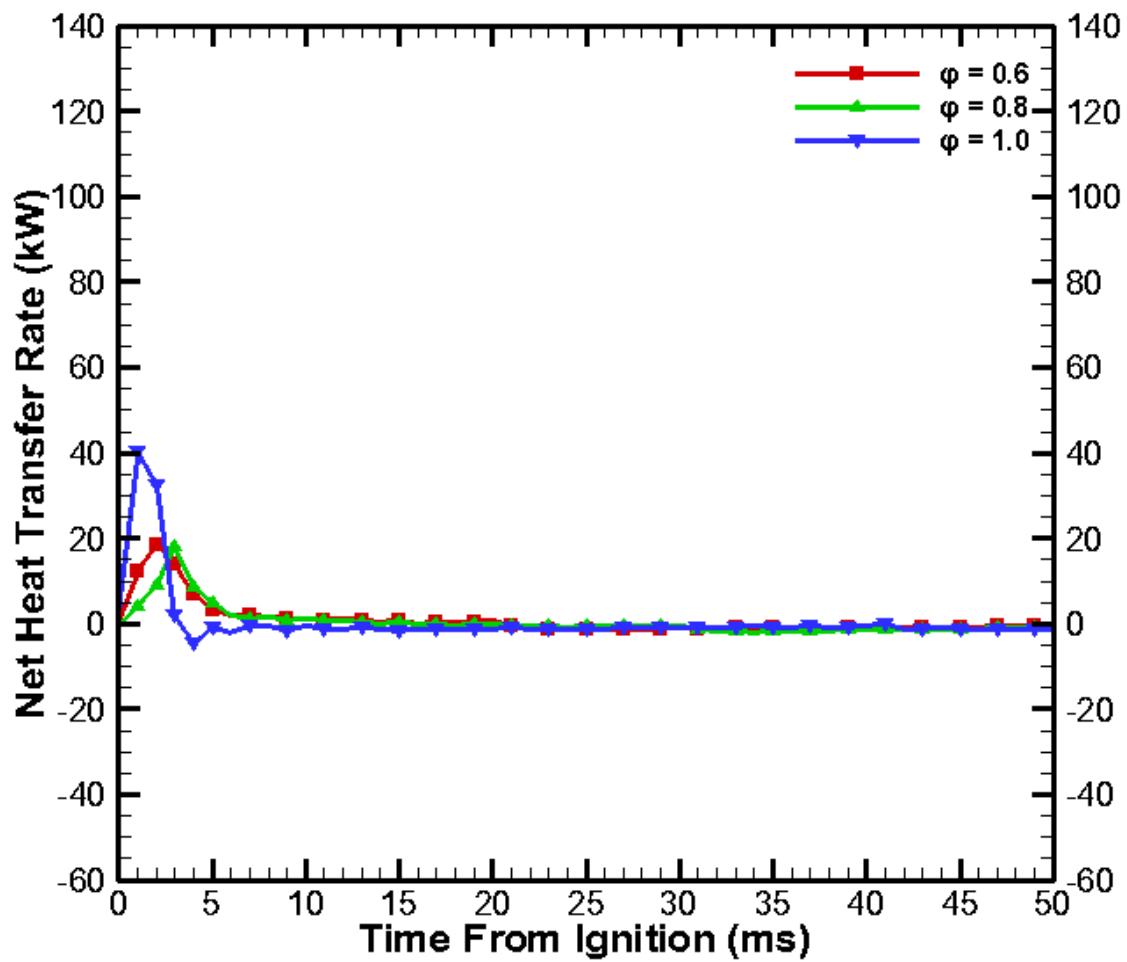
b) Net heat transfer rates for $t = 20, 30,$ and 40 ms (Chapter 3).



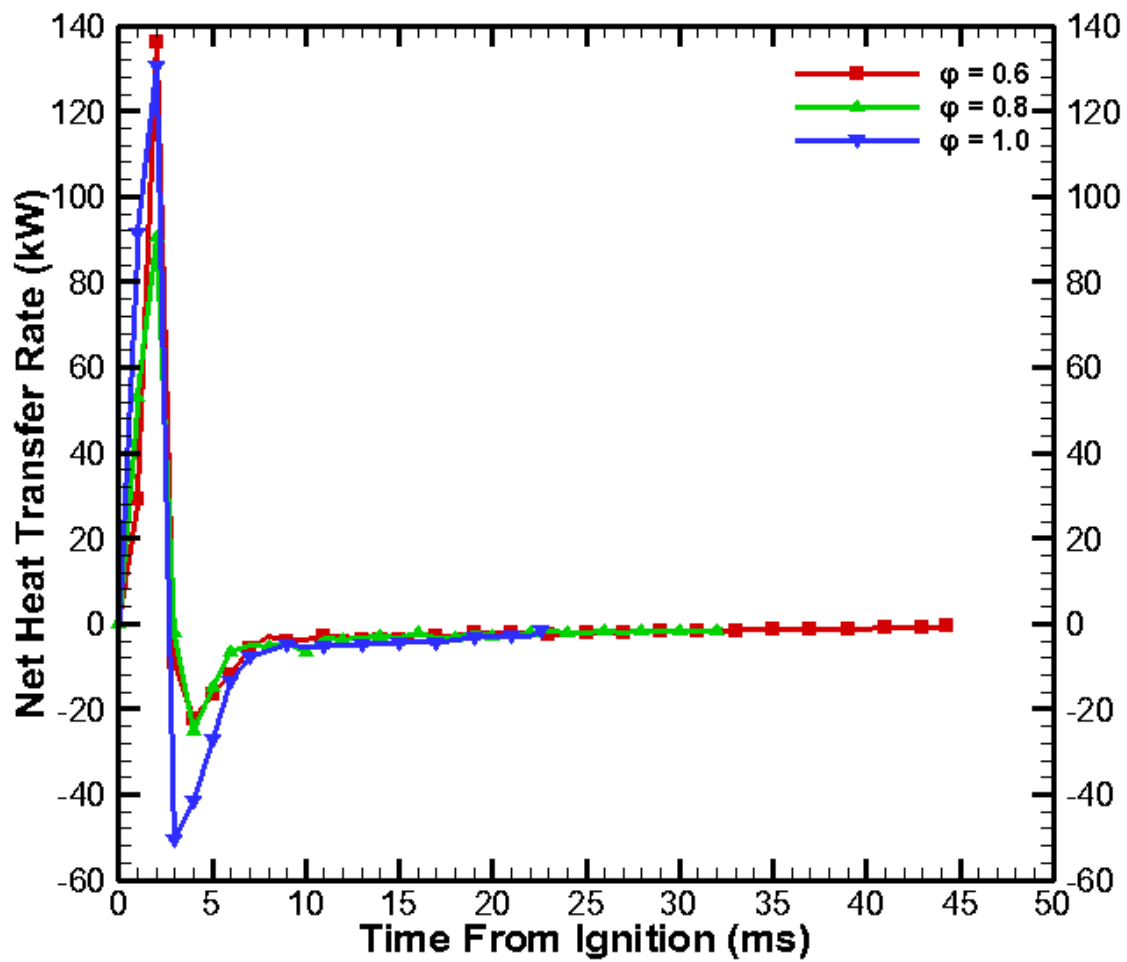
c) Net heat transfer rates for $t = 60, 80, 240,$ and 540 ms (Chapter 3).



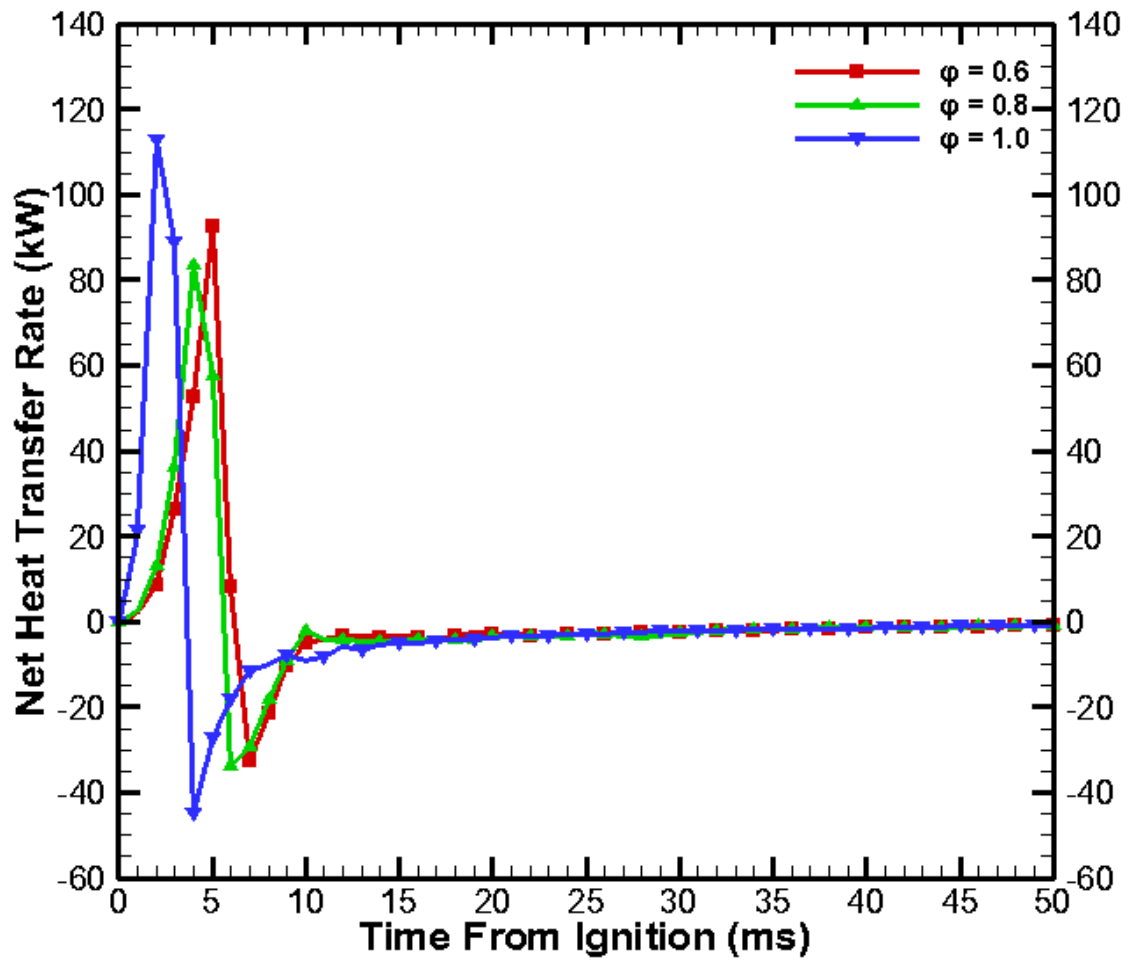
d) Net heat transfer rates at varying equivalence ratios for $t = 3$ ms (Chapter 4).



e) Net heat transfer rates at varying equivalence ratios for $t = 10$ ms (Chapter 4).



f) Net heat transfer rates at varying equivalence ratios for $t = t_{\text{end}}$ (Chapter 4).



g) Net heat transfer rates at varying equivalence ratios for $t = t_{\text{end}} + 50$ ms (Chapter 4).